INTERACTION OF WATER WAVES WITH A DENSITY-STRATIFIED FLUID IN A RECTANGULAR TRENCH

by
Francis Chi Kin Ting

W.M. Keck Laboratory of Hydraulics and Water Resources
Division of Engineering and Applied Science
CALIFORNIA INSTITUTE OF TECHNOLOGY
Pasadena, California

Report No. KH-R-50

June 1989

Interaction of Water Waves with a Density-Stratified Fluid in a Rectangular Trench

by

Francis Chi Kin Ting

Project Supervisor:

Fredric Raichlen
Professor of Civil Engineering

Supported by:

Office of Naval Research
Contract: N00014-84-C-0617

W. M. Keck Laboratory of Hydraulics and Water Resources
Division of Engineering and Applied Science
California Institute of Technology
Pasadena, California

Report No. KH-R-50 June 1989

Acknowledgements

I would like to thank my advisor, Fredric Raichlen, for suggesting the topic of this thesis and for offering his assistance throughout this investigation. I am grateful to him for introducing me to experimental research in water waves; I have always cherished this invaluable experience. I would also like to thank him for arranging my financial support.

I would like to thank members of my thesis committee: Professors Norman Brooks, John Hall, John List, and Ted Wu, for their time and suggestions. The discussions with Professors Gerald Whitham and Jörg Imberger are also appreciated.

I am indebted to many people who provided assistance throughout all phases of this research project. The entire staff of the hydraulics laboratory, Elton Daly, Rich Eastvedt, Joe Fontana, Leonard Montenegro, and Hai Vu, provided expert assistance in the design and construction of the experimental equipment. Dr. James Skjelbreia introduced me to the art of data acquisition and gave me his macros. Dr. Liyuan Liang and Dr. Rueen Fang Wang started me using TEX with their macros, which greatly facilitated the preparation of this document. I would also like to thank Nancy Tomer for her skillful drawings. Rayma Harrison, Gunilla Hastrup, and Joan Mathews were always there to help and gave me encouragement during hard times. They and the others gave W. M. Keck Laboratory a homey atmosphere.

I cannot express in words my deepest appreciation for having the opportunitiy

to receive a first class education at Caltech. It is here that I was first introduced to basic research; a world that was previously unknown to me. At Caltech I have learned deeper meaning between man and nature.

I dedicate this thesis to my parents without whose love and devotion this would not have been possible. They provided me with the best education possible in my earlier years, an opportunity which does not come naturally in the part of the world where I was born.

This study was funded by the Office of Naval Research under contract N00014-84-C-0617. This report was published through support of the Miriam and Omar J. Lillevang fund at the California Institute of Technology.

This report is essentially the thesis of the same title submitted by the writer on March 13, 1989 to the California Institute of Technology, in partial fulfillment of the requirements for the degree of Doctor of Philosophy in Civil Engineering.

Abstract

The interaction of normally incident time-periodic water waves with a density-stratified fluid in a rectangular trench is studied experimentally and theoretically; the fluid outside the trench is homogeneous.

This investigation has focused on the excitation of internal waves in the trench by surface waves, and the effects of the internal oscillations on the waves on the free surface. The study shows that, when the frequency of the incoming surface waves corresponds to the natural frequency of oscillation of the internal waves in the trench, the amplitude of the internal waves becomes large compared to the amplitude of the surface waves. The effects of the internal waves on the surface waves were very small in the experiments.

A two-layer model and a three-layer model are developed and applied to a particular constant-depth channel and trench configuration used in the experiments. The two-layer model is also applied to a rectangular trench in an infinite region. These models treat steady-state wave motions of infinitesimal amplitude for all ranges of fluid depth relative to the wavelength of the surface waves, and include a vigorous treatment of the effects of energy dissipation in the laminar boundary layers adjacent to the solid surfaces and at the density interface. In the two-layer model the stratified fluid in the trench is represented by two homogeneous fluids of different densities; in the three-layer model these two fluids are separated in between by a transition region of linear density variation.

Fresh water and salt water were used to model density stratification in the

experiments. The effects of surface wave amplitude and density distribution on the internal motion in the trench were investigated for small density differences compared to the density of water. A new technique using a scanning laser beam and detector system was developed to measure internal wave amplitudes. Satisfactory agreement with the theoretical predictions was obtained. The effects of nonlinearity and viscous dissipation on the internal motions were more pronounced when the depth of the heavier fluid was small compared to the wavelength of the internal waves in the trench.

For a trench in an infinite region, the two-layer model also predicts that large surface wave reflections occur when the trench is "at internal resonance," and a significant portion of the incident wave energy can be dissipated within the trench.

The investigation has provided insight with regard to both the dynamics of wave-trench interaction and the design of navigation channels in density-stratified fluids for reducing the potential of wave-induced internal resonance.

Table of Contents

List of Figures

List of Tables

List of Symbols

Symbol	Definition
	Roman Symbols
$A_j, \hat{A}_n, B_j, \hat{B}_n$	• coefficents of spatial complex potential function ϕ of two-layer fluid in trench region (3.1.20), (3.4.7) • coefficients of spatial complex fluid velocities u' and w' of three-layer fluid in trench region (3.2.53a), (3.2.53b)
a_{S_i}	amplitude of incident wave in infinite region (3.4.5)
arg	argument of a complex number
$2b$	width of wave tank
$(\ )_B$	subscript denoting the bottom boundary layer
$C, \hat{C}_n, D, E,$ $F, \hat{F}_n$	• coefficients of spatial complex potential function ϕ of homogeneous fluid in constant-depth channel region (3.1.22a), (3.1.22b) • coefficients of spatial complex fluid velocities u' and w' of homogeneous fluid in constant-depth channel region, (3.2.54a)–(3.2.54d)
$C, D, \hat{D}_n,$ $E, \hat{F}_n$	coefficients of spatial complex potential function ϕ of homogeneous fluid in infinite region (3.4.8a), (3.4.8b)
d	depth of rectangular trench
D_a	apparent diffusion coefficient
D_m	molecular diffusion coefficient (5.2.8)
$f(z)$	complex coefficient of w (3.2.11)
$(\ )_{F_{MW}}$	subscript denoting the free surface meniscus boundary layer

g	acceleration of gravity
h	• depth of homogeneous fluid outside the trench region • depth of lower fluid (§ 3.3.1)
h'	depth of upper fluid (§ 3.3.1)
h_0	characteristic depth of fluid (3.3.3)
h_1	depth of upper fluid
h_2	depth of lower fluid
$H_I(x)$	wave height of interfacial wave (3.1.36a)
$H_S(x)$	wave height of surface wave (3.1.35a)
H_{S_i}	wave height of incident wave (5.3.1)
H_{S_r}	wave height of reflected wave (5.3.1)
H_{S_t}	wave height of transmitted wave (5.3.1)
i	$\sqrt{-1}$
$(\,)_i$	subscript denoting the various fluid regions in constant-depth channel and trench
$(\,)_I$	subscript denoting the interfacial boundary layer
$(\,)_{I_{MW}}$	subscript denoting the interfacial meniscus boundary layer
$(\,)_j$	• subscript denoting the propagating mode in two-layer fluid; 1 for surface mode, and 2 for interfacial mode • subscript denoting the jth propagating mode in three-layer fluid; ($j = 1, 2, \ldots$)
J	number of propagating modes in three-layer fluid retained in truncated series (3.2.61)
k	wave number of propagating mode in homogeneous fluid (3.1.25a), (3.2.43a)
k_0	wave number of propagating mode in two-layer fluid at $O(\bar{\varepsilon}^0)$ (3.3.45c)
k_1	complex wave number of propagating mode in two-layer fluid at $O(\bar{\varepsilon})$ (3.3.45c)

$\hat{k}_n$	wave number of non-propagating mode in homogeneous fluid (3.1.25b), (3.2.43b)
K	• wave number in two-layer fluid (3.1.7), equals iK_j for propagating mode, and $\hat{K}_n$ for non-propagating mode • wave number in continuous stratified fluid (3.2.11), equals K_j for propagating mode, and $i\hat{K}_n$ for non-propagating mode
K_0	$\frac{\sigma^2}{g}$
K_j	wave number of propagating mode in two-layer fluid (3.1.18a) and in three-layer fluid (3.2.46a)
$\hat{K}_n$	wave number of non-propagating mode in two-layer fluid (3.1.18b) and in three-layer fluid (3.2.46b)
K_r	reflection coefficient
K_t	transmission coefficient
$\overline{KE}$	kinetic energy density of progressive wave (3.1.39), (3.2.73)
ℓ	width of rectangular trench
L	length of constant-depth channel measured from mean position of wave plate to upstream edge of the trench
$\mathbf{n}$	a directional unit vector pointing outwards from the fluid region
$(\ )_n$	subscript denoting the nth non-propagating wave mode
N	number of non-propagating modes retained in truncated series (3.1.28), (3.2.61)
$\mathcal{N}$	buoyancy frequency (3.2.13)
$\overline{\mathcal{N}}$	$\sqrt{\frac{g}{\delta}\frac{\Delta\rho}{\rho_1}}$ (3.2.44e)
p	pressure of fluid
$\overline{p}(z)$	mean pressure of fluid with respect to time
p'	pressure fluctuation of fluid due to wave motion
$\overline{PE}$	potential energy density of progressive wave (3.1.40), (3.2.74)

$\mathbf{q}$	coefficient of $\mathbf{U}$ (3.3.45b), (3.3.81b)
$\tilde{Q}_i(z)$	volume flux across a vertical plane, $\int_{-(h_1+h_2+\delta)}^{z} \tilde{u}' dz$ (3.2.62)
R	amplification factor (3.1.37), (3.2.70), (3.4.18)
R^*	amplitude ratio of interfacial wave to surface wave in two-layer fluid (5.2.18)
S	• stroke of bulkhead wave generator • surface boundary of fluid (§ 3.3.1)
t	time
T	wave period
u	component of fluid velocity in the x direction
u'	spatial component of u (3.2.52a)
$\tilde{u}'$	truncated series of u' (3.2.61)
$\mathbf{u}$	two- or three- dimensional fluid velocity vector, (u, w) or (u, v, w)
$\mathbf{U}$	rotational part of $\mathbf{u}$, (U, V, W) (3.3.8)
v	component of fluid velocity in the y direction
$\mathcal{V}$	inviscid core of fluid outside the boundary layers
w	component of fluid velocity in the z direction
$(\ )_W$	subscript denoting the side-wall boundary layer
w'	spatial component of w (3.2.52b)
$\tilde{w}'$	truncated series of w' (3.2.67)
x	x-coordinate of Cartesian coordinate system
x_N	local Cartesian coordinate with direction normal to the boundary layer and pointing into the inviscid core
x_{T_1}, x_{T_2}	local Cartesian coordinates with directions tangential to the boundary layer
$X(x)$	separable function of x (3.1.6)

y	y-coordinate of Cartesian coordinate system
z	z-coordinate of Cartesian coordinate system
$Z(z)$	separable function of z (3.1.6)
Z_j	normalized eigenfunction of propagating mode (3.1.19a)–(3.119b), (3.1.23a), (3.2.41a), (3.2.50a)–(3.2.50c)
$\hat{Z}_n$	normalized eigenfunction of non-propagating mode (3.1.19c)–(3.1.19d), (3.1.23b), (3.2.41b), (3.2.50d)–(3.2.50f)

Greek Symbols

α	• eigenvalue parameter • $\frac{\mu'}{\mu}$ (§ 3.3.1)
α^*	modulus of decay (3.3.116)
β	• eigenvalue parameter • $\frac{\rho'}{\rho}$ (§ 3.3.1)
λ	wavelength
σ	angular wave frequency, $\frac{2\pi}{T}$
σ_0	angular wave frequency at O($\overline{\varepsilon}^0$) (3.3.81c)
σ_1	angular wave frequency at O($\overline{\varepsilon}$) (3.3.81c)
δ	thickness of transition region in three-layer fluid
δ_w	Stokes length (3.3.2)
ρ	• density of fluid • density of fluid in lower layer (§ 3.3.1)
ρ_0	a reference density in the Boussinesq approximation (3.2.16)
ρ'	• fluctuation of fluid density due to wave motion • density of fluid in upper layer (§ 3.3.1)
$\overline{\rho}$	mean density of fluid with respect to time
ρ_1	density of fluid in upper layer

ρ_2	density of fluid in lower layer
$\Delta\rho$	$\rho_2 - \rho_1$
μ	• dynamic viscosity of fluid • dynamic viscosity of fluid in lower layer (§ 3.3.1)
μ'	dynamic viscosity of fluid in upper layer (§ 3.3.1)
ν	• kinematic viscosity of fluid • kinematic viscosity of fluid in lower layer (§ 3.3.1)
ν'	kinematic viscosity of fluid in upper layer (§ 3.3.1)
ξ	dimensionless boundary layer coordinate (3.3.41)
ϕ	spatial complex potential function (3.1.1), (3.4.1)
Φ	time-dependent complex velocity potential (3.1.1), (3.3.8), (3.4.1)
Φ_{S_i}	time-dependent complex velocity potential of incident wave in constant-density infinite region (3.4.6)
$\tilde{\phi}$	truncated series of ϕ
φ, ϕ	eigenfunction or trial function
θ	phase angle of time-periodic motion defined for $-180°$ to $180°$
Θ	$\frac{N^2}{\sigma^2} - 1$
η	vertical displacement of a density interface or of a fluid element from its undisturbed position
η_{Si}	free surface elevation of incident wave in homogeneous fluid (3.4.5)
η_0	complex coefficient of η (3.2.17), (3.2.69)
ε	boundary layer parameter (3.3.26), (3.3.43)
$\bar{\varepsilon}$	boundary layer parameter (3.3.46)

Special Symbols

$(\ )^*$	superscript denoting a complex conjugate or a dimensional quantity

$( )'$	superscript distinguishing a flow quantity of the upper fluid from that of the lower fluid (§ 3.3.1)
$( )_0$	subscript denoting a flow quantity at $O(\overline{\varepsilon}^0)$ (§ 3.3.1)
$( )_1$	subscript denoting a flow quantity at $O(\overline{\varepsilon})$ (§ 3.3.1)
∇	gradient operator $\equiv \left(\frac{\partial}{\partial x}, \frac{\partial}{\partial y}, \frac{\partial}{\partial z}\right)$
$\mathcal{L}$	$\equiv -\frac{d^2}{dz^2}$

Explanations:

1. The equation number gives the equation where the symbol is defined.
2. When a section number appears in the definition, the meaning of the symbol is only used in the specified section.

1. INTRODUCTION

1.0 Introduction

This study is concerned with the generation of internal waves in a submarine trench that is partially filled with a heavier fluid; the fluid outside the trench is homogeneous. Such a situation may occur in harbors where the bottom is composed of very fine sediment.

Sediment is carried into the harbors by various coastal processes, which may include the following: onshore/offshore movement of sand by swell and storm waves, longshore transport due to wave and current action, and sedimentation from freshwater inland sources. In most cases, the sediment carried by longshore transport is composed of coarse material such as sand, which usually forms firm deposits on the bottom (sand bars). This must be dredged from harbor entrances and navigation channels to maintain the required underkeel clearance for smooth operation of the waterways. Thus, coarse material would not be of major concern with regard to the questions raised in this investigation.

On the other hand, sediment deposited from freshwater inland sources usually contains a significant portion of fine material such as silt and clay. Waves, currents, and the passage of ships can keep some of this material in suspension. Hence, in harbors with bottoms composed of fine materials there is usually a dense layer near the bottom with the thickness of this layer increasing because of major storms

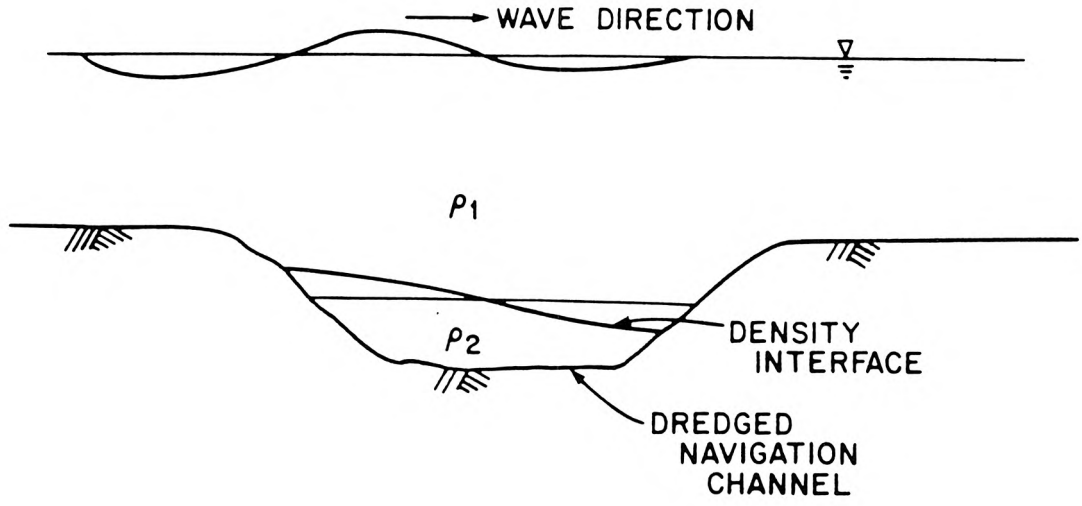

Figure 1.1. Schematic drawing of a dredged navigation channel.

and other extreme events. Indeed, because of this, in those harbors it is difficult to define the actual elevation of the bottom. For example, at Europort (Holland) the bottom is defined as that elevation where the specific gravity of the silt-water mixture is 1.2. In this country an example of a harbor where this type of dense lower layer is present is in Norfolk, Virginia. Such a layer could exist in a navigation channel dredged into the bottom where fine sediments are put into suspension by waves, currents, ships, etc. The density-stratified fluid in these channels can have an influence on the kinematics around the perimeter of the trench as a result of internal waves generated in the stratified fluid. The excitation of internal waves, which can affect the water particle velocities in the trench, is the subject of this study.

An important aspect of wave-trench interaction with a heavier fluid in the trench is the excitation of internal waves within the trench; this is illustrated in figure 1.1. The dynamic pressure from surface waves propagating past the trench induces a flow in the trench that displaces the dense fluid and, through the action of buoyancy forces, generates internal waves that propagate to-and-fro between the walls of the trench. When the frequency of the propagating surface waves corresponds to the natural frequency of the internal motions in the trench, the interfacial waves can attain large amplitudes relative to the surface waves, due to the comparatively small potential energy involved in a given deformation of the density interface. Thus, for a particular trench geometry relative to the characteristic length scale of the surface waves, the density-stratified fluid within the channel may be excited into a mode of resonant oscillation.

The motivation for this work is the effect of waves on dredged navigation channels with a layer of fine sediment in suspension near the bottom. Resonant oscillations of internal waves in such channels are of engineering importance because large amplitude fluid motions within the trench would result in locally large velocities near its boundaries, leading to more serious bottom erosion. Because of this, more sediment would be entrained in the bottom regions than would normally occur near a bottom that is undisturbed by internal waves. Because the wave-induced oscillations within the dredged channel are related directly to the spectral energy content of the incident waves, in different locations certain specific dimensions may be more susceptible than others to these motions. Hence, with regard to maintenance dredging in harbors, more maintenance would be required in some channels.

The density stratification in a navigation channel can also affect ship maneuverability. The phenomenon of "dead water" is a well-known experience to seamen in the polar regions. Along the Norwegian coast, in regions where ice melts or where rivers flow into the fjords, a light layer of fresh water frequently overlies heavier

saline water. If the density interface is near the keel of a ship, at certain speeds the ship must spend large amounts of power on the creation of internal waves. Thus, it is anticipated that ships navigating in stratified channels could also generate internal waves, and with the possibility of internal resonance, the hydrodynamic forces on vessels may be significantly different from those experienced in unstratified channels.

1.1 Objectives and Scope

The objective of this study is to examine, both experimentally and theoretically, the dynamics of internal wave motion in a stratified rectangular trench due to surface waves that propagate in a direction perpendicular to the longitudinal axis of the trench. We hope to be able to infer the kinematics from the dynamics of the interfacial motion within the trench, and hence the effects of density stratification on the channel shape.

It is intended that the results of this study will assist in the design of navigation channels that may be density-stratified to reduce the potential of wave-induced internal resonance. However, this study does not present a comprehensive numerical model that would incorporate nonlinear effects, arbitrary density stratification, and variable trench geometry. Instead, several theoretical models were constructed to approximate various flow situations and the results were compared with experimental measurements. This approach, we hope, can offer physical insight into the dynamics of wave-trench interaction in a stratified fluid.

A common method for treating wave propagation over a bottom where the depth changes discontinuously is to find the solutions of wave motions in separate regions of constant depths and then match the solutions at the common boundaries of the different fluid regions. This method will be used to treat the problem of wave interaction with a rectangular trench that contains a heavier fluid in the trench. In

the experimental phase of this study, we require that the theoretical results can be compared directly to the experimental measurements. The case of a trench in an infinite ocean could not be modelled in the laboratory due to wave reflections from the ends of the wave tank. Hence, much of the theoretical work will be done with a chosen experimental set-up. The theoretical predictions obtained will be compared to the experimental results. The problem of wave propagation over a rectangular trench in an infinite region will be studied only theoretically.

As surface waves propagate past the channel, the flow conditions within the trench can be related to changes in the velocity near the bottom due to the geometry of the trench and the effect of flow separation at its edges. For water, viscous effects are primarily limited to the boundary layers near the trench perimeter and regions of flow separation, so that the general pattern of velocities outside the boundary layers can be predicted reasonably well by the inviscid theory. Indeed, flow separation at the edges of the trench may yield a flow within the trench that is very different from that described by an inviscid model. For this reason, the inviscid problem will be investigated first, followed by a treatment of viscous dissipation by boundary layer methods, and the treatment of flow separation will be discussed only with respect to the experimental results. It will be assumed that the fluid motions in the trench are excited by small amplitude water waves, and the models that will be developed are valid for all ranges of water depth relative to the wavelength of the surface waves. The interfacial wave amplitude is greatly enhanced if radiation losses from the trench region are reduced, so that energy of the internal wave is largely trapped within the channel. Hence, it will be assumed that the stratified fluid is confined to the trench, and outside the trench the fluid is assumed to be homogeneous.

Among the density distributions that will be considered, the two-layer fluid that will be considered first represents the simplest case of density stratification, and may be a reasonably realistic model for stratified channels. In addition, the most

prominent internal waves are those generated at a sharp density interface. Because in a miscible fluid a density discontinuity is evened out by molecular diffusion and wave-induced internal mixing, the effects of a diffuse interface will be examined and treated as a three-layer model. In the analysis, a diffuse interface is approximated by a three-layer fluid composed of two homogeneous fluids of different densities separated by a transition region of linear density variation. In order to formulate this problem analytically, the Boussinesq approximation will be made. This neglects variations of density in the Navier-Stokes equations in so far as they affect inertia, but retains them in the buoyancy term. Thus, the three-layer model is limited in its application to a fluid whose overall density variations are small.

If the effects of flow separation are neglected, the maximum amplitudes of the internal waves in the trench are limited by viscous dissipation in the boundary layers and radiation losses from the trench region; the latter represent the energy in the surface waves scattered by the trench. The theoretical analysis will include a vigorous treatment of the effects of energy dissipation using boundary layer methods; the fluid motion within the boundary layer is assumed to be laminar. In the two-layer model, it will be assumed that viscous dissipation takes place in the boundary layers adjacent to the density interface and at the solid surfaces. In the three-layer model the density of the stratified fluid in the trench is continuous, hence energy dissipation in the boundary layers is significant only at the solid surfaces. The effects of wave damping will be incorporated into the inviscid models by a perturbation expansion scheme.

Laboratory experiments were done to verify the analyses. The response of a fresh water–salt water fluid in a rectangular trench in a wave tank, to surface waves generated by a bulkhead wave generator, was studied by varying the surface wave height, the wave period, and the density distribution in the trench. The major objectives of the experimental investigation have been to test the validity of the

theoretical models, and to examine the importance of different physical effects such as density stratification and viscous dissipation on the dynamics of wave-trench interaction.

1.2 Thesis Outline

In Chapter 2, a review of previous work relevant to this study is presented. Chapter 3 contains the theoretical analysis performed for this study. This analysis consists of a two-layer model and a three-layer model both applicable to small amplitude simple-harmonic wave motion in an inviscid fluid, a treatment of wave damping in the two-layer fluid and the three-layer fluid by boundary layer methods, and a perturbation scheme to incorporate the effects of energy dissipation in the boundary layers into the two-layer and the three-layer inviscid models. These are applied to a particular configuration of a rectangular trench in a wave tank, which permits definitive experiments to be conducted and compared to the theory. Then the problem of wave propagation over a rectangular trench with a two-layer fluid in the trench and a homogeneous fluid in an infinite region outside the trench is formulated in a similar manner. The experimental equipment and procedures used in this study are described in Chapter 4. In Chapter 5, the results of laboratory experiments and theoretical models are presented and discussed. The major conclusions drawn from this investigation are presented in Chapter 6.

2. LITERATURE REVIEW

2.0 Introduction

The study of wave-trench interaction is closely related to other studies pertaining to wave propagation over rapidly changing bottoms. That is, bottoms where the fractional changes in the depths of the fluid are large within a wavelength of the propagating waves. This is because the methods used to treat these problems are often very similar. Submarine features that belong to this category include continental shelf-breaks, seamounts, and submarine canyons. Artificial structures may include submerged breakwaters and navigation channels. Numerous studies have been devoted to the phenomenon of wave scattering, in which strong wave reflection can occur for suitable dimensions of the bottom obstacle relative to the wavelength of the propagating waves. For stratified fluids, the generation of internal waves through interaction of surface waves with the ocean bottom has also received a lot of attention. Practical interests of these phenomena may be related to tsunamis propagation from deep ocean onto the continental shelf, the coastal generation of internal tides, protection of harbors from storm surge by submerged breakwaters, as well as maintenance dredging in navigation channels.

This chapter will review literature relating to wave propagation over rapidly changing ocean bottoms. The literature that relates to homogeneous fluid is reviewed first. This is discussed because many of the techniques used in treating this

problem are also applicable to a layered fluid. Next, previous work on stratified flows that have relevance to this study will be covered. Wave damping due to boundary friction, which has not received much attention in previous studies, plays an important role in internal wave generation in submarine trenches. The techniques that have been used in the past to study this process will also be reviewed.

2.1 Surface Wave Propagation over Rapidly Changing Bottoms

When the wavelength of the surface waves is large compared to the horizontal length scale of depth variation, the uneven bottom may be approximated by a series of separate regions of constant depths. The solution of the problem generally falls into one of two basic approximate theories, a linear theory in which the wave amplitude is sufficiently small compared to the wavelength and the water depth, and the shallow water theory where the depth of the fluid is considered small with respect to a characteristic wavelength. The shallow water theory also leads to a nonlinear theory for initial value problems. Because the focus of this study is on linear problems, the literature review will be limited to the linear approaches.

In problems related to surface wave scattering by bottom obstacles, almost all researchers have treated the fluid as inviscid. The linear inviscid problems are often solved for steady-state flow conditions also, because more general cases could be treated using Fourier superposition. The inviscid assumption and the steady-state condition lead to potential flow problems of the boundary value type. Some investigators have treated steady-state potential flow problems by conformal mapping. A general analysis of this method for wave propagation over variable-depth geometries was given by Kreisel (1949); the two-dimensional fluid domain was mapped into a rectangular strip, and the velocity potential was obtained in the form of a linear integral equation solvable by iteration for some regular bottom geometries. Asymptotic solutions were found by Kreisel (1949) for the upper and lower bounds of the

reflection coefficient, which is defined as the ratio of the amplitude of the reflected wave to the amplitude of the incident wave. The term "transmission coefficient" is also used in wave diffraction problems, this is defined as the ratio of the amplitude of the transmitted wave to the amplitude of the incident wave. Kreisel (1949) also derived some theorems that can be used to compare the reflection coefficients for obstacles of different sizes or geometries. The conformal mapping algorithm developed by Kreisel (1949) was applied by Miles (1982) to obtain the reflection coefficient for a rectangular trench where the depths before and after the trench were equal (symmetric trench). In his analysis, Miles assumed that the surface wave was long when compared to the width of the trench and the water depth.

The conformal mapping approach, though elegant in its mathematical composition, often presents the solution in an intricate implicit form, which is not suitable for numerical evalution. A common method employed in the solution of problems involving abrupt transitions of fluid depth is to match the solution along a boundary that separates the regions of different depths. In this method the fluid domain is divided into separate regions of constant depths. Horizontal velocities and velocity potentials are matched along common fluid boundaries. The matching procedure results in sets of linear integral equations, which may be solved by a host of approximate methods. Examples of this approach are found in Bartholomeusz (1958), Newman (1965b), Miles (1967), Mei and Black (1969), and Kirby and Dalrymple (1983). As an example, Newman (1965b) studied the reflection and transmission of waves normally incident on a single step between finite- and infinite-depth regions. Newman expanded the velocity potential as an infinite series of a complete, orthonormal set. Physically, the fluid motion was described by a linear superposition of progressive waves propagating in both directions, and locally bounded standing waves that decayed exponentially with distance from the step. The series expansion of the velocity potential was truncated after a finite number of terms, and the re-

sult was a finite system of algebraic equations, which were solved numerically with standard methods. In this manner the velocity potential was found for the entire fluid domain.

Miles (1967) presented a variational method to obtain an approximate solution for waves scattered by a single step between two finite-depth regions, without the necessity of solving the integral equations directly. After matching the horizontal velocities and velocity potentials at the step, Miles related the complex transmission and reflection coefficients, which included both the amplitude and phase of the scattered waves, to a "scattering matrix" that had associated variational integrals. The variational integrals were functions of the unknown horizontal velocities at the step, and their values were stationary with respect to first-order variations of a trial velocity about the true velocity at the step. Specifically, Miles (1967) used the horizontal velocities of the propagating waves in the constant-depth regions before and after the step as a first order approximation to the unknown horizontal velocity at the step; the contributions of the non-propagating standing waves were neglected. The scattering matrix determined therefrom was correct to the second order according to the variational principle. Miles applied the variational formulation to the asymptotic case of a single step between finite- and infinite-depth regions, and achieved good results compared to the numerical solution by Newman (1965b) in the far field of an infinite step. Note that the near-field solution, where the non-propagating standing waves are of first order importance, cannot be found by this method. Thus, the variational approach cannot be used to study the problem of oscillation of internal waves in a trench that is density-stratified.

Lee, Ayer, and Chiang (1980), and Lee and Ayer (1981) studied surface wave diffraction due to a submarine trench. These investigators presented a transform method that is quite effective for an arbitrary shaped trench. In their method an unknown vertical velocity distribution was located along a line drawn across the

"mouth" of the trench, separating the fluid domain into two regions: an infinite rectangular region of constant depth and a finite region representing the trench itself. An explicit solution for each region was then found in terms of this unknown vertical velocity distribution across the "mouth" of the trench. In the infinite region outside the trench the solution was found by Fourier transform. In the trench the solution was found by separation of variables for a rectangular trench (Lee and Ayer, 1981), and by the boundary integral method for a trench of irregular geometry (Lee, Ayer, and Chiang, 1980). The final solution was obtained by matching the vertical velocities numerically along the common fluid boundary.

The methods discussed above are valid for all ranges of water depth relative to the wavelength of the propagating waves. The asymptotic behaviour in the limit of shallow water waves can be obtained by letting $kh \to 0$, where k is the wave number and h is the water depth. In general, the long wave theory as treated in Lamb (1945, § 169) is derived separately by assuming that the vertical acceleration is negligible, so that the momentum equation in the vertical direction reduces to an equation of hydrostatic pressure. Consequently, the horizontal velocity is independent of the vertical coordinate z. Lamb (1945, § 176) obtained the transmission and reflection coefficients for a long wave propagating over a single step between finite-depth regions, by imposing continuity of total mass flow and surface elevation at the step. Bartholomeusz (1958) questioned that the hydrostatic assumption is invalid in the neighborhood of the step. Bartholomeusz formulated the same problem for arbitrary kh and showed that Lamb's result is the correct asymptotic limit as $kh \to 0$. Miles (1967) pointed out that Lamb's assumptions are equivalent to neglecting the non-propagating standing waves as $kh \to 0$; a solution that neglects the non-propagating standing waves is often called a plane-wave approximation. Miles (1967) constructed a plane-wave approximation for arbitrary kh for the problem of wave propagation over a step between finite-depth regions and compared with the

more accurate numerical results obtained by Newman (1965b) for the asymptotic case of a single step between finite- and infinite-depth regions. Miles (1967) showed that the plane-wave approximation to the magnitude of the transmission coefficient was within 5% of Newman's result (1965b) for all wavelengths, but the corresponding approximation to the reflection coefficient was satisfactory only for small values of kh. Kirby and Dalrymple (1983) studied the diffraction of obliquely incident surface waves by an asymmetric trench, where the water depths before and after the trench were constant but not necessarily equal. Kirby and Dalrymple used both the more accurate numerical technique in Newman (1965b) and the plane-wave approximation, and found significant differences between the two results for all ranges of wavelength in one case where the ratio of the water depth in the trench region to that in the infinite region was large. These studies indicate that the locally bounded non-propagating waves can affect the wave scattering process significantly.

For a rectangular trench, Lee and Ayer (1981) considered wave propagation in a direction perpendicular to the longitudinal axis of the trench only, whereas Miles (1982), and Kirby and Dalrymple (1983) dealt with obliquely incident waves also. In addition, Kirby and Dalrymple (1983) treated the more general problem of an asymmetric trench. It is noted that surface wave diffraction due to an asymmetric trench with a heavier fluid in the trench had been studied by Lassiter (1972); this work will be discussed more fully in § 2.2. It was found that, for a particular symmetric trench where the water depths before and after the trench were equal, there existed an infinite number of discrete wave frequencies at which the incident wave was fully transmitted, the maximum and minimum values of the transmission and reflection coefficients appeared periodically, but the effect of the trench on wave transmission decreased monotonically as the wave number increased. For the plane-wave approximation, total transmission of an obliquely incident wave occurred for $k\ell = n\pi$, $n = 0, 1, 2, \ldots$ (even mode), and maximum reflection occurred for

$k\ell = (n - \frac{1}{2})\pi$, $n = 1, 2, \ldots$ (odd mode), where k is the wave number component normal to the trench axis for the propagating waves in the trench region, and ℓ is the trench width. For the full problem, which includes both the propagating and non-propagating waves, the above results are corrected by a phase shift, which can be large for a deep trench. It was shown in Lighthill (1980, § 3.3) that the effect of the bottom on the surface wave is negligible when the ratio of the water depth to the wavelength of the surface wave is greater than 0.28, because the kinetic energy at the bottom is reduced to approximately 3% of that in the entire fluid column. Hence, for a symmetric trench, the change in water depth at the trench has a negligible effect on wave transmission when the wave number is sufficiently large. However, the results of Lassiter (1972), and Kirby and Dalrymple (1983) showed that in the case of an asymmetric trench, the reflection coefficient is non-zero for all ranges of wave number. For obliquely incident waves, Miles (1982), and Kirby and Dalrymple (1983) showed that the transmission coefficient is greatly reduced when the wave number component for the incident wave in the direction of the trench axis exceeds the wave number for the propagating waves in the trench region.

So far, the primary interest in submarine trenches was in the scattering of the surface waves. No attention was given to the dynamics of the fluid within the trench itself. Ting and Raichlen (1986) investigated the motion of fluid in a rectangular trench due to normally incident periodic waves. Ting and Raichlen defined the kinetic energy ratio:

$$KE_r = \frac{KE_t}{KE_i} \tag{2.1}$$

where KE_t is the average kinetic energy over one wave period per unit area of the fluid within the trench, and KE_i is the average kinetic energy per unit area of the incident wave in the infinite region. Using the formulation of Lee and Ayer (1981), Ting and Raichlen (1986) computed the frequency response of KE_r for various channel-trench aspect ratios. The kinetic energy ratio had the periodic

behaviour as in the transmission and reflection coefficients, which could be related to a resonant condition in the trench. However, $KE_r < 1$ for the typical trench geometries studied. Thus it appears that trench resonance in a homogeneous fluid does not enhance fluid motion within the trench to a significant extent.

2.2 Internal Wave Studies

In this section previous work on internal waves that has relevance to this study will be reviewed. Interest will be focused on the generation of internal waves through interaction of surface waves with submarine topographic features. This is discussed because many of the physical processes involved and their methods of analysis can be related to the problem of wave-trench interaction in a stratified fluid. The linear approaches will be emphasized here. A wealth of knowledge on stratified flows, including many results on internal waves, can be found in the books by Turner (1973) and Yih (1980).

Of interest to this study is the transfer of wave energy between surface and internal waves due to large variations of the bottom topography within a wavelength of the surface waves. An example of this process is given by the coastal generation of internal tides. The energy transfer from surface tides to internal tides typically takes place at the steep continental shelf-breaks; a similar situation can also occur at a submarine trench with a heavier fluid in the trench. The oceanic thermocline is often very sharp, whereas the fractional change in density over the total depth is small: of the order of a few parts per thousand. The most prominent internal wave is given by the lowest internal mode, which has a wavelength much larger than the thickness of the diffuse density interface, so that the fluid motion is close to that in a two-fluid system. Rattray (1960) obtained analytical solutions for internal tides generated at a continental shelf-break, using the long wave equations in a rotating two-fluid system. The resulting internal tides removed energy continuously from

the surface tides by forming internal progressive waves that travelled seawards. The amplitude of the internal tides could be large compared to the surface tides. Kelly (1969) studied wave diffraction in a two-layer fluid due to a step change in the fluid depth, where the fluid in the shallower region was homogeneous and the fluid in the deeper region was two-layer stratified. Kelly formulated the problem in the same manner as Miles (1967) for the constant density case; transmission and reflection coefficients were obtained by matching horizontal velocities and velocity potentials for the separate regions of constant depths along a vertical boundary at the step and by applying the variational approximation used by Miles. Kelly's analysis approached the homogeneous fluid result as $\rho_1/\rho_2 \to 1$ for fixed $K_0 h$, where $K_0 = \sigma^2/g$, σ is the circular wave frequency, g is the acceleration of gravity, h is the total depth of the two-layer fluid, and ρ_1 and ρ_2 are the density of the upper fluid and of the lower fluid, respectively. On the other hand, if ρ_1/ρ_2 was allowed to approach unity in the shallow water limit, the analysis yielded Lamb's results (1945, § 176) for the transmitted and reflected surface wave amplitudes due to an incident wave, whereas the amplitude of the resulting internal wave tended to infinity. Kelly (1960) showed that the shallow water theory is applicable only if the ratio $K_0 h/(1 - \rho_1/\rho_2)$ is sufficiently small. Hence, an additional scale parameter is involved in developing approximate theories with regard to internal long waves, namely the fractional change in density over the total depth of the fluid.

Lassiter (1972) solved for the transmission and reflection coefficients in the case of normally incident progressive waves propagating past an asymmetric trench with a two-layer fluid in the trench. Lassiter formulated the problem in terms of complementary variational integrals and by matching horizontal velocities and velocity potentials for the trench regions and the regions before and after the trench along vertical boundaries at the upstream and downstream edges of the trench, in a manner similar to Kelly (1969) for a single step. However, Lassiter's variational

formulation yielded the upper and lower bounds for the transmission and reflection coefficients. As in Miles (1967), the variational method does not yield the velocity potential in the near field, hence the internal wave motions in the trench were not studied. Lassiter (1972) applied his formulation to the asymptotic case of a homogeneous fluid, but the results for the homogeneous case were shown to be incorrect by Kirby and Dalrymple (1983).

In the case of a layered system where homogeneous fluids of different densities are separated by surfaces of density discontinuity, the fluid motion in each layer may be supposed to be irrotational; a potential function may be defined in each layer, as in the work of Kelly (1969) and Lassiter (1972). The fluid motion is not irrotational in a continuously stratified fluid, due to the generation of vorticity. This special feature of stratified flows can be deduced from the Navier-Stokes equations (see Turner, 1973, p. 7). Working directly from the equations of motion, Love (1891) derived the differential equation (Love's equation) governing infinitesimal wave motion of an inviscid, incompressible continuously stratified fluid. For simple-harmonic motion, the governing differential system is reduced to a Sturm-Liouville system, from which many properties of infinitesimal waves in a heterogeneous ideal fluid may be derived. A unified treatment of this problem was given by Yih (1960). Additional results with regard to the properties of the eigenfunctions and corresponding eigenvalues were given by Yanowitch (1962).

Simple analytical solutions of the Sturm-Liouville system are not possible in general; the exponential density distribution is the only known case to have analytical solutions for both finite and infinite fluid depths (see Burnside (1889), and Love (1891)). A linear density profile, accompanied by the Boussinesq approximation, also has analytical solutions. The Boussinesq approximation neglects variations of density in the Navier-Stokes equations in so far as they affect inertia, but retains them in the buoyancy term. Propagation of internal waves on sloping bottoms

for the case of constant density gradient had been studied in detail by Wunsch (1968,1969). However, the more important density structure for this study is a three-layer fluid in the trench region; the continuously stratified fluid is composed of two homogeneous fluids of different densities separated in between by a transition region of linear density variation. The three-layer density distribution is a closer realization than the two-fluid system to the actual density profile in the trench that contains a diffuse salinity interface. The three-layer density distribution has been used by many investigators to approximate the oceanic thermocline. For example, Sanford (1984) had employed a three-layer model to study interaction of high frequency internal waves with the bottom boundary layer. A numerical approach to solving the Sturm-Liouville system is necessary for other density structures.

The nature of the standing internal waves within the trench is a major concern in this study. Thorpe (1968) had made an extensive study, both theoretical and experimental, of standing internal waves at the interface of two fluids and in a continuously stratified fluid. For the two-layer problem, his method of analysis followed that of Penney and Price (1952) on standing surface waves of finite amplitude, and Hunt (1961) on standing internal waves at the interface between two semi-infinite fluids. The procedure is similar to the perturbation scheme in Stokes second order progressive surface wave theory. Thorpe (1968) represented the finite amplitude wave solutions in the form of power series expansions with respect to the wave slope as the expansion parameter. As in the finite amplitude surface wave, the second order term of the internal wave solution distorts the symmetric waveform of the linear solution given by the first order term, whereas the distance from trough to crest remains the same for second order approximation. The ratio of the coefficient of the second order term to that of the first therefore represents a measure of nonlinear effects in the finite amplitude internal wave. Thorpe (1968) showed that the presence of the upper fluid reduces the amplitude of the higher harmonics

in the wave profile. This conclusion was first reached by Hunt (1961) on standing waves at the interface between two semi-infinite fluids.

Thorpe (1968) checked his finite amplitude wave theory with experiments in three depth limits: (a) a deep upper fluid and a deep lower fluid; (b) a shallow upper fluid and a deep lower fluid; and (c) a shallow lower fluid and a deep upper fluid. Thorpe's experimental apparatus consisted of a rectangular tank with transparent perspex walls at front and back, and side walls fitted with plungers that could be moved in and out of the tank in simple-harmonic motion. The fluids in the tank were fresh water and salt water; these were contained in a polythene bag, which was itself supported by the tank. The plunger motion generated the standing internal waves whose amplitudes were measured using a vertical rule. Thorpe's experiments were limited to weakly nonlinear waves where the second order effects in the internal wave profiles were small compared to the first order effects, and Thorpe obtained good agreement between the observed and predicted wave profiles.

2.3 Wave Damping

In this section the literature that relates to wave damping is discussed for homogeneous fluid and for stratified fluid, the literature review is limited to linear theory with laminar boundary layer flows. It is noted that laminar boundary layer flows are applicable mainly to laboratory conditions (see, for example, Zelt, 1986), but with controlled laboratory experiments, they can offer physical insight into the competitive role of damping among other physical effects.

The damping of periodic progressive surface waves advancing down a uniform rectangular channel has been studied by Biesel (1949), Ursell (1952), and Hunt (1952), among others. They considered, respectively, a channel of finite depth but of infinite width, a channel with side walls but of infinite depth, and a channel of finite width and depth. It was assumed that the motion was to a first approximation

irrotational, except near the boundaries where viscous boundary layers of thickness proportional to $(\nu/\sigma)^{1/2}$ were formed, where ν is the kinematic viscosity of the fluid and σ is the circular wave frequency. Energy dissipation took place in (a) the boundary layers adjacent to the solid surfaces, (b) the boundary layer at the free surface, and (c) the body of the fluid. These contributions were respectively proportional to $\nu^{1/2}$, $\nu^{3/2}$ and ν (see, for example, Mei, 1983). Thus the boundary layers adjacent to the solid surfaces contributed most of the dissipation. Viscosity caused a slow attenuation of the wave amplitude and also decreased the phase speed of wave propagation. For plane progressive waves advancing down a rectangular channel, the difference in the flux of wave energy between two vertical sections of the channel must be equal to the rate of energy loss in the fluid between the two vertical sections. Hence, by balancing energy propagation and dissipation in this control region, the rate of amplitude attenuation was found. There are shortcomings in this method of analysis, which yields only the attenuation rate of the wave amplitude, but not the change in wavelength (or phase speed) due to viscosity. Furthermore, the analysis provides no information on the mechanism of energy transfer in the fluid. For instance, it is not known how the energy lost in the boundary layers is replenished by energy flows from the essentially inviscid main fluid body. Ursell (1952) found that the rate of energy dissipation in the boundary layers adjacent to the side walls of the channel could not be balanced by the rate of pressure working from the main fluid body on the side-wall boundary layers. Ursell pointed out that mathematical singularities must exist at the surface meniscus along lines where the free surface meets the side walls, which provide the pressure force for feeding energy from the main fluid body into the side-wall boundary layers. However, the details of this process were not clear.

In a manner similar to the progressive wave problem, Case and Parkinson (1957), and Keulegan (1959), applied the method of energy balance to obtain the atten-

uation rate of the decay of standing surface waves in cylinders and in rectangular basins, respectively. These investigators also carried out extensive experiments to check their theories. Case and Parkinson (1957) found that their experimental results were extremely sensitive to the conditions of the solid surfaces. They emphasized that extreme care must be exercised in comparing the results of experiments with theoretical predictions that are based on the ideal condition of very smooth walls. A somewhat different situation was encountered by Keulegan (1959). Keulegan found that the observed dissipation for distilled water in lucite basins was several times larger than that observed in glass basins, which he attributed to different behaviour of the fluid that adhered to the walls during wave motion.

A different approach was taken by Johns (1968) who found the complex damping rate (both amplitude attenuation and frequency correction) in a two-layer fluid with fixed upper and lower boundaries and infinite lateral extent. The complex damping rate in a two-layer fluid of infinite depth and lateral extent had been found by Harrison (1908). Johns (1968) developed the solutions in terms of stream function separately in the essentially inviscid fluid body, in the boundary layers adjacent to the solid surfaces, and in the boundary layers at the density interface of the two fluids, in the form of series expansions with respect to a small boundary layer parameter. The solutions inside and outside the boundary layer were joined at a position in an overlapped region where both solutions were valid, then coefficients of the series were calculated successively order by order. This method of matched asymptotic expansions was employed by Dore (1968) to derive formulae for the damping rates in a non-homogeneous fluid with general density and viscosity distributions, for the cases of finite depth with either free or fixed upper boundary.

The algebra involved in the technique used by John (1968) and Dore (1968) is extremely tedious. Some of the mathematical difficulties can be circumvented by the use of Green's theorem with the series expansion. Green's theorem was

applied by Chernous'ko (1966) in calculating the damping rate of free oscillations of a homogeneous fluid in a container of arbitrary shape. A similar approach was applied by Dore (1969a,b) to obtain the damping rate in progressive waves at the interface of two fluids bounded by fixed upper and lower boundaries and of infinite lateral extent, and to the decay of small amplitude oscillations of a non-homogeneous viscous fluid with general density and viscosity distributions that completely filled a rectangular tank.

The process of energy transfer in a homogeneous fluid bounded by solid walls and a free surface was examined by Mei and Liu (1973) using an order of magnitude argument. In calculating the damping rates, they presented a perturbation expansion scheme with application of Green's theorem in a manner similar to Chernous'ko (1966) and Dore (1969a,b). Mei and Liu's (1973) unique contribution was that their analysis revealed a thin meniscus boundary layer in the neighborhood along the lines of intersection between the free surface and the side walls. This region serves as a "gateway" of energy transfer to the side-wall boundary layers from the surface waves. The meniscus boundary layer behaves like a mathematical singularity in the perturbation analysis. By applying the formal analysis to standing waves in a circular basin, Mei and Liu (1973) were able to balance the energy dissipation in the side-wall boundary layer by work done by the pressure force from the surface meniscus and the inviscid fluid body.

3. THEORETICAL ANALYSIS

3.0 Introduction

This chapter presents the results of the theoretical analysis conducted for this study. The problem of surface wave propagation over a rectangular trench with a heavier fluid in the trench is treated by using the linear wave theory along with steady-state flow conditions. In § 3.1 an analysis is presented for the steady-state response of a two-layer density-stratified fluid in a rectangular trench that is placed at one end of a constant-depth channel; wave motion is generated by a vertical bulkhead wave generator, which moves in simple-harmonic motion at the other end of the channel. This particular arrangement was chosen for theoretical analysis because these flow conditions could be modelled in the wave tank, where experiments were conducted to test the validity of the theoretical models. The case of a three-layer continuously stratified fluid in the trench, with constant density in the top and bottom layers and a constant density gradient in the middle layer, is treated in § 3.2. The boundary conditions of the three-layer problem are the same as those of the two-layer problem. The fluid is assumed to be inviscid in both cases. In § 3.3 viscous damping is analyzed for the attenuation of a time-periodic progressive wave advancing down a uniform rectangular channel, and for the decay of a time-periodic standing wave in a rectangular basin; in these problems the fluid is density stratified and bounded by solid boundaries and a free surface. It is assumed that the

entire loss of the energy of waves is localized in laminar boundary layers adjacent to the density interface and at the solid surfaces. A perturbation expansion scheme is employed to incorporate the slow rate of viscous damping into the inviscid models. Finally, in § 3.4 the two-layer model developed in § 3.1 for the laboratory conditions is modified to treat the problem of surface wave propagation over a rectangular trench in an infinite region.

3.1 A Two-Layer Model

A definition sketch for the two-layer model is presented in figure 3.1.1. It is seen that the fluid domain consists of a two-layer fluid in a rectangular trench that is connected to a constant-depth channel; the trench is closed at its downstream end by a vertical wall. The fluid in the constant-depth channel is homogeneous with the trench at one end and a vertical boundary that moves in simple-harmonic motion at the opposite end. The following assumptions are made in the analysis: (a) the two fluids in the trench are immiscible and homogeneous, (b) the fluids are incompressible, (c) the fluid motion is two-dimensional, (d) the fluid motion is irrotational, (e) the fluid motion is at steady-state condition, and (f) the displacement of the moving vertical boundary at $x = -L$ is small compared to the wavelength and the water depth so that the equations can be linearized. Referring to figure 3.1.1, the origin of the x-coordinate is located above the edge of the trench with $z = 0$ at the undisturbed free surface and measured positive upwards. The fluid domain is divided into the following four regions labelled in figure 3.1.1:

Region 1	$\rho = \rho_1,$	$-h_1 < z < 0,$	$0 < x < \ell$
Region 2	$\rho = \rho_2,$	$-(h_1 + h_2) < z < -h_1,$	$0 < x < \ell$
Region 3	$\rho = \rho_1,$	$-h < z < 0,$	$-L < x < -L/2$
Region 4	$\rho = \rho_1,$	$-h < z < 0,$	$-L/2 < x < 0$

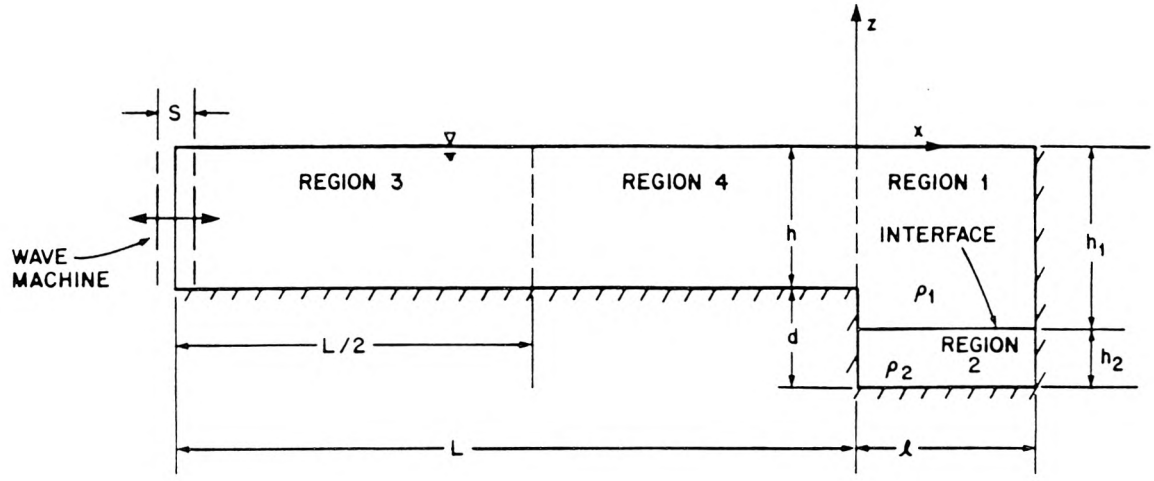

Figure 3.1.1. Definition sketch of the two-layer model.

wherein ρ_1 and ρ_2 are the densities of the upper and lower fluids, respectively, and the other symbols are defined in figure 3.1.1.

The method of analysis is as follow. The Laplace equation is solved using the linearized boundary conditions on the free surface, on the density interface, and on the solid bottom; these will be discussed. Velocity potentials in the constant-depth channel and in the trench region are obtained in the form of eigenfunction expansions. In doing so, the boundary conditions at $x = -L$ and at $x = \ell$ are employed. The horizontal velocities and velocity potentials are matched along a vertical boundary at the upstream edge of the trench, that is, at $x = 0$. This procedure results in sets of linear integral equations, which are solved numerically. Note that in a long channel, at a few depths from the moving boundary and the

trench, the velocity potential is very nearly a superposition of simple wave trains, with the amplitudes of the locally bounded non-propagating standing waves decaying exponentially with distance from $x = -L$ and $x = 0$. Thus, to facilitate the numerical treatment of this problem we have divided the constant-depth channel into two regions at $x = -L/2$. We assume that at this location the wave motion consists of the left- and right-going progressive waves only.

3.1.1 The Boundary-Value Problem

For steady-state motion of an inviscid irrotational fluid, the velocity potential may be written in the form:

$$\Phi(x, z, t) = \phi(x, z)e^{-i\sigma t}, \tag{3.1.1}$$

the potential function $\phi(x, z)$ must satisfy the Laplace equation:

$$\frac{\partial^2 \phi}{\partial x^2} + \frac{\partial^2 \phi}{\partial z^2} = 0 \tag{3.1.2}$$

in the entire fluid domain along with the following linearized boundary conditions:

$$\frac{\partial \phi}{\partial z} - \frac{\sigma^2}{g}\phi = 0 \qquad \text{on} \qquad z = 0, \quad -L < x < \ell, \tag{3.1.3a}$$

$$\rho_1 \left(\frac{\partial \phi_1}{\partial z} - \frac{\sigma^2}{g}\phi_1 \right) = \rho_2 \left(\frac{\partial \phi_2}{\partial z} - \frac{\sigma^2}{g}\phi_2 \right) \qquad \text{on} \qquad z = -h_1, \quad 0 < x < \ell, \tag{3.1.3b}$$

$$\frac{\partial \phi_1}{\partial z} = \frac{\partial \phi_2}{\partial z} \qquad \text{on} \qquad z = -h_1, \quad 0 < x < \ell, \tag{3.1.3c}$$

$$\frac{\partial \phi}{\partial z} = 0 \qquad \text{on} \qquad z = -(h_1 + h_2), \quad 0 < x < \ell$$

$$\text{and} \qquad z = -h, \quad -L < x < 0, \tag{3.1.3d}$$

$$\frac{\partial \phi}{\partial x} = 0 \qquad \text{on} \qquad -(h_1 + h_2) < z < -h, \quad x = 0$$

$$\text{and} \qquad -(h_1 + h_2) < z < 0, \quad x = \ell, \tag{3.1.3e}$$

$$\frac{\partial \phi_3}{\partial x} = \frac{i}{2} S\sigma \qquad \text{on} \qquad -h < z < 0, \quad x = -L. \tag{3.1.3f}$$

The matching conditions at $x = 0$ are:

$$\phi_1 = \phi_4 \qquad \text{on} \qquad -h < z < 0, \quad x = 0, \tag{3.1.4a}$$

$$\frac{\partial \phi_1}{\partial x} = \frac{\partial \phi_4}{\partial x} \qquad \text{on} \qquad -h < z < 0, \quad x = 0. \tag{3.1.4b}$$

In the above equations, σ represents the circular frequency, which is 2π/wave period, g is the acceleration of gravity, S is the stroke of the wave generator, and the subscripts (1, 2, 3, and 4), respectively, denote the appropriate regions shown in figure 3.1.1. Equations 3.1.3a and 3.1.3b are obtained from the linearized kinematic and dynamic boundary conditions on the free surface and on the density interface. The dynamic boundary condition on the density interface is the condition of continuity of pressure. There are two kinematic boundary conditions on the density interface; the first kinematic boundary condition is the condition of continuity of vertical velocity (equation 3.1.3c), and the second kinematic boundary condition is the condition that a fluid particle in contact with the density interface must stay on this surface at all times. The latter condition also applies on the free surface. The dynamic boundary condition on the free surface is the condition that the free surface must be a surface of constant pressure. Equations (3.1.3d) and (3.1.3e) are the kinematic boundary conditions on the solid surfaces, which state that the component of fluid velocity normal to a solid surface must vanish. On the surface of the moving vertical boundary at $x = -L$, the horizontal component of the fluid velocity must be the same as the velocity of the moving boundary. If the displacement of the moving boundary is small compared to the wavelength and the water depth, its actual position may be neglected, the resulting linearized equation is given by (3.1.3f). The first matching condition (equation 3.1.4a), is obtained from the condition of continuity of vertical velocity at $x = 0$, that is:

$$\frac{\partial}{\partial z}(\phi_1(0,z) - \phi_4(0,z)) = 0, \qquad -h < z < 0. \tag{3.1.5}$$

From (3.1.5), $\phi_1(0,z)$ and $\phi_4(0,z)$ can differ only by a constant, and from (3.1.3a)

this constant must be zero. Hence the velocity potential is continuous at $x = 0$. Equation 3.1.4*b* is the condition of continuity of horizontal velocity at $x = 0$.

3.1.2 The Solution in the Trench Region $(0 < x < \ell)$

We seek separable solutions for ϕ_1 and ϕ_2 in the two regions in the form:

$$\phi_{1,2}(x,z) = X_{1,2}(x) \cdot Z_{1,2}(z). \tag{3.1.6}$$

Substituting (3.1.6) into (3.1.2), we obtain two ordinary differential equations:

$$\frac{d^2X_{1,2}}{dx^2} - K^2\, X_{1,2} = 0, \tag{3.1.7a}$$

$$\frac{d^2Z_{1,2}}{dz^2} + K^2\, Z_{1,2} = 0 \tag{3.1.7b}$$

where K is the separation constant, and the subscripts 1 and 2 refer to Region 1 and Region 2, respectively.

The differential equations (3.1.7*a*) and (3.1.7*b*) have the general solutions:

$$X_{1,2} = A_{1,2}e^{Kx} + B_{1,2}e^{-Kx}, \tag{3.1.8a}$$

$$Z_{1,2} = C_{1,2}e^{iKx} + D_{1,2}e^{-iKx} \tag{3.1.8b}$$

where A_i, B_i, C_i, and D_i, $(i = 1, 2)$ are arbitrary constants.

Let us examine the ordinary differential equation (3.1.7*b*). The boundary conditions are given by substituting (3.1.6) into (3.1.3*a*)–(3.1.3*d*). Thus, we have:

$$\mathcal{L}Z_1 = K^2 Z_1, \qquad -h_1 < z < 0, \tag{3.1.9a}$$

$$\mathcal{L}Z_2 = K^2 Z_2, \qquad -(h_1 + h_2) < z < -h_1, \tag{3.1.9b}$$

$$\frac{dZ_1}{dz} - \frac{\sigma^2}{g} Z_1 = 0 \qquad \text{on} \qquad z = 0, \tag{3.1.9c}$$

$$\rho_1 \left(\frac{dZ_1}{dz} - \frac{\sigma^2}{g} Z_1 \right) = \rho_2 \left(\frac{dZ_2}{dz} - \frac{\sigma^2}{g} Z_2 \right) \qquad \text{on} \qquad z = -h_1, \tag{3.1.9d}$$

$$\frac{dZ_1}{dz} = \frac{dZ_2}{dz} \qquad \text{on} \qquad z = -h_1, \tag{3.1.9e}$$

$$\frac{dZ_2}{dz} = 0 \qquad \text{on} \qquad z = -(h_1 + h_2) \tag{3.1.9f}$$

in which $\mathcal{L} = -d^2/dz^2$. Equations (3.1.9a)–(3.1.9f) constitute an eigenvalue problem. We are interested in the case where σ is held fixed and K^2 is the eigenvalue parameter, with the corresponding eigenfunction given by $Z(z)$. Note that $Z(z)$ is represented by different functions in Region 1 and Region 2. We define a trial function that is continuous within each region (1 and 2), and has continuous 1st and 2nd derivatives, and satisfies the boundary conditions of that region. For any two trial functions $U(z)$ and $V(z)$, we define the inner product $(\mathcal{L}U, V)$ by:

$$(\mathcal{L}U, V) = \rho_1 \int_{-h_1}^{0} (\mathcal{L}U)V\,dz + \rho_2 \int_{-(h_1+h_2)}^{-h_1} (\mathcal{L}U)V\,dz. \tag{3.1.10}$$

Integrating by parts twice in (3.1.10) and applying the boundary conditions (3.1.9c)–(3.1.9f), there follows:

$$(\mathcal{L}U, V) = (U, \mathcal{L}V). \tag{3.1.11}$$

The eigenvalue problem (3.1.9) is therefore self-adjoint. Let α and β be any two different eigenvalues of the problem with corresponding eigenfuctions given by $\varphi(z)$ and $\psi(z)$, respectively. Then (3.1.11) gives:

$$\begin{aligned} &(\mathcal{L}\varphi, \psi) = (\varphi, \mathcal{L}\psi) \\ \Rightarrow &(\alpha\varphi, \psi) = (\varphi, \beta\psi) \\ \Rightarrow &(\alpha - \beta)(\varphi, \psi) = 0 \\ \Rightarrow &(\varphi, \psi) = 0, \qquad (\alpha \neq \beta). \end{aligned} \tag{3.1.12}$$

Let us assume that $\varphi(z)$ and $\psi(z)$ are linearly independent and both correspond to the same eigenvalue α. The Wronskian $W(z)$ is defined as:

$$W(z) = \varphi\frac{d\psi}{dz} - \psi\frac{d\varphi}{dz} \tag{3.1.13}$$

in each region where $\varphi(z)$ and $\psi(z)$ are differentiable. $W(z)$ vanishes identically over an interval if and only if $\varphi(z)$ and $\psi(z)$ are linearly dependent. Equation (3.1.13)

gives:

$$\frac{dW}{dz} = \psi(\mathcal{L}\varphi) - \varphi(\mathcal{L}\psi) = \psi(\alpha\varphi) - \varphi(\alpha\psi) = 0. \tag{3.1.14}$$

Thus $W(z)$ is a constant, so that its vanishing at a point implies its identical vanishing in the entire interval where $\varphi(z)$ and $\psi(z)$ are differentiable. Since:

$$\begin{aligned} W(z) &= \varphi\frac{d\psi}{dz} - \psi\frac{d\varphi}{dz} \\ &= \left(\varphi - \frac{g}{\sigma^2}\frac{d\varphi}{dz}\right)\frac{d\psi}{dz} - \left(\psi - \frac{g}{\sigma^2}\frac{d\psi}{dz}\right)\frac{d\varphi}{dz}, \end{aligned} \tag{3.1.15}$$

it follows from (3.1.9c) and (3.1.9f) that $W(z) \equiv 0$ in each interval $(-h_1 < z < 0)$ and $(-(h_1 + h_2) < z < -h_1)$. Hence φ and ψ are linearly dependent. To each eigenvalue α there corresponds only one eigenfunction $\varphi(z)$. After normalization, the eigenfunctions are orthogonal in the sense that:

$$\rho_1 \int_{-h_1}^{0} \varphi\psi dz + \rho_2 \int_{-(h_1+h_2)}^{-h_1} \varphi\psi dz = \begin{cases} 0, & \varphi \neq \psi; \\ 1, & \varphi = \psi. \end{cases} \tag{3.1.16}$$

Now let φ^* be the complex conjugate of φ. Multiplying the differential equations by $\rho\varphi^*$, integrating between $-(h_1 + h_2)$ and 0 layer by layer in the ordinary sense and applying the boundary conditions (3.1.9c) and (3.1.9d), we obtain:

$$\begin{aligned} &\rho_1\frac{\sigma^2}{g}|\varphi(0)|^2 + (\rho_2 - \rho_1)\frac{g}{\sigma^2}\left|\frac{d\varphi}{dz}(-h_1)\right|^2 \\ &= \int_{-(h_1+h_2)}^{0} \rho\left|\frac{d\varphi}{dz}\right|^2 dz - \alpha \int_{-(h_1+h_2)}^{0} \rho|\varphi|^2 dz \end{aligned} \tag{3.1.17}$$

wherein ρ is the density in each layer. It can be seen that α is real. Furthermore, the integrals are positive and the non-integral terms are positive and finite, thus the negative values of α must be finite. However, the positive values of α have no upper bound because the oscillation of the eigenfunction φ increases with α. The eigenvalues can be obtained by solving (3.1.9) analytically. The solutions of $Z(z)$ are of the form given by (3.1.8b), and the four boundary conditions (equations 3.1.9c–3.1.9f) provide four equations with four unknowns C_1, C_2, D_1, and D_2. The equations

are linear and homogeneous in these four unknowns, and therefore, for a solution to exist, the determinant of these equations must vanish. The condition that the determinant must vanish defines the relationships for the eigenvalues of K^2. There are two negative values and an infinite number of positive values of K^2. We designate them by: $-{K_j}^2$, $(j = 1, 2)$ and $\hat{K}_n^2$, $(n = 1, 2, \ldots)$. The eigenvalues are defined by the following relationships:

$$\sigma^4 \left(\frac{\rho_2}{\rho_1} \coth K_j h_1 \coth K_j h_2 + 1 \right) - \sigma^2 \frac{\rho_2}{\rho_1} \left(\coth K_j h_1 + \coth K_j h_2 \right) g K_j + \left(\frac{\rho_2}{\rho_1} - 1 \right) g^2 {K_j}^2 = 0, \qquad (j = 1, 2) \tag{3.1.18a}$$

and

$$\sigma^4 \left(\frac{\rho_2}{\rho_1} \cot \hat{K}_n h_1 \cot \hat{K}_n h_2 - 1 \right) + \sigma^2 \frac{\rho_2}{\rho_1} \left(\cot \hat{K}_n h_1 + \cot \hat{K}_n h_2 \right) g \hat{K}_n + \left(\frac{\rho_2}{\rho_1} - 1 \right) g^2 \hat{K}_n^2 = 0, \qquad (n = 1, 2, \ldots). \tag{3.1.18b}$$

From (3.1.8b), and (3.1.9c)–(3.1.9f), the eigenfunctions of $Z(z)$ are determined to an arbitrary constant. The normalized eigenfunctions are given by:

$$Z_{j1}(z) = -\frac{K_0 \sinh K_j z + K_j \cosh K_j z}{(\Lambda_j^s)^{1/2} (K_j \sinh K_j h_1 - K_0 \cosh K_j h_1)}, \tag{3.1.19a}$$

$$Z_{j2}(z) = \frac{\cosh K_j (z + h_1 + h_2)}{(\Lambda_j^s)^{1/2} \sinh K_j h_2}, \tag{3.1.19b}$$

$$\hat{Z}_{n1}(z) = -\frac{\hat{K}_n \cos \hat{K}_n z + K_0 \sin \hat{K}_n z}{(\Lambda_n^s)^{1/2} (\hat{K}_n \sin \hat{K}_n h_1 + K_0 \cos \hat{K}_n h_1)}, \tag{3.1.19c}$$

$$\hat{Z}_{n2}(z) = \frac{\cos \hat{K}_n (z + h_1 + h_2)}{(\Lambda_n^s)^{1/2} \sin \hat{K}_n h_2}, \tag{3.1.19d}$$

$$\begin{aligned} \Lambda_j^s &= \rho_1 \int_{-h_1}^{0} \left[\frac{K_0 \sinh K_j z + K_j \cosh K_j z}{K_j \sinh K_j h_1 - K_0 \cosh K_j h_1} \right]^2 dz + \rho_2 \int_{-(h_1+h_2)}^{-h_1} \frac{\cosh^2 K_j (z + h_1 + h_2)}{\sinh^2 K_j h_2} dz \\ &= -\frac{\rho_1}{2} \left[\frac{(K_0^2 - K_j^2) h_1 - K_0 + K_0 \cosh 2K_j h_1 - \frac{1}{2} K_j^{-1} (K_j^2 + K_0^2) \sinh 2K_j h_1}{(K_j \sinh K_j h_1 - K_0 \cosh K_j h_1)^2} \right] \\ &\quad + \frac{\rho_2}{2 \sinh^2 K_j h_2} \left[h_2 + \frac{\sinh 2K_j h_2}{2K_j} \right] \end{aligned} \tag{3.1.19e}$$

$$\Lambda_n^s = \rho_1 \int_{-h_1}^{0} \left[\frac{\hat{K}_n \cos \hat{K}_n z + K_0 \sin \hat{K}_n z}{\hat{K}_n \sin \hat{K}_n h_1 + K_0 \cos \hat{K}_n h_1} \right]^2 dz + \rho_2 \int_{-(h_1+h_2)}^{-h_1} \frac{\cos^2 \hat{K}_n (z + h_1 + h_2)}{\sin^2 \hat{K}_n h_2} dz$$

$$= \frac{\rho_1}{2} \left[\frac{(K_0^2 + \hat{K}_n^2) h_1 - K_0 + K_0 \cos 2\hat{K}_n h_1 + \frac{1}{2} \hat{K}_n^{-1} (\hat{K}_n^2 - K_0^2) \sin 2\hat{K}_n h_1}{\left(\hat{K}_n \sin \hat{K}_n h_1 + K_0 \cos \hat{K}_n h_1 \right)^2} \right]$$

$$+ \frac{\rho_2}{2 \sin^2 \hat{K}_n h_2} \left[h_2 + \frac{\sin 2\hat{K}_n h_2}{2\hat{K}_n} \right] \qquad (3.1.19f)$$

in which $K_0 = \sigma^2/g$. The eigenfunctions in (3.1.19) have been previously derived by Kelly (1969).

We expand the spatial potential function $\phi(x, z)$ in terms of a series of products of the functions $X(x)$ and $Z(z)$, in the form:

$$\phi_{1,2}(x, z) = \sum_{j=1,2} \left(A_j e^{iK_j x} + B_j e^{-iK_j x} \right) Z_{j1,2}(z)$$

$$+ \sum_n \left(\hat{A}_n e^{\hat{K}_n x} + \hat{B}_n e^{-\hat{K}_n x} \right) \hat{Z}_{n1,2}(z) \qquad (3.1.20)$$

in which A_j, B_j, $(j = 1, 2)$, and $\hat{A}_n$, $\hat{B}_n$, $(n = 1, 2, \ldots)$ are unknown constants to be determined from the boundary and matching conditions.

Equation (3.1.18a) is the dispersion relation for a two-layer fluid, and K_j is physically equivalent to the wave number defined as 2π/wavelength. There are two real solutions of K_j for a given value of σ, corresponding to the wave numbers for two possible systems of waves: surface mode and interfacial mode. These two modes have the same wave period but different wavelengths. The surface mode has the smaller root of (3.1.18a) which we term K_1, that is, larger wavelength, whereas the interfacial mode has the larger root designated by K_2, that is, smaller wavelength. For the surface mode, the motion of a two-layer fluid is very close to that of a homogeneous fluid of the same total fluid depth. The wave motion at the density interface is in phase with the wave motion at the free surface and has been decreased by nearly the amount that the particle oscillations would have been decreased in amplitude if there had been no variation in density with depth. The velocity potential is almost continuous across the density interface. For the interfacial mode,

the motion of a two-layer fluid has the largest amplitude at the density interface, the wave motion at the density interface is 180° out of phase with the wave motion at the free surface. Moreover, the velocity potential is discontinuous at the density interface, hence the density interface is also a vortex sheet. For a basic treatment of surface and interfacial waves in a two-layer fluid, readers are referred to Gill (1982), and Neumann and Pierson (1966). These authors also discussed the special cases of long waves (Gill, 1982), and of a shallow interface in a deep fluid and of a deep interface in a deep fluid (Neumann and Pierson, 1966). For these particular cases, K_j can be obtained in explicit forms from (3.1.18a).

For a given value of σ, equation (3.1.18b) has an infinite number of real roots $\hat{K}_n$, corresponding to the wave numbers of the non-propagating modes of local disturbances in a two-layer fluid. In (3.1.20), wave motion in the two-layer fluid is seen to be represented by a linear superposition of the left- and right- going progressive waves of the surface and interfacial modes (the first summation), and an infinite number of locally bounded standing waves (the second summation) that decay exponentially with distance from the two ends of the trench. To compute the eigenvalues of K^2, approximate solutions were found from (3.1.18a) and (3.1.18b) by direct substitution, and were then refined by Regula Falsi iteration (see, for example, Carnahan, Luther and Wilkes, 1969).

From the the boundary condition at $x = \ell$ (the second of equation 3.1.3e), we have:

$$B_j = A_j e^{2iK_j\ell}, \qquad (j = 1, 2), \tag{3.1.21a}$$

$$\hat{B}_n = \hat{A}_n e^{2\hat{K}_n\ell}, \qquad (n = 1, 2, \ldots). \tag{3.1.21b}$$

Thus, the velocity potentials in the trench region are given by (3.1.20) with B_j, $(j = 1, 2)$ and $\hat{B}_n$, $(n = 1, 2, \ldots)$ given by (3.1.21a) and (3.1.21b), respectively. The eigenvalues and eigenfunctions are given by (3.1.18) and (3.1.19). The unknown

coefficients A_j, $(j = 1, 2)$ and $\hat{A}_n$, $(n = 1, 2, \ldots)$ must be found by matching at $x = 0$ the horizontal velocity and velocity potential with the solutions in the constant-depth channel.

3.1.3 The Solution in the Constant-Depth Channel $(-L < x < 0)$

In a manner similar to that presented in § 3.1.2, the potential functions in the constant-depth channel can be written as:

$$\phi_3(x,z) = \left(Ce^{ik(x+L)} + De^{-ik(x+L)}\right) Z(z) + \sum_n \hat{C}_n e^{-\hat{k}_n(x+L)} \hat{Z}_n(z), \tag{3.1.22a}$$

$$\phi_4(x,z) = \left(Ee^{ikx} + Fe^{-ikx}\right) Z(z) + \sum_n \hat{F}_n e^{\hat{k}_n x} \hat{Z}_n(z) \tag{3.1.22b}$$

in which C, D, E, F, and $\hat{C}_n$, $\hat{F}_n$, $(n = 1, 2, \ldots)$ are unknown constants to be determined. For the homogeneous fluid, the corresponding eigenvalue problem consists of (3.1.7b), (3.1.9c), and (3.1.9f) with the subscripts 1 and 2 dropped because there is only one fluid in this region. The eigenfunctions of $Z(z)$ are determined to an arbitrary constant by imposing the boundary condition on the bottom (equation 3.1.9f). After normalization, the eigenfunctions are given by:

$$Z(z) = (\Lambda^h)^{-1/2} \cosh k(z+h), \tag{3.1.23a}$$

$$\hat{Z}_n(z) = (\Lambda_n^h)^{-1/2} \cos \hat{k}_n(z+h), \tag{3.1.23b}$$

$$\Lambda^h = \rho_1 \int_{-h}^{0} \cosh^2 k(z+h)dz = \frac{\rho_1}{2}\left[h + \frac{1}{2k}\sinh 2kh\right], \tag{3.1.23c}$$

$$\Lambda_n^h = \rho_1 \int_{-h}^{0} \cos^2 \hat{k}_n(z+h)dz = \frac{\rho_1}{2}\left[h + \frac{1}{2\hat{k}_n}\sin 2\hat{k}_n h\right]. \tag{3.1.23d}$$

The eigenfunctions are orthogonal in the sense that:

$$\rho_1 \int_{-h}^{0} \varphi\psi dz = \begin{cases} 0, & \varphi \neq \psi; \\ 1, & \varphi = \psi \end{cases} \tag{3.1.24}$$

where $\varphi(z)$ and $\psi(z)$ are any two eigenfunctions given by (3.1.23). The eigenvalues k and $\hat{k}_n$, $(n = 1, 2, \ldots)$ are defined by the following relationships:

$$\sigma^2 = gk \tanh kh, \tag{3.1.25a}$$

$$\sigma^2 = -g\hat{k}_n \tan \hat{k}_n h, \qquad (n = 1, 2, \ldots). \tag{3.1.25b}$$

The unknown coefficients in the potential function ϕ_3 are related through the boundary condition at the wavemaker (equation 3.1.3f) as follows (see, for example, Ursell, Dean and Yu, 1960):

$$C - D = \frac{S\sigma\rho_1}{2k} \int_{-h}^{0} Z(z)dz, \tag{3.1.26a}$$

$$\hat{C}_n = -\frac{iS\sigma\rho_1}{2\hat{k}_n} \int_{-h}^{0} \hat{Z}_n dz, \qquad (n = 1, 2, \ldots). \tag{3.1.26b}$$

The assumption that the wave motion is a superposition of simple wave trains at $x = -L/2$ gives:

$$E = Ce^{ikL}, \tag{3.1.27a}$$

$$F = De^{-ikL}. \tag{3.1.27b}$$

3.1.4 Matching the Solutions

The potential functions in the trench region and in the constant-depth channel are given by (3.1.20) and (3.1.22) in terms of the unknown coefficients. The solutions must be matched at $x = 0$ to obtain the sets of equations from which the unknown coefficients can be determined. Because there are an infinite number of unknown coefficients in the infinite series, an infinite number of simultaneous equations are needed. For numerical evalution, the infinite series of the potential functions are truncated after a finite number of terms given by N. We are then left with $(2N+3)$ unknown coefficients: A_j $(j = 1, 2)$, C, and $\hat{A}_n$, $\hat{F}_n$, $(n = 1, 2, \ldots, N)$. We obtain

$(2N+3)$ equations by matching the solutions in the trench region and the constant-depth channel along a vertical boundary at the upstream edge of the trench, that is, at $x = 0$. First we consider the condition of continuity of horizontal velocity at $x = 0$ (equation 3.1.4b). Let $U(z)$ be the horizontal velocity at $x = 0$, it follows from (3.1.20) that:

$$U(z) = \frac{\partial \tilde{\phi}_1}{\partial x}(0,z) = \sum_{j=1,2} iK_j\left(A_j - B_j\right) Z_{j1}(z) + \sum_{n=1}^{N} \hat{K}_n \left(\hat{A}_n - \hat{B}_n\right) \hat{Z}_{n1}(z), \quad (-h_1 < z < 0) \tag{3.1.28a}$$

$$= \frac{\partial \tilde{\phi}_2}{\partial x}(0,z) = \sum_{j=1,2} iK_j\left(A_j - B_j\right) Z_{j2}(z) + \sum_{n=1}^{N} \hat{K}_n \left(\hat{A}_n - \hat{B}_n\right) \hat{Z}_{n2}(z) \quad (-(h_1+h_2) < z < -h_1) \tag{3.1.28b}$$

in which $\tilde{\phi}$ denotes the truncated series of ϕ. Equation (3.1.22b) gives:

$$U(z) = \frac{\partial \tilde{\phi}_4}{\partial x}(0,z) = ik\left(E - F\right) Z(z) + \sum_{n=1}^{N} \hat{k}_n \hat{F}_n \hat{Z}_n(z). \quad (-h < z < 0) \tag{3.1.29}$$

First multiplying $U(z)$ by $\rho\varphi(z)$, where $\varphi(z)$ is an eigenfunction for the two-fluid system given by (3.1.19), and then integrating between $-(h_1+h_2)$ and 0 layer by layer in the ordinary sense, after this is done for each eigenfunction of the orthonormal set, we get:

$$\rho_1 \int_{-h_1}^{0} \frac{\partial \tilde{\phi}_1}{\partial x}(0,z) Z_{j1}(z)dz + \rho_2 \int_{-(h_1+h_2)}^{-h_1} \frac{\partial \tilde{\phi}_2}{\partial x}(0,z) Z_{j2}(z)dz$$

$$= \rho_1 \int_{-h}^{0} \frac{\partial \tilde{\phi}_4}{\partial x}(0,z) Z_{j1}(z)dz, \qquad (j = 1,2) \tag{3.1.30a}$$

and

$$\rho_1 \int_{-h_1}^{0} \frac{\partial \tilde{\phi}_1}{\partial x}(0,z) \hat{Z}_{n1}(z)dz + \rho_2 \int_{-(h_1+h_2)}^{-h_1} \frac{\partial \tilde{\phi}_2}{\partial x}(0,z) \hat{Z}_{n2}(z)dz$$

$$= \rho_1 \int_{-h}^{0} \frac{\partial \tilde{\phi}_4}{\partial x}(0,z) \hat{Z}_{n1}(z)dz, \qquad (n = 1,2,\ldots,N) \tag{3.1.30b}$$

in which the boundary condition at $x = 0$ (the first of (3.1.3e)) has been used. Invoking the orthogonality property of the eigenfunctions of Z (equation 3.1.16), we obtain $(N + 2)$ integral equations from (3.1.30a) and (3.1.30b) as follow:

$$iK_j\,(A_j - B_j) = \rho_1 \int_{-h}^{0} \frac{\partial \tilde{\phi}_4}{\partial x}(0,z) Z_{j1}(z)dz, \qquad (j = 1,2), \tag{3.1.31a}$$

$$\hat{K}_n \left(\hat{A}_n - \hat{B}_n\right) = \rho_1 \int_{-h}^{0} \frac{\partial \tilde{\phi}_4}{\partial x}(0,z) \hat{Z}_{n1}(z)dz, \qquad (n = 1,2,\ldots,N). \tag{3.1.31b}$$

The remaining $(N+1)$ equations are constructed from the condition of continuity of ϕ at $x = 0$ (equation 3.1.4a). From (3.1.20) and (3.1.22b), we have:

$$\tilde{\phi}(0,z) = \tilde{\phi}_1(0,z) = \sum_{j=1,2} (A_j + B_j) Z_{j1}(z) + \sum_{n=1}^{N} \left(\hat{A}_n + \hat{B}_n\right) \hat{Z}_{n1}(z),$$
$$(-h < z < 0) \tag{3.1.32a}$$

$$= \tilde{\phi}_4(0,z) = (E + F) Z(z) + \sum_{n=1}^{N} \hat{F}_n \hat{Z}_n(z).$$
$$(-h < z < 0) \tag{3.1.32b}$$

Next we obtain the $(N + 1)$ integral equations in a manner similar to (3.1.30a) and (3.1.30b) but this time we employ the set of eigenfunctions for the homogeneous fluid (equation 3.1.23) and integrate only from $-h$ to 0, it follows:

$$\rho_1 \int_{-h}^{0} \tilde{\phi}_4(0,z) Z(z)dz = \rho_1 \int_{-h}^{0} \tilde{\phi}_1(0,z) Z(z)dz, \tag{3.1.33a}$$

$$\rho_1 \int_{-h}^{0} \tilde{\phi}_4(0,z) \hat{Z}_n dz = \rho_1 \int_{-h}^{0} \tilde{\phi}_1(0,z) \hat{Z}_n dz, \qquad (n = 1,2,\ldots,N). \tag{3.1.33b}$$

Invoking the orthogonality property of the eignenfunctions of Z (equation 3.1.24), we get:

$$E + F = \rho_1 \int_{-h}^{0} \tilde{\phi}_1(0,z) Z(z)dz, \tag{3.1.34a}$$

$$\hat{F}_n = \rho_1 \int_{-h}^{0} \tilde{\phi}_1(0,z) Z(z)dz, \qquad (n = 1,2,\ldots,N). \tag{3.1.34b}$$

The integrals in (3.1.31) and (3.1.34) can be evaluated in terms of trigonometric functions and hyperbolic functions. The set of $(2N+3)$ simultaneous equations are solved numerically as a linear matrix equation. After the coefficients are found, the horizontal velocity and velocity potential at $x = 0$ are computed using (3.1.20) and (3.1.22) and the matching conditions (equations 3.1.4a and 3.1.4b) are checked for the solution accuracy. We have not proved that the series expansion (3.1.20) is complete and can represent the potential function $\phi(x, z)$, which satisfies the Laplace equation and linearized boundary conditions. However, we are certain that all the propagating modes (there are only two) that correspond to waves are included in the series. These are the surface mode and the interfacial mode given by the first summation of (3.1.20). If we neglect the infinite series that contains the non-propagating modes, the solution is a plane-wave approximation of the full problem. We found, numerically, that the series expansion for the two-layer fluid (equation 3.1.20) converges much faster than that for the homogeneous fluid (equation 3.1.22). Thus the contributions of the non-propagating modes to the series expansions are negligible after the first few terms. However, a series with a large number of terms does make the matrix equation obtained from (3.1.31) and (3.1.34) more ill-conditioned, consequently the accuracy of the solution declines. In this study we use $N = 3$, which gives a good match of the horizontal velocity and velocity potential at $x = 0$.

3.1.5 Analysis of Wave Amplitude

After the unknown coefficients of the series expansions are found, the velocity potentials are determined for the entire fluid domain. The fluid velocities and wave amplitudes are readily obtained from the velocity potentials. The amplitude and phase of the surface wave are given by linear theory to be:

$$\frac{H_S}{2} = |\eta_S| = \left| -\frac{1}{g}\frac{\partial \Phi}{\partial t} \right|_{z=0}, \qquad (3.1.35a)$$

$$\theta_S = \arg\left\{-\frac{1}{g}\frac{\partial\Phi}{\partial t}\right\}_{z=0} \tag{3.1.35b}$$

where H is the wave height, θ is the phase angle, η is the surface elevation, "arg" is the argument of a complex number, and the subscript S denotes the free surface. The velocity potential Φ is of the form (3.1.1) with the spatial potential function ϕ given by (3.1.20) in the trench region and (3.1.22) in the constant-depth channel. From the linearized kinematic boundary condition on the density interface, the amplitude and phase of the interfacial waves are given by:

$$\frac{H_I}{2} = |\eta_I| = \left|\frac{i}{\sigma}\frac{\partial\Phi}{\partial z}\right|_{z=-h_1}, \tag{3.1.36a}$$

$$\theta_I = \arg\left\{\frac{i}{\sigma}\frac{\partial\Phi}{\partial z}\right\}_{z=-h_1} \tag{3.1.36b}$$

in which the subscript I denotes the density interface. Of importance to this study is the amplitude of the interfacial wave relative to the amplitude of the surface wave. In the experiments, the motion of the density interface was measured at a location near the upstream wall of the trench. Thus, we define an amplification factor R as the ratio of the interfacial wave height at $x = 0$ to the surface wave height at the end wall ($x = \ell$), that is:

$$R = \frac{\{H_I\}_{x=0}}{\{H_S\}_{x=\ell}}. \tag{3.1.37}$$

The phase shift between the interfacial motion at $x = 0$ and the surface motion at $x = \ell$ is given by:

$$\theta = \{\theta_I\}_{x=0} - \{\theta_S\}_{x=\ell}. \tag{3.1.38}$$

The theoretical predictions of (3.1.37) and (3.1.38) are compared with the results of experiments in Chapter 5.

3.1.6 Wave Energies of Internal Waves and the Variational Principle

Wave damping of interfacial waves is analyzed in § 3.3 but it is convenient to present the kinetic and potential energies of wave motion in a two-layer fluid here.

We will also show that the differential system given by (3.1.9) has a variational principle, that is, the system of equations (3.1.9a)–(3.1.9f) can be obtained by making some function stationary. The statement that a physical system so acts that some function of its behaviour is least (or greatest) is often a useful starting point for theoretical analysis. For instance, in finite element analysis, the differential equations and boundary conditions are often cast into a variational formulation in the form of an integral equation, which is then minimized by standard methods to obtain the dependent variables of the problem. Thus the variational formulation could be useful in the analysis of the problem of wave propagation over a stratified trench of arbitrary geometry. In addition, important results with regard to the properties of the eigenfunctions and eigenvalues of the two-layer problem are also given by the variational principle; these will be discussed.

First, let us write down the kinetic energy and the potential energy of a progressive wave in a two-layer fluid. The average kinetic energy of a progressive wave per unit width, per unit length, over one wave period is given by:

$$\begin{aligned}\overline{KE} &= \frac{1}{\lambda T}\int_{t}^{t+T}\int_{x}^{x+\lambda}\int_{-(h_1+h_2)}^{0}\frac{1}{2}\rho(u^2+w^2)dzdxdt \\ &= \frac{1}{4}\int_{-(h_1+h_2)}^{0}\rho\left[-K^2|\varphi|^2+\left|\frac{d\varphi}{dz}\right|^2\right]dz \qquad (3.1.39)\end{aligned}$$

wherein $u(x,z,t)$ and $w(x,z,t)$ are the horizontal and vertical components of the fluid velocity, respectively, T is the wave period, λ is the wavelength, ρ is the density of the fluid, and $\varphi(z)$ denotes the eigenfunction of the two-fluid system given by (3.1.19a) and (3.1.19b) for the propagating waves with $K = iK_j$, $(j = 1,2)$ the corresponding eigenvalue (wave number). The integration in (3.1.39) is done layer by layer. With no loss of generality, we have assumed that the amplitude of the progressive wave is unity. The average potential energy per unit width, per unit

length, over one wave period attributable to the progressive wave is given by:

$$\overline{PE} = \frac{1}{\lambda T}\int_{t}^{t+T}\int_{x}^{x+\lambda}\frac{1}{2}\left[\rho_1 g\eta_S{}^2 + (\rho_2-\rho_1)g\eta_I{}^2\right]dxdt$$
$$= \frac{1}{4}\left[\rho_1\frac{\sigma^2}{g}|\varphi(0)|^2 + (\rho_2-\rho_1)\frac{g}{\sigma^2}\left|\frac{d\varphi}{dz}(-h_1)\right|^2\right]. \qquad (3.1.40)$$

As seen in (3.1.17), the total energy of wave motion is equally partitioned in the form of kinetic and potential energies. As in many conservative systems, it is expected that the two-layer fluid will move so that the time average of the difference between kinetic and potential energies will be stationary. Thus the two-fluid system is characterized by a variational principle. Seen in this light, we consider making the following functional stationary:

$$Q(\varphi) = \int_{-(h_1+h_2)}^{0}\rho\left[\left(\frac{d\varphi}{dz}\right)^2 - K^2\varphi^2\right]dz - \rho_1\frac{\sigma^2}{g}[\varphi(0)]^2 - (\rho_2-\rho_1)\frac{g}{\sigma^2}\left[\frac{d\varphi}{dz}(-h_1)\right]^2. \qquad (3.1.41)$$

Let $\tilde{\varphi}(z) = \varphi(z) + \epsilon\zeta$, where $\tilde{\varphi}(z)$ is a perturbation of $\varphi(z)$, ϵ is a perturbation parameter, and ζ is an arbitrary function that satisfies the boundary conditions of $\varphi(z)$. The perturbed functional is:

$$\tilde{Q}(\tilde{\varphi}) = \int_{-(h_1+h_2)}^{0}\rho\left[\left(\frac{d\tilde{\varphi}}{dz}\right)^2 - K^2\tilde{\varphi}^2\right]dz - \rho_1\frac{\sigma^2}{g}[\tilde{\varphi}(0)]^2 - (\rho_2-\rho_1)\frac{g}{\sigma^2}\left[\frac{d\tilde{\varphi}}{dz}(-h_1)\right]^2. \qquad (3.1.42)$$

Differentiating $\tilde{Q}(\tilde{\varphi})$ with respect to ϵ and setting the derivative to zero, we get:

$$\int_{-(h_1+h_2)}^{0}\rho\left[\frac{d\varphi}{dz}\frac{d\zeta}{dz} - K^2\varphi\zeta\right]dz - \rho_1\frac{\sigma^2}{g}\varphi(0)\zeta(0)$$
$$-(\rho_2-\rho_1)\frac{g}{\sigma^2}\left[\frac{d\varphi}{dz}(-h_1)\right]\left[\frac{d\zeta}{dz}(-h_1)\right] = 0. \qquad (3.1.43)$$

Integration by parts yields:

$$-\rho_1\int_{-h_1}^{0}\zeta\left[\frac{d^2\varphi}{dz^2} + K^2\varphi\right]dz - \rho_2\int_{-(h_1+h_2)}^{-h_1}\zeta\left[\frac{d^2\varphi}{dz^2} + K^2\varphi\right]dz$$

$$+\rho_1\zeta(0)\left[\frac{d\varphi}{dz}(0)-\frac{\sigma^2}{g}\varphi(0)\right]+\rho_1\frac{d\varphi}{dz}(-h_1)\left[\frac{g}{\sigma^2}\frac{d\zeta}{dz}(-h_1)-\zeta(-h_1)\right]$$
$$-\rho_2\frac{d\varphi}{dz}(-h_1)\left[\frac{g}{\sigma^2}\frac{d\zeta}{dz}(-h_1)-\zeta(-h_1)\right]$$
$$-\rho_2\zeta(-h_1-h_2)\frac{d\varphi}{dz}(-h_1-h_2)=0. \qquad (3.1.44)$$

Because $\zeta(z)$ is arbitrary and $\zeta(z)$ satisfies the boundary conditions of $\varphi(z)$, equation (3.1.44) implies that the $\varphi(z)$ that makes $Q(\varphi)$ stationary also satisfies the differential system given by (3.1.9).

An equivalent statement of the variational principle is to make the following functional stationary:

$$\Omega(\psi)=\int_{-(h_1+h_2)}^{0}\rho\left[\left(\frac{d\psi}{dz}\right)^2\right]dz-\rho_1\frac{\sigma^2}{g}[\psi(0)]^2-(\rho_2-\rho_1)\frac{g}{\sigma^2}\left[\frac{d\psi}{dz}(-h_1)\right]^2 \qquad (3.1.45a)$$

subject to the auxillary condition that:

$$\int_{-(h_1+h_2)}^{0}\rho\psi^2dz=\text{constant}. \qquad (3.1.45b)$$

Here $\psi(z)$ is a trial function, which satisfies the boundary conditions at $z=0$, $z=-h_1$, and $z=-(h_1+h_2)$. Suppose we normalize $\psi(z)$ with respect to the density function $\rho(z)$, such that:

$$\int_{-(h_1+h_2)}^{0}\rho\psi^2dz=1 \qquad (3.1.46)$$

then the $\psi(z)$, which makes Ω stationary is a normalized eigenfunction of the differential system, and the corresponding value of $\Omega(\psi)$ is the associated eigenvalue. The last result is readily obtained from (3.1.45a) through integration by parts.

3.2 A Three-Layer Model

In this analysis, the density distribution in the trench is represented by a three-layer fluid, which is composed of two homogeneous fluids of different densities in

the upper and the lower layers separated in between by a transition region of linear density variation; the top of the density transition region is located beneath the edge of the trench (figure 3.2.1). The fluid is assumed to be inviscid and incompressible, but the motion is not irrotational, due to generation of vorticity in the continuously stratified transition layer. A partial differential equation (Love's equation) is obtained from the equations of motion by standard perturbation procedure. For simple-harmonic motion, the Love's equation is reduced to a second order ordinary differential equation with variable coefficients, which together with the boundary conditions specify an eigenvalue problem. For arbitrary density distributions that are gravitationally stable, the eigenvalues and eigenfunctions must be found numerically. By applying the Boussinesq approximation to the three-layer fluid, the ordinary differential equation is changed into one with constant coefficients. The Boussinesq approximation neglects variations of density in the Navier-Stokes equations in so far as they affect inertia, but retains them in the buoyancy term. The eigenvalue problem can now be solved analytically, but the eigenvalue parameter occurs in the boundary conditions. In fact the problem is not self-adjoint, so the associated self-adjoint problem must be found that has a set of mutually orthogonal eigenfunctions. A solution in the trench region is expanded in terms of an infinite series of these eigenfunctions. A similar procedure yields the series expansion solutions in the constant-depth channel. The horizontal and vertical velocities are matched along a vertical boundary at the upstream edge of the trench to obtain a set of linear integral equations, which are solved numerically for the unknown coefficients.

The constant-depth channel and trench arrangement for this analysis (figure 3.2.1) is essentially the same as shown in figure 3.1.1, except for the density distribution in the trench, and we shall use the same notation here unless specifically stated otherwise.

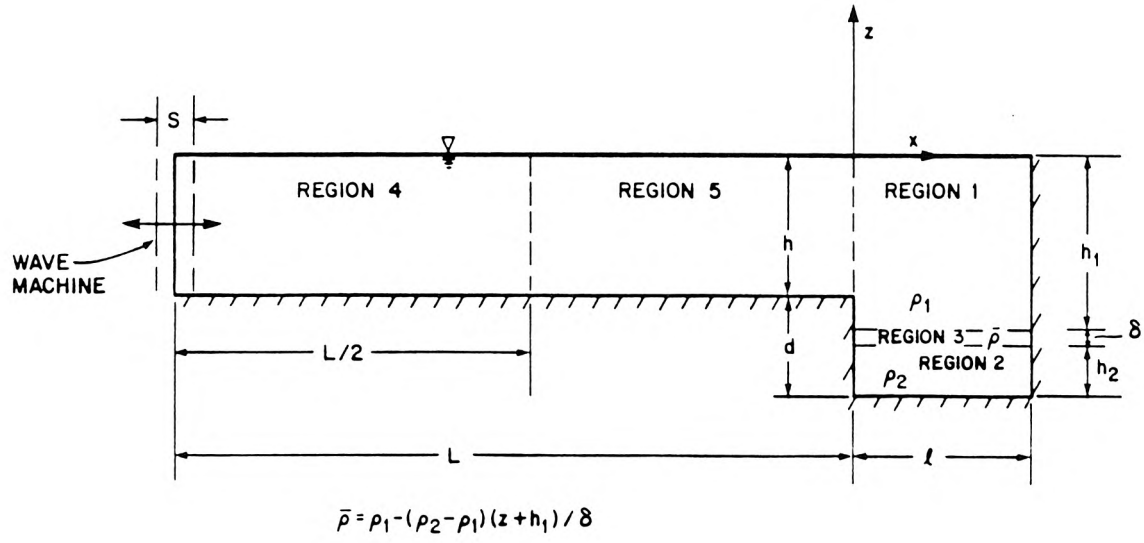

Figure 3.2.1. Definition sketch of the three-layer model.

3.2.1 The Governing Equations in a Continuously Stratified Fluid

Let (x, z) be a Cartesian coordinate system with z extending positive upwards from the undisturbed free surface and the bottom located at $z = -(h_1 + h_2 + \delta)$, where h_1, h_2, and δ respectively, are the depths of the upper layer, the lower layer, and the density transition region. The horizontal and vertical components of the fluid velocity in the positive x direction and the positive z direction are denoted by $u(x, z, t)$ and by $w(x, z, t)$, respectively. The mean pressure $\overline{p}(z)$, is related to the mean density $\overline{\rho}(z)$, by the hydrostatic condition:

$$\frac{d\overline{p}}{dz} = -\overline{\rho}g. \tag{3.2.1}$$

The equation of mass conservation is:

$$\frac{\partial \rho}{\partial t} + \frac{\partial(\rho u)}{\partial x} + \frac{\partial(\rho w)}{\partial z} = 0 \tag{3.2.2}$$

in which the density is given by $\rho = \overline{\rho} + \rho'$, where $\overline{\rho}(z)$ is the mean density and $\rho'(x, z, t)$ is the density fluctuation due to the wave motion. Because the fluid is incompressible, we must have:

$$\frac{D\rho}{Dt} = 0, \qquad \frac{D}{Dt} \equiv \frac{\partial}{\partial t} + \mathbf{u} \cdot \nabla \tag{3.2.3}$$

in which $\mathbf{u}$ represents the velocity vector. The equations of motion for an inviscid fluid are:

$$\rho \frac{D\mathbf{u}}{Dt} = -\nabla p - \rho g \nabla z \tag{3.2.4}$$

in which the pressure is given by $p = \overline{p} + p'$, where $\overline{p}(z)$ is the mean pressure, and $p'(x, z, t)$ is the pressure fluctuation due to the wave motion. If second order terms in the perturbation quantities are neglected, equations (3.2.2)–(3.2.4) become:

$$\frac{\partial \rho}{\partial t} + w\frac{\partial \overline{\rho}}{\partial z} + \overline{\rho}\left(\frac{\partial u}{\partial x} + \frac{\partial w}{\partial z}\right) = 0, \tag{3.2.5}$$

$$\frac{\partial \rho}{\partial t} + w\frac{\partial \overline{\rho}}{\partial z} = 0, \tag{3.2.6}$$

$$\overline{\rho}\frac{\partial \mathbf{u}}{\partial t} = -\nabla p - \rho g \nabla z. \tag{3.2.7}$$

The equation of mass conservation (3.2.2) and the equation of incompressibility (3.2.3) lead to the continuity equation:

$$\nabla \cdot \mathbf{u} = \frac{\partial u}{\partial x} + \frac{\partial w}{\partial z} = 0. \tag{3.2.8}$$

Differentiating the linearized equation of motion in the x direction with respect to z and the linearized equation of motion in the z direction with respect to x, then eliminating the terms involving p from the two equations obtained, we get:

$$\overline{\rho}\frac{\partial}{\partial t}\left(\frac{\partial w}{\partial x} - \frac{\partial u}{\partial z}\right) - \frac{\partial \overline{\rho}}{\partial z}\frac{\partial u}{\partial t} + g\frac{\partial \rho}{\partial x} = 0. \tag{3.2.9}$$

Differentiation of (3.2.9) with respect to t and then with respect to x yields, after using (3.2.6) and (3.2.8), Love's equation:

$$\overline{\rho}\frac{\partial^2}{\partial t^2}\left(\frac{\partial^2 w}{\partial x^2}+\frac{\partial^2 w}{\partial z^2}\right)+\frac{\partial \overline{\rho}}{\partial z}\frac{\partial^3 w}{\partial z \partial t^2}-g\frac{\partial \overline{\rho}}{\partial z}\frac{\partial^2 w}{\partial x^2}=0. \tag{3.2.10}$$

We shall investigate steady-state wave motion of the form:

$$w(x,z,t)=f(z)e^{i(Kx-\sigma t)} \tag{3.2.11}$$

in which K is the wave number and σ is the circular frequency. Substitution of (3.2.11) into (3.2.10) yields:

$$\frac{d}{dz}\left(\overline{\rho}\frac{df}{dz}\right)+\overline{\rho}K^2\left(\frac{\mathcal{N}^2}{\sigma^2}-1\right)f=0. \tag{3.2.12}$$

In (3.2.12), $\mathcal{N}$ is the buoyancy frequency (Brunt-Väisälä frequency) given by:

$$\mathcal{N}^2(z)=-\frac{g}{\overline{\rho}}\frac{d\overline{\rho}}{dz}. \tag{3.2.13}$$

In a stratified fluid, an element of fluid displaced a small distance vertically from its equilibrium position induces a body force in the direction of the fluid element's original position. The simple-harmonic motion produced by this restoring force has a circular frequency of oscillation equal to the buoyancy frequency $\mathcal{N}$. Internal waves are impossible if:

$$\sigma^2>\mathcal{N}^2(z) \tag{3.2.14}$$

everywhere in the fluid, where σ is the excitation frequency (see, for example, Yih, 1977). In the following analysis, internal waves in a continuously stratified fluid are defined to be those waves where $f(z)$ vanishes at least once in the interval $-(h_1+h_2+\delta)<z<0$. From (3.2.11), $f(z)$ is by definition the amplitude of the vertical velocity, hence $f(-h_1-h_2-\delta)=0$ because the vertical velocity must vanish on the bottom. Internal waves have at least one other zero of $f(z)$ in the interval $-(h_1+h_2+\delta)\leq z<0$. This property distinguishes internal waves from free surface

waves, which are generated only at the free surface and whose only zero of $f(z)$ is at $z = -(h_1 + h_2 + \delta)$.

When the density variation in the quiescent fluid is small compared to a fluid density ρ_0, the mean density $\overline{\rho}(z)$ in the first term of (3.2.7) may be replaced by ρ_0; this produces only a small error in the inertia term. But if the reference state of hydrostatic pressure is removed from (3.2.7) it is clear that the density variation is of primary importance in the buoyancy term. When the previous derivation is carried out with the Boussinesq approximation, equations (3.2.12) and (3.2.13) become:

$$\frac{d^2 f}{dz^2} + K^2 \left(\frac{\mathcal{N}^2}{\sigma^2} - 1 \right) f = 0, \tag{3.2.15}$$

$$\mathcal{N}^2(z) = -\frac{g}{\rho_0} \frac{d\overline{\rho}}{dz}. \tag{3.2.16}$$

Notice that $\mathcal{N}$ is constant when the density variation is linear, and zero when the density is constant.

Now let us derive the boundary conditions for a stratified fluid that has piecewise continuous density distribution. The fluid has a free surface and possibly one or more surfaces of density discontinuity in the interior, which divide the fluid into layers of continuously stratified fluids. If the displacement of a surface of density discontinuity from its undisturbed position is:

$$\eta(x, z, t) = \eta_0(z) e^{i(Kx - \sigma t)} \tag{3.2.17}$$

where η_0 is the wave amplitude, then a kinematic boundary condition on this surface is given by:

$$w = \frac{\partial \eta}{\partial t}. \tag{3.2.18}$$

Because the pressure in the fluids above and below the surface of density discontinuity must be the same on the interface, the dynamic boundary condition is:

$$p_\ell = p_u \Rightarrow p'_\ell - \overline{\rho}_\ell g \eta = p'_u - \overline{\rho}_u g \eta \tag{3.2.19}$$

in which the subscripts u and ℓ denote the upper fluid and the lower fluid, respectively. From (3.2.8) and (3.2.11), the horizontal velocity is found to be:

$$u(x,z,t) = \frac{i}{K}\frac{df}{dz}e^{i(Kx-\sigma t)}. \tag{3.2.20}$$

Upon using (3.2.20) and the linearized equation of motion in the x direction from (3.2.7), the pressure fluctuation is found to be:

$$p'(x,z,t) = i\overline{\rho}\frac{\sigma}{K^2}\frac{df}{dz}e^{i(Kx-\sigma t)}. \tag{3.2.21}$$

The substitution of p' into (3.2.19) yields the dynamic boundary condition on the density interface:

$$\left(\overline{\rho}\frac{df}{dz}\right)_u - \left(\overline{\rho}\frac{df}{dz}\right)_\ell + \frac{gK^2}{\sigma^2}(\overline{\rho}_\ell - \overline{\rho}_u)f = 0. \tag{3.2.22}$$

On the free surface, equation (3.2.22) reduces to:

$$\frac{df}{dz} - \frac{gK^2}{\sigma^2}f = 0 \qquad \text{on} \qquad z = 0. \tag{3.2.23}$$

The boundary condition on the bottom is:

$$f(z) = 0 \qquad \text{on} \qquad z = (-h_1 + h_2 + \delta). \tag{3.2.24}$$

By definition, $f(z)$ is continuous everywhere, and from (3.2.22) df/dz is continuous where $\overline{\rho}$ is continuous. Note that the three-layer fluid previously described belongs to this density distribution; its density is continuous in the interval $-(h_1+h_2+\delta) < z < 0$ but the density gradient has finite jumps at $z = -h_1$ and $z = -(h_1+\delta)$.

3.2.2 The Eigenvalue Problem with the Boussinesq Approximation

It is recalled that the Boussinesq approximation neglects variations of density in the inertia term of the Navier-Stokes equations. In the case where the Boussinesq approximation has been made and the density of the fluid is continuous in the interval $-(h_1+h_2+\delta) < z < 0$, the governing differential system consists of (3.2.15),

(3.2.16), (3.2.23), and (3.2.24). These equations together specify an eigenvalue problem, which is stated as follows:

$$\frac{d^2f}{dz^2} + K^2\left(\frac{\mathcal{N}^2}{\sigma^2} - 1\right) f = 0, \qquad -(h_1 + h_2 + \delta) < z < 0, \tag{3.2.25a}$$

$$\frac{df}{dz} - \frac{gK^2}{\sigma^2} f = 0 \qquad \text{on} \qquad z = 0, \tag{3.2.25b}$$

$$f = 0 \qquad \text{on} \qquad z = -(h_1 + h_2 + \delta) \tag{3.2.25c}$$

where

$$\mathcal{N}^2(z) = -\frac{g}{\rho_0}\frac{d\overline{\rho}}{dz}. \tag{3.2.25d}$$

In (3.2.25), f and df/dz are continuous everywhere while d^2f/dz^2 is continuous in the region where $d\overline{\rho}/dz$ is continuous. We are interested in the case where σ is held fixed and K^2 is the eigenvalue parameter. This is not a standard Sturm-Liouville problem because the eigenvalue parameter occurs in the free surface boundary condition. Let us define an inner product $(\mathcal{L}\varphi,\psi)$ by:

$$(\mathcal{L}\varphi, \psi) = \int_{-(h_1+h_2+\delta)}^{0} (\mathcal{L}\varphi)\psi dz, \qquad \mathcal{L} \equiv -\frac{d^2}{dz^2} \tag{3.2.26}$$

in which $\varphi(z)$ and $\psi(z)$ are any two trial functions, which are continuous and have continuous 1st derivative and piecewise continuous 2nd derivative in the interval $-(h_1 + h_2 + \delta) < z < 0$, the trial functions φ and ψ also satisfy the the boundary conditions at $z = 0$ and $z = -(h_1 + h_2 + \delta)$. The integration in (3.2.26) is carried out layer by layer in the ordinary sense for each region where d^2/dz^2 is continuous; this is implied throughout this section. Integration by parts yields:

$$\begin{aligned}(\mathcal{L}\varphi, \psi) &= -\int_{-(h_1+h_2+\delta)}^{0} \psi\frac{d^2\varphi}{dz^2} dz \\ &= -\left[\psi\frac{d\varphi}{dz} - \varphi\frac{d\psi}{dz}\right]_{-(h_1+h_2+\delta)}^{0} - \int_{-(h_1+h_2+\delta)}^{0} \varphi\frac{d^2\psi}{dz^2} dz.\end{aligned} \tag{3.2.27}$$

We cannot eliminate the terms in the square bracket in (3.2.27) because the eigenvalue parameter occurs in the free surface boundary condition. The eigenvalue problem defined by (3.2.25) is not self-adjoint, so that we cannot find the orthogonality conditions for an eigenfunction expansion.

Let us put (3.2.25) in a vector form which we can do the normal eigenfunction expansion. Consider the space of vectors with the first component a trial function and the second component a scalar, for any two such vectors U and V given by:

$$U = \begin{pmatrix} \varphi(z) \\ \varphi_0 \end{pmatrix}, \qquad V = \begin{pmatrix} \psi(z) \\ \psi_0 \end{pmatrix} \tag{3.2.28}$$

we define the inner product:

$$(U, V) = \int_{-(h_1+h_2+\delta)}^{0} \varphi\psi dz - \varphi_0\psi_0. \tag{3.2.29}$$

We further specify a subspace S of vectors such that $\varphi(-h_1 - h_2 - \delta) = 0$ and $\varphi_0 = \varphi(0)$. Then all vectors $U \in S$ are of the form:

$$U(z) = \begin{pmatrix} \varphi(z) \\ \varphi(0) \end{pmatrix} \qquad \text{and} \qquad \varphi(-h_1 - h_2 - \delta) = 0. \tag{3.2.30}$$

Let:

$$\mathcal{L}U \equiv - \begin{pmatrix} \frac{d^2\varphi}{dz^2}(z) \\ \frac{d\varphi}{dz}(0) \end{pmatrix}, \tag{3.2.31}$$

then our original eigenvalue problem can be stated as follows:

$$\mathcal{L}U = \alpha R U, \qquad U \in S \tag{3.2.32a}$$

where

$$\alpha = K^2, \quad R = \begin{pmatrix} \frac{\mathcal{N}^2}{\sigma^2} - 1 & 0 \\ 0 & -\frac{q}{\sigma^2} \end{pmatrix}. \tag{3.2.32b}$$

Now:

$$(\mathcal{L}U, V) = - \int_{-(h_1+h_2+\delta)}^{0} \frac{d^2\varphi}{dz^2}\psi dz + \frac{d\varphi}{dz}(0)\psi(0)$$

$$= -\left[\frac{d\varphi}{dz}\psi - \frac{d\psi}{dz}\varphi\right]_{-(h_1+h_2+\delta)}^{0} - \int_{-(h_1+h_2+\delta)}^{0} \frac{d^2\psi}{dz^2}\varphi dz + \frac{d\varphi}{dz}(0)\psi(0)$$

$$= -\int_{-(h_1+h_2+\delta)}^{0} \frac{d^2\psi}{dz^2}\varphi dz + \frac{d\psi}{dz}(0)\varphi(0)$$

$$= (U, \mathcal{L}V). \tag{3.2.33}$$

Hence (3.2.32) is self-adjoint. The eigenvectors of the adjoint problem are written as:

$$U_n(z) = \begin{pmatrix} \varphi_n(z) \\ \varphi_n(0) \end{pmatrix}, \qquad (n = 1, 2, \ldots). \tag{3.2.34}$$

Let α and β be any two different eigenvalues of the adjoint problem, and U and V the corresponding eigenvectors. It follows from (3.2.33) that:

$$\begin{aligned} &(\mathcal{L}U, V) = (U, \mathcal{L}V) \\ \Rightarrow &(\alpha RU, V) = (U, \beta RV) \\ \Rightarrow &(\alpha - \beta)(RU, V) = 0 \\ \Rightarrow &(RU, V) = 0, \qquad (\alpha \neq \beta). \end{aligned} \tag{3.2.35}$$

An equivalent form of (3.2.35) is:

$$\int_{-(h_1+h_2+\delta)}^{0} \left(\frac{\mathcal{N}^2}{\sigma^2} - 1\right)\varphi\psi dz + \frac{g}{\sigma^2}\varphi(0)\psi(0) = 0, \qquad (\alpha \neq \beta). \tag{3.2.36}$$

Following the same procedure in § 3.1.2 for the two-layer fluid, the Wronskian can be used to show that each eigenvalue corresponds to only one eigenvector. Now that we have the orthogonality condition (3.2.36), we may expand a given vector $F(z)$ in terms of a series of these eigenvectors, in the form:

$$F(z) = \begin{pmatrix} f(z) \\ f(0) \end{pmatrix} = \sum_{n=1}^{\infty} C_n U_n(z) \tag{3.2.37a}$$

where

$$C_n = \frac{(RF, U_n)}{(RU_n, U_n)}, \qquad U_n(z) = \begin{pmatrix} \varphi_n(z) \\ \varphi_n(0) \end{pmatrix}, \tag{3.2.37b}$$

$$(RF, U_n) = \int_{-(h_1+h_2+\delta)}^{0} \left(\frac{\mathcal{N}^2}{\sigma^2} - 1\right) f(z)\varphi_n(z)dz + \frac{g}{\sigma^2} f(0)\varphi_n(0), \qquad (3.2.37c)$$

$$(RU_n, U_n) = \int_{-(h_1+h_2+\delta)}^{0} \left(\frac{\mathcal{N}^2}{\sigma^2} - 1\right) \varphi_n^2(z)dz + \frac{g}{\sigma^2}\varphi_n^2(0). \qquad (3.2.37d)$$

It is clear that (3.2.36) and (3.2.37) give the orthogonality condition and the eigenfunction expansion for the original problem, which cannot be found by standard procedures for Sturm-Liouville systems. Let φ^* be the complex conjugate of φ, an eigenfunction of (3.2.25), multiplying (3.2.25a) by $\rho_0\varphi^*$, integrating between $-(h_1+h_2+\delta)$ and 0, and applying the boundary conditions (3.2.25b) and (3.2.25c), we get:

$$\rho_0 \frac{gK^2}{\sigma^2}|\varphi(0)|^2 - \frac{gK^2}{\sigma^2} \int_{-(h_1+h_2+\delta)}^{0} \frac{d\overline{\rho}}{dz}|\varphi|^2 dz$$

$$- \int_{-(h_1+h_2+\delta)}^{0} \rho_0 \left|\frac{d\varphi}{dz}\right|^2 dz - K^2 \int_{-(h_1+h_2+\delta)}^{0} \rho_0|\varphi|^2 dz = 0. \qquad (3.2.38)$$

It can be seen that K^2 is real, but the positive and negative values of K^2 have no upper and lower bounds. Inspection of (3.2.11) shows that the positive values of K^2 correspond to the wave numbers of the propagating waves while the negative values of K^2 correspond to the wave numbers of the locally bounded standing waves that do not propagate. In § 3.2.4 it will be shown that the first two terms in (3.2.38) are proportional to the potential energy of wave motion, whereas the last two terms in (3.2.38) are proportional to the kinetic energy of wave motion. Hence (3.2.38) shows that the total energy of wave motion in a continuously stratified fluid is equally partitioned in the form of kinetic and potential energies.

Now we proceed to solve the eigenvalue problem (3.2.25) for a homogeneous fluid, and for a three-layer fluid.

3.2.2.1 Eigenvalues and Eigenfunctions of a Homogeneous Fluid

The bottom of the homogeneous fluid in the constant-depth channel is specified at $z = -h$ with z measured positive upwards from the undisturbed free surface. In this region $d\bar{\rho}/dz = 0$, hence (3.2.25) reduces to:

$$\frac{d^2 f}{dz^2} - K^2 f = 0, \qquad -h < z < 0, \tag{3.2.39a}$$

$$\frac{df}{dz} - \frac{gK^2}{\sigma^2} f = 0 \qquad \text{on} \qquad z = 0, \tag{3.2.39b}$$

$$f = 0 \qquad \text{on} \qquad z = -h. \tag{3.2.39c}$$

Equation (3.2.39) has the general solution:

$$f(z) = Ae^{Kz} + Be^{-Kz} \tag{3.2.40}$$

where A and B are unknown constants. The function $f(z)$ is determined to an arbitrary constant by imposing the boundary condition on the bottom (equation 3.2.39c). After normalization, the eigenfunctions are given by:

$$Z(z) = (\Lambda^h)^{-1/2} \sinh k(z+h), \tag{3.2.41a}$$

$$\hat{Z}_n(z) = (\Lambda_n^h)^{-1/2} \sin \hat{k}_n(z+h), \qquad (n = 1, 2, \ldots), \tag{3.2.41b}$$

$$\begin{aligned} \Lambda^h &= -\int_{-h}^{0} \sinh^2 k(z+h)dz + \frac{g}{\sigma^2}\sinh^2 kh \\ &= -\frac{1}{2}\left(\frac{1}{2k}\sinh 2kh - h\right) + \frac{g}{\sigma^2}\sinh^2 kh, \end{aligned} \tag{3.2.41c}$$

$$\begin{aligned} \Lambda_n^h &= -\int_{-h}^{0} \sin^2 \hat{k}_n(z+h)dz + \frac{g}{\sigma^2}\sin^2 \hat{k}_n h \\ &= \frac{1}{2}\left(\frac{1}{2\hat{k}_n}\sin 2\hat{k}_n h - h\right) + \frac{g}{\sigma^2}\sin^2 \hat{k}_n h. \end{aligned} \tag{3.2.41d}$$

The eigenfunctions are orthogonal in the sense that:

$$-\int_{-h}^{0} \varphi\psi dz + \frac{g}{\sigma^2}\varphi(0)\psi(0) = \begin{cases} 0, & \varphi \neq \psi; \\ 1, & \varphi = \psi \end{cases} \tag{3.2.42}$$

where $\varphi(z)$ and $\psi(z)$ are any two normalized eigenfunctions. In (3.2.41), k^2 and $-\hat{k}_n^2$, $(n = 1, 2, \ldots)$ are the eigenvalues of K^2. The eigenvalues are defined by the following relationships:

$$\sigma^2 = gk \tanh kh, \tag{3.2.43a}$$

$$\sigma^2 = -g\hat{k}_n \tan \hat{k}_n h, \qquad (n = 1, 2, \ldots). \tag{3.2.43b}$$

Equations (3.2.43a) and (3.2.43b) can be obtained by substitution of (3.2.41a) and (3.2.41b) into (3.2.39b).

3.2.2.2 Eigenvalues and Eigenfunctions of a Three-Layer Fluid

The density distribution of the three-layer fluid in the trench region (figure 3.2.1) is specified as follows:

$$\overline{\rho}(z) = \begin{cases} \rho_1, & -h_1 < z < 0; \\ \rho_1 - \Delta\rho(z + h_1)/\delta, & -(h_1 + \delta) < z < -h_1; \\ \rho_2, & -(h_1 + h_2 + \delta) < z < -(h_1 + \delta) \end{cases}$$

where $\Delta\rho = \rho_2 - \rho_1$. From (3.2.25) the governing differential system is given by:

$$\frac{d^2 f}{dz^2} - K^2 f = 0, \qquad -h_1 < z < 0 \qquad \text{and}$$

$$-(h_1 + h_2 + \delta) < z < -(h_1 + \delta), \tag{3.2.44a}$$

$$\frac{d^2 f}{dz^2} + K^2 \left(\frac{\overline{\mathcal{N}}^2}{\sigma^2} - 1 \right) f = 0, \qquad -(h_1 + \delta) < z < -h_1, \tag{3.2.44b}$$

$$\frac{df}{dz} - \frac{gK^2}{\sigma^2} f = 0 \qquad \text{on} \qquad z = 0, \tag{3.2.44c}$$

$$f = 0 \qquad \text{on} \qquad z = -(h_1 + h_2 + \delta) \tag{3.2.44d}$$

where

$$\overline{\mathcal{N}}^2 = \frac{g}{\delta} \frac{\Delta\rho}{\rho_1} \tag{3.2.44e}$$

and

$$f, \frac{df}{dz} \quad \textit{continuous} \qquad \textit{on} \qquad z = -h_1 \quad \textit{and} \quad z = -(h_1 + \delta).$$

Equation (3.2.44) has the general solutions:

$$f_1(z) = A_1 e^{Kz} + B_1 e^{-Kz}, \tag{3.2.45a}$$

$$f_2(z) = A_2 e^{Kz} + B_2 e^{-Kz}, \tag{3.2.45b}$$

$\overline{\mathcal{N}} \neq \sigma$:

$$f_3(z) = A_3 \cos K \left(\frac{\overline{\mathcal{N}}^2}{\sigma^2} - 1 \right)^{1/2} z + B_3 \sin K \left(\frac{\overline{\mathcal{N}}^2}{\sigma^2} - 1 \right)^{1/2} z, \tag{3.2.45c}$$

$\overline{\mathcal{N}} = \sigma$:

$$f_3(z) = A_3 z + B_3 \tag{3.2.45d}$$

where A_1, B_1, A_2, B_2, A_3, and B_3 are unknown constants. The subscripts (1, 2, and 3) denote the respective regions shown in figure (3.2.1).

First let us consider the case where $\overline{\mathcal{N}} \neq \sigma$. The two boundary conditions (equations 3.2.44c and 3.2.44d) and the four matching conditions (continuity of f and df/dz on $z = -h_1$ and $z = -(h_1 + \delta)$) provide six equations with six unknowns. The equations are linear and homogeneous in these six unknowns, and therefore, for a solution to exist, the determinant of these equations must vanish. The condition that the determinant must vanish defines the following relationships for the eigenvalues of K^2:

$$\Theta^{1/2} \cos\left(\Theta^{1/2} K_j \delta\right) \left(\coth K_j h_2 + \frac{K_j \cosh K_j h_1 - K_0 \sinh K_j h_1}{K_j \sinh K_j h_1 - K_0 \cosh K_j h_1} \right)$$
$$- \sin\left(\Theta^{1/2} K_j \delta\right) \left(\Theta - \frac{K_j \cosh K_j h_1 - K_0 \sinh K_j h_1}{K_j \sinh K_j h_1 - K_0 \cosh K_j h_1} \coth K_j h_2 \right) = 0$$
$$(j = 1, 2, \ldots) \tag{3.2.46a}$$

and

$$\Theta^{1/2} \cosh\left(\Theta^{1/2} \hat{K}_n \delta\right) \left(\cot \hat{K}_n h_2 + \frac{\hat{K}_n \cos \hat{K}_n h_1 - K_0 \sin \hat{K}_n h_1}{\hat{K}_n \sin \hat{K}_n h_1 + K_0 \cos \hat{K}_n h_1} \right)$$
$$+ \sinh\left(\Theta^{1/2} \hat{K}_n \delta\right) \left(\Theta + \frac{\hat{K}_n \cos \hat{K}_n h_1 - K_0 \sin \hat{K}_n h_1}{\hat{K}_n \sin \hat{K}_n h_1 + K_0 \cos \hat{K}_n h_1} \cot \hat{K}_n h_2 \right) = 0$$
$$(n = 1, 2, \ldots) \tag{3.2.46b}$$

in which $\Theta = (\overline{\mathcal{N}}^2/\sigma^2 - 1) \neq 0$, $K_0 = \sigma^2/g$, and K_j^2, $(j = 1, 2, \ldots)$ and $-\hat{K}_n^2$, $(n = 1, 2, \ldots)$ are the eigenvalues of K^2. Notice that (3.2.46a) has an infinite number of roots of K_j if and only if $\Theta > 0$. The smallest root K_1 is the wave number of the surface mode. The next root K_2 is the wave number of the primary internal mode. The surface mode and the primary internal mode usually have wavelengths much larger than δ, so that $K\delta \ll 1$ and (3.2.46a) may be approximated by:

$$\left(\coth K_j h_2 + \frac{K_j \cosh K_j h_1 - K_0 \sinh K_j h_1}{K_j \sinh K_j h_1 - K_0 \cosh K_j h_1}\right)$$
$$-K_j\delta\left(\Theta - \frac{K_j \cosh K_j h_1 - K_0 \sinh K_j h_1}{K_j \sinh K_j h_1 - K_0 \cosh K_j h_1} \coth K_j h_2\right) = 0.$$
$$(j = 1, 2) \tag{3.2.47}$$

With the substitution of $\overline{\mathcal{N}}$ from (3.2.44e), and some alegbra, we obtain the following dispersion relation:

$$\sigma^4\left(\coth K_j h_1 \coth K_j h_2 + 1 + K_j\delta(\coth K_j h_1 + \coth K_j h_2)\right)$$
$$-\sigma^2\left(\frac{\rho_2}{\rho_1}\coth K_j h_1 + \coth K_j h_2 + K_j\delta(\coth K_j h_1 \coth K_j h_2 + 1)\right) gK_j$$
$$+\left(\frac{\rho_2}{\rho_1} - 1\right) g^2 K_j^2 = 0, \qquad (j = 1, 2). \tag{3.2.48}$$

Notice the similarity between (3.2.48) and the dispersion relation for the two-layer fluid given by (3.1.18a). Equation 3.2.48 is not as exact as (3.1.18a) because the Boussinesq approximation is made in the three-layer problem. In particular, if we put $\delta = 0$ in (3.2.48), the equation does not reduce exactly to (3.2.18a) because in the three-layer problem the density ratio ρ_2/ρ_1 in the inertia term is approximated by unity; this is due to the Boussinesq approximation. Equation (3.2.48) indicates that when $K_j\delta$ is small, the wave numbers for the first two propagating modes of the three-layer fluid would be similar to the wave numbers of the surface mode and the interfacial mode in the two-layer fluid. When $\Theta < 0$, the trigonometric functions sine and cosine in (3.2.46a) become the hyperbolic sine and hyperbolic

cosine, consequently K_j has only one real root corresponding to the wave number of the surface mode. Thus internal waves are impossible in the three-layer fluid when the forcing frequency σ is greater than the buoyancy frequency $\overline{\mathcal{N}}$.

When $\Theta = 0$, equation (3.2.45d) should be used instead of (3.2.45c). The dispersion relation corresponding to (3.2.46a) is given by the following for $\overline{\mathcal{N}} = \sigma$:

$$\begin{aligned}&\sigma^2 \left(\coth Kh_1 \coth Kh_2 + 1 + K\delta \coth Kh_2\right)\\ =&gK \left(\coth Kh_1 + \coth Kh_2 + K\delta \coth Kh_1 \coth Kh_2\right).\end{aligned} \tag{3.2.49}$$

Equation (3.2.49) reduces to (3.2.43a) when $K\delta = 0$. It is seen in (3.2.49) that K has only one real root corresponding to the wave number of the surface wave; there is no internal wave. Equations (3.2.46a) and (3.2.49) show that internal waves in the three-layer fluid are possible only when $\sigma < \overline{\mathcal{N}}$; when $\sigma \geq \overline{\mathcal{N}}$ only the surface mode exists. In this study we are interested in internal waves in a submarine trench, hence the case $\Theta = 0$ will not be considered in the following analysis.

Equation 3.2.46b always has an infinite number of real roots, these are the wave numbers of the locally bounded standing waves that do not propagate.

Any five of the six unknowns of the homogeneous equations can be determined in terms of the remaining unknown, therefore $f(z)$ is determined to an arbitrary constant. After normalization, the eigenfunctions are given by:

$$\begin{aligned}Z_{j1}(z) = &(\Lambda_j^s)^{-1/2} \left(\Theta^{1/2} \cos\left(\Theta^{1/2} K_j \delta\right) + \coth K_j h_2 \sin\left(\Theta^{1/2} K_j \delta\right)\right)\\ &\cdot \left(\frac{K_0 \cosh K_j z + K_j \sinh K_j z}{K_0 \cosh K_j h_1 - K_j \sinh K_j h_1}\right), \qquad (j = 1, 2, \ldots),\end{aligned} \tag{3.2.50a}$$

$$Z_{j2}(z) = (\Lambda_j^s)^{-1/2} \Theta^{1/2} \left(\frac{\sinh K_j (z + h_1 + h_2 + \delta)}{\sinh K_j h_2}\right), \tag{3.2.50b}$$

$$\begin{aligned}Z_{j3}(z) = &(\Lambda_j^s)^{-1/2} \Big(\Theta^{1/2} \cos\left(\Theta^{1/2} K_j (z + h_1 + \delta)\right)\\ &+ \coth K_j h_2 \sin\left(\Theta^{1/2} K_j (z + h_1 + \delta)\right)\Big),\end{aligned} \tag{3.2.50c}$$

$$\hat{Z}_{n1}(z) = (\Lambda_n^s)^{-1/2} \left(\Theta^{1/2} \cosh\left(\Theta^{1/2} \hat{K}_n \delta\right) + \cot \hat{K}_n h_2 \sinh\left(\Theta^{1/2} \hat{K}_n \delta\right)\right)$$

$$\cdot \left(\frac{K_0 \cos \hat{K}_n z - \hat{K}_n \sin \hat{K}_n z}{K_0 \cos \hat{K}_n h_1 + \hat{K}_n \sin \hat{K}_n h_1} \right), \qquad (n = 1, 2, \ldots), \tag{3.2.50d}$$

$$\hat{Z}_{n2}(z) = (\Lambda_n^s)^{-1/2} \Theta^{1/2} \left(\frac{\sin \hat{K}_n (z + h_1 + h_2 + \delta)}{\sin \hat{K}_n h_2} \right), \tag{3.2.50e}$$

$$\hat{Z}_{n3}(z) = (\Lambda_n^s)^{-1/2} \Big(\Theta^{1/2} \cosh \left(\Theta^{1/2} \hat{K}_n (z + h_1 + \delta) \right) + \cot \hat{K}_n h_2 \sinh \left(\Theta^{1/2} \hat{K}_n (z + h_1 + \delta) \right) \Big), \tag{3.2.50f}$$

$$\begin{aligned} \Lambda_j^s = & - \left(\frac{h_2 \Theta}{2 \sinh^2 K_j h_2} \right) \left(\frac{\sinh 2K_j h_2}{2K_j h_2} - 1 \right) + \left(\frac{\Theta \delta}{2} \right) \left\{ \left(\frac{\sin \left(2\Theta^{1/2} K_j \delta \right)}{2\Theta^{1/2} K_j \delta} + 1 \right) \Theta \right. \\ & \left. - \left(\frac{\coth K_j h_2}{K_j \delta} \right) \left(\cos \left(2\Theta^{1/2} K_j \delta \right) - 1 \right) - \coth^2 K_j h_2 \left(\frac{\sin \left(2\Theta^{1/2} K_j \delta \right)}{2\Theta^{1/2} K_j \delta} - 1 \right) \right\} \\ & - \frac{1}{2} \left\{ K_0^2 h_1 \left(\frac{\sinh 2K_j h_1}{2K_j h_1} + 1 \right) - K_0 (1 + \cosh 2K_j h_1) \right. \\ & \left. + K_j^2 h_1 \left(\frac{\sinh 2K_j h_1}{2K_j h_1} - 1 \right) \right\} \\ & \cdot \left(\frac{\Theta^{1/2} \cos \left(\Theta^{1/2} K_j \delta \right) + \coth K_j h_2 \sin \left(\Theta^{1/2} K_j \delta \right)}{K_0 \cosh K_j h_1 - K_j \sinh K_j h_1} \right)^2, \end{aligned} \tag{3.2.50g}$$

$$\begin{aligned} \Lambda_n^s = & \left(\frac{h_2 \Theta}{2 \sin^2 \hat{K}_n h_2} \right) \left(\frac{\sin 2\hat{K}_n h_2}{2\hat{K}_n h_2} - 1 \right) + \left(\frac{\Theta \delta}{2} \right) \left\{ \left(\frac{\sinh \left(2\Theta^{1/2} \hat{K}_n \delta \right)}{2\Theta^{1/2} \hat{K}_n \delta} + 1 \right) \Theta \right. \\ & \left. + \left(\frac{\cot \hat{K}_n h_2}{\hat{K}_n \delta} \right) \left(\cosh \left(2\Theta^{1/2} \hat{K}_n \delta \right) - 1 \right) + \cot^2 \hat{K}_n h_2 \left(\frac{\sinh \left(2\Theta^{1/2} \hat{K}_n \delta \right)}{2\Theta^{1/2} \hat{K}_n \delta} - 1 \right) \right\} \\ & - \frac{1}{2} \left\{ K_0^2 h_1 \left(\frac{\sin 2\hat{K}_n h_1}{2\hat{K}_n h_1} + 1 \right) - K_0 (1 + \cos 2\hat{K}_n h_1) \right. \\ & \left. - \hat{K}_n^2 h_1 \left(\frac{\sin 2\hat{K}_n h_1}{2\hat{K}_n h_1} - 1 \right) \right\} \\ & \cdot \left(\frac{\Theta^{1/2} \cosh \left(\Theta^{1/2} \hat{K}_n \delta \right) + \cot \hat{K}_n h_2 \sinh \left(\Theta^{1/2} \hat{K}_n \delta \right)}{K_0 \cos \hat{K}_n h_1 + \hat{K}_n \sin \hat{K}_n h_1} \right)^2. \end{aligned} \tag{3.2.50h}$$

In (3.2.50), the subscripts (1, 2, and 3) denote the respective regions shown in figure 3.2.1. The normalizing constants Λ_j^s, $(j = 1, 2, \ldots)$, and Λ_n^s, $(n = 1, 2, \ldots)$ are obtained by direct substitution of (3.2.50a)–(3.2.50f) into (3.2.37d). The eigenfunc-

tions are orthogonal in the sense that:

$$\int_{-(h_1+h_2+\delta)}^{0} \left(\frac{\mathcal{N}^2}{\sigma^2} - 1\right) \varphi\psi dz + \frac{g}{\sigma^2}\varphi(0)\psi(0) = \begin{cases} 0, & \varphi \neq \psi; \\ 1, & \varphi = \psi \end{cases} \tag{3.2.51}$$

wherein $\mathcal{N} = 0$ in $-(h_1 + h_2 + \delta) < z < -(h_1 + \delta)$ and in $-h_1 < z < 0$, and $\mathcal{N} = \overline{\mathcal{N}}$ in $-(h_1 + \delta) < z < -h_1$. The functions φ and ψ are any two normalized eigenfunctions.

Now we have found the sets of mutually orthogonal eigenfunctions for the homogeneous fluid (equation 3.2.41) and for the three-layer fluid (equation 3.2.50). We may expand the horizontal velocities and the vertical velocities in the constant-depth channel and in the trench region in terms of a series of these eigenfunctions. Then the horizontal and vertical velocities must be matched along a vertical boundary at the upstream edge of the trench to obtain a set of simultaneous equations in terms of the unknown coefficients, which can then be solved by standard methods.

3.2.3 The Trench Model

The fluid domain is divided into five regions as shown in figure (3.2.1):

Region 1 $\quad \overline{\rho} = \rho_1, \quad -h_1 < z < 0, \quad 0 < x < \ell$

Region 2 $\quad \overline{\rho} = \rho_2, \quad -(h_1 + h_2 + \delta) < z < -(h_1 + \delta), \quad 0 < x < \ell$

Region 3 $\quad \overline{\rho} = \rho_1 - \Delta\rho(z + h_1)/\delta, \quad -(h_1 + \delta) < z < -h_1, \quad 0 < x < \ell$

Region 4 $\quad \overline{\rho} = \rho_1, \quad -h < z < 0, \quad -L < x < -L/2$

Region 5 $\quad \overline{\rho} = \rho_1, \quad -h < z < 0, \quad -L/2 < x < 0$

where ρ_1 and ρ_2 are the densities of the upper fluid and of the lower fluid, respectively, and $\Delta\rho = \rho_2 - \rho_1$; the other symbols are defined in figure 3.2.1. As in the two-layer model, we divide the constant-depth channel into two regions (4 and 5) at $x = -L/2$. We assume that at this location the wave motion is represented by the propagating modes only; the amplitudes of the locally bounded non-propagating

modes decrease exponentially with distance from $x = -L$ and $x = 0$, so that their contributions at $x = -L/2$ are negligible.

For steady-state motion, the horizontal velocity $u(x, z, t)$ and the vertical velocity $w(x, z, t)$ may be written in the form:

$$u(x, z, t) = u'(x, z)e^{-i\sigma t}, \tag{3.2.52a}$$

$$w(x, z, t) = w'(x, z)e^{-i\sigma t}. \tag{3.2.52b}$$

Equations (3.2.52a) and (3.2.52b) are of the form (3.2.20) and (3.2.11). The eigenfunctions in (3.2.41) and (3.2.50) take the role of $f(z)$ in (3.2.11) and (3.2.20). The spatial velocities $u'(x, z)$ and $w'(x, z)$ may be expanded in terms of a series of the orthogonal modes found in § 3.2.2. The solutions in the trench region are written as:

$$\begin{aligned} u'_{1,2,3}(x, z) = &\sum_{j=1}^{\infty} \frac{i}{K_j} \left(A_j e^{iK_j x} - B_j e^{-iK_j x} \right) \frac{d}{dz} \Big(Z_{j1,2,3}(z) \Big) \\ &- \sum_{n=1}^{\infty} \frac{1}{\hat{K}_n} \left(\hat{A}_n e^{\hat{K}_n x} - \hat{B}_n e^{-\hat{K}_n x} \right) \frac{d}{dz} \Big(\hat{Z}_{n1,2,3}(z) \Big), \end{aligned} \tag{3.2.53a}$$

$$\begin{aligned} w'_{1,2,3}(x, z) = &\sum_{j=1}^{\infty} \left(A_j e^{iK_j x} + B_j e^{-iK_j x} \right) Z_{j1,2,3}(z) \\ &+ \sum_{n=1}^{\infty} \left(\hat{A}_n e^{\hat{K}_n x} + \hat{B}_n e^{-\hat{K}_n x} \right) \hat{Z}_{n1,2,3}(z). \end{aligned} \tag{3.2.53b}$$

In (3.2.53a) and (3.2.53b), A_j, B_j, $(j = 1, 2, \ldots)$, and $\hat{A}_n$, $\hat{B}_n$, $(n = 1, 2, \ldots)$ are unknown constants to be determined from the boundary and matching conditions. In both equations the first summation represents propagating waves consisting of the free surface mode and the infinite number of internal modes, and the second summation represents local disturbances that do not propagate. Similarly, the solutions in the constant-depth channel are written as:

$$\begin{aligned} u'_4(x, z) = &\frac{i}{k} \left(C e^{ik(x+L)} - D e^{-ik(x+L)} \right) \frac{dZ}{dz}(z) \\ &+ \sum_{n=1}^{\infty} \frac{1}{\hat{k}_n} \hat{C}_n e^{-\hat{k}_n(x+L)} \frac{d\hat{Z}_n}{dz}(z), \end{aligned} \tag{3.2.54a}$$

$$u_5'(x,z) = \frac{i}{k}\left(Ee^{ikx} - F^{-ikx}\right)\frac{dZ}{dz}(z) - \sum_{n=1}^{\infty}\frac{1}{\hat{k}_n}\hat{F}_n e^{\hat{k}_n x}\frac{d\hat{Z}_n}{dz}(z), \quad (3.2.54b)$$

$$w_4'(x,z) = \left(Ce^{ik(x+L)} + De^{-ik(x+L)}\right)Z(z) + \sum_{n=1}^{\infty}\hat{C}_n e^{-\hat{k}_n(x+L)}\hat{Z}_n(z), \quad (3.2.54c)$$

$$w_5'(x,z) = \left(Ee^{ikx} + Fe^{-ikx}\right)Z(z) + \sum_{n=1}^{\infty}\hat{F}_n e^{\hat{k}_n x}\hat{Z}_n(z) \quad (3.2.54d)$$

in which C, D, E, F, and $\hat{C}_n$, $\hat{F}_n$, $(n = 1, 2, \ldots)$ are unknown constants to be determined. Notice that in (3.2.53) and (3.2.54) u' and w' satisfy the continuity equation (3.2.8).

The fluid velocities in the trench region and in the constant-depth channel must satisfy the following additional boundary conditions:

$$u = 0 \qquad \text{on} \qquad -(h_1 + h_2 + \delta) < z < -h, \quad x = 0, \quad (3.2.55a)$$

$$u = 0 \qquad \text{on} \qquad -(h_1 + h_2 + \delta) < z < 0, \quad x = \ell, \quad (3.2.55b)$$

$$u_4 = \frac{i}{2}S\sigma e^{-i\sigma t} \qquad \text{on} \qquad -h < z < 0, \quad x = -L \quad (3.2.55c)$$

where S is the stroke of the wave generator. The matching conditions are the conditions of continuity of horizontal velocity and of vertical velocity at $x = 0$, that is:

$$u_1 = u_5 \qquad \text{on} \qquad -h < z < 0, \quad x = 0, \quad (3.2.56a)$$

$$w_1 = w_5 \qquad \text{on} \qquad -h < z < 0, \quad x = 0. \quad (3.2.56b)$$

Equation (3.2.55b) implies:

$$B_j = A_j e^{2iK_j\ell}, \qquad (j = 1, 2, \ldots), \quad (3.2.57a)$$

$$\hat{B}_n = \hat{A}_n e^{2\hat{K}_n\ell}, \qquad (n = 1, 2, \ldots). \quad (3.2.57b)$$

Integrating (3.2.55c), and after using (3.2.52a) and (3.2.54a), we get:

$$\frac{i}{k}(C - D)Z(z) + \sum_{n=1}^{\infty}\frac{1}{\hat{k}_n}\hat{C}_n\hat{Z}_n(z) = \frac{iS\sigma}{2}(z + h). \quad (3.2.58)$$

Note that the integration of (3.2.55c) yields the volume flux between $-h$ and z, the constant of integration is determined from the condition that the volume flux must be zero at $z = -h$. Now (3.2.58) is in the form (3.2.37a), it is seen that if the right hand side of (3.2.58) is given the role of $f(z)$ in (3.2.37a), the unknown constants on the left hand side of (3.2.58) can be found using (3.2.37b), thus, we have:

$$\begin{aligned} C - D &= -ik\left(-\int_{-h}^{0}\frac{iS\sigma}{2}(z+h)Z\,dz + \frac{g}{\sigma^2}\left(\frac{iS\sigma h}{2}\right)Z(0)\right) \\ &= \frac{S\sigma}{2k}\left(\Lambda^h\right)^{-1/2}\sinh kh, \qquad (3.2.59a) \\ \hat{C}_n &= \hat{k}_n\left(-\int_{-h}^{0}\frac{iS\sigma}{2}(z+h)\hat{Z}_n\,dz + \frac{g}{\sigma^2}\left(\frac{iS\sigma h}{2}\right)\hat{Z}_n(0)\right) \\ &= -\frac{iS\sigma}{2\hat{k}_n}\left(\Lambda_n^h\right)^{-1/2}\sin\hat{k}_n h. \qquad (3.2.59b) \end{aligned}$$

We assume that the wave motion is asymptotically a superposition of simple wave trains at $x = -L/2$, hence:

$$E = Ce^{ikL}, \qquad (3.2.60a)$$

$$F = De^{-ikL}. \qquad (3.2.60b)$$

3.2.3.1 Matching the Solutions

The spatial horizontal and vertical velocities in the trench region and in the constant-depth channel are given by (3.2.53) and (3.2.54) in terms of the unknown coefficients. These velocities must be matched at $x = 0$ to obtain the sets of equations from which the unknown coefficients can be determined. Because there are an infinite number of unknown coefficients in the infinite series, an infinite number of simultaneous equations are needed. For numerical evalution, we truncate the infinite series in (3.2.53) and (3.2.54) after a finite number of terms given by J for the propagating modes and N for the non-propagating modes, we are then left with $(J+2N+1)$ unknowns: A_j, $(j = 1,2,\ldots,J)$, C, and $\hat{A}_n$, $\hat{F}_n$, $(n = 1,2,\ldots,N)$.

We obtain $(J+2N+1)$ equations by matching the horizontal and vertical velocities in the trench region and in the constant-depth channel along a vertical boundary at the upstream edge of the trench, that is, at $x = 0$. First we consider the condition of continuity of horizontal velocity at $x = 0$ (equation 3.2.56a). Let $\tilde{u}'$ be the truncated velocity of u', then (3.2.53a) yields:

$$\tilde{u}'_{1,2,3}(0,z) = \sum_{j=1}^{J} \frac{i}{K_j}\left(A_j - B_j\right)\frac{d}{dz}\Big(Z_{j1,2,3}(z)\Big) - \sum_{n=1}^{N} \frac{1}{\hat{K}_n}\left(\hat{A}_n - \hat{B}_n\right)\frac{d}{dz}\Big(\hat{Z}_{n1,2,3}(z)\Big). \tag{3.2.61}$$

Integrating (3.2.61) between $-(h_1+h_2+\delta)$ and z, we obtain the volume flux $\tilde{Q}(z)$ at $x = 0$:

$$\begin{aligned}\tilde{Q}_{1,2,3}(z) &= \int_{-(h_1+h_2+\delta)}^{z} \tilde{u}'(0,z)dz \\ &= \sum_{j=1}^{J} \frac{i}{K_j}\left(A_j - B_j\right) Z_{j1,2,3}(z) - \sum_{n=1}^{N} \frac{1}{\hat{K}_n}\left(\hat{A}_n - \hat{B}_n\right)\hat{Z}_{n1,2,3}(z)\end{aligned} \tag{3.2.62}$$

in which $\tilde{Q}_i$, $(i = 1,2,3)$ denotes the volume flux between $-(h_1+h_2+\delta)$ and z in region i. From (3.2.54b), we have:

$$u'_5(0,z) = \frac{i}{k}\left(E - F\right)\frac{dZ}{dz}(z) - \sum_{n=1}^{N} \frac{1}{\hat{k}_n}\hat{F}_n\frac{d\hat{Z}_n}{dz}(z). \tag{3.2.63}$$

Integrating between $-h$ and z, we get:

$$\begin{aligned}\tilde{Q}_5(z) &= \int_{-h}^{z} \tilde{u}'_5(0,z)dz \\ &= \frac{i}{k}\left(E - F\right)Z(z) - \sum_{n=1}^{N} \frac{1}{\hat{k}_n}\hat{F}_n\hat{Z}_n(z).\end{aligned} \tag{3.2.64}$$

Equations (3.2.55a) and (3.2.56a) imply that:

$$\tilde{Q}_1(z) = \tilde{Q}_5(z), \qquad -h < z < 0, \tag{3.2.65a}$$

$$\tilde{Q}_1(z) = 0, \qquad -h_1 < z < -h, \tag{3.3.65b}$$

$$\tilde{Q}_2(z) = 0, \qquad -(h_1+h_2+\delta) < z < -(h_1+\delta), \tag{3.2.65c}$$

$$\tilde{Q}_3(z) = 0, \qquad -(h_1+\delta) < z < -h_1. \tag{3.2.65d}$$

Note that $\tilde{Q}_i$ is continuous in z, and the matching is done over the larger depth $(h_1 + h_2 + \delta)$ in order to satisfy the boundary condition on the upstream wall of the trench (equation 3.2.55a). Now we can apply (3.2.37) to obtain $(J + N)$ linear integral equations. The right hand side of (3.2.65) is given the role of $f(z)$ in (3.2.37a), then the unknown constants in the series expansions of $\tilde{Q}_{1,2,3}$ are given by:

$$\frac{i}{K_j}(A_j - B_j) = -\int_{-h}^{0} \tilde{Q}_5(z) Z_{j1}(z) dz + \frac{g}{\sigma^2}\tilde{Q}_5(0) Z_{j1}(0),$$
$$(j = 1, 2, \ldots, J) \qquad (3.2.66a)$$

$$-\frac{1}{\hat{K}_n}\left(\hat{A}_n - \hat{B}_n\right) = -\int_{-h}^{0} \tilde{Q}_5(z) \hat{Z}_{n1}(z) dz + \frac{g}{\sigma^2}\tilde{Q}_5(0) \hat{Z}_{n1}(0).$$
$$(n = 1, 2, \ldots, N) \qquad (3.2.66b)$$

The remaining $(N+1)$ equations are constructed from the condition of continuity of vertical velocity at $x = 0$ (equation 3.2.56b). In this case, we only need to be concerned with the vertical velocities in the interval between $-h$ and 0. From (3.2.53b) and (3.2.54d), the truncated series of the vertical velocities at $x = 0$ are given by:

$$\tilde{w}_1'(0, z) = \sum_{j=1}^{J}(A_j + B_j) Z_{j1}(z) + \sum_{n=1}^{N}(\hat{A}_n + \hat{B}_n)\hat{Z}_{n1}(z), \qquad (3.2.67a)$$

$$\tilde{w}_5'(0, z) = (E + F) Z(z) + \sum_{n=1}^{N} \hat{F}_n \hat{Z}_n(z). \qquad (3.2.67b)$$

This time $\tilde{w}_1'(0, z)$ is given the role of $f(z)$ to take advantage of the orthogonality relationships of the eigenfunctions for the homogeneous fluid. From (3.2.37) and (3.2.67), we obtain:

$$E + F = -\int_{-h}^{0} \tilde{w}_1'(0, z) Z(z) dz + \frac{g}{\sigma^2}\tilde{w}_1'(0, 0) Z(0), \qquad (3.2.68a)$$

$$\hat{F}_n = -\int_{-h}^{0} \tilde{w}_1'(0, z) \hat{Z}_n(z) dz + \frac{g}{\sigma^2}\tilde{w}_1'(0, 0) \hat{Z}_n(0).$$
$$(n = 1, 2, \ldots, N) \qquad (3.2.68b)$$

The integrals in (3.2.66) and (3.2.68) can be evaluated in terms of trigonometric functions and hyperbolic functions. The set of $(J+2N+1)$ simultaneous equations are solved numerically as a linear matrix equation. As in the two-layer problem, we have not proved that the series expansions in (3.2.53) and (3.2.54) are complete. In the numerical analysis, we have used $J = 2$ and $N = 3$. In our experiments, the thickness of the density transition region between the upper fluid and the lower fluid was small compared to the total depth of the fluid. Thus, the free surface mode and the primary internal mode dominate the wave motion in the trench region.

3.2.3.2 Analysis of Wave Amplitude

After the unknown coefficients of the series expansions are found, the horizontal velocity and the vertical velocity are determined for the entire fluid domain. For the problem of oscillation of internal waves in a trench, we are more interested in the amplitude of the internal wave relative to the amplitude of the surface wave. From linear theory, the vertical displacement η of a fluid element from its undisturbed position is obtained by integrating the vertical velocity with respect to t, that is:

$$\begin{aligned} \eta(x,z,t) &= \eta_0(z)e^{i(Kx-\sigma t)} \\ &= \int w\,dt = \frac{i}{\sigma}w'e^{-i\sigma t} \end{aligned} \tag{3.2.69}$$

in which we have applied (3.2.52*b*). In (3.2.69), η_0 is the amplitude of vertical displacement, and w' is given by (3.2.53) in the trench region and (3.2.54) in the constant-depth channel. The phase angle of wave motion is given by the argument of η. The amplification factor R is defined as the ratio of the internal wave amplitude at $x = 0$ to the surface wave amplitude at $x = \ell$, that is:

$$R(z) = \frac{|\eta(0,z,t)|}{|\eta(\ell,0,t)|}. \tag{3.2.70}$$

The phase shift θ between the internal motion and the surface motion at these

locations is given by:

$$\theta(z) = \arg\Big\{\eta(0,z,t)\Big\} - \arg\Big\{\eta(\ell,0,t)\Big\} \tag{3.2.71}$$

where "arg" is the argument of a complex number. Note that for a progressive wave propagating in the positive x direction, equations (3.2.11) and (3.2.69) yield:

$$\eta(x,z,t) = \frac{i}{\sigma} f(z) e^{i(Kx-\sigma t)}. \tag{3.2.72}$$

3.2.4 Wave Energies of Internal Waves and the Variational Principle

The analysis of wave damping for the three-layer fluid is presented in § 3.3.2 but it is convenient to present the kinetic and potential energies of wave motion here. For a continuously stratified fluid with the Boussinesq approximation, the average kinetic energy of a progressive wave per unit width, per unit length, over one wave period is:

$$\begin{aligned}\overline{KE} &= \frac{1}{\lambda T}\int_t^{t+T}\int_x^{x+\lambda}\int_{-(h_1+h_2+\delta)}^{0} \frac{1}{2}\rho_0(u^2+w^2)dzdxdt \\ &= \frac{1}{4}\int_{-(h_1+h_2+\delta)}^{0} \rho_0\left(|f|^2 + \frac{1}{K^2}\left|\frac{df}{dz}\right|^2\right)dz\end{aligned} \tag{3.2.73}$$

wherein λ is the wavelength. The last result in (3.2.73) is obtained by direct substitution of u and w from (3.2.11) and (3.2.20). The average potential energy per unit width, per unit length, over one wave period attributable to the progressive wave is given by:

$$\begin{aligned}\overline{PE} &= -\frac{1}{\lambda T}\int_t^{t+T}\int_x^{x+\lambda}\int_{-(h_1+h_2+\delta)}^{0} \frac{1}{2}\frac{d\overline{\rho}}{dz} g\eta^2 dzdxdt + \frac{1}{\lambda T}\int_t^{t+T}\int_x^{x+\lambda}\frac{1}{2}\rho_0 g\eta^2(0)dxdt \\ &= \frac{g}{4\sigma^2}\left(-\int_{-(h_1+h_2+\delta)}^{0}\frac{d\overline{\rho}}{dz}|f|^2dz + \rho_0|f(0)|^2\right)\end{aligned} \tag{3.2.74}$$

in which (3.2.72) has been used. Equations (3.2.73) and (3.2.74) also hold without the Boussinesq approximation but ρ_0 should be replaced by $\overline{\rho}(z)$. By inspection of

(3.2.38), it is seen that the total energy of wave motion is equally partitioned; one half in the form of kinetic energy, the other half in the form of potential energy.

The system of equations (3.2.25) also has a variational principle, which can be related to the kinetic and potential energies of wave motion. As in many conservative systems, it is expected that the stratified fluid will move so that the time average of the difference between the kinetic energy and the potential energy will be stationary. Thus we consider making the following functional stationary:

$$Q(f) = \int_{-(h_1+h_2+\delta)}^{0} \rho_0 \left[f^2 + \frac{1}{K^2}\left(\frac{df}{dz}\right)^2 \right] dz + \frac{g}{\sigma^2} \int_{-(h_1+h_2+\delta)}^{0} \frac{d\overline{\rho}}{dz} f^2 dz - \frac{\rho_0 g}{\sigma^2} f^2(0). \tag{3.2.75}$$

Let $\tilde{f}(z) = f(z) + \epsilon\zeta(z)$, where $\tilde{f}(z)$ is a perturbation of $f(z)$, ϵ is a perturbation parameter, and $\zeta(z)$ is an arbitrary function that satisfies the boundary conditions of $f(z)$. From (3.2.75), the perturbed functional $\tilde{Q}(\tilde{f})$ is:

$$\tilde{Q}(\tilde{f}) = \int_{-(h_1+h_2+\delta)}^{0} \rho_0 \left[\tilde{f}^2 + \frac{1}{K^2}\left(\frac{d\tilde{f}}{dz}\right)^2 \right] dz + \frac{g}{\sigma^2} \int_{-(h_1+h_2+\delta)}^{0} \frac{d\overline{\rho}}{dz} \tilde{f}^2 dz - \frac{\rho_0 g}{\sigma^2} \tilde{f}^2(0). \tag{3.2.76}$$

Differentiating $\tilde{Q}(\tilde{f})$ with respect to ϵ and setting the derivative to zero, we get:

$$\int_{-(h_1+h_2+\delta)}^{0} \rho_0 \left[f\zeta + \frac{1}{K^2}\frac{df}{dz}\frac{d\zeta}{dz} \right] dz + \frac{g}{\sigma^2} \int_{-(h_1+h_2+\delta)}^{0} \frac{d\overline{\rho}}{dz} f\zeta dz - \frac{\rho_0 g}{\sigma^2} f(0)\zeta(0) = 0. \tag{3.2.77}$$

Integration by parts yields:

$$\begin{aligned} &\int_{-(h_1+h_2+\delta)}^{0} \zeta \left[\frac{d^2 f}{dz^2} + K^2 \left(-\frac{g}{\sigma^2}\frac{1}{\rho_0}\frac{d\overline{\rho}}{dz} - 1 \right) f \right] dz \\ &-\zeta(0)\left[\frac{df}{dz} - \frac{gK^2}{\sigma^2} f \right]_{z=0} + \left[\zeta \frac{df}{dz} \right]_{z=-(h_1+h_2+\delta)} = 0. \end{aligned} \tag{3.2.78}$$

Because $\zeta(z)$ is arbitrary and $\zeta(z)$ satisfies the boundary conditions of $f(z)$, equation (3.2.78) implies that the $f(z)$ that makes $Q(f)$ stationary also satisfies the differential system given by (3.2.25).

An equivalent statement of the variational principle is to make the following functional stationary:

$$\Omega(\psi) = \int_{-(h_1+h_2+\delta)}^{0} \left(\frac{d\psi}{dz}\right)^2 dz \qquad (3.2.79a)$$

subject to the auxillary condition that:

$$\int_{-(h_1+h_2+\delta)}^{0} \left(-\frac{g}{\sigma^2}\frac{1}{\rho_0}\frac{d\overline{\rho}}{dz} - 1\right)\psi^2 dz + \frac{g}{\sigma^2}\psi^2(0) = \text{constant}. \qquad (3.2.79b)$$

Notice that (3.2.79b) defines the orthogonality condition of the eigenvalue problem (cf. equation 3.2.51). The function $\psi(z)$ is a trial function, which satisfies the boundary conditions of the differential system. If all the trial functions of $\psi(z)$ are normalized such that the left hand side of (3.2.79b) equals to unity, then the $\psi(z)$, which makes Ω stationary, is a normalized eigenfunction of (3.2.25), and the corresponding value of $\Omega(\psi)$ is the associated eigenvalue. The latter result is readily obtained from (3.2.79a) through integration by parts.

3.3 Wave Damping in Density-Stratified Fluid

In this section an analytical treatment of viscous effects on surface and internal waves is presented, based on linear wave theory. The energy dissipation in a stratified fluid is studied for the two-layer and the three-layer fluids discussed in § 3.1 and § 3.2. We assume that the free surface is uncontaminated and flow separation does not occur in the fluid; thus, energy dissipation is significant only in the boundary layers adjacent to the solid surfaces and at the density interface. It has been shown for homogeneous fluids of small viscosity that energy dissipation in the boundary layers adjacent to the solid surfaces, in the boundary layer at the free surface, and in the body of the fluid, are respectively proportional to $\nu^{1/2}$, $\nu^{3/2}$ and ν (see, for example, Mei, 1983), where ν is the kinematic viscosity. In § 3.1 we have seen that, for two inviscid fluids, the vertical velocities across the density interface are equal,

but the horizontal components of the velocity are discontinuous. In addition, the fluid motion has substantial tangential velocity at the solid boundaries. Of course, these results follow from the neglect of the effects of viscosity, which can be seen directly from the Navier-Stokes equations:

$$\rho\frac{D\mathbf{u}}{Dt} = -\nabla p - \rho g\nabla z + \mu\nabla^2\mathbf{u} \tag{3.3.1}$$

in which μ is the dynamic viscosity; the flow is assumed to be laminar. The last term in (3.3.1) is the result of molecular viscosity; its effect is to produce diffusion of momentum, with a diffusivity $\nu = \mu/\rho$. Hence, the discontinuity of the velocity profile at the interface is possible only in the absence of viscosity. Mathematically, equation (3.3.1) is changed from a second order partial differential equation into a first order equation (Euler equations) after neglecting the term involving viscosity. With the Euler equations, it is not possible to satisfy all the physical boundary conditions. Indeed, when the Euler equations are adopted we cannot impose the no-slip boundary condition at the solid surfaces, or at the interface between two immiscible fluids. Viscosity, however small, will instantaneously annul such a discontinuity by the diffusion of momentum. This is accomplished by the action of shear stresses in the fluid. By the definition of viscosity, a gradient of velocity generates a shear stress equal to the dynamic viscosity μ times the velocity gradient. This shear stress causes the retardation of fluid in the boundary layers adjacent to the solid surfaces and at the density interface. If the value of μ is very small, the boundary layers are very thin at these surfaces because the shear stress can be sufficient to generate the necessary retardation only if the velocity gradient is very large. Hence, the overall fluid motion outside the boundary layers can be predicted well by the Euler equations; only within the very thin boundary layers do we need to include the viscous term. This is particularly important because the complete Navier-Stokes equations are too difficult to analyze for arbitrary flows. Flow separation, if it exists, may alter the flow pattern significantly from that predicted by the Euler equations.

An estimate of the oscillatory boundary layer thickness near a smooth wall is given by the Stokes length:

$$\delta_w = \sqrt{\frac{2\nu}{\sigma}} \tag{3.3.2}$$

after G. G. Stokes (1851). Two typical laboratory conditions for experiments conducted in this investigation are: (i) $h_1 = 22.8\,\text{cm}$, $h_2 = 7.6\,\text{cm}$, $T = 8.0\,\text{sec}$; and (ii) $h_1 = 26.6\,\text{cm}$, $h_2 = 3.8\,\text{cm}$, $T = 11.0\,\text{sec}$, with $\nu = 0.01\,\text{cm}^2\text{sec}^{-1}$ and $\rho_2/\rho_1 = 1.05$. Let us define the relative boundary layer thickness as:

$$\frac{\delta_w}{h_0} = \frac{1}{h_0}\sqrt{\frac{2\nu}{\sigma}} \tag{3.3.3}$$

in which h_0 is a characteristic depth of the fluid. For the surface wave, h_0 should be taken as the total depth $(h_1 + h_2)$ because the overall fluid motion is very close to that of a homogeneous fluid of the same depth if the density variations are small. Then from (3.3.3) the relative boundary layer thicknesses in (i) and (ii) are respectively 0.0052 and 0.0062, which are very small. On the other hand, the interfacial wave motion is related to the density difference between the upper fluid and the lower fluid, and the depths h_1 and h_2. Therefore, a suitable h_0 for the internal wave should be the smaller depth h_2. Then the relative boundary layer thicknesses for the internal waves, corresponding to (i) and (ii) are about 0.02 and 0.05, respectively.

The boundary layer thickness at the density interface cannot be specified for our experiments that use a miscible fluid. We shall show experimentally in § 5.2.5 that a thin transition region of continuous density variation between the upper fluid and the lower fluid reduces the energy dissipation at the interface substantially. Nevertheless, the approximation inherent in the analysis of the two-layer problem requires that the interfacial wave amplitude be much smaller than the thicknesses of the boundary layers adjacent to the oscillating interface. This condition will be discussed more fully in § 3.3.1.

The laminar boundary layer may become turbulent at a sufficiently large value of the Reynolds number. A Reynolds number Re, based on the maximum fluid velocity immediately outside the boundary layer U, and the Stokes length δ_w, is written as $\mathrm{Re} = U\delta_w/\nu$. According to Jonnson (1978), the critical wave Reynolds number, $\mathrm{Re}_{\mathrm{crit}}$, for transition to turbulent boundary layer flow on a smooth bottom is:

$$\mathrm{Re}_{\mathrm{crit}} \approx 563. \tag{3.3.4}$$

Assuming a two-layer fluid and small density difference, an estimate for U is given by the linear nondispersive theory as follows:

$$U \approx \frac{H_S}{h_1 + h_2}\sqrt{g(h_1 + h_2)} \qquad \text{(surface mode)}, \tag{3.3.5a}$$

$$U \approx \frac{H_I}{h_2}\sqrt{g'\frac{h_1 h_2}{h_1 + h_2}} \qquad \text{(internal mode)} \tag{3.3.5b}$$

where $g' = g(\rho_2 - \rho_1)/\rho_2$, and H_S, H_I are the surface wave height and the interfacial wave height, respectively. Notice that the internal wave has much smaller particle velocity than the surface wave because the phase speed of the internal wave is only a fraction of that of the surface wave. From (3.3.4) and (3.3.5), the conditions for the boundary layer to remain laminar are:

$$\frac{H_S}{(h_1 + h_2)} < \frac{563\nu}{\delta_w}\frac{1}{\sqrt{g(h_1 + h_2)}} \qquad \text{(surface mode)}, \tag{3.3.6a}$$

$$\frac{H_I}{h_2} < \frac{563\nu}{\delta_w}\sqrt{\frac{h_1 + h_2}{g' h_1 h_2}} \qquad \text{(internal mode)}. \tag{3.3.6b}$$

Using (3.3.6) and the laboratory conditions stated previously, the relative wave height for the surface wave $H_S/(h_1 + h_2)$ must be less than 0.21 and 0.17 in (i) and (ii), respectively, for the boundary layer to remain laminar. These values of the relative wave height are much larger than the limits for small amplitude waves. The corresponding limits of the relative wave height for the internal wave H_I/h_2 are respectively 2.27 and 2.38, which are extremely large values of the wave height

parameter. Therefore, the boundary layer is expected to remain laminar whenever the conditions for small amplitude waves are fulfilled. These limiting conditions emphasize the differences in the effects of viscosity on the surface wave and the internal wave.

3.3.1 Wave Damping in a Two-Layer Fluid

To obtain a viscous correction to the two-layer inviscid model presented in § 3.1, we follow a perturbation analysis similar to that used by Mei and Liu (1973) for a homogeneous fluid. Let (x, y, z) be a Cartesian coordinate system with z extending positive upwards from the undisturbed free surface. The bottom corresponds to $z = -(h' + h)$ and the density interface is at $z = -h'$. Assuming small amplitude motion and laminar flow, the linearized momentum equations for the upper layer can be written as:

$$\frac{\partial \mathbf{u}'}{\partial t} = -\frac{1}{\rho'}\nabla P' + \frac{\mu'}{\rho'}\nabla^2 \mathbf{u}' - g\nabla z \tag{3.3.7}$$

in which $\mathbf{u}'$ is the velocity vector (u, v, w), P' is the total pressure, ρ' is the density of the upper fluid, μ' is the dynamic viscosity of the upper fluid, and g is the acceleration of gravity. In this analysis we distinguish the physical variables in the upper layer by prime; the subscripts (1 and 2) are reserved for use in the perturbation analysis. The velocity $\mathbf{u}'$ can be split into a potential part $\nabla\Phi'$ and a rotational part $\mathbf{U}'$, that is:

$$\mathbf{u}' = \nabla\Phi' + \mathbf{U}' \tag{3.3.8}$$

where

$$\nabla^2\Phi' = 0 \tag{3.3.9}$$

and

$$\nabla \cdot \mathbf{U}' = 0, \qquad \mathbf{U}' = (U', V', W'). \tag{3.3.10}$$

The total pressure is written as:

$$P' = -\rho' g z + p' = -\rho' g z - \rho' \frac{\partial \Phi'}{\partial t} \tag{3.3.11}$$

where p' is the dynamic pressure in the upper layer. Substitution of (3.3.8) and (3.3.11) into (3.3.7), and after using (3.3.9) and (3.3.10), we get:

$$\frac{\partial \mathbf{U}'}{\partial t} = \nu' \nabla^2 \mathbf{U}' \tag{3.3.12}$$

in which $\nu' = \mu'/\rho'$ is the kinematic viscosity. On the free surface, the linearized kinematic boundary condition is given by:

$$\frac{\partial \eta'}{\partial t} = \frac{\partial \Phi'}{\partial z} + W' \qquad \text{on} \qquad z = 0. \tag{3.3.13}$$

Assuming that the free surface is uncontaminated, the normal stress must vanish there, that is:

$$\frac{\partial \Phi'}{\partial t} + g\eta' + \frac{2\mu'}{\rho'} \frac{\partial w'}{\partial z} = 0 \qquad \text{on} \qquad z = 0 \tag{3.3.14}$$

as well as the tangential stresses:

$$\mu' \left(\frac{\partial u'}{\partial z} + \frac{\partial w'}{\partial x} \right) = \mu' \left(\frac{\partial v'}{\partial z} + \frac{\partial w'}{\partial y} \right) = 0 \qquad \text{on} \qquad z = 0. \tag{3.3.15}$$

On the solid surfaces S', the fluid velocities must satisfy the no-slip boundary condition:

$$\nabla \Phi' + \mathbf{U}' = 0 \qquad \text{on} \qquad S'. \tag{3.3.16}$$

Equations (3.3.7)–(3.3.10), (3.3.12), and (3.3.16) are the same for the lower layer. The total pressure in the lower layer is written as:

$$P = \rho' g h' - \rho g (z + h') + p = \rho' g h' - \rho g (z + h') - \rho \frac{\partial \Phi}{\partial t} \tag{3.3.17}$$

where p is the dynamic pressure in the lower layer. The linearized kinematic boundary conditions on the density interface are:

$$\frac{\partial \eta}{\partial t} = \frac{\partial \Phi}{\partial z} + W \qquad \text{on} \qquad z = -h', \tag{3.3.18a}$$

$$\frac{\partial \eta}{\partial t} = \frac{\partial \Phi'}{\partial z} + W' \qquad \text{on} \qquad z = -h', \tag{3.3.18b}$$

$$\nabla \Phi + \mathbf{U} = \nabla \Phi' + \mathbf{U}' \qquad \text{on} \qquad z = -h'. \tag{3.3.18c}$$

The normal stress must be continuous at the density interface, that is:

$$\rho\left(\frac{\partial\Phi}{\partial t}+g\eta\right)+2\mu\frac{\partial w}{\partial z}=\rho'\left(\frac{\partial\Phi'}{\partial t}+g\eta\right)+2\mu'\frac{\partial w'}{\partial z}\qquad\text{on}\qquad z=-h' \tag{3.3.19}$$

and so are the tangential stresses:

$$\mu\left(\frac{\partial u}{\partial z}+\frac{\partial w}{\partial x}\right)=\mu'\left(\frac{\partial u'}{\partial z}+\frac{\partial w'}{\partial x}\right)\qquad\text{on}\qquad z=-h', \tag{3.3.20a}$$

$$\mu\left(\frac{\partial v}{\partial z}+\frac{\partial w}{\partial y}\right)=\mu'\left(\frac{\partial v'}{\partial z}+\frac{\partial w'}{\partial y}\right)\qquad\text{on}\qquad z=-h'. \tag{3.3.20b}$$

In the perturbation analysis that follows, it is crucial to nondimensionalize each variable by a characteristic quantity. In studying the time-periodic progressive waves in a long channel, one usually defines the circular frequency σ as given and real. Dimensionless variables may be defined as:

$$\begin{aligned}(x^*,y^*,z^*)&=\frac{g}{\sigma^2}(x,y,z),\\(u^*,v^*,w^*)&=a_0\sigma(u,v,w),\\t^*&=\frac{t}{\sigma},\\p^*&=\rho g a_0 p,\\\Phi^*&=\frac{a_0 g}{\sigma}\Phi,\\\eta^*&=a_0\eta\end{aligned}$$

where the starred symbols represent the original dimensional variables and a_0 is a typical wave amplitude. Henceforth all the equations are dimensionless unless specifically stated otherwise. The scaling is such that all the previously defined dimensionless variables are of order unity. The dimensionless equations are:

$$\mathbf{u}'=\nabla\Phi'+\mathbf{U}',\qquad \mathbf{u}=\nabla\Phi+\mathbf{U}, \tag{3.3.21}$$

$$\nabla^2\Phi'=0,\qquad \nabla^2\Phi=0, \tag{3.3.22}$$

$$\nabla\cdot\mathbf{U}'=0,\qquad \nabla\cdot\mathbf{U}=0, \tag{3.3.23}$$

$$p' = -\frac{\partial \Phi'}{\partial t}, \qquad p = -\frac{\partial \Phi}{\partial t}, \tag{3.3.24}$$

$$\frac{\partial \mathbf{U}'}{\partial t} = \varepsilon'^2 \nabla^2 \mathbf{U}', \qquad \frac{\partial \mathbf{U}}{\partial t} = \varepsilon^2 \nabla^2 \mathbf{U} \tag{3.3.25}$$

where

$$\varepsilon' = \frac{\sigma^2}{g}\left(\frac{\nu'}{\sigma}\right)^{1/2}, \tag{3.3.26a}$$

$$\varepsilon = \frac{\sigma^2}{g}\left(\frac{\nu}{\sigma}\right)^{1/2}. \tag{3.3.26b}$$

The kinematic boundary condition on the free surface is:

$$\frac{\partial \eta'}{\partial t} = \frac{\partial \Phi'}{\partial z} + W' \qquad \text{on} \qquad z = 0. \tag{3.3.27}$$

The dynamic stress conditions on the free surface are given as follows:

normal:

$$\frac{\partial \Phi'}{\partial t} + \eta' + 2\varepsilon'^2 \frac{\partial w'}{\partial z} = 0 \qquad \text{on} \qquad z = 0, \tag{3.3.28}$$

tangential:

$$\varepsilon'^2 \left(\frac{\partial u'}{\partial z} + \frac{\partial w'}{\partial x}\right) = \varepsilon'^2 \left(\frac{\partial v'}{\partial z} + \frac{\partial w'}{\partial y}\right) = 0 \qquad \text{on} \qquad z = 0. \tag{3.3.29}$$

The no-slip boundary condition in the upper layer is:

$$\nabla \Phi' + \mathbf{U}' = 0 \qquad \text{on} \qquad S' = S'_W, \tag{3.3.30}$$

in which S'_W is the side wall. The linearized kinematic boundary conditions on the density interface are:

$$\frac{\partial \eta}{\partial t} = \frac{\partial \Phi}{\partial z} + W \qquad \text{on} \qquad z = -h', \tag{3.3.31a}$$

$$\frac{\partial \eta}{\partial t} = \frac{\partial \Phi'}{\partial z} + W' \qquad \text{on} \qquad z = -h' \tag{3.3.31b}$$

and

$$\nabla \Phi + \mathbf{U} = \nabla \Phi' + \mathbf{U}' \qquad \text{on} \qquad z = -h'. \tag{3.3.32}$$

The equation for the continuity of normal stress at the interface is:

$$\frac{\partial \Phi}{\partial t} + \eta + 2\varepsilon^2 \frac{\partial w}{\partial z} = \beta \left(\frac{\partial \Phi'}{\partial t} + \eta + 2\varepsilon'^2 \frac{\partial w}{\partial z} \right) \qquad \text{on} \qquad z = -h' \tag{3.3.33}$$

in which $\beta = \rho'/\rho$. The tangential stresses are continuous at the interface, hence, we have:

$$\frac{\partial u}{\partial z} + \frac{\partial w}{\partial x} = \alpha \left(\frac{\partial u'}{\partial z} + \frac{\partial w'}{\partial x} \right) \qquad \text{on} \qquad z = -h', \tag{3.3.34a}$$

$$\frac{\partial v}{\partial z} + \frac{\partial w}{\partial y} = \alpha \left(\frac{\partial v'}{\partial z} + \frac{\partial w'}{\partial y} \right) \qquad \text{on} \qquad z = -h' \tag{3.3.34b}$$

in which $\alpha = \mu'/\mu$. The no-slip boundary condition in the lower layer is given by:

$$\nabla \Phi + \mathbf{U} = 0 \qquad \text{on} \qquad S = S_W + S_B \tag{3.3.35}$$

where S_W is the side wall, and S_B is the bottom.

Combining (3.3.27) and (3.3.28), we have:

$$\frac{\partial^2 \Phi'}{\partial t^2} + \frac{\partial \Phi'}{\partial z} + W' + 2\varepsilon'^2 \frac{\partial^2 w'}{\partial t \partial z} = 0 \qquad \text{on} \qquad z = 0. \tag{3.3.36}$$

Substitution of (3.3.21) into (3.3.29) yields:

$$\varepsilon'^2 \left(2\frac{\partial^2 \Phi'}{\partial x \partial z} + \frac{\partial W'}{\partial x} \right) + \varepsilon'^2 \frac{\partial U'}{\partial z} = 0, \tag{3.3.37a}$$

$$\varepsilon'^2 \left(2\frac{\partial^2 \Phi'}{\partial y \partial z} + \frac{\partial W'}{\partial y} \right) + \varepsilon'^2 \frac{\partial V'}{\partial z} = 0. \tag{3.3.37b}$$

Equation (3.3.37) indicates that $\partial U'/\partial z$ and $\partial V'/\partial z$ can be of $O(1)$. Because $z = O(\varepsilon')$ in the free surface boundary layer, U' and V' are of $O(\varepsilon')$. Then $\partial W'/\partial z = O(\varepsilon')$ from the continuity equation (equation 3.3.23), and this implies that $W' = O(\varepsilon'^2)$. Equation (3.3.36) can be approximated by:

$$\frac{\partial^2 \Phi'}{\partial t^2} + \frac{\partial \Phi'}{\partial z} + W' = O(\varepsilon'^2) \qquad \text{on} \qquad z = 0. \tag{3.3.38}$$

Mei and Liu (1973) pointed out that W' is of the same order as the other terms in (3.3.38) only in a thin strip of the meniscus boundary layer along the intersection

between the free surface and the side wall. Because the rotational part of the velocity varies quickly from $[-\partial\Phi'/\partial z]_{z=0}$ at the wall (assumed vertical) to zero within a horizontal distance of $O(\varepsilon')$ away from the wall, its global effect can only be felt at $O(\varepsilon')$. This point will be discussed more fully during the perturbation analysis.

Inside the interfacial boundary layers, U, U', V, $V' = O(1)$. By continuity, W and W' are respectively of $O(\varepsilon)$ and $O(\varepsilon')$. Hence (3.3.33) can be approximated by:

$$\frac{\partial^2\Phi}{\partial t^2} + \frac{\partial\Phi}{\partial z} + W = \beta\left(\frac{\partial^2\Phi'}{\partial t^2} + \frac{\partial\Phi'}{\partial z} + W'\right) \qquad \text{on} \qquad z = -h' \qquad (3.3.39)$$

in which (3.3.31a) and (3.3.31b) have been used. Again, W and W' are of the same order as the other terms only within the interfacial meniscus boundary layers. Substituting (3.3.21) into (3.3.34a) and (3.3.34b), we get:

$$2\frac{\partial^2\Phi}{\partial x\partial z} + \frac{\partial U}{\partial z} + \frac{\partial W}{\partial x} = \alpha\left(2\frac{\partial^2\Phi'}{\partial x\partial z} + \frac{\partial U'}{\partial z} + \frac{\partial W'}{\partial x}\right) \quad \text{on} \quad z = -h', \ (3.3.40a)$$

$$2\frac{\partial^2\Phi}{\partial y\partial z} + \frac{\partial V}{\partial z} + \frac{\partial W}{\partial y} = \alpha\left(2\frac{\partial^2\Phi'}{\partial y\partial z} + \frac{\partial V'}{\partial z} + \frac{\partial W'}{\partial y}\right) \quad \text{on} \quad z = -h'. \ (3.3.40b)$$

Notice that in (3.3.40a), $\partial^2\Phi/\partial x\partial z = O(1)$, $\partial U/\partial z = O(1/\varepsilon)$, and $\partial W/\partial x = O(\varepsilon)$. We recall that in obtaining the dimensionless equations, each physical variable was scaled by a characteristic quantity, so that all the previously defined dimensionless variables are of the order unity. However, this scaling was based on the inviscid wave theory because the irrotational component of the fluid velocity dominates the flow outside the boundary layer. Inside a boundary layer, the tangential components of $\mathbf{U}$ and $\nabla\Phi$ are comparable. The rotational part introduces a much smaller boundary layer length scale into the problem. In particular, the tangential component of $\mathbf{U}$ varies rapidly within the dimensionless distance $O(\varepsilon)$. As we shall see later in the perturbation analysis, the solutions are developed systematically in powers of a boundary layer parameter, where the terms of different orders are separated. It is convenient to use local coordinates when working with the boundary layer equations.

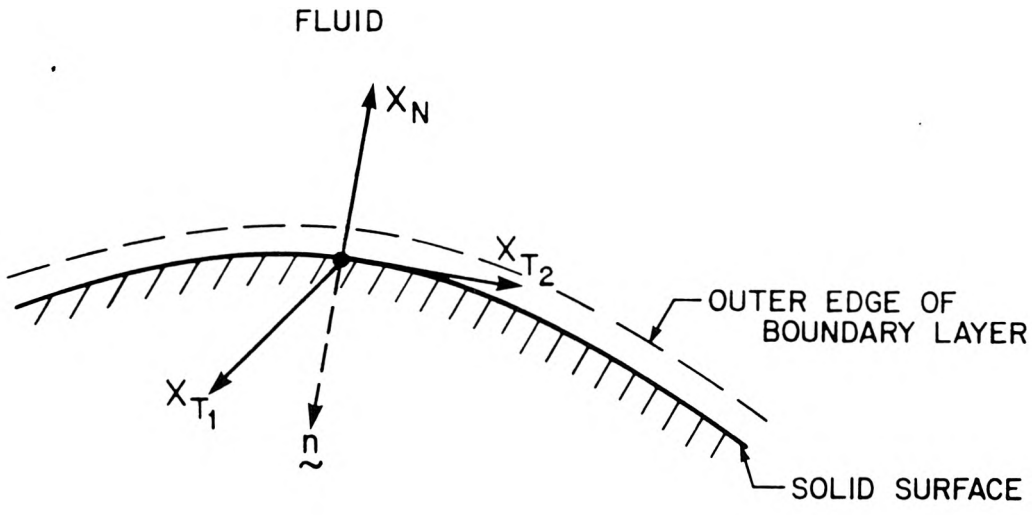

Figure 3.3.1. Boundary layer coordinate system.

This is shown in figure 3.3.1; the unit directional vectors $\mathbf{x_N}$, $\mathbf{x_{T_1}}$, and $\mathbf{x_{T_2}}$ form a local Cartesian coordinate system, with $\mathbf{x_N}$ being in the normal direction pointing into the fluid. The normal coordinate x_N is scaled as follows:

$$\xi' = \frac{x_N}{\varepsilon'} \qquad \text{so that} \qquad \mathbf{U}' = \mathbf{U}'(\mathbf{x_T}, \xi', t) \tag{3.3.41a}$$

and

$$\xi = \frac{x_N}{\varepsilon} \qquad \text{so that} \qquad \mathbf{U} = \mathbf{U}(\mathbf{x_T}, \xi, t). \tag{3.3.41b}$$

In terms of the local coordinate system the continuity equation becomes:

$$-\frac{\partial}{\partial \xi'}(\mathbf{n}\cdot\mathbf{U}') + \varepsilon'\left(\frac{\partial U'_{T_1}}{\partial x_{T_1}} + \frac{\partial U'_{T_2}}{\partial x_{T_2}}\right) = 0, \tag{3.3.42a}$$

$$-\frac{\partial}{\partial \xi}(\mathbf{n}\cdot\mathbf{U}) + \varepsilon\left(\frac{\partial U_{T_1}}{\partial x_{T_1}} + \frac{\partial U_{T_2}}{\partial x_{T_2}}\right) = 0. \tag{3.3.42b}$$

In studying standing waves in a bounded region the wave number k is usually given and is real, then the appropriate dimensionless variables are given by:

$$
\begin{aligned}
(u^*, v^*, w^*) &= a_0(gk)^{1/2}(u, v, w), \\
(x^*, y^*, z^*) &= \frac{1}{k}(x, y, z), \\
t^* &= \frac{1}{(gk)^{1/2}}t, \\
p^* &= \rho g a_0 p, \\
\Phi^* &= \frac{a_0(gk)^{1/2}}{k}\Phi, \\
\eta^* &= a_0\eta.
\end{aligned}
$$

Besides (3.3.26a) and (3.3.26b), all the dimensionless equations previously stated remain unchanged. With this scaling, the new boundary layer parameters are given by:

$$\varepsilon' = \frac{k\nu'^{1/2}}{(gk)^{1/4}}, \tag{3.3.43a}$$

$$\varepsilon = \frac{k\nu^{1/2}}{(gk)^{1/4}}. \tag{3.3.43b}$$

It is appropriate here to examine the validity of the present analysis. The inherent assumption of the linear wave theory requires that the wave amplitude is small compared to a characteristic depth of the fluid, so that the boundary conditions can be linearized. In formulating this problem, we have in addition replaced the viscous layers adjacent to the oscillating free surface and the density interface by boundary layers adjacent to $z = 0$ and $z = -h'$. This approximation is legitimate provided that the wave amplitudes are so small that the oscillating surfaces do not pass out of the viscous regions. Hence, it is necessary that:

$$H_S \ll \delta_S, \tag{3.3.44a}$$

$$H_I \ll \delta_I \tag{3.3.44b}$$

where H_S, H_I are the surface wave height and the interfacial wave height, respectively, and δ_S, δ_I are the respective thicknesses of the boundary layers. Thus, it appears at first sight that (3.3.44a) and (3.3.44b) would impose a severe restriction on the usefulness of the theory. However, the boundary layer method requires that the thickness of the boundary layer be very thin compared to a characteristic depth of the fluid (see equation 3.3.3), otherwise the overall motion of the fluid cannot be described by the inviscid theory alone, and viscosity becomes important in the body of the fluid. Therefore, the basic assumptions inherent in the present analysis already imply that the wave amplitude and the thickness of the boundary layer are both small compared to a characteristic fluid depth. It follows that (3.3.44a) and (3.3.44b) may not be unduly restrictive. A similar argument has been put forward by Johns (1968).

3.3.1.1 Plane Progressive Waves in a Uniform Rectangular Channel

A two-layer fluid of total depth $(h' + h)$ is contained in a long rectangular channel of width $2b$. The upper fluid is of depth h' and of density ρ'. The lower fluid is of depth h and of density ρ. Let (x, y, z) be a Cartesian coordinate system with the x axis on the undisturbed free surface coinciding with the channel axis and z measured positive upwards (figure 3.3.2). The side walls of the rectangular channel are located at $y = b$ and $y = -b$. The wave motion is assumed to be two-dimensional. We introduce the following perturbation expansions:

$$\Phi = [\phi_0(y,z) + \overline{\varepsilon}\phi_1(y,z) + O(\overline{\varepsilon}^2)]e^{i(kx-t)}, \tag{3.3.45a}$$

$$\mathbf{U} = [\mathbf{q_0}(x_T,\xi) + \overline{\varepsilon}\mathbf{q_1}(x_T,\xi) + O(\overline{\varepsilon}^2)]e^{i(kx-t)}, \tag{3.3.45b}$$

$$k = k_0 + \overline{\varepsilon}k_1 + O(\overline{\varepsilon}^2) \tag{3.3.45c}$$

wherein $\overline{\varepsilon}$ is a boundary layer parameter, and the subscripts $(0, 1, 2, \ldots)$ denote the

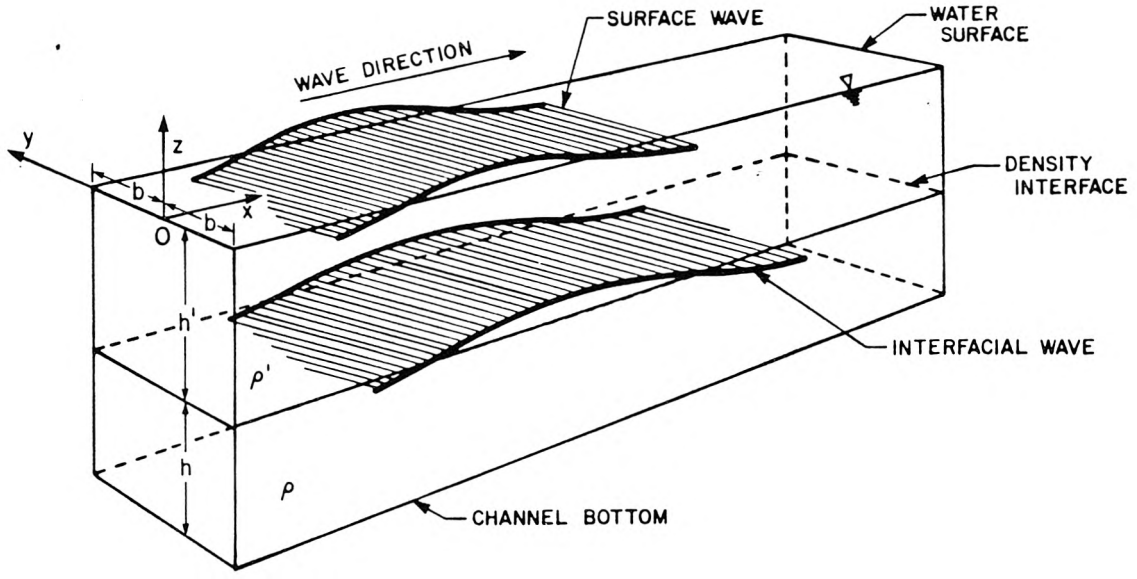

Figure 3.3.2. Schematic drawing of surface and interfacial waves advancing down a uniform rectangular channel that is partially filled with a two-layer fluid.

order of approximation. From (3.3.26a) and (3.3.26b), we have:

$$\frac{\varepsilon'}{\varepsilon} = \left(\frac{\nu'}{\nu}\right)^{1/2} = \left(\frac{\mu'\rho}{\mu\rho'}\right)^{1/2} = O(1).$$

Hence, we may assume that:

$$O(\varepsilon') = O(\varepsilon) = O(\bar{\varepsilon}). \tag{3.3.46}$$

Let us examine (3.3.45) for a moment, it is seen that the wave number k in the exponent of the velocity potential Φ and the rotational part of the fluid velocity U is expanded in terms of the boundary layer parameter $\bar{\varepsilon}$ as shown in (3.3.45c). In the following analysis, we determine k to $O(\bar{\varepsilon})$ and show that k_0 represents the determined wave number based on the inviscid theory and is real, and the first order term $\bar{\varepsilon}k_1$ is complex; the damping rate is given by $\bar{\varepsilon}k_1$. It is seen in (3.3.45a) and

(3.3.45b) that the real part of the damping rate contributes a viscous correction of $O(\bar{\varepsilon})$ to the inviscid wave number k_0, whereas the imaginary part of the damping rate gives the rate of amplitude attenuation. When (3.3.45a)–(4.3.45c) are substituted into the dimensionless equations and the terms of different orders are separated, we obtain the following problems:

(1) Inviscid solution of $O(\bar{\varepsilon}^0)$:

$$\frac{d^2\phi_0'}{dz^2} = k_0^2\phi_0', \qquad -h' < z < 0, \tag{3.3.47a}$$

$$\frac{d^2\phi_0}{dz^2} = k_0^2\phi_0, \qquad -(h'+h) < z < -h', \tag{3.3.47b}$$

$$\frac{d\phi_0'}{dz} - \phi_0' = 0 \qquad \text{on} \qquad z = 0, \tag{3.3.47c}$$

$$\frac{d\phi_0}{dz} - \phi_0 = \beta\left(\frac{d\phi_0'}{dz} - \phi_0'\right) \qquad \text{on} \qquad z = -h', \tag{3.3.47d}$$

$$\frac{d\phi_0}{dz} = \frac{d\phi_0'}{dz} \qquad \text{on} \qquad z = -h', \tag{3.3.47e}$$

$$\frac{d\phi_0}{dz} = 0, \qquad \text{on} \qquad z = -(h'+h). \tag{3.3.47f}$$

The inviscid problem has been treated in § 3.1. The solutions, in dimensionless form, are given by:

$$\phi_0'(z) = C'(k_0 \cosh k_0 z + \sinh k_0 z), \tag{3.3.48a}$$

$$\phi_0(z) = C'\frac{(\cosh k_0 h' - k_0 \sinh k_0 h')}{\sinh k_0 h} \cosh k_0(z + h' + h) \tag{3.3.48b}$$

in which C' is an arbitrary constant. The wave number k_0 is given by the dispersion relation:

$$(\coth k_0 h \coth k_0 h' + \beta) - k_0(\coth k_0 h + \coth k_0 h') + k_0^2(1-\beta) = 0. \tag{3.3.49}$$

(2) Interfacial boundary layer correction of $O(\bar{\varepsilon}^0)$:

$$\frac{d^2U_0'}{d\xi'^2} = -iU_0', \qquad \xi' = \frac{z+h'}{\varepsilon'}, \tag{3.3.50a}$$

$$\frac{d^2U_0}{d\xi^2} = -iU_0, \qquad \xi = -\frac{z+h'}{\varepsilon}, \tag{3.3.50b}$$

$$U_0' \to 0, \qquad \xi' \to \infty, \tag{3.3.50c}$$

$$U_0 \to 0, \qquad \xi \to \infty, \tag{3.3.50d}$$

$$ik_0\phi_0 + U_0 = ik_0\phi_0' + U_0' \qquad \text{on} \qquad z = -h', \tag{3.3.50e}$$

$$\frac{dU_0}{dz} = \alpha\frac{dU_0'}{dz} \qquad \text{on} \qquad z = -h'. \tag{3.3.50f}$$

Equations (3.3.50a)–(3.3.50d) imply:

$$U_{0I}'(\xi') = D'e^{-\frac{1}{\sqrt{2}}(1-i)\xi'}, \tag{3.3.51a}$$

$$U_{0I}(\xi) = De^{-\frac{1}{\sqrt{2}}(1-i)\xi} \tag{3.3.51b}$$

in which D' and D are unknown constants, and the subscript I denotes the density interface. Substitution of (3.3.51a) and (3.3.51b) into (3.3.50e) and (3.3.50f) yields:

$$D' = ik_0[\phi_0(-h') - \phi_0'(-h')] + D, \tag{3.3.52a}$$

$$\frac{D}{\varepsilon} = -\alpha\frac{D'}{\varepsilon'}. \tag{3.3.52b}$$

Upon using (3.3.47d) and (3.3.47e), we obtain:

$$D' = \frac{ik_0}{\beta}(\beta - 1)\left[\phi_0 - \frac{d\phi_0}{dz}\right]_{z=-h'} + D, \tag{3.3.53a}$$

$$D = -\frac{ik_0}{1+(\alpha\beta)^{1/2}}(\beta - 1)\left(\frac{\alpha}{\beta}\right)^{1/2}\left[\phi_0 - \frac{d\phi_0}{dz}\right]_{z=-h'}. \tag{3.3.53b}$$

It is noted that the velocity components U, V, and W were originally used to denote the rotational part of the fluid velocity $\mathbf{U}$. For simplicity, in (3.3.50) and (3.3.51) we have omitted the exponential term $e^{i(kx-t)}$ and used the same symbols to denote the velocity components of $\mathbf{q}$ that are independent of x and t; this is implied in the following analysis unless specifically stated otherwise.

(3) Bottom and side-wall boundary layer correction of order $O(\overline{\varepsilon}^0)$:

$$\frac{\partial^2 U_0}{\partial \xi^2} = -iU_0, \qquad \xi = \frac{z+(h'+h)}{\varepsilon} \quad \text{and} \quad \xi = \frac{b \mp y}{\varepsilon}, \tag{3.3.54a}$$

$$\frac{\partial^2 W_0}{\partial \xi^2} = -iW_0, \qquad \xi = \frac{b \mp y}{\varepsilon}, \tag{3.3.54b}$$

$$U_0 = -ik_0\phi_0 \qquad \text{on} \qquad \xi = 0, \tag{3.3.54c}$$

$$W_0 = -\frac{d\phi_0}{dz} \qquad \text{on} \qquad \xi = 0, \tag{3.3.54d}$$

$$U_0, W_0 \to 0, \qquad \xi \to \infty. \tag{3.3.54e}$$

This is the classical Stokes' problem for unsteady flow of a semi-infinite fluid caused by a plate oscillating in its own plane (see, for example, Yih, 1977). The solutions are given by:

$$U_{0B}(\xi) = -ik_0\phi_0(-(h'+h))e^{-\frac{1}{\sqrt{2}}(1-i)\xi}, \qquad \xi = \frac{z+(h'+h)}{\varepsilon}, \tag{3.3.55a}$$

$$U_{0W}(z,\xi) = -ik_0\phi_0(z)e^{-\frac{1}{\sqrt{2}}(1-i)\xi}, \qquad \xi = \frac{b \mp y}{\varepsilon}, \tag{3.3.55b}$$

$$W_{0W}(z,\xi) = -\frac{d\phi_0}{dz}(z)e^{-\frac{1}{\sqrt{2}}(1-i)\xi}, \qquad \xi = \frac{b \mp y}{\varepsilon} \tag{3.3.55c}$$

in which the subscripts B and W denote the bottom and the side wall, respectively. Equations (3.3.55b) and (3.3.55c) are the same in the upper layer.

(4) Inviscid correction of order $O(\overline{\varepsilon}^1)$:

$$\frac{\partial^2 \phi_1'}{\partial y^2} + \frac{\partial^2 \phi_1'}{\partial z^2} = k_0^2\phi_1' + 2k_0k_1\phi_0' \qquad \text{in} \qquad \mathcal{V}', \tag{3.3.56a}$$

$$\frac{\partial^2 \phi_1}{\partial y^2} + \frac{\partial^2 \phi_1}{\partial z^2} = k_0^2\phi_1 + 2k_0k_1\phi_0 \qquad \text{in} \qquad \mathcal{V}, \tag{3.3.56b}$$

$$\frac{\partial \phi_1'}{\partial z} - \phi_1' = -\frac{W_0'}{\overline{\varepsilon}} \qquad \text{on} \qquad S'_{F_{MW}}, \tag{3.3.56c}$$

$$\frac{\partial \phi_1}{\partial z} - \phi_1 + W_1 = \beta\left(\frac{\partial \phi_1'}{\partial z} - \phi_1' + W_1'\right) \qquad \text{on} \qquad S_I, \tag{3.3.56d}$$

$$\frac{\partial \phi_1}{\partial z} - \phi_1 + \frac{W_0}{\overline{\varepsilon}} = \beta\left(\frac{\partial \phi_1'}{\partial z} - \phi_1' + \frac{W_0'}{\overline{\varepsilon}}\right) \qquad \text{on} \qquad S_{I_{MW}}, \tag{3.3.56e}$$

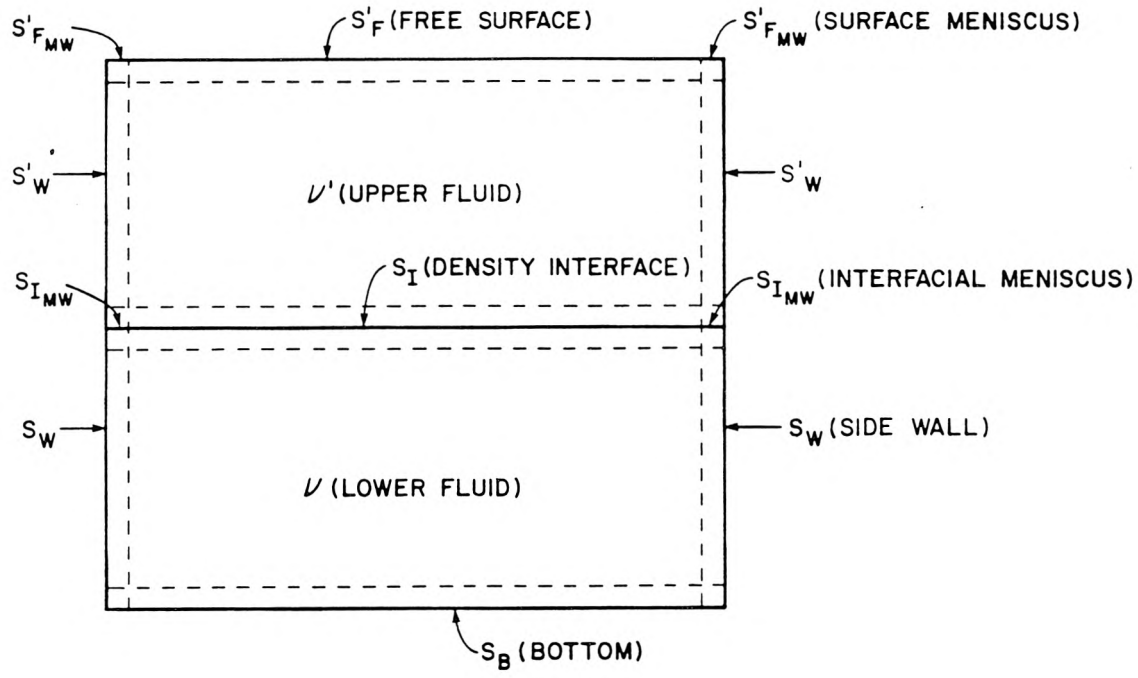

Figure 3.3.3. Division of a two-layer viscous fluid into regions of the boundary layers and the inviscid cores. The dash lines denote the interface between the boundary layers and the inviscid cores.

$$\frac{\partial \phi_1}{\partial z} + W_1 = \frac{\partial \phi_1'}{\partial z} + W_1' \qquad \text{on} \qquad S_I, \tag{3.3.56f}$$

$$\frac{\partial \phi_1}{\partial z} + \frac{W_0}{\overline{\varepsilon}} = \frac{\partial \phi_1'}{\partial z} + \frac{W_0'}{\overline{\varepsilon}} \qquad \text{on} \qquad S_{I_{MW}}, \tag{3.3.56g}$$

$$\mathbf{n} \cdot \nabla \phi_1' = -\mathbf{n} \cdot \mathbf{q}_1' \qquad \text{on} \qquad S_W', \tag{3.3.56h}$$

$$\mathbf{n} \cdot \nabla \phi_1 = -\mathbf{n} \cdot \mathbf{q}_1 \qquad \text{on} \qquad S_W + S_B \tag{3.3.56i}$$

wherein $\mathcal{V}'$ is the body of the upper fluid, $\mathcal{V}$ is the body of the lower fluid, S_I is the density interface, S_W' is the side wall of the upper layer, S_W is the side wall of the lower layer, S_B is the bottom, and $S_{F_{MW}}'$, $S_{I_{MW}}$ represent an area of $O(\overline{\varepsilon})$ of the free surface meniscus boundary layer and of the interfacial meniscus boundary layer, respectively. A schematic drawing of a cross section of the rectangular channel with the various regions of interest is shown in figure 3.3.3.

Let us examine (3.3.56d) and (3.3.56e) for a moment. These two equations apply in the region of the density interface. Inside the interfacial boundary layers, the tangential components of $\mathbf{U}$ and $\nabla\Phi$ are comparable, and are both of the order unity. From continuity consideration, the normal component $W = O(\overline{\varepsilon})$, and this is effective over the entire density interface S_I. When the terms of $O(\overline{\varepsilon})$ are collected from (3.3.39) after substitution of (3.3.45), equation (3.3.56d) is obtained. In the neighborhood along the intersection between the interface and the side wall, W is of the order unity, but it acts only over a narrow strip of width $O(\overline{\varepsilon})$, so that its integrated effect is of significance only at $O(\overline{\varepsilon})$. Mathematically, inside the meniscus boundary layer, W is treated as a singular concentrated forcing function. That is, by expanding:

$$W = \overline{\varepsilon}\left[\frac{W_0}{\overline{\varepsilon}} + O(\overline{\varepsilon}^0)\right] \tag{3.3.57}$$

over a strip of width $O(\overline{\varepsilon})$. When (3.3.57) is substituted into (3.3.39) and the terms of $O(\overline{\varepsilon})$ are collected, equation (3.3.56e) is obtained. Equations (3.3.56c) and (3.3.56g) are obtained in the same manner.

Now let us find the unknown k_1. If $\phi_0'^*$ is the complex conjugate of ϕ_0', $\phi_0'^*$ also satisfies (3.3.47) and (3.3.56). Applying Green's formula to $\phi_0'^*$ and ϕ_1', we have:

$$\int_{\mathcal{V}'}\left(\phi_0'^*\nabla^2\phi_1' - \phi_1'\nabla^2\phi_0'^*\right)d\mathcal{V} = \int_{S'}\left(\phi_0'^*\frac{\partial\phi_1'}{\partial n} - \phi_1'\frac{\partial\phi_0'^*}{\partial n}\right)dS \tag{3.3.58}$$

in which $S' = S_F' + S_{F_{MW}}' + S_W' + S_I + S_{I_{MW}}$, where S_F' is the free surface; $\mathbf{n}$ is a unit normal vector pointing away from the fluid; $\nabla^2\phi' \equiv \partial^2\phi'/\partial y^2 + \partial^2\phi'/\partial z^2$. Upon using (3.3.47) and (3.3.56), equation (3.3.58) becomes:

$$\begin{aligned} 2k_0k_1\int_{\mathcal{V}'}|\phi_0'|^2 d\mathcal{V} = &-\int_{S_{F_{MW}}'}\phi_0'^*\frac{W_0'}{\overline{\varepsilon}}dS - \int_{S_W'}\phi_0'^*[\mathbf{n}\cdot\mathbf{q}_1']dS \\ &+\int_{S_I+S_{I_{MW}}}\left(\phi_0'^*\frac{\partial\phi_1'}{\partial n} - \phi_1'\frac{\partial\phi_0'^*}{\partial n}\right)dS. \end{aligned} \tag{3.3.59}$$

In the lower layer, Green's formula yields:

$$\int_{\mathcal{V}}\left(\phi_0^*\nabla^2\phi_1 - \phi_1\nabla^2\phi_0^*\right)d\mathcal{V} = \int_S\left(\phi_0^*\frac{\partial\phi_1}{\partial n} - \phi_1\frac{\partial\phi_0^*}{\partial n}\right)dS \tag{3.3.60}$$

where $S = S_I + S_{I_{MW}} + S_W + S_B$. Again, use of (3.3.47) and (3.3.56) yields:

$$2k_0k_1\int_{\mathcal{V}}|\phi_0|^2d\mathcal{V} = -\int_{S_B+S_W}\phi_0^*[\mathbf{n}\cdot\mathbf{q_1}]dS + \int_{S_I+S_{I_{MW}}}\left(\phi_0^*\frac{\partial\phi_1}{\partial n} - \phi_1\frac{\partial\phi_0^*}{\partial n}\right)dS. \tag{3.3.61}$$

Notice that in (3.3.59) and (3.3.61) k_1 is given in terms of the unknowns $\mathbf{q}_1'$, ϕ_1', and $\mathbf{q_1}$, ϕ_1, respectively. The rotational components of the fluid velocities $\mathbf{q}_1'$ and $\mathbf{q_1}$ can be found from the continuity equation. Integration of (3.3.42a) and (3.3.42b) yields:

$$\mathbf{n}\cdot\mathbf{q}_1' = \frac{\varepsilon'}{\overline{\varepsilon}}\int_{\infty}^{\xi'}\left(ik_0U' + \frac{\partial U_T'}{\partial x_T}\right)_0 d\xi', \tag{3.3.62a}$$

$$\mathbf{n}\cdot\mathbf{q_1} = \frac{\varepsilon}{\overline{\varepsilon}}\int_{\infty}^{\xi}\left(ik_0U + \frac{\partial U_T}{\partial x_T}\right)_0 d\xi. \tag{3.3.62b}$$

To eliminate ϕ_1' and ϕ_1 from k_1, multiply (3.3.59) by β and add the equation obtained to (3.3.61), then write k_1 in the form:

$$\begin{aligned} k_1 =& \frac{1}{2k_0\left(\beta\int_{\mathcal{V}'}|\phi_0'|^2d\mathcal{V} + \int_{\mathcal{V}}|\phi_0|^2d\mathcal{V}\right)} \\ &\cdot\left\{\beta\int_{S_I+S_{I_{MW}}}\left(\phi_0'^*\frac{\partial\phi_1'}{\partial n} - \phi_1'\frac{\partial\phi_0'^*}{\partial n}\right)dS\right. \\ &+\int_{S_I+S_{I_{MW}}}\left(\phi_0^*\frac{\partial\phi_1}{\partial n} - \phi_1\frac{\partial\phi_0^*}{\partial n}\right)dS - \beta\int_{S'_{F_{MW}}}\phi_0'^*\frac{W_0'}{\overline{\varepsilon}}dS \\ &\left.-\beta\int_{S_W'}\phi_0'^*[\mathbf{n}\cdot\mathbf{q}_1']dS - \int_{S_B+S_W}\phi_0^*[\mathbf{n}\cdot\mathbf{q_1}]dS\right\}. \end{aligned} \tag{3.3.63}$$

Upon using the boundary conditions at the interface given in (3.3.47) and (3.3.56), the terms involving ϕ_1' and ϕ_1 cancel out between the first two integrals inside the curly bracket. Hence, we obtain:

$$k_1 = k_{1I'} + k_{1I} + k_{1I'_{MW}} + k_{1I_{MW}} + k_{1F_{MW}} + k_{1W'} + k_{1W} + k_{1B} \tag{3.3.64}$$

where

$$k_{1I'} = \frac{1}{\Gamma\cdot|C'|^2}\int_{S_I}\beta\phi_0'^*W_1'dS, \tag{3.3.65a}$$

$$k_{1I} = -\frac{1}{\Gamma \cdot |C'|^2} \int_{S_I} \phi_0^* W_1 dS, \tag{3.3.65b}$$

$$k_{1I'_{MW}} = \frac{1}{\Gamma \cdot |C'|^2} \int_{S_{I_{MW}}} \beta \phi_0'^* \frac{W_0'}{\overline{\varepsilon}} dS, \tag{3.3.65c}$$

$$k_{1I_{MW}} = -\frac{1}{\Gamma \cdot |C'|^2} \int_{S_{I_{MW}}} \phi_0^* \frac{W_0}{\overline{\varepsilon}} dS, \tag{3.3.65d}$$

$$k_{1F_{MW}} = -\frac{1}{\Gamma \cdot |C'|^2} \int_{S'_{F_{MW}}} \beta \phi_0'^* \frac{W_0'}{\overline{\varepsilon}} dS, \tag{3.3.65e}$$

$$k_{1W'} = -\frac{1}{\Gamma \cdot |C'|^2} \int_{S'_W} \beta \phi_0'^* [\mathbf{n} \cdot \mathbf{q}_1'] dS, \tag{3.3.65f}$$

$$k_{1W} = -\frac{1}{\Gamma \cdot |C'|^2} \int_{S_W} \phi_0^* [\mathbf{n} \cdot \mathbf{q}_1] dS, \tag{3.3.65g}$$

$$k_{1B} = -\frac{1}{\Gamma \cdot |C'|^2} \int_{S_B} \phi_0^* [\mathbf{n} \cdot \mathbf{q}_1] dS. \tag{3.3.65h}$$

The common denominator $\Gamma \cdot |C'|^2$ is given by:

$$\begin{aligned}
\Gamma &= \frac{2k_0}{|C'|^2} \left\{ \beta \int_{\mathcal{V}'} |\phi_0'|^2 d\mathcal{V} + \int_{\mathcal{V}} |\phi_0|^2 d\mathcal{V} \right\} \\
&= \frac{4k_0 b}{|C'|^2} \left\{ \beta \int_{-h'}^{0} |\phi_0'|^2 dz + \int_{-(h'+h)}^{-h'} |\phi_0|^2 dz \right\} \\
&= b \Big\{ \beta \left(k_0^2 (\sinh 2k_0 h' + 2k_0 h') + 2k_0 (1 - \cosh 2k_0 h') + (\sinh 2k_0 h' - 2k_0 h') \right) \\
&\quad + \frac{(\cosh k_0 h' - k_0 \sinh k_0 h')^2}{\sinh^2 k_0 h} (\sinh 2k_0 h + 2k_0 h) \Big\}.
\end{aligned} \tag{3.3.66}$$

Now let us evaluate the terms in (3.3.64). For the first term and the second term the integration over S_I is taken over an area of unit length and of width $2b$ at $z = -h'$. From (3.3.65a) and (3.3.65b), we get:

$$k_{1I'} = \frac{2b}{\Gamma \cdot |C'|^2} \left[\beta \phi_0'^* W_1' \right]_{z=-h'}, \tag{3.3.67a}$$

$$k_{1I} = -\frac{2b}{\Gamma \cdot |C'|^2} \left[\phi_0^* W_1 \right]_{z=-h'}. \tag{3.3.67b}$$

From (3.3.62a) and (3.3.62b), we obtain:

$$\begin{aligned}
\left[W_1' \right]_{S_I} &= -\frac{\varepsilon'}{\overline{\varepsilon}} \int_{\infty}^{\xi'} ik_0 U_{0I}' d\xi' \\
&= -\frac{(1-i)}{\sqrt{2}} \frac{\varepsilon'}{\overline{\varepsilon}} k_0 D' e^{-\frac{1}{\sqrt{2}}(1-i)\xi'}
\end{aligned} \tag{3.3.68a}$$

and

$$[W_1]_{S_I} = \frac{\varepsilon}{\overline{\varepsilon}} \int_{\infty}^{\xi} ik_0 U_{0I} d\xi$$
$$= \frac{(1-i)}{\sqrt{2}} \frac{\varepsilon}{\overline{\varepsilon}} k_0 D e^{-\frac{1}{\sqrt{2}}(1-i)\xi} \qquad (3.3.68b)$$

in which we have used (3.3.51a) and (3.3.51b). Direct substitution yields:

$$\overline{\varepsilon} k_{1I'} = -\sqrt{2}(1+i)\Gamma^{-1}\varepsilon' k_0^2 b \frac{(\beta-1)}{1+(\alpha\beta)^{1/2}}$$
$$\cdot (\coth k_0 h - k_0)(k_0 \cosh k_0 h' - \sinh k_0 h')$$
$$\cdot (\cosh k_0 h' - k_0 \sinh k_0 h') \qquad (3.3.69a)$$

and

$$\overline{\varepsilon} k_{1I} = \sqrt{2}(1+i)\Gamma^{-1}\varepsilon k_0^2 b \frac{(\beta-1)}{1+(\alpha\beta)^{1/2}} \left(\frac{\alpha}{\beta}\right)^{1/2}$$
$$\cdot (\coth k_0 h - k_0) \coth k_0 h$$
$$\cdot (\cosh k_0 h' - k_0 \sinh k_0 h')^2. \qquad (3.3.69b)$$

For the third term and the fourth term in (3.3.64), the integration over $S_{I_{MW}}$ is taken over a thin strip of width $O(\overline{\varepsilon})$ of the interfacial meniscus boundary layers at $y = b$ and $y = -b$. From (3.3.65c) and (3.3.65d), we obtain:

$$k_{1I'_{MW}} = \frac{2}{\Gamma \cdot |C'|^2} \int_0^{\infty} \beta \left[\phi_0'^* \frac{W'_{0W}}{\overline{\varepsilon}}\right]_{z=-h'} \varepsilon' d\xi', \qquad (3.3.70a)$$

$$k_{1I_{MW}} = -\frac{2}{\Gamma \cdot |C'|^2} \int_0^{\infty} \left[\phi_0^* \frac{W_{0W}}{\overline{\varepsilon}}\right]_{z=-h'} \varepsilon d\xi. \qquad (3.3.70b)$$

Direct substitution yields:

$$\overline{\varepsilon} k_{1I'_{MW}} = \sqrt{2}(1+i)\Gamma^{-1}\varepsilon' \beta k_0 (k_0 \cosh k_0 h' - \sinh k_0 h')$$
$$\cdot (k_0 \sinh k_0 h' - \cosh k_0 h'), \qquad (3.3.71a)$$

$$\overline{\varepsilon} k_{1I_{MW}} = \sqrt{2}(1+i)\Gamma^{-1}\varepsilon k_0 (k_0 \sinh k_0 h' - \cosh k_0 h')^2 \coth k_0 h. \qquad (3.3.71b)$$

Similarly, equation (3.3.65e) gives:

$$\begin{aligned}\overline{\varepsilon}k_{1F_{MW}} &= -\frac{2}{\Gamma\cdot|C'|^2}\int_0^\infty \beta\left[\phi_0'^{*}\frac{W'_{0W}}{\overline{\varepsilon}}\right]_{z=0}\varepsilon' d\xi' \\ &= \sqrt{2}(1+i)\Gamma^{-1}\varepsilon'\beta k_0^2. \end{aligned} \tag{3.3.72}$$

For the side-wall boundary layer, substitution of (3.3.55b) and (3.3.55c) into (3.3.62a) yields:

$$\begin{aligned}[\mathbf{n}\cdot\mathbf{q}_1']_{S'_W} &= \frac{\varepsilon'}{\overline{\varepsilon}}\left(k_0^2\phi_0' - \frac{d^2\phi_0'}{dz^2}\right)\int_\infty^{\xi'} e^{-\frac{1}{\sqrt{2}}(1-i)\xi'}d\xi' \\ &= 0 \end{aligned} \tag{3.3.73}$$

where the last line is due to (3.3.47a). Equation (3.3.73) also holds in the lower layer, hence, we have:

$$\overline{\varepsilon}k_{1W'} = 0, \tag{3.3.74a}$$

$$\overline{\varepsilon}k_{1W} = 0. \tag{3.3.74b}$$

On the channel bottom, equations (3.3.55a) and (3.3.62b) give:

$$\begin{aligned}[\mathbf{n}\cdot\mathbf{q}_1]_{S_B} &= \frac{\varepsilon}{\overline{\varepsilon}}\int_\infty^{\xi} ik_0U_{0B}d\xi \\ &= -\frac{(1+i)}{\sqrt{2}}\frac{\varepsilon}{\overline{\varepsilon}}k_0^2\phi_0(-(h'+h))e^{-\frac{1}{\sqrt{2}}(1-i)\xi}. \end{aligned} \tag{3.3.75}$$

From (3.3.65h), we get:

$$\begin{aligned}\overline{\varepsilon}k_{1B} &= -\frac{2b}{\Gamma\cdot|C'|^2}\left[\overline{\varepsilon}\phi_0^*(-h'-h)[\mathbf{n}\cdot\mathbf{q}_1]_{S_B}\right] \\ &= \sqrt{2}(1+i)\Gamma^{-1}\varepsilon k_0^2 b\frac{(\cosh k_0h' - k_0\sinh k_0h')^2}{\sinh^2 k_0h}. \end{aligned} \tag{3.3.76}$$

In dimensional form, these damping rates are given by:

$$\begin{aligned}\overline{\varepsilon}k_{1I'} = &-\sqrt{2}(1+i)\Gamma^{-1}k_0^2 b\left(\frac{\nu'}{\sigma}\right)^{1/2}\left(1-\frac{\rho'}{\rho}\right)\left(\frac{\rho\nu^{1/2}}{\rho\nu^{1/2}+\rho'\nu'^{1/2}}\right) \\ &\cdot\left(\coth k_0h - \frac{gk_0}{\sigma^2}\right)\left(\sinh k_0h' - \frac{gk_0}{\sigma^2}\cosh k_0h'\right)\end{aligned}$$

$$\cdot \left(\cosh k_0 h' - \frac{gk_0}{\sigma^2} \sinh k_0 h'\right), \tag{3.3.77a}$$

$$\overline{\varepsilon} k_{1I} = -\sqrt{2}(1+i)\Gamma^{-1} k_0^2 b \left(\frac{\nu}{\sigma}\right)^{1/2} \left(1 - \frac{\rho'}{\rho}\right) \left(\frac{\rho \nu'^{1/2}}{\rho \nu^{1/2} + \rho' \nu'^{1/2}}\right) \cdot \left(\coth k_0 h - \frac{gk_0}{\sigma^2}\right) \left(\cosh k_0 h' - \frac{gk_0}{\sigma^2} \sinh k_0 h'\right)^2 \coth k_0 h, \tag{3.3.77b}$$

$$\overline{\varepsilon} k_{1I'_{MW}} = \sqrt{2}(1+i)\Gamma^{-1} k_0 \left(\frac{\nu'}{\sigma}\right)^{1/2} \left(\frac{\rho'}{\rho}\right) \left(\sinh k_0 h' - \frac{gk_0}{\sigma^2} \cosh k_0 h'\right) \cdot \left(\cosh k_0 h' - \frac{gk_0}{\sigma^2} \sinh k_0 h'\right), \tag{3.3.77c}$$

$$\overline{\varepsilon} k_{1I_{MW}} = \sqrt{2}(1+i)\Gamma^{-1} k_0 \left(\frac{\nu}{\sigma}\right)^{1/2} \left(\cosh k_0 h' - \frac{gk_0}{\sigma^2} \sinh k_0 h'\right)^2 \coth k_0 h, \tag{3.3.77d}$$

$$\overline{\varepsilon} k_{1F_{MW}} = \sqrt{2}(1+i)\Gamma^{-1} \left(\frac{gk_0^2}{\sigma^2}\right) \left(\frac{\nu'}{\sigma}\right)^{1/2} \left(\frac{\rho'}{\rho}\right), \tag{3.3.77e}$$

$$\overline{\varepsilon} k_{1W'} = 0, \tag{3.3.77f}$$

$$\overline{\varepsilon} k_{1W} = 0, \tag{3.3.77g}$$

$$\overline{\varepsilon} k_{1B} = \sqrt{2}(1+i)\Gamma^{-1} k_0^2 b \left(\frac{\nu}{\sigma}\right)^{1/2} \frac{1}{\sinh^2 k_0 h} \cdot \left(\cosh k_0 h' - \frac{gk_0}{\sigma^2} \sinh k_0 h'\right)^2 \tag{3.3.77h}$$

where

$$\Gamma = b\left\{\frac{\rho'}{\rho}\left(\left(\frac{gk_0}{\sigma^2}\right)^2 (\sinh 2k_0 h' + 2k_0 h') + 2\left(\frac{gk_0}{\sigma^2}\right)(1 - \cosh 2k_0 h') + (\sinh 2k_0 h' - 2k_0 h')\right) + \left(\cosh k_0 h' - \frac{gk_0}{\sigma^2} \sinh k_0 h'\right)^2 \cdot \frac{(\sinh 2k_0 h + 2k_0 h)}{\sinh^2 k_0 h}\right\}.$$

Mei and Liu (1973) found in a similar manner, the complex damping rate for time-periodic progressive free surface waves in a rectangular channel. Their result, in dimensional form, is given by:

$$\varepsilon k_1 = (1+i)\frac{k_0}{b}\left(\frac{\nu}{2\sigma}\right)^{1/2} \left(\frac{2k_0 b + \sinh 2k_0 h}{2k_0 h + \sinh 2k_0 h}\right) \tag{3.3.78}$$

wherein h is the depth of the homogeneous fluid, and $2b$ is the width of the rectangular channel. The attenuation rate, which is the imaginary part of εk_1, had been found by Hunt (1957). As a check on the results in (3.3.77), we consider two limits in which (3.3.77) reduces to the damping rates for a homogeneous fluid. These limits are: (i) $\rho' = 0$, $(\nu'/\nu)^{1/2} = O(1)$; (ii) $\rho' = \rho$, $\nu' = \nu$. In case (i), it is easy to show that (3.3.77) reduces to:

$$\varepsilon k_{1I'_{MW}} = 0, \tag{3.3.79a}$$

$$\varepsilon k_{1I_{MW}} = (1+i)\frac{k_0}{b}\left(\frac{\nu}{2\sigma}\right)^{1/2}\left(\frac{\sinh 2k_0h}{2k_0h+\sinh 2k_0h}\right), \tag{3.3.79b}$$

$$\varepsilon k_{1F_{MW}} = 0, \tag{3.3.79c}$$

$$\varepsilon k_{1W'} = 0, \tag{3.3.79d}$$

$$\varepsilon k_{1W} = 0, \tag{3.3.79e}$$

$$\varepsilon k_{1B} = (1+i)\frac{k_0}{b}\left(\frac{\nu}{2\sigma}\right)^{1/2}\left(\frac{2k_0b}{2k_0h+\sinh 2k_0h}\right). \tag{3.3.79f}$$

Notice that $\varepsilon k_{1I'}$ and εk_{1I} are excluded from (3.3.79). This is because the results in (3.3.77) do not strictly apply in this limit. In particular, equations (3.3.50), (3.3.56d), and (3.3.56f) are not applicable to an air-water interface. Besides this, the present analysis remains valid, provided that the expansion parameter $\overline{\varepsilon}$ is of the same order in both layers. It can be seen in (3.3.46) that this condition is fulfilled; though the density of air is much less than the density of water, $(\nu'/\nu)^{1/2} = O(1)$ for air and water.

In case (ii), we have:

$$\varepsilon k_{1I'} = 0, \tag{3.3.80a}$$

$$\varepsilon k_{1I} = 0, \tag{3.3.80b}$$

$$\varepsilon k_{1I'_{MW}} = -(1+i)\frac{k_0}{b}\left(\frac{\nu}{2\sigma}\right)^{1/2}\left(\frac{\sinh 2k_0h}{2k_0(h'+h)+\sinh 2k_0(h'+h)}\right), \tag{3.3.80c}$$

$$\varepsilon k_{1I_{MW}} = (1+i)\frac{k_0}{b}\left(\frac{\nu}{2\sigma}\right)^{1/2}\left(\frac{\sinh 2k_0h}{2k_0(h'+h)+\sinh 2k_0(h'+h)}\right), \tag{3.3.80d}$$

$$\varepsilon k_{1F_{MW}} = (1+i)\frac{k_0}{b}\left(\frac{\nu}{2\sigma}\right)^{1/2}\left(\frac{\sinh 2k_0(h'+h)}{2k_0(h'+h)+\sinh 2k_0(h'+h)}\right), \quad (3.3.80e)$$

$$\varepsilon k_{1W'} = 0, \quad (3.3.80f)$$

$$\varepsilon k_{1W} = 0, \quad (3.3.80g)$$

$$\varepsilon k_{1B} = (1+i)\frac{k_0}{b}\left(\frac{\nu}{2\sigma}\right)^{1/2}\left(\frac{2k_0 b}{2k_0(h'+h)+\sinh 2k_0(h'+h)}\right). \quad (3.3.80h)$$

Clearly, the total damping rates given by (3.3.78), (3.3.79), and (3.3.80) are the same.

The mechanism of energy transfer in a homogeneous fluid has been discussed in detail by Mei and Liu (1973), similar conclusions may be drawn for a two-layer fluid. It can be shown that the imaginary parts of the integrals in the numerator of (3.3.63) represent the average rates of work being done by the pressure force on the interface between the boundary layers and the fluid outside the boundary layers. Notice that in (3.3.65) only the rotational velocity components normal to the boundary layers contribute to the work done. This is because the potential part of the velocity normal to the boundary layer is out of phase with the dynamic pressure to $O(\overline{\varepsilon})$. Moreover, the rotational velocity components acting normal to the side-wall boundary layers ($y = \pm b$) are zero to $O(\overline{\varepsilon})$ owing to the two-dimensional nature of this problem (see equation 3.3.73). Hence, there is no energy exchange through the interface between the side-wall boundary layers and the inviscid core. Indeed, Ursell (1952) found that the rate of energy dissipation in the side-wall boundary layers could not be balanced by the rate of work done by the pressure force from the main fluid body on the outer edge of the side-wall boundary layers. Mei and Liu (1973) showed by energy balance that the energy dissipated in the side-wall boundary layers originates from the inviscid core and is fed into the meniscus boundary layers by the pressure force, and then transmitted essentially undiminished to the side-wall boundary layers. This result is clearly shown in (3.3.79*b*); the imaginary part of $\varepsilon k_{1I_{MW}}$ represents the rate of work done by the pressure force on the inter-

face between the meniscus boundary layer and the side-wall boundary layer. Thus, the meniscus boundary layer serves as a "gateway" of energy flow from waves to the side-wall boundary layer where it is then dissipated. For a detailed description of the mechanism of energy transfer in the neighborhood of the meniscus boundary layer, the readers are referred to Mei and Liu (1973). It is also seen in (3.3.79f) that the energy dissipated in the bottom boundary layer is obtained from work being done by the pressure force of the inviscid core on the outer edge of the bottom boundary layer.

When the densities in the upper and the lower layers are equal, that is, $\rho' = \rho$, the two-layer fluid becomes a homogeneous fluid. The results in (3.3.80) are in agreement with the above discussion. Equations (3.3.80c)–(3.3.80e) show that the damping rates $\varepsilon k_{1I'_{MW}}$ and $\varepsilon k_{1I_{MW}}$ are equal in magnitude but have opposite signs, and are both less than $\varepsilon k_{1F_{MW}}$. This is because part of the wave energy fed into the side-wall boundary layer through the surface meniscus is dissipated in the boundary layer above $z = -h'$, at $z = -h'$ the remaining energy is fed from above through a narrow strip of width $O(\varepsilon)$ of the side-wall boundary layer by the pressure force into the part of the side-wall boundary layer between $z = -(h' + h)$ and $z = -h'$ where it is then dissipated.

In this section, an analytical treatment of wave damping in a two-layer fluid is presented based on linear theory. We assume that the entire loss of energy of waves is localized in the boundary layers adjacent to the solid surfaces and at the density interface, and the flow is laminar within the boundary layers. The damping rates for plane progressive waves in a two-layer fluid is obtained by expanding the velocity potential and the rotational part of the fluid velocity in terms of a boundary layer parameter. The results are used in § 3.3.3 to incorporate the effects of wave damping into the inviscid two-layer model treated in § 3.1.

3.3.1.2 Standing Waves in a Rectangular Basin

A two-layer fluid of total depth $(h' + h)$ is contained in a rectangular basin of length ℓ and of width $2b$. Let the physical variables in the upper layer be distinguished by primes. The upper layer is of depth h' and the lower layer is of depth h. The densities of the upper fluid and of the lower fluid are ρ' and ρ, respectively. A Cartesian coordinate system is defined as shown in figure 3.3.4. The (x, y) plane is taken at the undisturbed free surface with z measured positive upwards. The walls of the basin are located at $x = 0$, $x = \ell$, $y = -b$, and $y = b$. The wave motion in the basin is assumed to be two-dimensional so that no cross-waves are generated in the y direction. The perturbation analysis for the standing waves is virtually identical to that of the progressive waves presented in § 3.3.1.1. In this case, the wave number k is assumed to be real and fixed. The following perturbation expansions are introduced:

$$\Phi = [\phi_0(x, y, z) + \overline{\varepsilon}\phi_1(x, y, z) + O(\overline{\varepsilon}^2)]e^{-i\sigma t}, \tag{3.3.81a}$$

$$\mathbf{U} = [\mathbf{q_0}(\mathbf{x_T}, \xi) + \overline{\varepsilon}\mathbf{q_1}(\mathbf{x_T}, \xi) + O(\overline{\varepsilon}^2)]e^{-i\sigma t}, \tag{3.3.81b}$$

$$\sigma = \sigma_0 + \overline{\varepsilon}\sigma_1 + O(\overline{\varepsilon}^2). \tag{3.3.81c}$$

When (3.3.81a)–(3.3.81c) are substituted into the dimensionless equations and the orders are separated, we obtain the following problems:

(1) Inviscid solution of $O(\overline{\varepsilon}^0)$:

$$\frac{\partial^2 \phi_0'}{\partial x^2} + \frac{\partial^2 \phi_0'}{\partial z^2} = 0, \qquad -h' < z < 0, \tag{3.3.82a}$$

$$\frac{\partial^2 \phi_0}{\partial x^2} + \frac{\partial^2 \phi_0}{\partial z^2} = 0, \qquad -(h' + h) < z < -h', \tag{3.3.82b}$$

$$\frac{\partial \phi_0'}{\partial z} - \sigma_0^2 \phi_0' = 0 \qquad \text{on} \qquad z = 0, \tag{3.3.82c}$$

$$\frac{\partial \phi_0}{\partial z} - \sigma_0^2 \phi_0 = \beta \left(\frac{\partial \phi_0'}{\partial z} - \sigma_0^2 \phi_0' \right) \qquad \text{on} \qquad z = -h', \tag{3.3.82d}$$

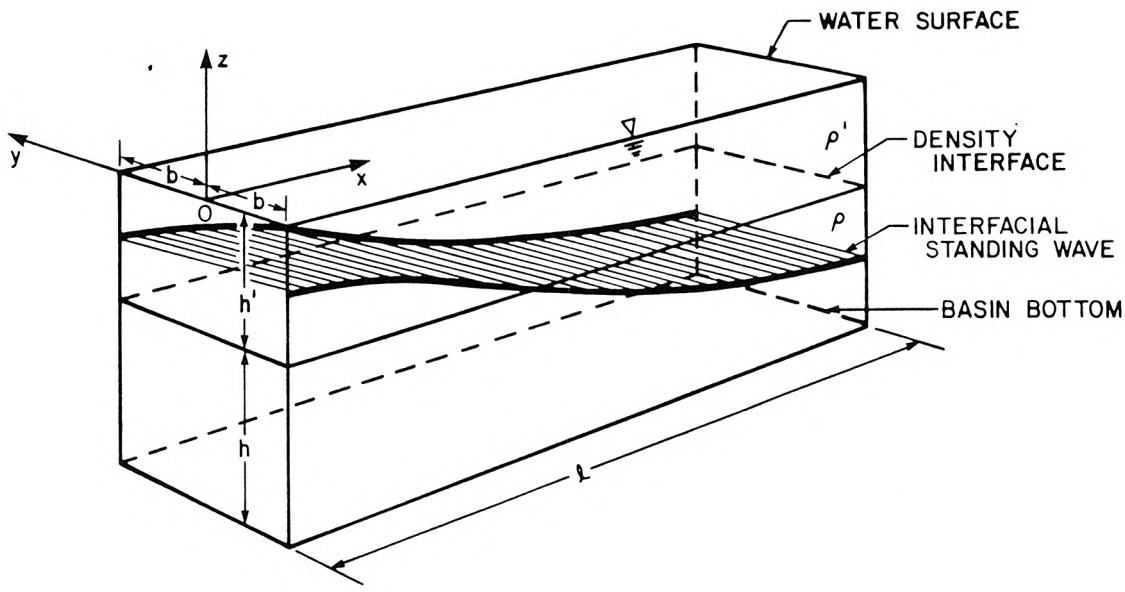

Figure 3.3.4. Schematic drawing of a standing interfacial wave in a rectangular basin that is partially filled with a two-layer fluid.

$$\frac{\partial \phi_0}{\partial z} = \frac{\partial \phi_0'}{\partial z} \qquad \text{on} \qquad z = -h', \tag{3.3.82e}$$

$$\frac{\partial \phi_0'}{\partial x} = 0 \qquad \text{on} \qquad x = 0, \quad -h' < z < 0$$

$$\text{and} \qquad x = \ell, \quad -h' < z < 0, \tag{3.3.82f}$$

$$\frac{\partial \phi_0}{\partial x} = 0 \qquad \text{on} \qquad x = 0 \quad -(h' + h) < z < -h'$$

$$\text{and} \qquad x = \ell, \quad -(h' + h) < z < -h', \tag{3.3.82g}$$

$$\frac{\partial \phi_0}{\partial z} = 0 \qquad \text{on} \qquad z = -(h' + h). \tag{3.3.82h}$$

The solutions are:

$$\phi_0'(x, z) = C'(\cosh z + \sigma_0^2 \sinh z) \cos x, \tag{3.3.83a}$$

$$\phi_0(x,z) = C' \frac{(\sigma_0^2 \cosh h' - \sinh h')}{\sinh h} \cosh(z + h' + h) \cos x, \qquad (3.3.83b)$$

$$\ell = n\pi \qquad (n = 1, 2, \ldots) \qquad (3.3.83c)$$

in which C' is an arbitrary constant. Note that all the physical quantities with the dimension of length have been scaled by the wave number k. The circular frequency σ_0 is given by the dispersion relation:

$$\sigma_0^4(\coth h \coth h' + \beta) - \sigma_0^2(\coth h + \coth h') + (1 - \beta) = 0. \qquad (3.3.84)$$

(2) Interfacial boundary layer correction of $O(\overline{\varepsilon}^0)$:

$$\frac{\partial^2 U_0'}{\partial \xi'^2} = -i\sigma_0 U_0', \qquad \xi' = \frac{z + h'}{\varepsilon'}, \qquad (3.3.85a)$$

$$\frac{\partial^2 U_0}{\partial \xi^2} = -i\sigma_0 U_0, \qquad \xi = -\frac{z + h'}{\varepsilon}, \qquad (3.3.85b)$$

$$U_0' \to 0, \qquad \xi' \to \infty, \qquad (3.3.85c)$$

$$U_0 \to 0, \qquad \xi \to \infty, \qquad (3.3.85d)$$

$$\frac{\partial \phi_0}{\partial x} + U_0 = \frac{\partial \phi_0'}{\partial x} + U_0' \qquad \text{on} \qquad z = -h', \qquad (3.3.85e)$$

$$\frac{\partial U_0}{\partial z} = \alpha \frac{\partial U_0'}{\partial z} \qquad \text{on} \qquad z = -h'. \qquad (3.3.85f)$$

The solutions are:

$$U_{0I}'(x, \xi') = D' e^{-\sqrt{\frac{\sigma_0}{2}}(1-i)\xi'}, \qquad (3.3.86a)$$

$$U_{0I}(x, \xi) = D e^{-\sqrt{\frac{\sigma_0}{2}}(1-i)\xi} \qquad (3.3.86b)$$

where the subscript I denotes the density interface, and D', D are functions of x given by:

$$D'(x) = \frac{1}{\beta}(\beta - 1)\left[\frac{\partial \phi_0}{\partial x} - \frac{1}{\sigma_0^2}\frac{\partial^2 \phi_0}{\partial x \partial z}\right]_{z=-h'} + D, \qquad (3.3.87a)$$

$$D(x) = -\frac{1}{1 + (\alpha\beta)^{1/2}}\left(\frac{\alpha}{\beta}\right)^{1/2}(\beta - 1)\left[\frac{\partial \phi_0}{\partial x} - \frac{1}{\sigma_0^2}\frac{\partial^2 \phi_0}{\partial x \partial z}\right]_{z=-h'}. \qquad (3.3.87b)$$

(3) Bottom and side-wall boundary layer correction of $O(\overline{\varepsilon}^0)$:

$$\frac{\partial^2 U_0}{\partial \xi^2} = -i\sigma_0 U_0, \qquad \text{on} \qquad \xi = \frac{z + h' + h}{\varepsilon}$$
$$\text{and} \qquad \xi = \frac{b \mp y}{\varepsilon}, \tag{3.3.88a}$$

$$\frac{\partial^2 W_0}{\partial \xi^2} = -i\sigma_0 W_0, \qquad \text{on} \qquad \xi = \frac{x}{\varepsilon}$$
$$\text{and} \qquad \xi = \frac{\ell - x}{\varepsilon}$$
$$\text{and} \qquad \xi = \frac{b \mp y}{\varepsilon}, \tag{3.3.88b}$$

$$U_0 = -\frac{\partial \phi_0}{\partial x} \qquad \text{on} \qquad \xi = 0, \tag{3.3.88c}$$

$$W_0 = -\frac{\partial \phi_0}{\partial z} \qquad \text{on} \qquad \xi = 0, \tag{3.3.88d}$$

$$U_0, W_0 \to 0, \qquad \xi \to \infty. \tag{3.3.88e}$$

The solutions are:

$$U_{0B}(x,\xi) = -\left[\frac{\partial \phi_0}{\partial x}(x,z)\right]_{z=-(h'+h)} e^{-\sqrt{\frac{\sigma_0}{2}}(1-i)\xi}, \qquad \xi = \frac{z + (h' + h)}{\varepsilon}, \tag{3.3.89a}$$

$$U_{0W}(x,z,\xi) = -\frac{\partial \phi_0}{\partial x}(x,z) e^{-\sqrt{\frac{\sigma_0}{2}}(1-i)\xi}, \qquad \xi = \frac{b + y}{\varepsilon}, \tag{3.3.89b}$$

$$\begin{aligned} W_{0W}(z,\xi) &= -\left[\frac{\partial \phi_0}{\partial z}(x,z)\right]_{x=0} e^{-\sqrt{\frac{\sigma_0}{2}}(1-i)\xi}, \qquad \xi = \frac{x}{\varepsilon}; \\ &= -\left[\frac{\partial \phi_0}{\partial z}(x,z)\right]_{x=\ell} e^{-\sqrt{\frac{\sigma_0}{2}}(1-i)\xi}, \qquad \xi = \frac{\ell - x}{\varepsilon}; \\ &= -\frac{\partial \phi_0}{\partial z}(x,z) e^{-\sqrt{\frac{\sigma_0}{2}}(1-i)\xi}, \qquad \xi = \frac{b \mp y}{\varepsilon} \end{aligned} \tag{3.3.89c}$$

wherein the subscripts W and B, respectively, denote the side wall and the bottom. Equations (3.3.89b) and (3.3.89c) also hold in the upper layer.

(4) Inviscid correction of $O(\overline{\varepsilon}^1)$:

$$\nabla^2\phi_1' = 0 \qquad \text{in} \qquad \mathcal{V}', \tag{3.3.90a}$$

$$\nabla^2\phi_1 = 0 \qquad \text{in} \qquad \mathcal{V}, \tag{3.3.90b}$$

$$\frac{\partial\phi_1'}{\partial z} - \sigma_0^2\phi_1' - 2\sigma_0\sigma_1\phi_0' + \frac{W_0'}{\overline{\varepsilon}} = 0 \qquad \text{on} \qquad S'_{F_{MW}}, \tag{3.3.90c}$$

$$\frac{\partial\phi_1}{\partial z} - \sigma_0^2\phi_1 - 2\sigma_0\sigma_1\phi_0 + W_1 = \beta\left(\frac{\partial\phi_1'}{\partial z} - \sigma_0^2\phi_1' - 2\sigma_0\sigma_1\phi_0' + W_1'\right) \qquad \text{on} \qquad S_I, \tag{3.3.90d}$$

$$\frac{\partial\phi_1}{\partial z} - \sigma_0^2\phi_1 - 2\sigma_0\sigma_1\phi_0 + \frac{W_0}{\overline{\varepsilon}} = \beta\left(\frac{\partial\phi_1'}{\partial z} - \sigma_0^2\phi_1' - 2\sigma_0\sigma_1\phi_0' + \frac{W_0'}{\overline{\varepsilon}}\right) \qquad \text{on} \qquad S_{I_{MW}}, \tag{3.3.90e}$$

$$\frac{\partial\phi_1}{\partial z} + W_1 = \frac{\partial\phi_1'}{\partial z} + W_1' \qquad \text{on} \qquad S_I, \tag{3.3.90f}$$

$$\frac{\partial\phi_1}{\partial z} + \frac{W_0}{\overline{\varepsilon}} = \frac{\partial\phi_1'}{\partial z} + \frac{W_0'}{\overline{\varepsilon}} \qquad \text{on} \qquad S_{I_{MW}}, \tag{3.3.90g}$$

$$\mathbf{n}\cdot\nabla\phi_1' = -\mathbf{n}\cdot\mathbf{q}_1' \qquad \text{on} \qquad S'_W, \tag{3.3.90h}$$

$$\mathbf{n}\cdot\nabla\phi_1 = -\mathbf{n}\cdot\mathbf{q}_1 \qquad \text{on} \qquad S_W + S_B. \tag{3.3.90i}$$

Let $\phi_0'^*$ denote the complex conjugate of ϕ_0'. Applying Green's formula to $\phi_0'^*$ and ϕ_1', we have:

$$\int_{\mathcal{V}'}(\phi_0'^*\nabla^2\phi_1' - \phi_1'\nabla^2\phi_0'^*)d\mathcal{V} = \int_{S'}\left(\phi_0'^*\frac{\partial\phi_1'}{\partial n} - \phi_1'\frac{\partial\phi_0'^*}{\partial n}\right)dS \tag{3.3.91}$$

where $S' = S'_F + S'_{F_{MW}} + S'_W + S_I + S_{I_{MW}}$, and $\mathbf{n}$ is a unit normal vector pointing away from the fluid. Upon using (3.3.82) and (3.3.90), equation (3.3.91) becomes:

$$2\sigma_0\sigma_1\int_{S'_F}|\phi_0'|^2dS = \int_{S'_{F_{MW}}}\phi_0'^*\frac{W_0'}{\overline{\varepsilon}}dS + \int_{S'_W}\phi_0'^*[\mathbf{n}\cdot\mathbf{q}_1']dS - \int_{S_I+S_{I_{MW}}}\left(\phi_0'^*\frac{\partial\phi_1'}{\partial n} - \phi_1'\frac{\partial\phi_0'^*}{\partial n}\right)dS. \tag{3.3.92}$$

In the lower layer, Green's formula gives:

$$\int_{\mathcal{V}}(\phi_0^*\nabla^2\phi_1 - \phi_1\nabla^2{\phi_0}^*)d\mathcal{V} = \int_S \left(\phi_0{}^*\frac{\partial\phi_1}{\partial n} - \phi_1\frac{\partial{\phi_0}^*}{\partial n}\right) dS \tag{3.3.93}$$

where $S = S_I + S_{I_{MW}} + S_W + S_B$. Upon using (3.3.82) and (3.3.90), we obtain:

$$0 = \int_{S_W+S_B} \phi_0{}^*[\mathbf{n}\cdot\mathbf{q_1}]dS - \int_{S_I+S_{I_{MW}}} \left(\phi_0{}^*\frac{\partial\phi_1}{\partial n} - \phi_1\frac{\partial{\phi_0}^*}{\partial n}\right) dS. \tag{3.3.94}$$

The unknowns $\mathbf{q}_1'$, $\mathbf{q_1}$ in (3.3.92), (3.3.94) are found from the continuity equation. Integration of (3.3.42a) and (3.3.42b) yields:

$$\mathbf{n}\cdot\mathbf{q}_1' = \frac{\varepsilon'}{\overline{\varepsilon}}\int_\infty^{\xi'}\left(\frac{\partial U_{T_1}'}{\partial x_{T_1}} + \frac{\partial U_{T_2}'}{\partial x_{T_2}}\right)_0 d\xi', \tag{3.3.95a}$$

$$\mathbf{n}\cdot\mathbf{q_1} = \frac{\varepsilon}{\overline{\varepsilon}}\int_\infty^{\xi}\left(\frac{\partial U_{T_1}}{\partial x_{T_1}} + \frac{\partial U_{T_2}}{\partial x_{T_2}}\right)_0 d\xi. \tag{3.3.95b}$$

Multipying (3.3.92) by β and adding the equations obtained to (3.3.94), we get:

$$\begin{aligned} 2\sigma_0\sigma_1\beta\int_{S_F'}|\phi_0'|^2dS = &-\beta\int_{S_I+S_{I_{MW}}}\left(\phi_0'{}^*\frac{\partial\phi_1'}{\partial n} - \phi_1'\frac{\partial{\phi_0'}^*}{\partial n}\right)dS \\ &-\int_{S_I+S_{I_{MW}}}\left(\phi_0{}^*\frac{\partial\phi_1}{\partial n} - \phi_1\frac{\partial\phi_0^*}{\partial n}\right)dS + \beta\int_{S'_{F_{MW}}}\phi_0'{}^*\frac{W_0'}{\overline{\varepsilon}}dS \\ &+\beta\int_{S_W'}\phi_0'{}^*[\mathbf{n}\cdot\mathbf{q}_1']dS + \int_{S_W+S_B}\phi_0{}^*[\mathbf{n}\cdot\mathbf{q_1}]dS. \end{aligned} \tag{3.3.96}$$

After applying the boundary conditions at the interface given in (3.3.82) and (3.3.90), the terms involving ϕ_1' and ϕ_1 are eliminated from the first two integrals on the right hand side of (3.3.96), and we obtain σ_1 immediately as:

$$\sigma_1 = \sigma_{1I'} + \sigma_{1I} + \sigma_{1I'_{MW}} + \sigma_{1I_{MW}} + \sigma_{1F_{MW}} + \sigma_{1W'} + \sigma_{1W} + \sigma_{1B} \tag{3..3.97}$$

where

$$\sigma_{1I'} = -\frac{1}{\Gamma\cdot|C'|^2}\int_{S_I}\beta\phi_0'{}^*W_1'dS, \tag{3.3.98a}$$

$$\sigma_{1I} = \frac{1}{\Gamma\cdot|C'|^2}\int_{S_I}\phi_0^*W_1dS, \tag{3.3.98b}$$

$$\sigma_{1I'_{MW}} = -\frac{1}{\Gamma\cdot|C'|^2}\int_{S_{I_{MW}}}\beta\phi_0'{}^*\frac{W_0'}{\overline{\varepsilon}}dS, \tag{3.3.98c}$$

$$\sigma_{1I_{MW}} = \frac{1}{\Gamma \cdot |C'|^2} \int_{S_{I_{MW}}} \phi_0^* \frac{W_0}{\overline{\varepsilon}} dS, \tag{3.3.98d}$$

$$\sigma_{S'_{1F_{MW}}} = \frac{1}{\Gamma \cdot |C'|^2} \int_{S_{F_{MW}}} \beta \phi_0'^* \frac{W_0'}{\overline{\varepsilon}} dS, \tag{3.3.98e}$$

$$\sigma_{1W'} = \frac{1}{\Gamma \cdot |C'|^2} \int_{S'_W} \beta \phi_0'^* [\mathbf{n} \cdot \mathbf{q}_1'] dS, \tag{3.3.98f}$$

$$\sigma_{1W} = \frac{1}{\Gamma \cdot |C'|^2} \int_{S_W} \phi_0^* [\mathbf{n} \cdot \mathbf{q}_1] dS, \tag{3.3.98g}$$

$$\sigma_{1B} = \frac{1}{\Gamma \cdot |C'|^2} \int_{S_B} \phi_0^* [\mathbf{n} \cdot \mathbf{q}_1] dS. \tag{3.3.98h}$$

The common denominator $\Gamma \cdot |C'|^2$ is given by:

$$\begin{aligned}
\Gamma &= \frac{2\sigma_0}{|C'|^2} \left\{ \beta \int_{S'_F} |\phi_0'|^2 dS - \frac{(\beta - 1)}{\sigma_0^4} \int_{S_I} \left| \frac{\partial \phi_0}{\partial z} \right|^2 dS \right\} \\
&= \frac{4\sigma_0 b}{|C'|^2} \left\{ \beta \int_0^\ell |\phi_0'|^2_{z=0} dx - \frac{(\beta - 1)}{\sigma_0^4} \int_0^\ell \left| \frac{\partial \phi_0}{\partial z} \right|^2_{z=-h'} dx \right\} \\
&= 2\sigma_0 b\ell \left\{ \beta + \frac{(1 - \beta)}{\sigma_0^4} (\sinh h' - \sigma_0^2 \cosh h')^2 \right\}
\end{aligned} \tag{3.3.99}$$

in which (3.3.83a) and (3.3.83b) have been used. Now let us evaluate the terms in (3.3.97). For the first term and the second term the integration over S_I is taken over the plane area of the density interface, that is:

$$\sigma_{1I'} = -\frac{2b}{\Gamma \cdot |C'|^2} \int_0^\ell \beta \left[\phi_0'^* W_1' \right]_{z=-h'} dx, \tag{3.3.100a}$$

$$\sigma_{1I} = \frac{2b}{\Gamma \cdot |C'|^2} \int_0^\ell [\phi_0^* W_1]_{z=-h'} dx. \tag{3.3.100b}$$

The induced velocities normal to interfacial boundary layers are obtained using (3.3.95a) and (3.3.95b):

$$[W_1']_{z=-h'} = -\frac{\varepsilon'}{\overline{\varepsilon}} \int_\infty^{\xi'} \frac{\partial U_{0I}'}{\partial x} d\xi', \tag{3.3.101a}$$

$$[W_1]_{z=-h'} = \frac{\varepsilon}{\overline{\varepsilon}} \int_\infty^{\xi} \frac{\partial U_{0I}}{\partial x} d\xi. \tag{3.3.101b}$$

From (3.3.83), (3.3.86), (3.3.87), (3.3.100), and (3.3.101), we obtain:

$$\overline{\varepsilon}\sigma_{1I'} = \frac{(1+i)}{\sqrt{2\sigma_0}} \varepsilon' \Gamma^{-1} \frac{b\ell}{\sigma_0^2} \frac{(1-\beta)}{1 + (\alpha\beta)^{1/2}}$$

$$\cdot(\sigma_0^2\coth h-1)(\sigma_0^2\cosh h'-\sinh h')(\sigma_0^2\sinh h'-\cosh h'), \tag{3.3.102a}$$

$$\overline{\varepsilon}\sigma_{1I} = \frac{(1+i)}{\sqrt{2\sigma_0}}\varepsilon\Gamma^{-1}\frac{b\ell}{\sigma_0^2}\frac{(1-\beta)}{1+(\alpha\beta)^{1/2}}\left(\frac{\alpha}{\beta}\right)^{1/2}$$
$$\cdot(\sigma_0^2\coth h-1)(\sigma_0^2\cosh h'-\sinh h')^2\coth h. \tag{3.3.102b}$$

For the third term and the fourth term in (3.3.97), the integration over $S_{I_{MW}}$ is taken over a narrow strip of width $O(\overline{\varepsilon})$ of the interfacial meniscus boundary layer along the perimeter of the rectangular basin. By symmetry, only the integrals on $x=0$ and $y=b$ are needed. Equations (3.3.98c) and (3.3.98d) give:

$$\left[\sigma_{1I'_{MW}}\right]_{x=0} = -\frac{2b}{\Gamma\cdot|C'|^2}\int_0^\infty \beta\left[\phi_0'^*\frac{W'_{0W}}{\overline{\varepsilon}}\right]_{x=0,z=-h'}\varepsilon' d\xi', \tag{3.3.103a}$$

$$\left[\sigma_{1I'_{MW}}\right]_{y=b} = -\frac{1}{\Gamma\cdot|C'|^2}\int_0^\ell\int_0^\infty \beta\left[\phi_0'^*\frac{W'_{0W}}{\overline{\varepsilon}}\right]_{z=-h'}\varepsilon' d\xi' dx \tag{3.3.103b}$$

$$\left[\sigma_{1I_{MW}}\right]_{x=0} = \frac{2b}{\Gamma\cdot|C'|^2}\int_0^\infty \left[\phi_0^*\frac{W_{0W}}{\overline{\varepsilon}}\right]_{x=0,z=-h'}\varepsilon d\xi, \tag{3.3.103c}$$

$$\left[\sigma_{1I_{MW}}\right]_{y=b} = \frac{1}{\Gamma\cdot|C'|^2}\int_0^\ell\int_0^\infty \left[\phi_0^*\frac{W_{0W}}{\overline{\varepsilon}}\right]_{z=-h'}\varepsilon d\xi dx, \tag{3.3.103d}$$

Direct substitution of (3.3.83) and (3.3.89c) yields:

$$\left[\overline{\varepsilon}\sigma_{1I'_{MW}}\right]_{x=0} = -\frac{2(1+i)}{\sqrt{2\sigma_0}}\varepsilon'\beta b\Gamma^{-1}(\sigma_0^2\sinh h'-\cosh h')$$
$$\cdot(\sigma_0^2\cosh h'-\sinh h'), \tag{3.3.104a}$$

$$\left[\overline{\varepsilon}\sigma_{1I'_{MW}}\right]_{y=b} = -\frac{(1+i)}{2\sqrt{2\sigma_0}}\varepsilon'\beta\ell\Gamma^{-1}(\sigma_0^2\sinh h'-\cosh h')$$
$$\cdot(\sigma_0^2\cosh h'-\sinh h'), \tag{3.3.104b}$$

$$\left[\overline{\varepsilon}\sigma_{1I_{MW}}\right]_{x=0} = -\frac{2(1+i)}{\sqrt{2\sigma_0}}\varepsilon b\Gamma^{-1}(\sigma_0^2\cosh h'-\sinh h')^2\coth h, \tag{3.3.104c}$$

$$\left[\overline{\varepsilon}\sigma_{1I_{MW}}\right]_{y=b} = -\frac{(1+i)}{2\sqrt{2\sigma_0}}\varepsilon\ell\Gamma^{-1}(\sigma_0^2\cosh h'-\sinh h')^2\coth h. \tag{3.3.104d}$$

Similarly, the integration over $S'_{F_{MW}}$ in (3.3.98e) is evaluated in two parts, that is, on $x=0$ and $y=b$. We have:

$$\left[\sigma_{1F_{MW}}\right]_{x=0} = \frac{2b}{\Gamma\cdot|C'|^2}\int_0^\infty \beta\left[\phi_0'^*\frac{W'_{0W}}{\overline{\varepsilon}}\right]_{x=0,z=0}\varepsilon' d\xi', \tag{3.3.105a}$$

$$\left[\sigma_{1F_{MW}}\right]_{y=b} = \frac{1}{\Gamma \cdot |C'|^2} \int_0^{\ell} \int_0^{\infty} \beta \left[\phi_0'^* \frac{W_{0W}'}{\overline{\varepsilon}}\right]_{z=0} \varepsilon' d\xi' dx \qquad (3.3.105b)$$

Direct substitution yields:

$$\left[\overline{\varepsilon}\sigma_{1F_{MW}}\right]_{x=0} = -\frac{2(1+i)}{\sqrt{2\sigma_0}} \varepsilon' \beta b \Gamma^{-1} \sigma_0^2, \qquad (3.3.106a)$$

$$\left[\overline{\varepsilon}\sigma_{1F_{MW}}\right]_{y=b} = -\frac{(1+i)}{2\sqrt{2\sigma_0}} \varepsilon' \beta \ell \Gamma^{-1} \sigma_0^2. \qquad (3.3.106b)$$

For the side-wall boundary layers adjacent to the wall at $x = 0$, equations (3.3.95a) and (3.3.95b) yield:

$$\begin{aligned}[\mathbf{n} \cdot \mathbf{q}_1']_{x=0} &= \frac{\varepsilon'}{\overline{\varepsilon}} \int_{\infty}^{\xi'} \left[\frac{\partial W_{0W}'}{\partial z}\right]_{x=0} d\xi' \\ &= \frac{(1+i)}{\sqrt{2\sigma_0}} \frac{\varepsilon'}{\overline{\varepsilon}} \left[\frac{\partial^2 \phi_0'}{\partial z^2}\right]_{x=0} e^{-\sqrt{\frac{\sigma_0}{2}}(1-i)\xi'}, \qquad (3.3.107a)\end{aligned}$$

$$\begin{aligned}[\mathbf{n} \cdot \mathbf{q}_1]_{x=0} &= \frac{\varepsilon}{\overline{\varepsilon}} \int_{\infty}^{\xi} \left[\frac{\partial W_{0W}}{\partial z}\right]_{x=0} d\xi \\ &= \frac{(1+i)}{\sqrt{2\sigma_0}} \frac{\varepsilon}{\overline{\varepsilon}} \left[\frac{\partial^2 \phi_0}{\partial z^2}\right]_{x=0} e^{-\sqrt{\frac{\sigma_0}{2}}(1-i)\xi}, \qquad (3.3.107b)\end{aligned}$$

Owing to the two dimensional nature of this problem, the rotational velocity components normal to the side-wall boundary layers at $y = \pm b$ are zero to $O(\overline{\varepsilon})$. Hence:

$$\begin{aligned}[\overline{\varepsilon}\sigma_{1W'}]_{x=0} =& \frac{2b}{\Gamma \cdot |C'|^2} \int_{-h'}^{0} \beta \left[\phi_0'^* [\mathbf{n} \cdot \mathbf{q}_1']\right]_{x=0} dz \\ =& \frac{(1+i)}{2\sqrt{2\sigma_0}} \varepsilon' \beta b \Gamma^{-1} \Big\{ (\sinh 2h' + 2h') \\ & + 2\sigma_0^2 (1 - \cosh 2h') + \sigma_0^4 (\sinh 2h' - 2h') \Big\}, \qquad (3.3.108a)\end{aligned}$$

$$[\overline{\varepsilon}\sigma_{1W'}]_{y=b} = 0, \qquad (3.3.108b)$$

$$\begin{aligned}[\overline{\varepsilon}\sigma_{1W}]_{x=0} =& \frac{2b}{\Gamma \cdot |C'|^2} \int_{-(h'+h)}^{-h'} [\phi_0^* [\mathbf{n} \cdot \mathbf{q}_1]]_{x=0} dz \\ =& \frac{(1+i)}{2\sqrt{2\sigma_0}} \varepsilon b \Gamma^{-1} (\sinh 2h + 2h) \\ & \cdot \frac{(\sigma_0^2 \cosh h' - \sinh h')^2}{\sinh^2 h}, \qquad (3.3.108c)\end{aligned}$$

$$[\overline{\varepsilon}\sigma_{1W}]_{y=b} = 0. \qquad (3.3.108d)$$

On the channel bottom, we have:

$$[\mathbf{n}\cdot\mathbf{q}_1]_{S_B} = \frac{\varepsilon}{\bar{\varepsilon}}\int_{\infty}^{\xi}\frac{\partial U_{0B}}{\partial x}d\xi$$
$$= \frac{(1+i)}{\sqrt{2\sigma_0}}\frac{\varepsilon}{\bar{\varepsilon}}\left[\frac{\partial^2\phi_0}{\partial x^2}\right]_{z=-(h'+h)} e^{-\sqrt{\frac{\sigma_0}{2}}(1-i)\xi}. \qquad (3.3.109)$$

Hence:

$$\bar{\varepsilon}\sigma_{1B} = \frac{2b}{\Gamma\cdot|C'|^2}\int_0^{\ell}[\phi_0^*[\mathbf{n}\cdot\mathbf{q}_1]]_{z=-(h'+h)}\,dx$$
$$= -\frac{(1+i)}{\sqrt{2\sigma_0}}\varepsilon b\ell\Gamma^{-1}\frac{(\sigma_0^2\cosh h' - \sinh h')^2}{\sinh^2 h}. \qquad (3.3.110)$$

Returning to dimensional variables, the circular frequency σ_1 is written as:

$$\sigma_1 = 2\Big\{\left[\sigma_{1F_{MW}}\right]_{x=0} + \left[\sigma_{1W'}\right]_{x=0} + \left[\sigma_{1I'_{MW}}\right]_{x=0} + \left[\sigma_{1I_{MW}}\right]_{x=0}$$
$$+ \left[\sigma_{1W}\right]_{x=0}\Big\} + 2\Big\{\left[\sigma_{1F_{MW}}\right]_{y=b}\left[\sigma_{1I'_{MW}}\right]_{y=b} + \left[\sigma_{1I_{MW}}\right]_{y=b}\Big\}$$
$$+ \sigma_{1I'} + \sigma_{1I} + \sigma_{1S_B}. \qquad (3.3.111)$$

In (3.3.111), the first curly bracket represents that part of σ_1 due to the boundary layers adjacent to the wall at $x = 0$, the second curly bracket is due to the boundary layers adjacent to the wall at $b = 0$, and the factor of two accounts for the walls at $x = \ell$ and $y = -b$. The terms in (3.3.111) are given by:

$$\bar{\varepsilon}\sigma_{1I'} = (1+i)\Gamma^{-1}gk^2b\ell\left(\frac{\nu'}{2\sigma_0}\right)^{1/2}\left(1-\frac{\rho'}{\rho}\right)\left(\frac{\rho\nu^{1/2}}{\rho\nu^{1/2}+\rho'\nu'^{1/2}}\right)$$
$$\cdot\left(\coth kh - \frac{gk}{\sigma_0^2}\right)\left(\frac{\sigma_0^2}{gk}\sinh kh' - \cosh kh'\right)$$
$$\cdot\left(\frac{\sigma_0^2}{gk}\cosh kh' - \sinh kh'\right), \qquad (3.3.112a)$$

$$\bar{\varepsilon}\sigma_{1I} = (1+i)\Gamma^{-1}gk^2b\ell\left(\frac{\nu}{2\sigma_0}\right)^{1/2}\left(1-\frac{\rho'}{\rho}\right)\left(\frac{\rho\nu'^{1/2}}{\rho\nu^{1/2}+\rho'\nu'^{1/2}}\right)$$
$$\cdot\left(\coth kh - \frac{gk}{\sigma_0^2}\right)\left(\frac{\sigma_0^2}{gk}\cosh kh' - \sinh kh'\right)^2\coth kh, \qquad (3.3.112b)$$

$$\left[\overline{\varepsilon}\sigma_{1I'_{MW}}\right]_{x=0} = -2(1+i)\Gamma^{-1}gkb\left(\frac{\nu'}{2\sigma_0}\right)^{1/2}\left(\frac{\rho'}{\rho}\right)\left(\frac{\sigma_0^2}{gk}\sinh kh' - \cosh kh'\right) \cdot \left(\frac{\sigma_0^2}{gk}\cosh kh' - \sinh kh'\right), \tag{3.3.112c}$$

$$\left[\overline{\varepsilon}\sigma_{1I'_{MW}}\right]_{y=b} = -\frac{1}{2}(1+i)\Gamma^{-1}gk\ell\left(\frac{\nu'}{2\sigma_0}\right)^{1/2}\left(\frac{\rho'}{\rho}\right)\left(\frac{\sigma_0^2}{gk}\sinh kh' - \cosh kh'\right) \cdot \left(\frac{\sigma_0^2}{gk}\cosh kh' - \sinh kh'\right), \tag{3.3.112d}$$

$$\left[\overline{\varepsilon}\sigma_{1I_{MW}}\right]_{x=0} = -2(1+i)\Gamma^{-1}gkb\left(\frac{\nu}{2\sigma_0}\right)^{1/2}\left(\frac{\sigma_0^2}{gk}\cosh kh' - \sinh kh'\right)^2 \coth kh, \tag{3.3.112e}$$

$$\left[\overline{\varepsilon}\sigma_{1I_{MW}}\right]_{b=0} = -\frac{1}{2}(1+i)\Gamma^{-1}gk\ell\left(\frac{\nu}{2\sigma_0}\right)^{1/2}\left(\frac{\sigma_0^2}{gk}\cosh kh' - \sinh kh'\right)^2 \coth kh, \tag{3.3.112f}$$

$$\left[\overline{\varepsilon}\sigma_{1F_{MW}}\right]_{x=0} = -2(1+i)\Gamma^{-1}\sigma_0^2 b\left(\frac{\nu'}{2\sigma_0}\right)^{1/2}\left(\frac{\rho'}{\rho}\right), \tag{3.3.112g}$$

$$\left[\overline{\varepsilon}\sigma_{1F_{MW}}\right]_{b=0} = -\frac{1}{2}(1+i)\Gamma^{-1}\sigma_0^2\ell\left(\frac{\nu'}{2\sigma_0}\right)^{1/2}\left(\frac{\rho'}{\rho}\right), \tag{3.3.112h}$$

$$\left[\overline{\varepsilon}\sigma_{1W'}\right]_{x=0} = \frac{1}{2}(1+i)\Gamma^{-1}gkb\left(\frac{\nu'}{2\sigma_0}\right)^{1/2}\left(\frac{\rho'}{\rho}\right)\left\{(\sinh 2kh' + 2kh') + \frac{2\sigma_0^2}{gk}(1-\cosh 2kh') + \left(\frac{\sigma_0^2}{gk}\right)^2\left(\sinh 2kh' - 2kh'\right)\right\}, \tag{3.3.112i}$$

$$\left[\overline{\varepsilon}\sigma_{1W}\right]_{x=0} = \frac{1}{2}(1+i)\Gamma^{-1}gkb\left(\frac{\nu}{2\sigma_0}\right)^{1/2}\frac{(\sinh 2kh + 2kh)}{\sinh^2 kh} \cdot \left(\frac{\sigma_0^2}{gk}\cosh kh' - \sinh kh'\right)^2, \tag{3.3.112j}$$

$$\overline{\varepsilon}\sigma_{1B} = -(1+i)\Gamma^{-1}gk^2b\ell\left(\frac{\nu}{2\sigma_0}\right)^{1/2}\frac{1}{\sinh^2 kh} \cdot \left(\frac{\sigma_0^2}{gk}\cosh kh' - \sinh kh'\right)^2 \tag{3.3.112k}$$

where

$$\Gamma = 2\sigma_0 b\ell\left\{\frac{\rho'}{\rho} + \left(1 - \frac{\rho'}{\rho}\right)\left(\cosh kh' - \frac{gk}{\sigma_0^2}\sinh kh'\right)^2\right\}. \tag{3.3.113}$$

If both fluids have the same density and viscosity (i.e., $\rho' = \rho$, $\nu' = \nu$), equations

(3.3.112a)–(3.3.112k) reduce to:

$$\overline{\varepsilon}\sigma_{1I'} = 0, \tag{3.3.114a}$$

$$\overline{\varepsilon}\sigma_{1I} = 0, \tag{3.3.114b}$$

$$\left[\overline{\varepsilon}\sigma_{1I'_{MW}}\right]_{x=0} = (1+i)\frac{\sigma_0}{\ell}\left(\frac{\nu}{2\sigma_0}\right)^{1/2}\left(\frac{\sinh 2kh}{\sinh 2k(h'+h)}\right), \tag{3.3.114c}$$

$$\left[\overline{\varepsilon}\sigma_{1I'_{MW}}\right]_{y=b} = \frac{1}{4}(1+i)\frac{\sigma_0}{b}\left(\frac{\nu}{2\sigma_0}\right)^{1/2}\left(\frac{\sinh 2kh}{\sinh 2k(h'+h)}\right), \tag{3.3.114d}$$

$$\left[\overline{\varepsilon}\sigma_{1I_{MW}}\right]_{x=0} = -(1+i)\frac{\sigma_0}{\ell}\left(\frac{\nu}{2\sigma_0}\right)^{1/2}\left(\frac{\sinh 2kh}{\sinh 2k(h'+h)}\right), \tag{3.3.114e}$$

$$\left[\overline{\varepsilon}\sigma_{1I_{MW}}\right]_{b=0} = -\frac{1}{4}(1+i)\frac{\sigma_0}{b}\left(\frac{\nu}{2\sigma_0}\right)^{1/2}\left(\frac{\sinh 2kh}{\sinh 2k(h'+h)}\right), \tag{3.3.114f}$$

$$\left[\overline{\varepsilon}\sigma_{1F_{MW}}\right]_{x=0} = -(1+i)\frac{\sigma_0}{\ell}\left(\frac{\nu}{2\sigma_0}\right)^{1/2}, \tag{3.3.114g}$$

$$\left[\overline{\varepsilon}\sigma_{1F_{MW}}\right]_{b=0} = -\frac{1}{4}(1+i)\frac{\sigma_0}{b}\left(\frac{\nu}{2\sigma_0}\right)^{1/2}, \tag{3.3.114h}$$

$$\left[\overline{\varepsilon}\sigma_{1W'}\right]_{x=0} = \frac{1}{2}(1+i)\frac{\sigma_0}{\ell}\left(\frac{\nu}{2\sigma_0}\right)^{1/2}\left(1-\frac{\sinh 2kh - 2kh'}{\sinh 2k(h'+h)}\right), \tag{3.3.114i}$$

$$\left[\overline{\varepsilon}\sigma_{1W}\right]_{x=0} = \frac{1}{2}(1+i)\frac{\sigma_0}{\ell}\left(\frac{\nu}{2\sigma_0}\right)^{1/2}\left(\frac{\sinh 2kh + 2kh}{\sinh 2k(h'+h)}\right), \tag{3.3.114j}$$

$$\overline{\varepsilon}\sigma_{1B} = -(1+i)k\sigma_0\left(\frac{\nu}{2\sigma_0}\right)^{1/2}\left(\frac{1}{\sinh 2k(h'+h)}\right). \tag{3.3.114k}$$

From (3.3.111) and (3.3.114), the total damping rates due to the wall at $x = 0$, and the wall at $y = b$, are given by:

$$\sum\left[\overline{\varepsilon}\sigma_1\right]_{x=0} = -\frac{1}{2}(1+i)\frac{\sigma_0}{\ell}\left(\frac{\nu}{2\sigma_0}\right)^{1/2}\left(1-\frac{2k(h'+h)}{\sinh 2k(h'+h)}\right), \tag{3.3.115a}$$

$$\sum\left[\overline{\varepsilon}\sigma_1\right]_{y=b} = -\frac{1}{4}(1+i)\frac{\sigma_0}{b}\left(\frac{\nu}{2\sigma_0}\right)^{1/2}. \tag{3.3.115b}$$

On the bottom $z = -(h'+h)$, the damping rate is given by (3.3.114k). The imaginary parts of these damping rates agree with the attenuation rates found by Keulegan (1959).

In this section we have found the damping rates for standing waves in a rectangular basin that is partially filled with a two-layer fluid. The real part of the

damping rate represents a frequency shift due to viscous effect and the imaginary part of the damping rate is the attenuation rate responsible for the decay of wave amplitude. The decay of standing internal waves in a rectangular basin is studied in §5.2.5 using the results of experiments and the linear theory. In experimental investigation of wave damping the dimensionless parameter known as the modulus of decay is frequently used. Keulegan (1959) defined the modulus of decay α^* as:

$$\alpha^* = \frac{T}{2t}\int_0^t \frac{\gamma}{E}dt \tag{3.3.116}$$

wherein T is the wave period; γ and E are the rate of energy loss and the energy density of the wave, respectively, both averaged over one wave period. We have:

$$\frac{dE}{E} = -\frac{\gamma t}{E}. \tag{3.3.117}$$

Integrating (3.3.117) and applying (3.3.116), we obtain:

$$\frac{E}{E_0} = e^{-2\alpha^*\frac{t}{T}} \tag{3.3.118}$$

in which E_0 is the wave energy at $t = 0$. It can be shown that, in linear theory, γ/E is independent of the wave amplitude, and hence independent of t. Then equation (3.3.116) is reduced to:

$$\alpha^* = \frac{1}{2}\frac{\gamma T}{E}. \tag{3.3.119}$$

Thus, for small amplitude waves, the modulus of decay equals half the ratio of the energy dissipated during a completed wave cycle to the energy of the wave during that cycle. In addition, E is proportional to the square of the wave amplitude a, hence, we have:

$$a = a_0 e^{-\alpha^*\frac{t}{T}} \tag{3.3.120}$$

where a_0 is the wave amplitude at $t = 0$. Thus, the modulus of decay is related to the damping rate by:

$$\alpha^* = -\Im[\overline{\varepsilon}\sigma_1]T \tag{3.3.121}$$

in which $\Im$ denotes the imaginary part of a complex number.

3.3.2 Wave Damping in a Three-Layer Fluid

In § 3.3.1, the damping rates in a two-layer fluid were found by perturbation expansions and the application of Green's theorem. As we have seen, this approach yields both the attenuation rate and the viscous correction to the wave number or the circular frequency obtained using the inviscid theory. In addition, it is possible to infer from the damping rates the flow of energy in various parts of the fluid. Most importantly, the analysis provides a formal expansion scheme in which energy dissipation in the boundary layers can be incorporated into an inviscid model. A similar technique had been used by Dore (1969 a,b) to determine the damping rates of non-homogeneous viscous fluids of general density and viscosity distributions. Because the velocity potential does not exist in a continuously stratified fluid, Dore (1969 a,b) instead expanded the dynamic pressure in terms of a boundary layer parameter. The damping rates were found by separating the terms of different orders and by the application of Green's theorem in a manner similar to the two-layer problem. The same method can be applied here to the three-layer fluid, but the algebra involved will be very lengthy. Moreover, the analysis of the two-fluid system and the studies by Dore (1969 a,b) on continuously stratified fluids indicate that the real parts and the imaginary parts of the complex damping rates are equal in magnitude. Hence, instead of following the approach in § 3.3.1 we simply find the attenuation rate, and assume that the shift in wave number is the same.

The conventional method in finding the attenuation rate is by balancing the rate of decay of wave energy by the rate of energy dissipation. For the propagation of time-periodic surface waves in a long channel, the attenuation rate had been found by Hunt (1952) and Ursell (1952). We apply this method here to the three-layer fluid. Let (x, y, z) be a Cartesian coordinate system with the x axis on the undisturbed free surface coinciding with the channel axis and z extending positive upwards. The side walls of the rectangular channel are located at $y = b$ and $y = -b$.

The continuously stratified fluid is composed of two homogeneous fluids of different densities separated by a transition layer with a linear density variation. The upper fluid is of density ρ_1 and of depth h_1, between $z = -h_1$ and $z = -(h_1 + \delta)$ the density of the fluid increases linearly from ρ_1 to ρ_2. The depth of the lower fluid is h_2 and the bottom of the channel is at $z = -(h_1 + h_2 + \delta)$. The density of the fluid is approximated by ρ_1 when the buoyancy term is not involved; this is consistent with the Boussinesq approximation made in the three-layer model. The kinematic viscosity of the fluid ν is assumed to be constant. The wave motion is assumed to be two-dimensional in the (x, z) plane, and other assumptions stated in § 3.2 also apply here. For time-periodic plane progressive waves travelling in the positive x direction, the vertical velocity, the horizontal velocity, the dynamic pressure, and the vertical displacement of a fluid element from its undisturbed position are given by (3.2.11), (3.2.20), (3.2.21), and (3.2.72), respectively. For convenience we quote these equations as follows:

$$\eta_0(x,z,t) = \frac{i}{\sigma} f(z) A e^{i(Kx-\sigma t)}, \tag{3.3.122}$$

$$u_0(x,z,t) = \frac{i}{K}\frac{df}{dz} A e^{i(Kx-\sigma t)}, \tag{3.3.123}$$

$$w_0(x,z,t) = f(z) A e^{i(Kx-\sigma t)}, \tag{3.3.124}$$

$$p_0(x,z,t) = i\rho_1 \frac{\sigma}{K^2}\frac{df}{dz} A e^{i(Kx-\sigma t)} \tag{3.3.125}$$

where the subscript 0 denotes the inviscid solution. We may use the normalized eigenfunctions in (3.2.50) for $f(z)$. The orthogonality conditions (3.2.51) are not needed in this analysis, it is simpler to use an arbitrary constant A as the coefficient instead. From (3.2.50a)–(3.2.50c), we have:

$$\begin{aligned} f(z) = &\left(\Theta^{1/2}\cos\left(\Theta^{1/2}K\delta\right) + \coth Kh_2 \sin\left(\Theta^{1/2}K\delta\right)\right) \\ &\cdot \left(\frac{K_0\cosh Kz + K\sinh Kz}{K_0\cosh Kh_1 - K\sinh Kh_1}\right), \qquad -h_1 < z < 0, \qquad (3.3.126a) \\ =&\Theta^{1/2}\cos\left(\Theta^{1/2}K(z+h_1+\delta)\right) + \coth Kh_2 \sin\left(\Theta^{1/2}K(z+h_1+\delta)\right), \end{aligned}$$

$$-(h_1+\delta) < z < -h_1, \tag{3.3.126b}$$

$$= \Theta^{1/2}\left(\frac{\sinh K(z+h_1+h_2+\delta)}{\sinh Kh_2}\right), \qquad -(h_1+h_2+\delta) < z < -(h_1+\delta). \tag{3.3.126c}$$

All the symbols in (3.3.126) have been defined in § 3.2, and for simplicity we have dropped the subscripts (1 and 2) for the wave number K.

In the bottom boundary layer, the horizontal velocity u_B is given by the sum of the inviscid part u_0 and the viscous correction U_B, that is:

$$u_B = [u_0]_{z=-(h_1+h_2+\delta)} + U_B \tag{3.3.127}$$

where

$$U_B = -[u_0]_{z=-(h_1+h_2+\delta)} e^{-\sqrt{\frac{\sigma}{2\nu}}(1-i)(z+h_1+h_2+\delta)}, \tag{3.3.128}$$

and the subscript B denotes the bottom. Denote the rectangular coordinates by x_i, $(i = 1,2,3)$, with $x_1 = x$, $x_2 = y$, $x_3 = z$ and the corresponding velocity components by u_i. The rate of dissipation of mechanical energy per unit time in an incompressible fluid is given by:

$$\frac{dE}{dt} = \frac{1}{2\mu}\int_V \tau_{ij}^2 dV \tag{3.3.129}$$

where τ_{ij} are the components of the viscous stress tensor given by:

$$\tau_{ij} = \mu\left(\frac{\partial u_i}{\partial x_j} + \frac{\partial u_j}{\partial x_i}\right). \tag{3.3.130}$$

The average rate of energy dissipation over one wave period is given by:

$$\overline{\frac{dE}{dt}} = \frac{\mu}{4}\int_V \left|\frac{\partial u_i}{\partial x_j} + \frac{\partial u_j}{\partial x_i}\right|^2 dV. \tag{3.3.131}$$

In (3.3.129) and (3.3.131) summation over repeated indices is implied. The principal contribution to the integral in the bottom boundary layer in the region between x and $x + dx$ is:

$$\left[\overline{\frac{dE}{dt}}\right]_B = \frac{\mu}{2}\int_V \left|\frac{\partial u_1}{\partial x_3}\right|^2 dV$$

$$= \frac{\mu}{2}(2bdx)\int_{-(h_1+h_2+\delta)}^{\infty}\left|\frac{\partial U_B}{\partial z}\right|^2 dz.$$

$$= \sqrt{\frac{\nu}{2\sigma}}\frac{\rho_1\sigma bdx}{K^2}\left|\frac{df}{dz}\right|^2_{z=-(h_1+h_2+\delta)}\cdot|A|^2. \qquad (3.3.132)$$

By symmetry, we only need to consider the boundary layer adjacent to the side wall $y = b$. The horizontal velocity and the vertical velocity are given by:

$$u_W = [u_0]_{y=b} + U_W, \qquad (3.3.133a)$$

$$w_W = [w_0]_{y=b} + W_W \qquad (3.3.133b)$$

where

$$U_W = -[u_0]_{y=b}e^{-\sqrt{\frac{\sigma}{2\nu}}(1-i)(b-y)}, \qquad (3.3.134a)$$

$$W_W = -[w_0]_{y=b}e^{-\sqrt{\frac{\sigma}{2\nu}}(1-i)(b-y)}. \qquad (3.3.134b)$$

In (3.3.133) and (3.3.134) the subscript W denotes the side wall. The net contribution to the integral in (3.3.131) from the side-wall boundary layers at $y = b$ and $y = -b$ is given by:

$$\left[\overline{\frac{dE}{dt}}\right]_W = \frac{\mu}{2}\int_V\left(\left|\frac{\partial u_1}{\partial x_2}\right|^2 + \left|\frac{\partial u_3}{\partial x_2}\right|^2\right)dV$$

$$= -\frac{\mu}{2}(2dx)\int_{-(h_1+h_2+\delta)}^{0}\int_{-\infty}^{b}\left(\left|\frac{\partial U_W}{\partial y}\right|^2 + \left|\frac{\partial W_W}{\partial y}\right|^2\right)dydz$$

$$= \sqrt{\frac{\nu}{2\sigma}}\frac{\rho_1\sigma dx}{K}\int_{-(h_1+h_2+\delta)}^{0}\left(\frac{1}{K}\left|\frac{df}{dz}\right|^2 + K|f|^2\right)dz\cdot|A|^2. \qquad (3.3.135)$$

Equations (3.3.132) and (3.3.135) include all the energy losses that are proportional to $\nu^{1/2}$. It can be deduced from (3.3.129) that energy dissipation in the density transition region $(-h_1+\delta < z < -h_1)$ is proportional to ν, and therefore is neglected at the present order of approximation. The average rate at which work is done over one wave period across a section of the rectangular channel is:

$$\overline{\frac{dW}{dt}} = \frac{2b}{T}\int_t^{t+T}\int_{-(h_1+h_2+\delta)}^{0} p_0u_0dz$$

$$= \frac{\rho_1 \sigma b}{K^2} \int_{-(h_1+h_2+\delta)}^{0} \frac{1}{K} \left|\frac{df}{dz}\right|^2 dz \cdot |A|^2. \tag{3.3.136}$$

The integrals in (3.3.135) and (3.3.136) can be evaluated in terms of trigonometric and hyperbolic functions. For $\Theta > 0$, the results are:

$$\begin{aligned} 4 \int_{-(h_1+h_2+\delta)}^{0} \frac{1}{K} \left|\frac{df}{dz}\right|^2 dz = &\left(\frac{\Theta^{1/2} \cos\left(\Theta^{1/2} K\delta\right) + \coth Kh_2 \sin\left(\Theta^{1/2} K\delta\right)}{K_0 \cosh Kh_1 - K \sinh Kh_1} \right)^2 \\ &\cdot \Big\{ K_0^2 (\sinh 2Kh_1 - 2Kh_1) + K^2 (\sinh 2Kh_1 + 2Kh_1) \\ &+ 2K_0 K (1 - \cosh 2Kh_1) \Big\} \\ &+ \Theta^2 \left(2K\delta - \Theta^{-1/2} \sin\left(2\Theta^{1/2} K\delta\right) \right) \\ &+ \Theta \coth^2 Kh_2 \left(2K\delta + \Theta^{-1/2} \sin\left(2\Theta^{1/2} K\delta\right) \right) \\ &+ 2\Theta \coth Kh_2 \left(\cos\left(2\Theta^{1/2} K\delta\right) - 1 \right) \\ &+ \Theta \left(\frac{\sinh 2Kh_2 + 2Kh_2}{\sinh^2 Kh_2} \right), \end{aligned} \tag{3.3.137a}$$

$$\begin{aligned} 4 \int_{-(h_1+h_2+\delta)}^{0} K|f|^2 dz = &\left(\frac{\Theta^{1/2} \cos\left(\Theta^{1/2} K\delta\right) + \coth Kh_2 \sin\left(\Theta^{1/2} K\delta\right)}{K_0 \cosh Kh_1 - K \sinh Kh_1} \right)^2 \\ &\cdot \Big\{ K_0^2 (\sinh 2Kh_1 + 2Kh_1) + K^2 (\sinh 2Kh_1 - 2Kh_1) \\ &+ 2K_0 K (1 - \cosh 2Kh_1) \Big\} \\ &+ \Theta \left(2K\delta + \Theta^{-1/2} \sin\left(2\Theta^{1/2} K\delta\right) \right) \\ &+ \coth^2 Kh_2 \left(2K\delta - \Theta^{-1/2} \sin\left(2\Theta^{1/2} K\delta\right) \right) \\ &- 2 \coth Kh_2 \left(\cos\left(2\Theta^{1/2} K\delta\right) - 1 \right) \\ &+ \Theta \left(\frac{\sinh 2Kh_2 - 2Kh_2}{\sinh^2 Kh_2} \right). \end{aligned} \tag{3.3.137b}$$

The difference between the energy crossing the planes x and $x + dx$ is equal to the energy dissipated in the region between x and $x + dx$. From (3.3.132), (3.3.135), and (3.3.136), we have:

$$-\frac{b}{K} \int_{-(h_1+h_2+\delta)}^{0} \frac{1}{K} \left|\frac{df}{dz}\right|^2 dz \cdot d|A|^2$$

$$=\sqrt{\frac{\nu}{2\sigma}}\left\{\frac{b}{K}\left|\frac{df}{dz}\right|^2_{z=-(h_1+h_2+\delta)}+\int_{-(h_1+h_2+\delta)}^{0}\left(\frac{1}{K}\left|\frac{df}{dz}\right|^2+K|f|^2\right)dz\right\}\cdot|A|^2dx. \tag{3.2.138}$$

Now let us find the attenuation rate designated by K^*. With energy dissipation, equations (3.3.122)–(3.3.124) still apply if the coefficient A is written as:

$$A = A_0 e^{-K^* x} \tag{3.3.139}$$

where A_0 is a constant. Note that we have neglected the viscous correction to the wave number K; the method of energy balance cannot provide information on the shift in the wave number. The attenuation rate is obtained immediately through differentiation of (3.3.139). Hence, we have:

$$K^* = -\frac{1}{A}\frac{dA}{dx}. \tag{3.3.140}$$

Without loss of generality, A_0 may be taken as real, and hence A is real. From (3.3.138) and (3.3.140) the attenuation rate K^* is given by:

$$K^* = \frac{1}{2}\frac{\sqrt{\frac{\nu}{2\sigma}}\left\{\frac{b}{K}\left|\frac{df}{dz}\right|^2_{z=-(h_1+h_2+\delta)}+\int_{-(h_1+h_2+\delta)}^{0}\left(\frac{1}{K}\left|\frac{df}{dz}\right|^2+K|f|^2\right)dz\right\}}{\frac{b}{K}\int_{-(h_1+h_2+\delta)}^{0}\frac{1}{K}\left|\frac{df}{dz}\right|^2 dz}. \tag{3.3.141}$$

In (3.3.141), we have:

$$\left|\frac{df}{dz}\right|^2_{z=-(h_1+h_2+\delta)} = \frac{K^2\Theta}{\sinh^2 Kh_2} \tag{3.3.142}$$

by direct substitution from (3.3.126b). As discussed earlier, we may assume that the viscous correction to the wave number is equal in magnitude to the attenuation rate, hence the damping rate in the three-layer fluid is given by $(1+i)K^*$ (see equation 3.3.45c).

The concept of energy balance provides a simple method for determining the attenuation rate, but the amount of information obtained is very limited. A major

disadvantage of this method is its lack of a formal expansion scheme by which the effect of viscosity on the inviscid solution can be assessed order by order in terms of a boundary layer parameter. For instance, in obtaining (3.3.136) we have implicitly assumed that the wave energy is transferred along the channel by the irrotational component of the velocity.

In this section we have obtained the attenuation rate for a time-periodic progressive wave advancing down a uniform rectangular channel that is partially filled with a three-layer fluid. We assume that the entire loss of energy of waves is localized in the boundary layers adjacent to the side walls and at the bottom of the channel, and the flow is laminar within the boundary layers. The attenuation rate is obtained by balancing energy dissipation and energy flux in a contol segment of the rectangular channel. Because the method of energy balance does not yield the viscous correction to the wave number, we assume that this is the same as the attenuation rate. The above results are used in § 3.3.3 to incorporate the effects of wave damping into the inviscid three-layer model developed in § 3.2.

3.3.3 Trench Models with Boundary Layer Damping

For the two-layer problem, the fluid velocity **u** in the constant-depth channel and in the trench region can be written as a sum of an irrotational part, and a rotational part, as given in (3.3.21). If the boundary layers are very thin compared to a characteristic depth of the fluid, the potential function Φ, and the rotational part of the velocity **U**, can be expanded in terms of a boundary layer parameter, $\overline{\varepsilon}$, in the form given by (3.3.45*a*) and (3.3.45*b*), respectively. The horizontal velocities and the vertical velocities from the separate regions of constant depths must be continuous at the upstream edge of the trench, in addition to satisfying the boundary conditions of the constant-depth channel and trench arrangement as shown in figure 3.1.1. By equating coefficients of like power of $\overline{\varepsilon}$, a series of problems are defined. The solutions

at the lowest order are used to yield the next higher order of approximation, and so on. Hence, the perturbation procedure provides a plausible scheme by which the effect of viscosity can be incorporated into the solution. In practice, finding a solution to higher order than $O(\overline{\varepsilon})$ will be difficult. On the other hand, the inviscid model treated in § 3.1, which neglects the effect of viscosity completely, is clearly inadequate. In particular, the cumulative effect of viscosity on wave attenuation cannot be neglected, no matter how small viscosity is. Consider the wave machine generating surface waves continuously at the resonant frequency of the internal waves in the trench. If the viscosity of the fluids is very small, the surface waves and the internal waves will grow to large amplitudes, until the rate of energy input by the wave machine is balanced by the rate of energy dissipation in the fluids. It may take a long time before this steady-state condition is reached in the wave tank, but this final stage will be attained eventually. Hence, the cumulative effect of viscosity on wave attenuation is of first order importance over a period of time long compared to the wave period. It is seen in (3.3.45) that the rotational part of the velocity, $\mathbf{U}$, is comparable to the irrotational part of the velocity, $\nabla\Phi$, only in the boundary layer, which has a thickness of $O(\overline{\varepsilon})$. Thus, locally, the overall fluid motion can be described well by the lowest order velocity potential ϕ_0. On the other hand, the complex damping rate, given by the term $\overline{\varepsilon}k_1$, appears with the distance of propagation x as a product in the exponent of e. The effect of this term is to decrease the wave amplitude with distance, and hence with time. Because of this, k_1 must be included in the solution. Strictly speaking, the attenuation rate is given by the imaginary part of $\overline{\varepsilon}k_1$, the real part contributes only a small shift of $O(\overline{\varepsilon})$ in the wave number, and thus should be ignored in order to be consistent with the present order of approximation. However, it is often observed in experiments that viscous damping shifts the resonant peaks of the amplitude-frequency response curve slightly away from the inviscid natural frequencies. Hence, for a better prediction

of the location of the response curve, it is preferable to include the real part of $\overline{\varepsilon}k_1$. A similar argument can be applied to the three-layer fluid.

Boundary layer dissipation are incorporated into the inviscid models that were treated in § 3.1 and § 3.2 as follow: the wave numbers for the propagating waves in the exponents of the series representations in (3.1.20) and (3.1.22) for the two-layer problem, and in (3.2.53) and (3.2.54) for the three-layer problem, are expanded to $O(\overline{\varepsilon})$. Then the horizontal and vertical velocities in the constant-depth channel, and in the trench region, are matched at the upstream edge of the trench as before, to obtain the unknown coefficients in the eigenfunction expansions. Thus, all the equations in § 3.1 and § 3.2 are unchanged, except that the previous real wave number for the propagating wave in the exponent of e is replaced by the corresponding complex wave number, which includes both the attenuation rate and the shift in wave number to $O(\overline{\varepsilon})$. As we have seen, this modification is justified by the perturbation analysis.

3.4 A Two-Layer Model of a Rectangular Trench in an Infinite Region

In § 3.1 an analytical treatment is presented for the steady-state response of a two-layer density-stratified fluid in a rectangular trench that is placed at one end of a constant-depth channel; wave motion is generated by a vertical bulkhead wave generator which moves in simple-harmonic motion at the other end of the channel (figure 3.1.1). This particular arrangement was chosen for theoretical analysis because the conditions of wave propagation over a rectangular trench in an infinite region could not be modelled in the laboratory, due to wave reflections from the ends of the wave tank. With the arrangement shown in figure 3.1.1, the theoretical predictions that are obtained using the two-layer model treated in § 3.1 can be compared directly to the experimental measurements to establish the possibility

of using the same theoretical approach for the case with the infinite region; these results will be discussed in Chapter 5. In this section, the potential formulation presented in § 3.1 is employed to treat the problem of normally incident surface waves propagating over a rectangular trench in an infinite region, with a heavier fluid in the trench (figure 3.4.1). Let (x, z) be a Cartesian coordinate system with z extending positive upwards from the undisturbed free surface. We fix the origin of the x coordinate above one edge of the trench as shown in figure 3.4.1. The fluid in the trench is two-layer stratified, and the fluid outside the trench is homogeneous. The fluid domain is divided into four regions:

Region 1	$\rho = \rho_1,$	$-h_1 < z < 0,$	$0 < x < \ell$
Region 2	$\rho = \rho_2,$	$-(h_1 + h_2) < z < -h_1,$	$0 < x < \ell$
Region 3	$\rho = \rho_1,$	$-h < z < 0,$	$-\infty < x < 0$
Region 4	$\rho = \rho_1,$	$-h < z < 0,$	$0 < x < +\infty$

wherein ρ_1 and ρ_2 are the densities of the upper fluid and of the lower fluid, respectively, and the other symbols are defined in figure 3.4.1.

3.4.1 The Boundary-Value Problem

The basic assumptions and the method of analysis are the same as given in § 3.1 for the treatment of the laboratory problem. Assuming a steady-state solution for the velocity potential in the form:

$$\Phi(x, z, t) = \phi(x, z)e^{-i\sigma t}, \tag{3.4.1}$$

the spatial potential function $\phi(x, z)$ must satisfy the Laplace equation:

$$\frac{\partial^2 \phi}{\partial x^2} + \frac{\partial^2 \phi}{\partial z^2} = 0 \tag{3.4.2}$$

throughout the fluid domain along with the following linearized boundary conditions:

$$\frac{\partial \phi}{\partial z} - \frac{\sigma^2}{g}\phi = 0 \qquad \text{on} \qquad z = 0, \quad -\infty < x < +\infty, \tag{3.4.3a}$$

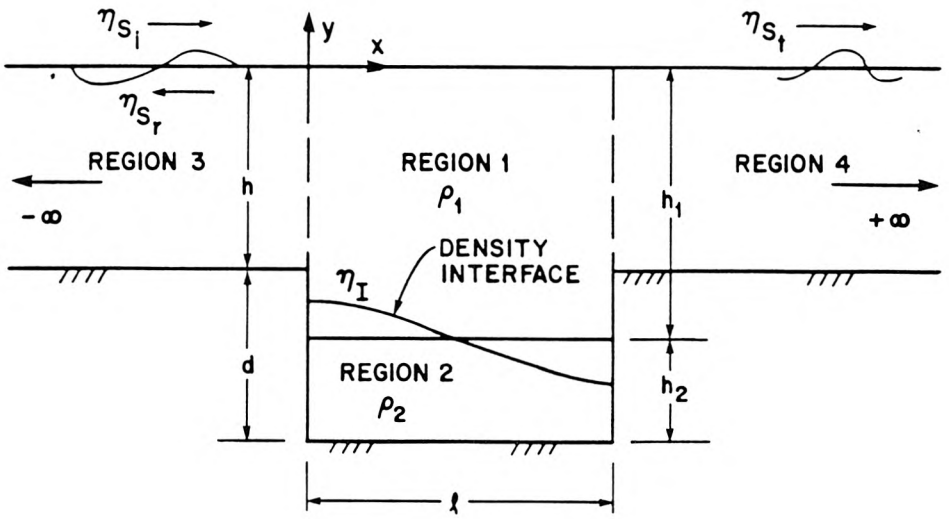

Figure 3.4.1. Definition sketch of a two-layer density-stratified rectangular trench in an infinite region.

$$\rho_1\left(\frac{\partial\phi_1}{\partial z}-\frac{\sigma^2}{g}\phi_1\right)=\rho_2\left(\frac{\partial\phi_2}{\partial z}-\frac{\sigma^2}{g}\phi_2\right) \qquad \text{on} \qquad z=-h_1, \quad 0<x<\ell, \tag{3.4.3b}$$

$$\frac{\partial\phi_1}{\partial z}=\frac{\partial\phi_2}{\partial z} \qquad \text{on} \qquad z=-h_1, \quad 0<x<\ell, \tag{3.4.3c}$$

$$\frac{\partial\phi}{\partial z}=0, \qquad \text{on} \qquad z=-(h_1+h_2), \quad 0<x<\ell$$

$$\text{and} \qquad z=-h, \quad -\infty<x<0 \quad \text{and} \quad \ell<x<+\infty, \tag{3.4.3d}$$

$$\frac{\partial\phi}{\partial x}=0, \qquad \text{on} \qquad -(h_1+h_2)<z<-h, \quad x=0 \quad \text{and} \quad x=\ell. \tag{3.4.3e}$$

The matching conditions at $x=0$ and $x=\ell$ are:

$$\phi_1=\phi_3 \qquad \text{on} \qquad -h<z<0, \quad x=0, \tag{3.4.4a}$$

$$\phi_1=\phi_4 \qquad \text{on} \qquad -h<z<0, \quad x=\ell, \tag{3.4.4b}$$

$$\frac{\partial \phi_1}{\partial x} = \frac{\partial \phi_3}{\partial x} \qquad \text{on} \qquad -h < z < 0, \quad x = 0, \tag{3.4.4c}$$

$$\frac{\partial \phi_1}{\partial x} = \frac{\partial \phi_4}{\partial x} \qquad \text{on} \qquad -h < z < 0, \quad x = \ell. \tag{3.4.4d}$$

In (3.4.3) and (3.4.4), the subscripts (1, 2, 3, and 4), respectively, denote the appropriate regions shown in figure 3.4.1. A time-periodic progressive wave train of wave amplitude a_{S_i} is assumed to be incident from $x = -\infty$ in region 3, in a direction perpendicular to the longitudinal axis of the trench. The free surface elevation of the incident wave is written as:

$$\eta_{S_i} = a_{S_i} e^{i(kx - \sigma t)}. \tag{3.4.5}$$

The velocity potential of the incident wave is given by linear theory (see, for example, Dean and Dalrymple, 1984) to be:

$$\Phi_{S_i}(x, z, t) = -\frac{i a_{S_i} g}{\sigma} \frac{\cosh k(z + h)}{\cosh kh} e^{i(kx - \sigma t)}. \tag{3.4.6}$$

The radiation conditions at $x = \pm\infty$ require that the scattered waves (the transmitted and the reflected waves) are asymptotically simple-harmonic wave trains travelling away from the trench region.

3.4.2 The Solutions in the Trench Region and in the Infinite Region

As in § 3.1 we expand the spatial potential function ϕ in terms of an infinite series of mutually orthogonal eigenfunctions. In the trench region $0 < x < \ell$, we have:

$$\begin{aligned} \phi_{1,2}(x, z) = & \sum_{j=1,2} \left(A_j e^{iK_j x} + B_j e^{-iK_j x} \right) Z_{j1,2}(z) \\ & + \sum_{n} \left(\hat{A}_n e^{\hat{K}_n x} + \hat{B}_n e^{-\hat{K}_n x} \right) \hat{Z}_{n1,2}(z) \end{aligned} \tag{3.4.7}$$

in which A_j, B_j, $(j = 1, 2)$, and $\hat{A}_n$, $\hat{B}_n$, $(n = 1, 2, \ldots)$ are unknown constants to be determined from the boundary and matching conditions at the trench. The wave

numbers K_j, $(j = 1, 2)$ and $\hat{K}_n$, $(n = 1, 2, \ldots)$, and the functions $Z_{j1,2}$, $(j = 1, 2)$ and $\hat{Z}_{n1,2}$, $(n = 1, 2, \ldots)$, respectively, are given by (3.1.18) and (3.1.19) for a two-layer fluid.

In the infinite regions $x < 0$ and $x > \ell$, the spatial potential functions in the homogeneous fluid are written as:

$$\phi_3(x, z) = \left(Ce^{ikx} + De^{-ikx}\right) Z(z) + \sum_n \hat{D}_n e^{\hat{k}_n x} \hat{Z}_n(z), \qquad (3.4.8a)$$

$$\phi_4(x, z) = Ee^{ik(x-\ell)} Z(z) + \sum_n \hat{E}_n e^{-\hat{k}_n(x-\ell)} \hat{Z}_n(z) \qquad (3.4.8b)$$

wherein we have used the radiation conditions at $x = \pm\infty$, and the assumption that the incident waves only come from $x = -\infty$. The unknown constants C, D, E, and $\hat{D}_n$, $\hat{E}_n$, $(n = 1, 2, \ldots)$ are to be determined from the incident wave condition at $x = -\infty$ and the matching conditions at the trench. The wave numbers k and $\hat{k}_n$, $(n = 1, 2, \ldots)$, and the functions Z and $\hat{Z}_n$, $(n = 1, 2, \ldots)$, respectively, are given by (3.1.25) and (3.1.23) for a homogeneous fluid.

3.4.3 Matching the Solutions

As in § 3.1 the infinite series of the spatial potential functions given by (3.4.7), (3.4.8*a*), and (3.4.8*b*) are truncated after a finite number of terms N. We are then left with $4N + 7$ unknowns: A_j, B_j, $(j = 1, 2)$, C, D, E, and $\hat{A}_n$, $\hat{B}_n$, $\hat{D}_n$, $\hat{F}_n$, $(n = 1, 2, \ldots, N)$. Note that in (3.4.8*a*), the unknown constant C is the complex coefficient of the velocity potential of the incident wave, hence from (3.4.6) and (3.4.8*a*), C is found to be:

$$C = -\frac{ia_{S_i} g}{\sigma(\Lambda^h)^{-1/2}} \frac{1}{\cosh kh} \qquad (3.4.9)$$

wherein we have used (3.1.23*a*). The remaining $(4N + 6)$ unknowns are found from the conditions of continuity of horizontal velocity and velocity potential at $x = 0$ and $x = \ell$ (equation 3.4.4). In the same manner as the treatment in § 3.1 the

horizontal velocities and velocity potentials from the trench region and the infinite regions before and after the trench are matched along vertical boundaries at $x = 0$ and $x = \ell$. Upon invoking the orthogonality conditions (3.1.16) and (3.1.24), we obtain $(4N + 6)$ linear integral equations, which are given as follows:

Continuity of $\partial\phi/\partial x$ at $x = 0$:

$$iK_j(A_j - B_j) = \rho_1 \int_{-h}^{0} \frac{\partial \tilde{\phi}_3}{\partial x}(0, z) Z_{j1}(z) dz, \qquad (j = 1, 2), \tag{3.4.10a}$$

$$\hat{K}_n(\hat{A}_n - \hat{B}_n) = \rho_1 \int_{-h}^{0} \frac{\partial \tilde{\phi}_3}{\partial x}(0, z) \hat{Z}_{n1}(z) dz, \qquad (n = 1, 2, \ldots, N). \tag{3.4.10b}$$

Continuity of $\partial\phi/\partial x$ at $x = \ell$:

$$iK_j \left(A_j e^{iK_j \ell} - B_j e^{-iK_j \ell}\right) = \rho_1 \int_{-h}^{0} \frac{\partial \tilde{\phi}_4}{\partial x}(\ell, z) Z_{j1}(z) dz, \qquad (j = 1, 2), \tag{3.4.11a}$$

$$\hat{K}_n \left(\hat{A}_n e^{\hat{K}_n \ell} - \hat{B}_n e^{-\hat{K}_n \ell}\right) = \rho_1 \int_{-h}^{0} \frac{\partial \tilde{\phi}_4}{\partial x}(\ell, z) \hat{Z}_{n1}(z) dz, \qquad (n = 1, 2, \ldots, N). \tag{3.4.11b}$$

Continuity of ϕ at $x = 0$:

$$C + D = \rho_1 \int_{-h}^{0} \tilde{\phi}_1(0, z) Z(z) dz, \tag{3.4.12a}$$

$$\hat{D}_n = \rho_1 \int_{-h}^{0} \tilde{\phi}_1(0, z) \hat{Z}_n(z) dz, \qquad (n = 1, 2, \ldots, N). \tag{3.4.12b}$$

Continuity of ϕ at $x = \ell$:

$$E = \rho_1 \int_{-h}^{0} \tilde{\phi}_1(\ell, z) Z(z) dz, \tag{3.4.13a}$$

$$\hat{E}_n = \rho_1 \int_{-h}^{0} \tilde{\phi}_1(\ell, z) \hat{Z}_n(z) dz, \qquad (n = 1, 2, \ldots, N). \tag{3.4.13b}$$

In (3.4.10)–(3.4.13), $\tilde{\phi}$ denotes the truncated series of ϕ. The integrals can all be evaluated in terms of trigonometric and hyperbolic functions. The set of $(4N+6)$ simultaneous equations are solved numerically as a linear matrix equation with $N = 3$.

3.4.4 Analysis of Wave Amplitude

The interaction of the incident surface waves with the stratified trench can be demonstrated most easily by the transmission and the reflection characteristics, and the amplitude amplification of the interfacial waves in the trench. The transmission coefficient K_t is defined as the ratio of the amplitude of the transmitted wave to the amplitude of the incident wave, and the reflection coefficient K_r is defined as the ratio of the amplitude of the reflected wave to the amplitude of the incident wave. The amplitude of the surface wave is given by (3.1.35a) in terms of the velocity potential Φ. By inspection of (3.4.8a) and (3.4.8b), it is clear that the constants C, D and E, respectively, represent the complex coefficients of the velocity potential of the incident wave, the reflected wave, and the transmitted wave. Hence, from (3.1.35a), (3.4.8a) and (3.4.8b), the transmission and reflection coefficients are given by:

$$K_t = \frac{|E|}{|C|} \tag{3.4.14}$$

and

$$K_r = \frac{|D|}{|C|} \tag{3.4.15}$$

The amplification factor R of the interfacial wave is defined as the ratio of the amplitude of the interfacial motion at $x = 0$ to the amplitude of the incident wave, that is:

$$R = \frac{|\eta_I|_{x=0}}{|\eta_{S_i}|} \tag{3.4.16}$$

where η_I and η_{S_i} are given by (3.1.36a) and (3.4.5), respectively. The velocity potential Φ is of the form (3.4.1), with the spatial potential function ϕ given by

(3.4.7) in the trench region.

As discussed in § 3.3.3, the above treatment for the inviscid problem can be slightly modified to include the effects of energy dissipation in the boundary layers. In the viscous theory, all the equations presented above remain unchanged. In the exponents of e in (3.4.7) the determined wave numbers for the propagating modes K_j, $(j = 1, 2)$ using the inviscid theory (equation 3.1.18a) are replaced by complex wave numbers, which include both the attenuation rate and the shift in wave number due to viscosity (see equation 3.3.45c); these have been found in § 3.3.1.1 for a time-periodic plane progressive wave in a two-layer fluid. Energy dissipation is assumed to take place in the boundary layers adjacent to the density interface and at the trench bottom. However, we neglect the contributions of the vertical walls at $x = 0$ and $x = \ell$; this will be discussed more fully in § 5.3. In addition, we assume that the surface waves are unattenuated in the infinite regions before and after the trench, thus the effects of energy dissipation on wave motion are due solely to wave-trench interaction. The numerical solutions of the inviscid and viscous theories are presented in § 5.3 for several specific flow conditions.

4. EXPERIMENTAL EQUIPMENT AND PROCEDURES

4.0 Introduction

The primary objective of the experimental investigation was to gain insight into the dynamics of internal wave motion in a stratified rectangular trench due to normally incident surface waves. Of interest were the effects of surface wave characteristics, density stratification and viscous dissipation on internal wave generation. We were also interested in the effects of a stratified trench on the incoming surface wave. As mentioned earlier, we required that the laboratory problem could be formulated theoretically, for this reason simple boundary conditions were chosen.

The major equipment included a wave tank and wave generator, a false bottom to create the trench, a system to measure interfacial wave amplitudes, stepping motor controlled resistance-type wave gages for measurement of surface wave amplitudes, a probe to measure fluid conductivity from which densities could be inferred, and a microcomputer for control and data acquisition. The original design of the wave tank and the wave generation system had been described in detail by Goring (1978), and this will be discussed only briefly herein. The hydraulic power supply was upgraded in this study with the installation of a new pump, which allowed for the prolonged operation of the wave generator. A unique contribution in this study was the development of an interfacial wave gage for measurement of internal wave amplitudes at a density interface.

4.1 Experimental Equipment

4.1.1 The Wave Tank

A schematic diagram of the wave tank with the false bottom in place is shown in figure 4.1.1. The wave tank was 120 ft (36.6 m) long, 2 ft (0.61 m) deep and 15.5 in (0.394 m) wide, and consisted of 12 identical modules. An additional module at one end of the wave tank contained a block section of the bed that could be moved vertically; this was used by Hammack (1972) to simulate waves generated by tectonic bottom displacements. This end module was not used in this study and was sealed off to avoid leakage. The side walls of each module were constructed of glass panels 5 ft (1.52 m) long, 25 in (63.5 cm) high and 0.5 in (1.27 cm) thick. Instrument carriages could be moved on circular 1 in (2.54 cm) diameter stainless steel rails mounted to the top flanges of the tank side walls with studs spaced at 2 ft (61 cm) intervals. The rails had been carefully leveled to within ± 0.001 ft (0.3 mm) of a still water surface in the wave tank. A steel tape graduated in meters and centimeters fixed to the top flanges of the tank side walls was used for positioning of instrument carriages.

A horizontal plywood false bottom was placed in the wave tank to create a rectangular trench 0.6 m long and 0.152 m deep. The upstream edge of the trench was located 19.15 m from the mean position of the wave plate. The portion of the wave tank downstream of the trench was not used in this study and was sealed off from the rest of the wave tank by a plywood vertical wall.

The plywood false bottom was largely constructed in units, each measuring 8 ft (2.44 m) long, 6 in (15.2 cm) deep and 15.25 in (38.7 cm) wide. Each unit was weighted with two 25 lb (11.36 kg) lead weights, one at each end to prevent it from floating, and ribs were placed at the 4 ft (1.22 m) center to strengthen the unit. The two units placed next to the trench were constructed in 2 ft (0.61 m) length and

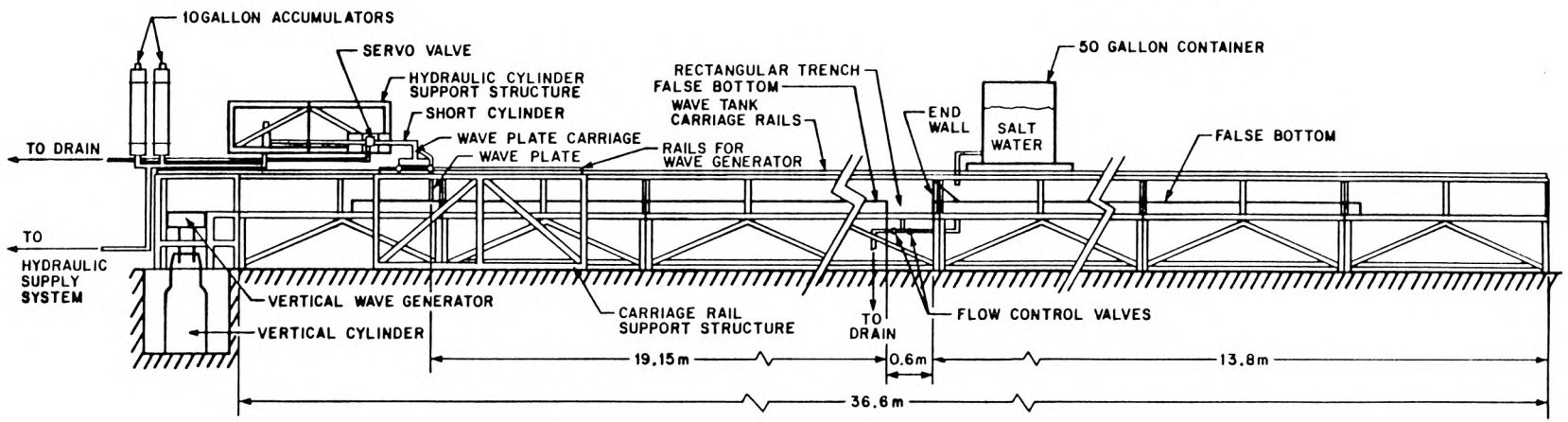

Figure 4.1.1. Schematic drawing of the wave tank and false bottom.

each had a vertical face at one end, which formed a side wall of the trench. Water filled the underside of the false bottom in the experiments, the gap between the false bottom and the glass walls of the wave tank was sealed with 0.375 in (0.95 cm) polyethylene rope. Some warping of the surface of the false bottom was noticeable at places after a period of use; the false bottom was horizontal to within ± 2 mm. This had a negligible effect on the surface wave whose wavelength was very long compared to the water depth. In the experiments, the still water level was measured relative to the floor of the wave tank where it formed the trench bottom.

4.1.2 The Wave Generator

The wave generator consisted of the hydraulic system, the servo-system, and the wave plate. The basic function of the hydraulic system was to supply fluid power to a hydraulic cylinder that extracted energy from the fluid and converted it into mechanical motion of the wave plate. It included an oil reservoir, a pump, a motor, several filters, two check valves, an unloading valve, several accumulators, a heat exchanger, piping, a servo-valve, and two hydraulic cylinders. The oil reservoir, which had a capacity of 180 gal ($0.681\,m^3$), provided a storage space for the hydraulic oil until it was called for by the system. A variable displacement pump, rated at 40 gpm ($0.00252\,m^3sec^{-1}$) at 2500 psi ($17,000\,KNm^{-2}$) created the flow of oil in the hydraulic system. It was powered by a 75 hp (56 KW), 1800 rpm electric motor. The operation of the pump and power supply could maintain a constant pressure in the hydraulic system for an indefinite period of time at the maximum output of the hydraulic cylinder. An unloading valve and a check valve were located downstream of the pump. The rated pressure of the hydraulic system was set at 2500 psi ($17,000\,KNm^{-2}$), when this pressure was reached, the unloading valve directed the flow of oil back to the oil reservoir; the check valve prevented a reverse flow through the pump from the pressurized system when the pump was not op-

erating. Two 10 gal ($0.038\,m^3$) accumulators precharged at 450 psi ($3000\,KNm^{-2}$) were located between the unloading valve and the check value to reduce hydraulic transients due to the operation of the pump. The temperature of the hydraulic oil flowing through the pump was regulated by a water cooled heat exchanger rated at 20 gpm ($0.00126\,m^3sec^{-1}$) at 75°F (23.9°C).

The servo-valve and the the hydraulic cylinder were the output components of the hydraulic system. The servo-valve (Moog Model 72-103) directed the flow of oil to either end of a double-acting hydraulic cylinder and thus controlled the motion of the wave plate, it was rated at 60 gpm ($0.0038\,m^3sec^{-1}$) at 40 ma current. Two 10 gal ($0.038\,m^3$) accumulators were located upstream of the servo-valve. They were precharged at 450 psi ($3000\,KNm^{-2}$) and were charged to the operating pressure of the hydraulic system, that is, 2500 psi ($17,000\,KNm^{-3}$), when the pump was operating. When the pump was shut down the accumulators could provide a reservoir to supply flows to the servo-valve. The hydraulic cylinder used in this study (Miller Model DER-77) had a 5 in (12.7 cm) bore and a 1.75 in (4.45 cm) rod with a maximum stroke of 16 in (40.6 cm). The net bearing area of the piston in the cylinder was $17.3\,in^2$ ($112\,cm^2$). The rod was connected at one end to a wave plate carriage that carried the wave plate that generated the waves. A second hydraulic cylinder (Miller Model DH77B) was not used in this study, it had a 2.5 in (6.35 cm) bore and a 1.375 in (3.49 cm) rod with a maximum stroke of 96 in (2.44 m). The net bearing area of the piston in the cylinder was $3.4\,in^2$ ($22\,cm^2$). The cylinder with the larger bore diameter was used because its larger piston area reduced the differential pressure required to overcome the static friction when the piston moved from its rest position. The return line downstream of the hydraulic cylinder was kept full by a second check valve located before the oil reservoir.

The function of the servo-system was to supply the servo-valve with the electric current necessary to drive the wave plate to follow a specified displacement-time his-

tory. It consisted of a function generator, a feedback device, and a servo-controller. A 1000 point displacement-time history of the wave plate was computed using a microcomputer, this was transmitted to the function generator memory through a DRV11–J 64 line parallel interface where the data were stored in binary form. The function generator converted the binary data into a voltage-time history proportional to the displacement-time history of the wave plate, this would be the voltage that should be applied across the servo-valve if frictional forces were absent. However, frictional forces in the hydraulic cylinder and at the wave plate inevitably distorted the desired trajectory. A feedback system consisting of a linear variable differential transformer (LVDT) measured the actual position of the piston in the hydraulic cylinder and returned a voltage to the servo-controller. The servo-controller compared the feedback voltage to the voltage from the function generator memory and adjusted the voltage applied across the servo-valve accordingly to minimize the difference between the desired piston position and the measured piston position. The resulting current generated by the applied voltage directed the servo-valve to regulate the flow rate of oil to either end of the double-acting cylinder, thus pushing the piston inside in one direction or the other; the quantity of flow through the servo-valve and hence the velocity of the piston was proportional to the magnitude of the current. The piston motion was transmitted to the wave plate through a rod and a wave plate carriage to generate the waves. A detailed description of the servo-system can be found in Goring (1978), its interfacing with the microcomputer is described in Synolakis (1986).

The wave plate was a rectangular plate 0.25 in (6.4 mm) thick, and made of aluminum with dimensions slightly smaller than the inside dimensions of the wave tank when the false bottom was in place. It was mounted vertically to the wave plate carriage, which rode on circular rails supported on a steel truss that was structurally independent from the wave tank. To avoid the problem of leakage around the wave

plate, it was sealed against the side walls and the false bottom by rubber windshield wiper blades.

4.1.3 The Interfacial Wave Gage

Internal waves at a fresh water–salt water interface have been measured by many researchers using various techniques. The simplest method is visual using photographs and motion-pictures of the interfacial waves; the density interface is made visible by colouring one of the fluid layers with dissolved dye. This approach is particularly useful when the profile of the interfacial wave is sought. Accuracy of measurement depends on the position of the observer; for example, a false reading can result if the observer's line of sight is not level with the dye interface. In addition, the relation of the dye interface to the density stratification is unknown. A frame by frame examination of motion pictures would be necessary in this case to obtain a time record of the motion.

Helal and Molines (1981) used an "interface follower" to follow a fresh water–salt water interface at a given conductivity (and hence salinity). Basically, the principle of this apparatus is to measure the conductivity and compare it with a chosen reference. An electric motor moves the conductivity probe in order to minimize the difference between the measured and referenced conductivity. Helal and Molines reported measurement accuracy of ± 0.1 mm with their instrument. We had also constructed a similar device but found the feedback system to be very unstable, and the instrument was never used in actual experiments.

A laser-optics detector system was used by Hammack (1980) and that instrument circumvented some of the difficulties discussed above. Hammack used a system of cylindrical lenses to transform a laser beam into a vertical sheet of light with a constant height that was directed horizontally across a wave tank containing a stratified fluid of water and salt water. The salt water was dyed dark blue with

dissolved dye. The light, after traversing the tank, was focused onto a photodiode that provided an output voltage proportional to the incident light intensity. Blue dye blocked the portion of light sheet that was incident on the dyed salt water below the interface. Thus, motions of the interface caused changes in the output signal of the photodiode. The amplitude of the interfacial motion was determined through calibration when the fluids were quiescent, by moving the gage up or down. Hammack (1980) found that the dye interface seen by the interfacial wave gage appeared in the upper portion of the diffuse salinity interface. This measurement system had certain limitations and drawbacks. The most significant limitation inherent in the technique of light intensity measurement is that many sources of noise may enter the signal. These may include variation in the intensity of the light source, light from extraneous sources, and electronic noise in the detector circuit. In addition, the calibration curves were inherently nonlinear due to spatial variation of light intensity in the vertical sheet of light produced by the cylindrical lenses. If the background signal changes during an experiment for reasons not related to the motion of the dye interface, an error may result using the measured calibration curves. Another problem faced by Hammack (1980) was that mixing of the fluids at the interface generated a high frequency signal, which was superimposed on the signal corresponding to the internal wave. This limited the amplitudes of the internal waves studied to those with a stable density interface.

For studying internal wave breaking and mixing, laser-induced fluorescence (LIF) has been used by other researchers as a non-intrusive method to measure fluid concentrations across a density interface with temporal and spatial resolution unattainable by conventional methods. In this technique, a laser fluorescent dye (e.g. Rhodamine 6G) is premixed with either the upper or the lower fluid. The dye fluoresces when excited by light in the visible spectrum at wavelengths characteristic of the dye. For a range of dye concentration, the fluorescence intensity is

proportional to the concentration of the dye, which is in turn related to the local concentrations of the dyed fluid. The instantaneous fluorescence signal is measured at a large number of points across the density interface by a scanned linear photodiode array and recorded in real time by a high speed data acquisition system. Recently, Hannoun and List (1988) used the LIF technique to study turbulent structure at a density interface of water and salt water; their paper also contains a survey of earlier work by other investigators.

An interfacial wave gage was developed in this study to measure internal wave amplitudes at a density interface. As in Hammack's laser-optics detector system, movement of the interface was detected by using a dyed fluid to partially block an incident sheet of light. But instead of producing the sheet of light by a system of cylindrical lenses and measuring the intensity of the light transmitted, the new instrument used a single scanning laser beam. The use of a scanning beam allowed the extent of light passing through the clear fluid to be measured in time, the motion of the dye interface did not depend directly on the change in the intensity of the light detected by the photodiode, hence eliminating problems inherent in light intensity measurements.

We now describe a simple method to generate a moving beam to sweep through the fluid vertically in a continuous fashion. Consider a light beam striking the face of a rotating prism as shown in figure 4.1.2. The refracted beam that emerges is parallel to the incident beam but is laterally displaced by an amount h depending upon the angle of incidence α and the size of the prism. The displacement h is obtained from Snell's law:

$$\frac{h}{\ell} = \left(\sin\alpha - \frac{\sin 2\alpha}{2\sqrt{n^2 - \sin^2\alpha}} \right) \tag{4.1.1}$$

where ℓ is the distance separating the two opposite faces through which the light beam enters and leaves the prism, and n is the index of refraction of the prism's

material. If the distance between the other two opposite faces is d, the range of α is given by $0 \leq \alpha \leq \tan^{-1} d/\ell$. In figure 4.1.3 the ratio of the beam displacement, h, to the dimension, ℓ, is plotted against the angle of incidence α. Note that the relation is almost linear for small α. If two opposite faces of the prism are masked and the moving beam is focused onto a photodiode, the output from the photodiode when displayed on an oscilloscope will look like a rectified rectangular wave as shown in figure 4.1.4. The voltage is proportional to the intensity of the transmitted beam. Twice in a complete revolution of the prism the voltage drops out for a period of time that equals the duration the incident beam is striking a masked surface of the prism. For the transmitted beam the prism's geometry can be chosen to limit the maximum angle of incidence (e.g., $\alpha \leq 20°$, with $d/\ell \leq 0.36$) so that the scan is approximately linear in time. The dimension of the scanned field will be determined by the size of the prism, and the prism's rotational speed will determine the scanning rate.

The light beam from a 0.5 mW helium-neon laser (Spectra-Physics Model 155) was aligned so that it was perpendicular to the glass walls of the wave tank (figure 4.1.4). The beam created by the rotating prism, after traversing the tank, was focused by a plano-convex lens (200 mm focal length, 125 mm diameter) onto a photodiode, which provided a voltage that was proportional to the intensity of the incident beam. By dyeing the salt water dark blue, a portion of the active duration of the scanning laser beam was blocked as the interface rose or fell during wave motion. The duration was a maximum when the interface did not rise to the lowest position of the scanned field, and it was a minimum when the interface rose to or above the top of the scanned field. An example of this is shown in figure 4.1.4 for a partially risen interface; the oscilloscope display was only for viewing the instantaneous signal during the experiment. The time duration of the unblocked signal was measured using a digital counter with a 10 MHz clock, the digital signal was

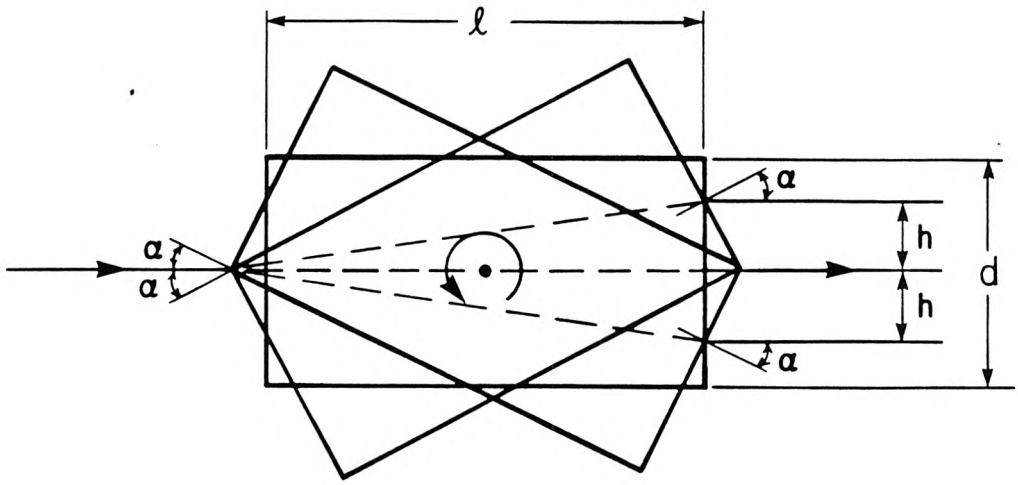

Figure 4.1.2. Schematic drawing of a rotating prism.

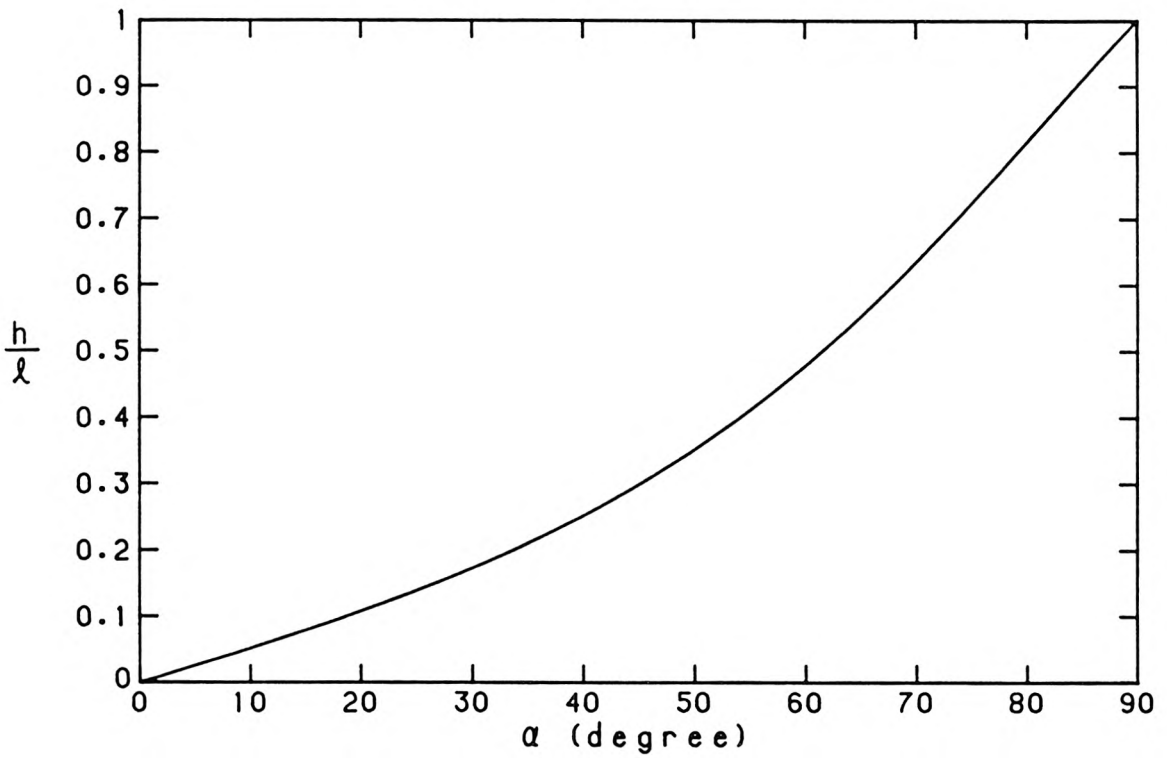

Figure 4.1.3. Variation of h/ℓ with angle of incidence of laser beam α obtained using (4.1.1).

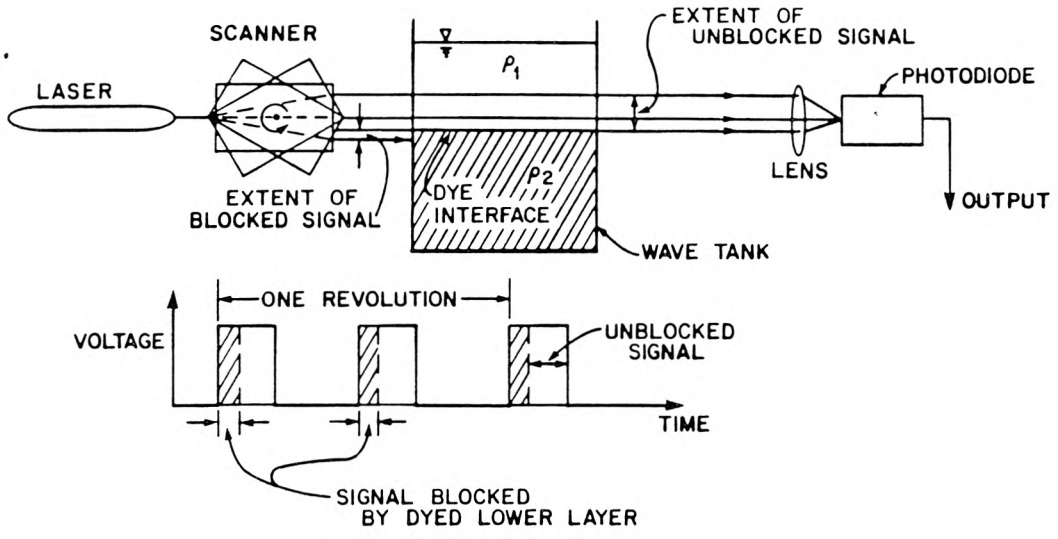

Figure 4.1.4. Schematic drawing of the interfacial wave gage and photodiode output.

converted into an analog output for recording by a microcomputer.

Two lucite prisms were constructed for this study. A summary of the characteristics of the prisms is given in table 4.1.1. Prism 1 was generally used for small amplitude internal waves, the small angles of incidence gave approximately linear calibration. The prism was mounted to an electric motor (Bodine Electric Company Type NSH-12) with the speed controller (Minarik Electric Company Model SL 14) set on high speed in all the experiments. The frequency of the rectangular wave as shown in figure 4.1.4 was measured by a frequency counter to be $\approx 94\,\mathrm{Hz}$, this implies a prism's rotational speed of 2820 rpm. Thus the prism completed one scan of the interface in $\approx 1/94\,\mathrm{sec}$, which was sufficient for the long period of the internal waves in the trench.

Characteristics	Prism 1	Prism 2
thickness (cm)	1.27	1.27
length, ℓ (cm)	13.0	10.0
width, d (cm)	7.6	17.0
maximum angle of incidence of laser beam, α_{max}	30°	60°
maximum vertical displacement of incident beam, h_{max} (cm)	2.4	4.05

Table 4.1.1. Characteristics of rotating prisms.

The interfacial wave gage was mounted to a frame that was shaped like an inverted U with the legs on the outside of the wave tank (figure 4.1.5), the frame was supported by a carriage that rode on the wave tank carriage rails. The wave gage was calibrated by raising and lowering the frame predetermined distances when the fluids were quiescent. Typical calibration curves for the two prisms are shown in figures 4.1.6*a* and 4.1.6*b*; the ordinate is the reading on a point gage attached to the U frame, and measured relative to the support carriage. A larger reading on the point gage corresponded to a lower position of the U frame and thus a shorter duration of the scanning beam striking the fluid above the dye interface. After calibration, the U frame was fixed in a vertical position where a lower portion of the beam's scanned field was blocked by the dyed salt water. Subsequent changes

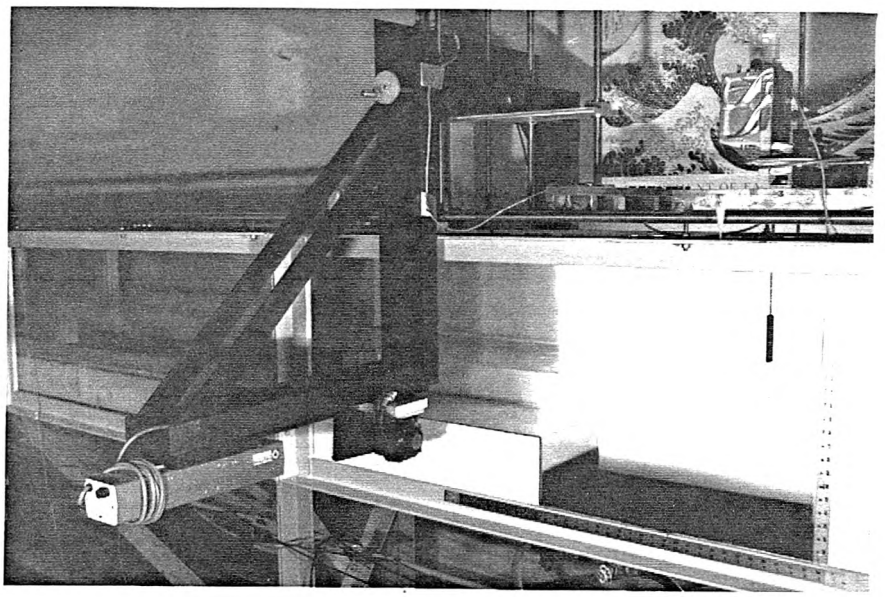

Figure 4.1.5. Overall view of the interfacial wave gage.

in the gage's output signal were due to movement of the interface as the result of molecular diffusion and/or wave motion.

The interfacial wave gage depended for accuracy on the two-dimensionality of the waves, and its operation was limited to a stable density interface. When the amplitudes of the internal waves were sufficiently large, vortex-induced mixing occurred at the interface. This induced a high frequency signal superimposed on that corresponding to the internal waves as in Hammack's (1980) laser-optics detector system. However, with a stable interface, the interfacial wave gage had extremely low noise-to-signal ratio. When the wave tank was filled only with fresh water the laser's scanned field was completely unblocked. It was found that the analog output produced by the gage could remain stable for an indefinite period of time.

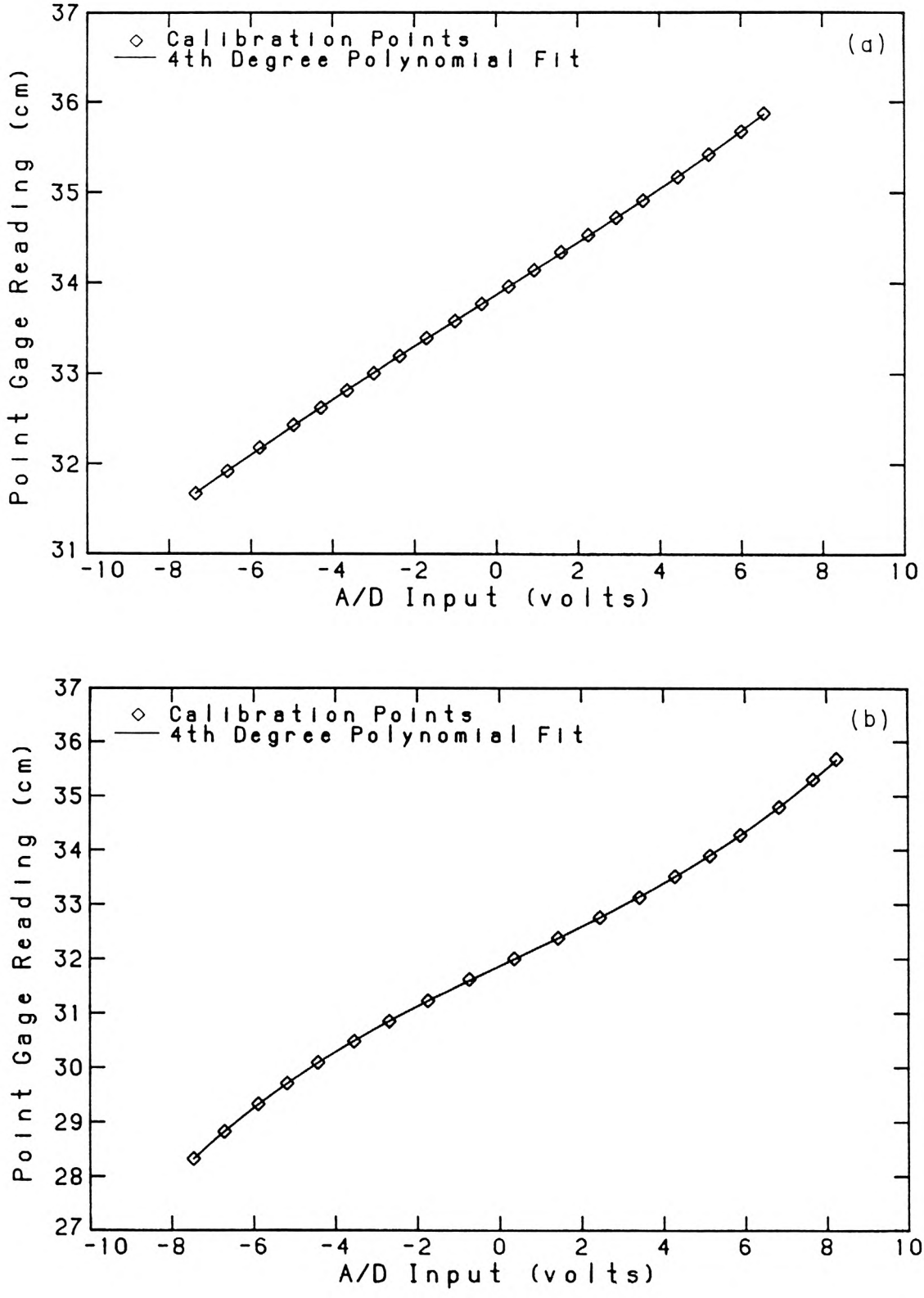

Figure 4.1.6. Typical calibration curves for the interfacial wave gage: (*a*) Prism 1, and (*b*) Prism 2.

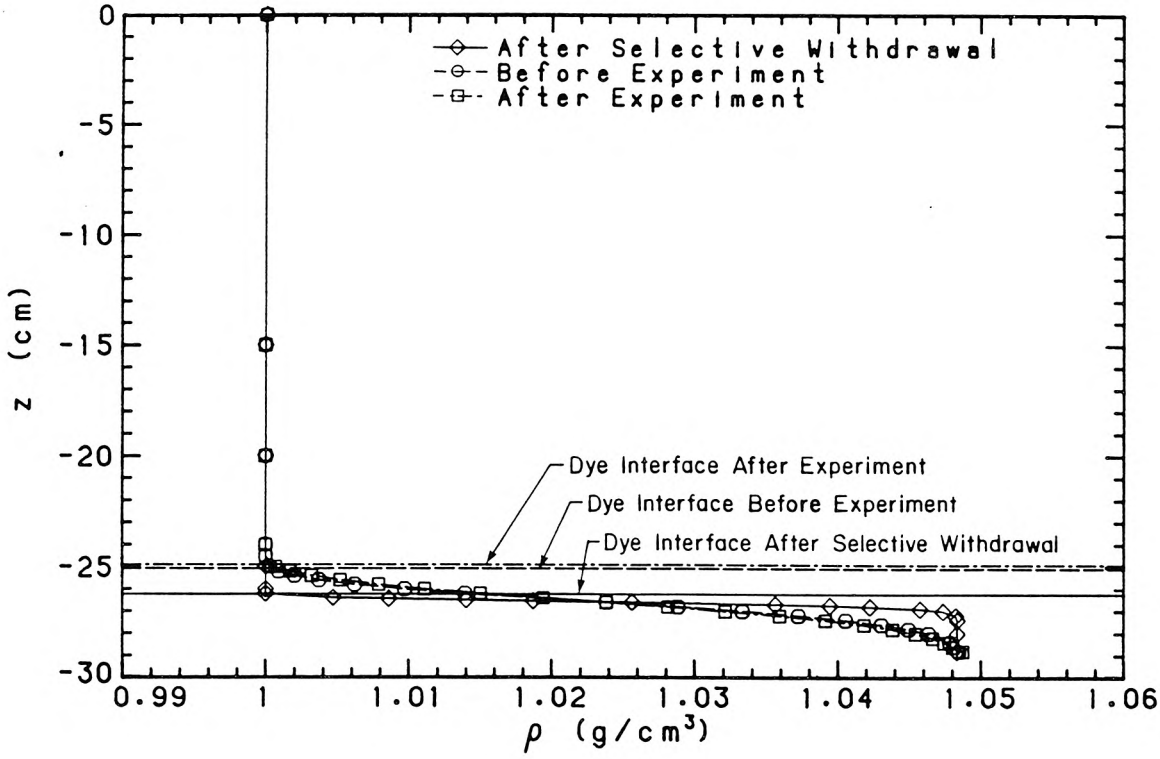

Figure 4.1.7. Locations of dye interfaces in relation to the density profiles at various times in a typical experiment.

The interfacial wave gage measured movement of the dye. To determine the location of the dye interface in the quiescent fluid, the interfacial wave gage was raised until the top of the laser scanned field coincided with the free surface and the reading on the point gage was recorded. The wave gage was then lowered to a position where the duration of output voltage detected by the photodiode started to decrease. This was due to the laser beam previously scanning clear fresh water intercepting the dye interface, and a portion of the active duration of the scanning beam was blocked by the dyed fluid. This duration change could be observed on the oscilloscope display as shown in figure 4.1.4, but was more easily detected by a voltmeter connected to the analog output of the digital counter. Knowing the dimension of the scanned field and the vertical displacement of the wave gage, the

location of the dye interface relative to the quiescent free surface was determined; typical examples are shown in figure 4.1.7. The ordinate is the distance below the still water surface, the total depth of the stratified fluid in the trench region was 30.4 cm and the depth of salt water was 3.8 cm. The initial stratification was prepared by withdrawing fluid from the interface after the filling process. The density profile and the location of the dye interface were measured initially and 7 hours later, and about 15 minutes after the experiment was conducted; the measurement of the density profile is described in § 4.1.5. It is seen in figure 4.1.7 that when the fluid is quiescent, the interfacial wave gage always sees the dye interface close to the top of the diffuse salinity interface.

4.1.4 The Surface Wave Gage

Surface wave amplitudes were measured using resistance wave gages. A photograph of a typical wave gage is shown in figure 4.1.8*a*. The wave gage consisted of a pair of stainless steel rods 0.74 mm in diameter, 9 cm long, and spaced 0.5 cm apart. The steel rods had sufficient stiffness to allow them to be supported at only one end; the other ends penetrated the water surface. The steel rods were insulated from each other at the support, but allowed a current to pass between them when the other ends were immersed in water. Under operating conditions the wave gage behaved as a variable resistor, which formed part of a Wheatstone bridge in a carrier preamplifier (Hewlett Packard 8805A) as shown in figure 4.1.8*b*. The resistance between the two steel rods was proportional to the depth of immersion in water. The Wheatstone bridge received a 2400 Hz, 4.5 volt excitation from the preamplifier. After balancing the bridge when the fluid was quiescent, subsequent changes in water surface elevation unbalanced the bridge circuit and induced an output voltage proportional to the change in the depth of immersion of the wave gage relative to its balanced position. The preamplifier monitored this output voltage which, after

demodulation and amplification, was recorded by a microcomputer.

The wave gage was mounted to a stepping motor (Hurst Model LAS, 768 steps per inch) and used in conjunction with a Hurst stepping motor controller, which permitted both continuous stepping at an adjustable frequency and single steps. The vertical position of wave gage could be adjusted to an accuracy of $\approx 1/30$ mm. A more severe problem came from signal drifting in the gage output voltage. The measured surface wave amplitudes were less than 4 mm in most of the experiments. A small drift in the wave record of a fraction of the measured wave amplitude was noticeable on occasions. This had little effect on the overall wave height because the wave gage calibrations were found to be approximately linear. To calibrate the wave gage, the Wheatstone bridge circuit first was balanced at a fixed gage immersion, and the gage output voltage, which was very nearly equal to zero, was recorded by a microcomputer. Then the wave gage was withdrawn to a known distance from the balanced position by means of the stepping motor and controller. The distance withdrawn and the gage output voltage were recorded, the voltage change relative to the balanced gage was computed and this value was used in constructing the calibration curve. To obtain the next calibration point the gage was returned to its balanced position and a "zero" voltage was recorded again, then the gage was immersed to the same distance as the distance last withdrawn and the microcomputer computed the change in the gage output voltage relative to the voltage recorded the last time the gage was at a balanced position. This procedure was repeated for various withdrawals and immersions to obtain the calibration curve. Thus signal drifting was corrected for in the calibration. Figure 4.1.9 shows two such calibration curves for the same gage obtained from two different experiments conducted on consecutive days. The two curves are almost identical and these results are typical of the gage calibrations. There was usually a time gap of 1.5–2 hours between the calibration of the gage and the start of the experiment; during this period the gage

(a)

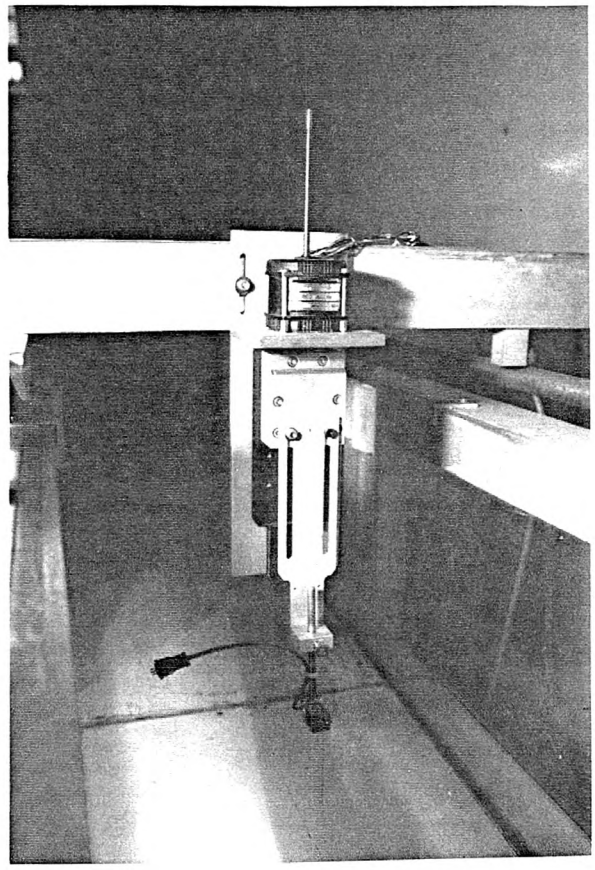

(b)

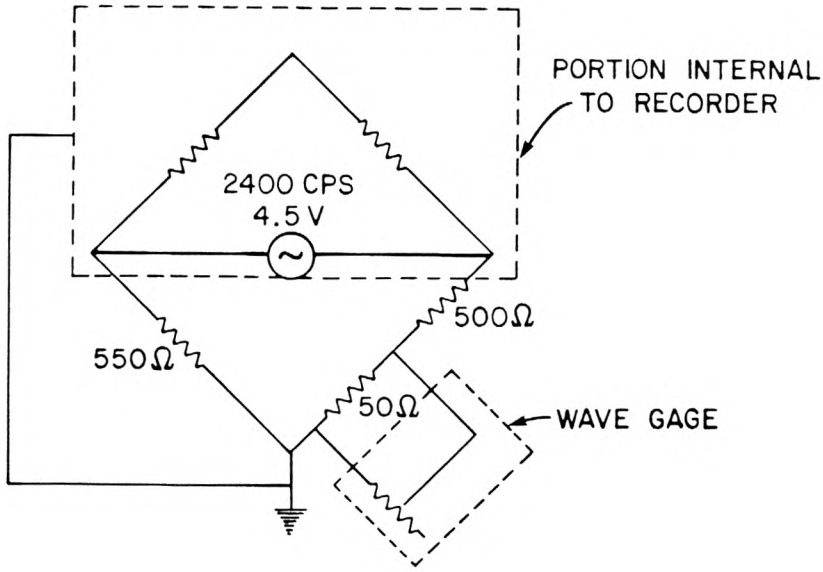

Figure 4.1.8. (*a*) Resistance wave gage and stepping motor, and (*b*) Circuit diagram for resistance wave gage (after Raichlen, 1965).

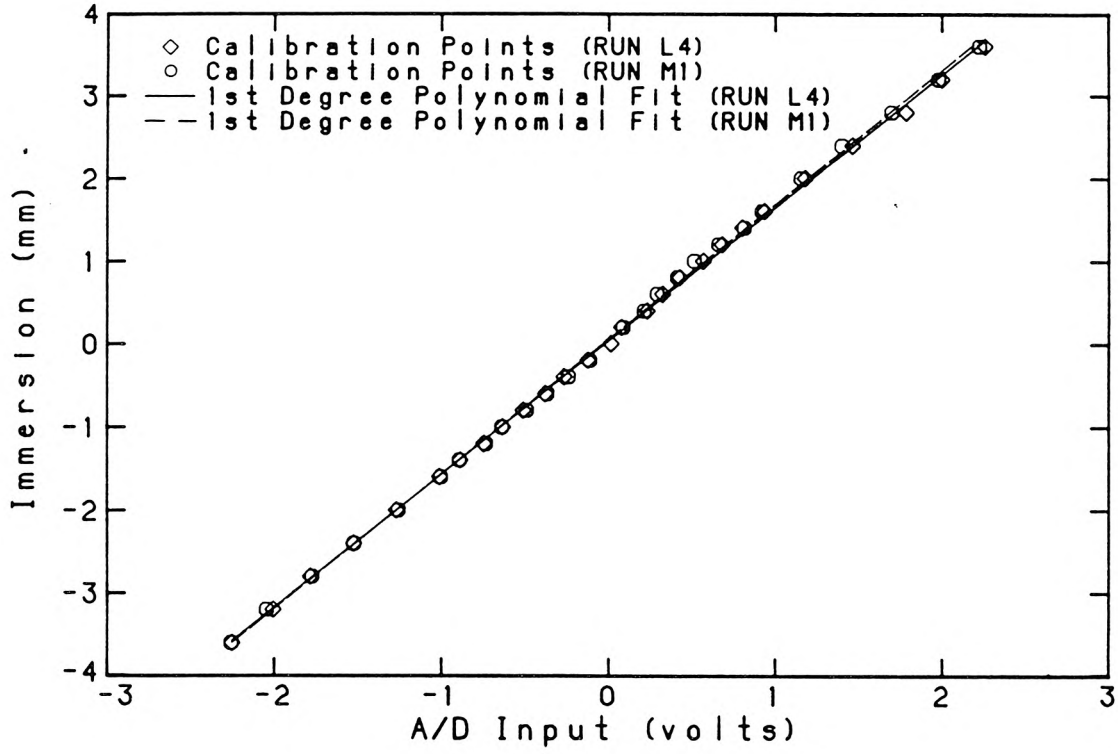

Figure 4.1.9. Calibrations of a wave gage from two experiments after correction for signal drifting.

output voltage had drifted. All the wave gages were rebalanced just before initiating the motion of the wave generator but the calibration curves initially obtained were used for data analysis. From the calibration curves shown in figure 4.1.9 this procedure was satisfactory. Signal drifting of the gage was generally small during the short period of the experiment (≈ 17 min).

It was found that the proximity of the two wave gages placed above the trench affected the gage output voltages when one of them was raised or lowered while the other remained stationary. For this reason these two gages were moved together during calibration to simulate the experimental condition; the wavelength of the surface waves in the tank was so long that surface elevation above the trench was almost level.

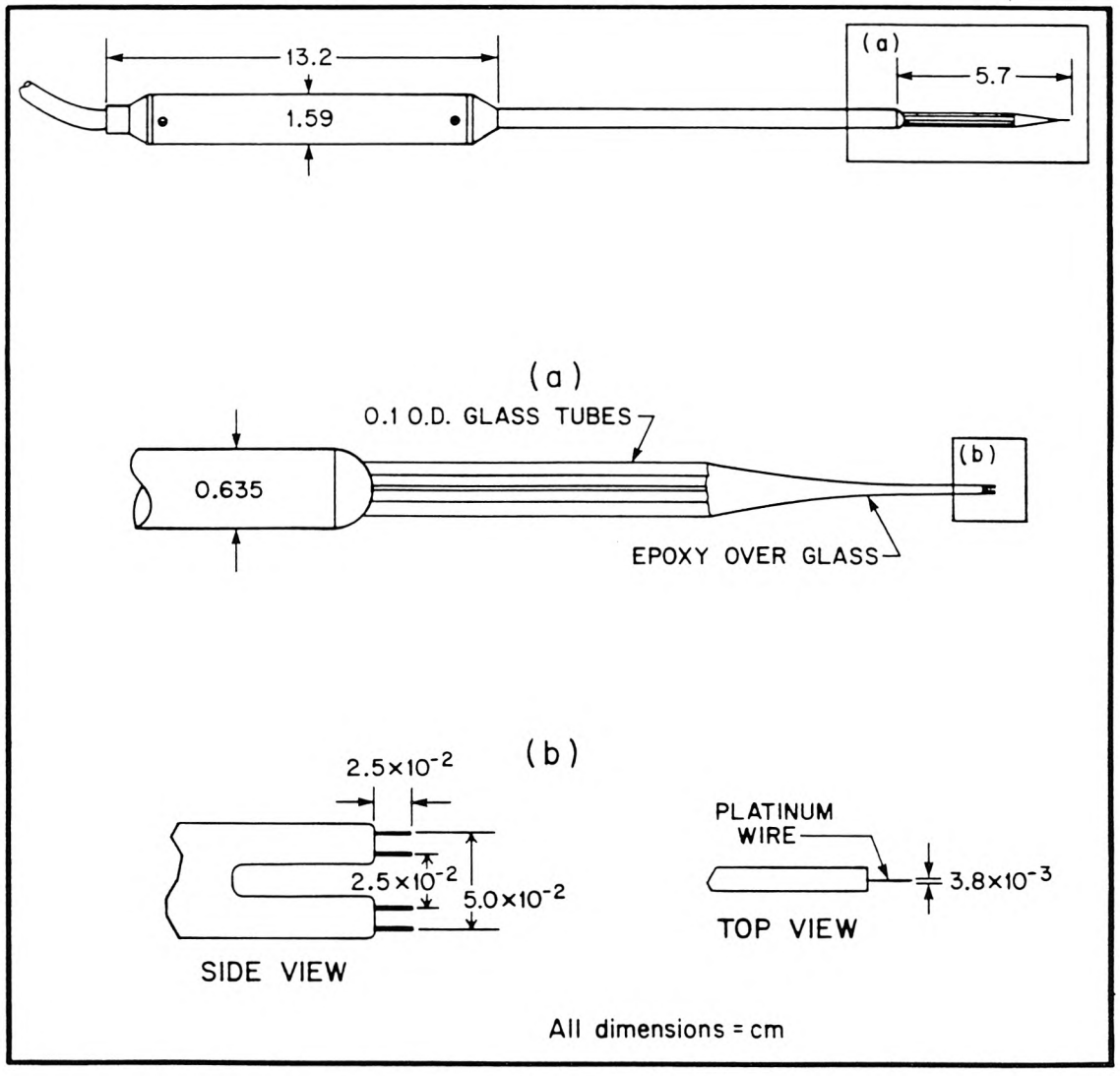

Figure 4.1.10 Views of the miniature four-electrode conductivity probe (after Head, 1983).

4.1.5 The Conductivity Probe

Density stratification was inferred from conductivity measurements that were made using a miniature four-electrode conductivity probe. The probe was calibrated using thirteen"standard" salt water solutions with densities ranging from $0.998\,\mathrm{gcm}^{-3}$ (fresh water) to about $1.065\,\mathrm{gcm}^{-3}$ (salt water). The solutions were prepared at the same temperature of the stratified fluid in the trench (20°C), and their exact densities were determined by weighting $100\,\mathrm{cm}^3$ of each solution in a volumetric flask. The probe was attached to a point gage. The electrode consisted of two pairs of platinum wires supported on a tapered glass tube, and the dimensions of the sampling volume were extremely small (figure 4.1.10). The probe had the properties of small spatial average, rapid time response, and stable calibration designed for accurate measurements of conductivity fluctuations in salt-stratified water flows. A typical calibration curve is shown in figure 4.1.11. A detailed discussion of the probe can be found in Head (1983). The electronic circuit for the conductivity probe was obtained from Imberger (1986).

4.1.6 Data Acquisition and Control

A LSI–11/23 microcomputer (Digital Equipment Corporation) running RT–11 V4.0 with a 256 KB RAM and an A/D–D/A interface board (Datel Model ST-LSI) was used to acquire data for the experimental investigation. The interface board had a digitizing error of ≈ 0.005 volt.

During the experiment, data were collected from up to 5 channels (1 for the wave plate, 4 for the wave gages) simultaneously. The MACRO routines that performed the data sampling were written by Skjelbreia (1982). Each run lasted for approximately 17 minutes. The sampling rate was 16.5 Hz per channel.

The computer storage system included a 30 MB winchester disk and a 0.5 MB floppy disk system. Data were transferred to a PDP–11/24 computer for analysis.

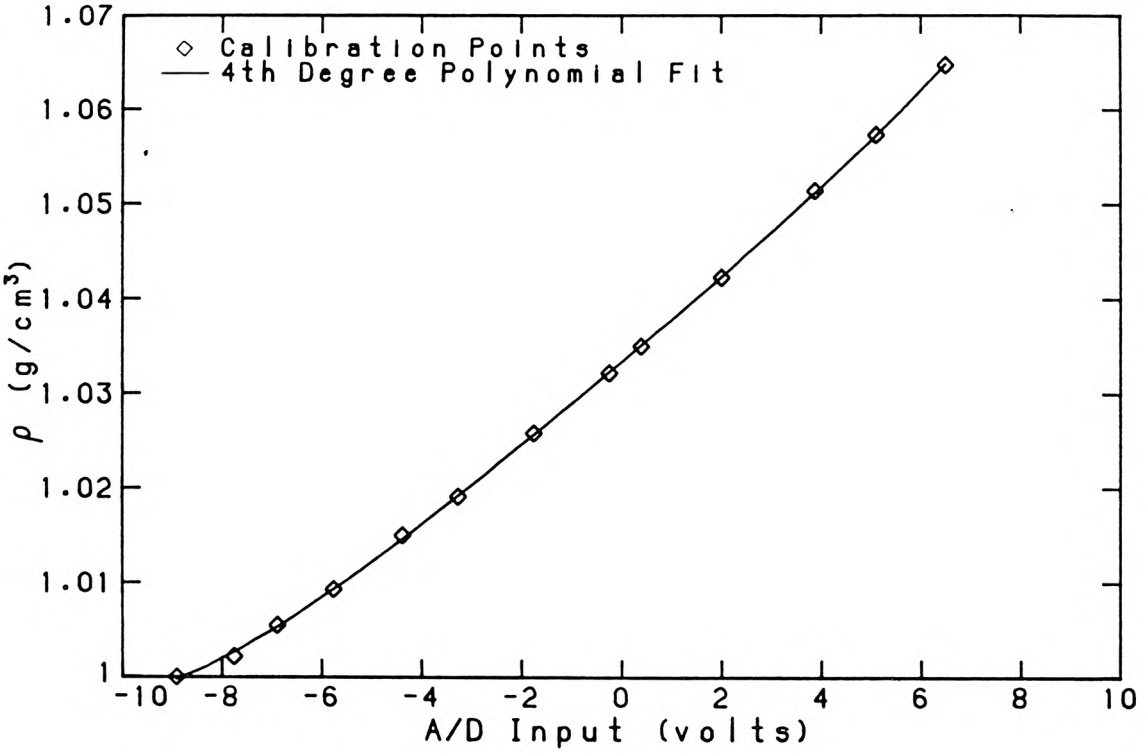

Figure 4.1.11. Typical conductivity probe calibration.

The LSI–11/23 microcomputer was also equipped with a DRV11–J 64 line parallel interface, which was used to transmit wave plate trajectory data to the function generator memory.

4.2 Experimental Procedures

Referring to figure 5.1.1 for the layout of a typical experiment, each experiment with stratified fluid in the trench consisted of four consecutive steps:

(1) Filling and Stratification: The trench was stratified with fresh water and salt water with a density difference of $\approx 5\%$. The wave tank was first filled with fresh water to a depth of 15.2 cm above the false bottom. Salt water was then introduced beneath the fresh water through a port in the bottom of the trench until the depth of salt water was about 2.5 cm above the desired depth h_2. This extra depth of fluid

contained the diffuse salinity interface created by the filling process. To reduce the thickness of the diffuse salinity interface, a conductivity probe was calibrated using standard solutions and placed at a distance h_2 above the trench bottom, a small plexiglas tube withdrew fluid from the diffuse layer until the probe gave a density reading of $1.025\,\mathrm{gcm}^{-3}$. Thus, the center of the diffuse salinity interface was located at the desired vertical distance above the trench bottom. The density profile was measured and the location of the dye interface was determined using the interfacial wave gage. The process of selective withdrawal reduced the thickness of the interface to $\approx 0.5\,\mathrm{cm}$. The thickness of the interface was defined as the ratio of the maximum density difference between the two layers to the maximum density gradient in the diffuse salinity interface. Then the density interface was allowed to diffuse to a thickness specified for the experiment. In the experiments in which a thin interface was used, calibration of the wave gages started immediately after the density profile was measured. The processes of filling the trench and selective withdrawal typically took a total of 3 hours. This procedure ensured standard preparation of the stratified fluid in the trench in each experiment. The actual times of measurement of the density profiles were recorded in each experiment.

(2) Calibration Step: About 1.5 hours before the estimated time for running the experiment another density profile and the new location of the dye interface were obtained; this step was bypassed in experiments with thin interfaces. Then the surface and interfacial wave gages were calibrated.

(3) Run Step: The wave generator was started, and at the same time data acquisition by the microcomputer was initiated. The time histories of the wave plate motion and of the motions of the water surface and the interface were recorded simultaneously from the start of the wave generator until the internal waves in the trench had reached steady-state conditions. This step took approximately 17 minutes.

The density profile and the location of the dye interface were measured again about 15 minutes after the wave generator was stopped. Then the wave generator was calibrated; this was not done before the experiment to avoid disturbing the stratified fluid in the trench.

(4) Data Reduction Step: Data analysis was performed on a PDP–11/24 computer. The software chose the best least-squares polynomial fit (up to the fourth degree) to the calibration curves and reduced the voltages recorded during the experiment to wave amplitudes and density stratifications.

5. RESULTS AND DISCUSSION

5.0 Introduction

The primary objective of this study is to investigate various aspects of the dynamics of internal wave motion in a stratified rectangular trench due to surface waves, that is, the effects of surface wave characteristics, density stratification, and viscous dissipation on internal wave generation in a trench. Also of interest are the effects of a stratified trench on the incident surface waves. Several theoretical models have been constructed that allow us to isolate individual physical processes. However, theoretical models cannot include all the physical effects found in real fluids; therefore, experiments were conducted to determine whether the assumptions made to develop the theoretical models are valid. From such a comparison we can determine whether the important physical effects are included in the models. Then if the experiments confirm the theories, there would be confidence that similar models could be used to treat other flow conditions.

This chapter is organized as follows. In § 5.1 some important considerations involved in planning the experimental investigation are discussed. In § 5.2 solutions based on theoretical models developed for a laboratory constant-depth channel and trench configuration are compared to experimental measurements. Finally, in § 5.3 the steady-state responses of a two-layer stratified fluid in a rectangular trench to normally incident surface waves in an infinite region outside the trench are obtained

for several specific flow conditions.

5.1 Experimental Considerations

5.1.1 End Reflections in Wave Tank Experiments

The experiments were conducted in a wave tank 36.6 m long, 0.61 m deep, and 0.394 m wide with glass walls throughout. Waves were generated at one end of the tank by a bulkhead wave generator that moved in simple-harmonic motion controlled by an electrohydraulic servo-system. The system accepted an input voltage from a memory device that could store a 1000 point voltage-time history; the time-displacement history of the mechanical movement was proportional to the time-voltage history of the input signal. A horizontal plywood false bottom was placed in the wave tank to create a rectangular trench 0.6 m long and 0.152 m deep. The upstream edge of the trench was located at a distance of 19.15 m from the mean position of the wave generator and an absorbing beach was placed at the other end of the tank to reduce the reflection of waves transmitted past the trench from the end of the tank. Thus, initially we attempted to model the condition of a trench in an infinite region. In early experiments, it was found that, due to the long waves used, the amplitudes of the reflected waves from the beach were greater than 30% of those of the incident waves. A method to eliminate beach reflection from the measured wave system is described in Dean and Ursell (1959). In this method, the amplitudes and phases of the surface wave and internal wave components are determined from wave measurements using linear superposition. Then this wave system is theoretically transformed into another wave system in which the amplitude of the reflected wave from the beach is zero. In other words, the contributions of beach reflection are subtracted from the original wave system. Thus, the wave components of the transformed system are directly comparable to the theoretical

predictions. This method was not used in this study because nonlinear effects were important in some experiments, hence the principle of superposition was not valid. The ratio of the phase speed of the surface wave to that of the internal wave was of $\dot{O}(\sqrt{\rho_2/\Delta\rho})$, where $\Delta\rho = \rho_2 - \rho_1$, hence it also was not feasible to terminate the experiments before the reflected waves from the beach arrived at the trench, because the internal waves in the trench had not reached steady-state conditions.

Because of the reflections from the beach and, thus, the uncertain boundary condition at the beach, the theoretical results using a model consisting of an infinite ocean and a rectangular trench could not be compared to these experimental results. Therefore, a different approach was taken to investigate this problem. The theoretical model treated was changed from one consisting of an infinite ocean to one that could be treated more easily experimentally. Then if the experiments confirmed the theory, there would be confidence that a similar analytical model could be used to treat the case of a trench in an infinite region. In the model that was chosen, the wave tank was terminated by a vertical, perfectly reflecting wall located at the downstream edge of the trench (figure 5.1.1). The locations of the surface and the internal wave measurements are shown in figure 5.1.1 and labelled as 1, 2, and 3 for the surface wave gages and 4 for the interfacial wave gage. Their exact locations are given in table 5.1.1. This problem could be formulated theoretically and the results compared directly to the experimental measurements to establish the possibility of using the same theoretical approach for the case with the infinite region.

5.1.2 The Choice of Channel and Trench Dimensions

The dimensions of the trench (0.6 m long, 0.152 m deep) were chosen based on theoretical calculations using the two-layer model. Fresh water and a salt water solution were used in this study, with a normalized density difference of $\approx 5\%$. This

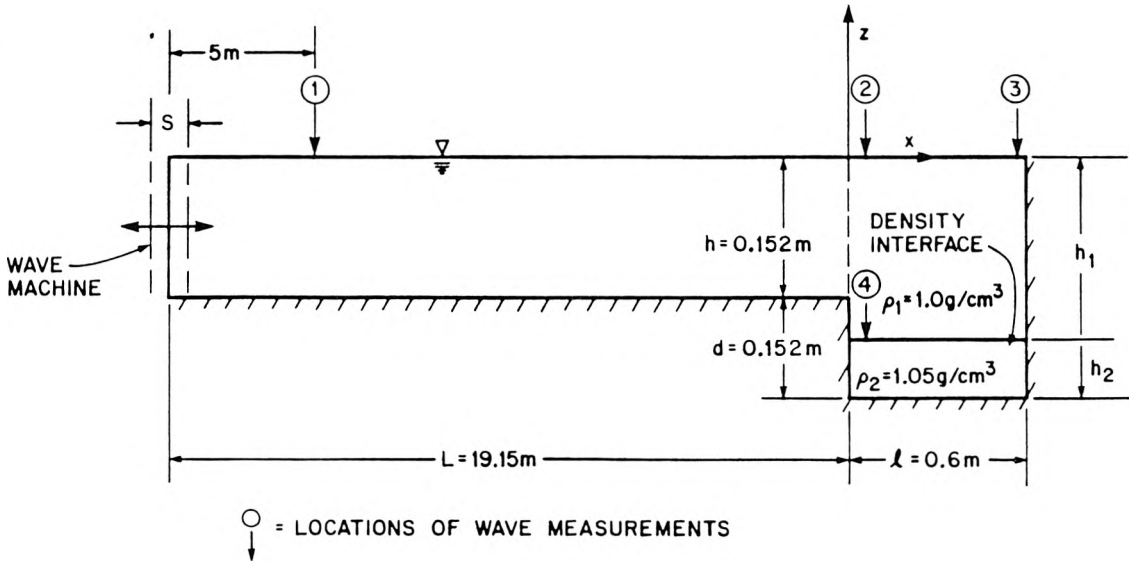

Figure 5.1.1. Experimental arrangement and locations of wave measurements.

difference was sufficiently large to provide a stable stratification during filling and during resonant conditions in the trench, yet sufficiently small to provide an adequate test of the theoretical results based on small density difference. In addition, it was reasonably representative of natural conditions. The primary consideration in determining the trench dimensions was that internal waves of various characteristics could be generated in the trench within the capacity of the wave generator. Water depth in the constant-depth channel was 15.2 cm in all the experiments. Two different depths of the heavier fluid in the trench were used in the experimental investigation: (i) $h_1 = 22.8\,\text{cm}$, $h_2 = 7.6\,\text{cm}$; and (ii) $h_1 = 26.6\,\text{cm}$, $h_2 = 3.8\,\text{cm}$. In (i), the lowest mode of standing internal waves in the trench had a natural period of oscillation $\approx 7.8\,\text{sec}$. The generated internal waves were similar to the Stokes

Wave Gage	x (m)
1	–14.15
2	0.01
3	0.585
4	0.01

Table 5.1.1. Locations of wave measurements.

second order finite amplitude surface waves (see, Thorpe 1968). In (ii), the depth of the lower fluid was small compared to the wavelength of the internal waves so that the generated internal waves were shallow water waves. The wave period for the lowest mode of oscillation of the internal waves in the trench was $\approx$ 10 sec. All the experiments with stratified fluid were conducted with the lowest mode of internal oscillations in the trench. Note that the standing surface waves, which had wavelengths much longer than those of the internal waves within the trench, resonated at the natural frequencies of oscillation of the constant-depth channel.

A second consideration in determining the trench dimensions was concerned with placing the trench within one module of glass panels (5 ft) of the side walls of the wave tank so that we had an unobstructed view of the trench and a portion of

the constant-depth channel.

Conditions within the trench were governed by surface waves in the fresh water filled constant-depth channel, which was 19.15 m long measured from the mean position of the wave plate to the upstream edge of the trench. A typical experiment started with quiescent fluid in the wave tank, a sinusoidal motion of the wave generator was maintained until a steady-state condition had been established in the trench. Steady-state condition is, by definition, considered to have taken place at time t when the relative variation of all positive extrema along the wave records is less than 5% from time t onwards. An estimate of the time required to establish a steady-state condition may be obtained by considering surface wave motion in a constant-depth channel without the trench. In this analysis, the origin is taken at the mean position of the wave generator. The surface elevation at time t after start of the wave generator (see Appendix) is:

$$\eta(x,t) = -\frac{Skh}{2}\frac{\cos k(x-L)}{\sin kL}e^{-i\sigma t} + \sum_{n=1}^{\infty}(-1)^n\frac{Sh}{L}\frac{(kL)^2}{(kL)^2-(n\pi)^2}\cos n\pi\left(\frac{x}{L}-1\right)e^{s_n t} \qquad (5.1.1)$$

where S is the stroke of the wave generator, h is the water depth, L is the channel length, and σ represents the circular frequency ($2\pi/T$ with T the wave period). The wave number k is:

$$k = \frac{\sigma}{\sqrt{gh}\left(1-\frac{1}{3}\frac{\sigma^2 h}{g}\right)^{1/2}}\left[1+(1+i)\left(\frac{\nu}{2\sigma}\right)^{1/2}\left(1+\frac{h}{b}\right)\frac{1}{2h}\right] \qquad (5.1.2)$$

wherein ν is the kinematic viscosity, and $2b$ is the width of the channel. The first term in (5.1.1) represents the steady-state solution and the summation term is the transient excitation that decays with time. The term s_n is:

$$s_n = -i(\sigma_n - \delta\sigma_n) - \delta\sigma_n, \qquad (n = 1,2,\ldots) \qquad (5.1.3)$$

where σ_n is the resonant frequency of the channel given by the inviscid theory:

$$\sigma_n = \frac{n\pi\sqrt{gh}}{L\left(1+\frac{1}{3}\left(\frac{n\pi h}{L}\right)^2\right)^{1/2}}, \qquad (n=1,2,\ldots) \tag{5.1.4}$$

and $\delta\sigma_n$ is the viscous correction:

$$\delta\sigma_n = \frac{\left(\frac{\nu\sigma}{2}\right)^{1/2}\left(1+\frac{h}{b}\right)}{2h\left(1+\frac{1}{3}\left(\frac{n\pi h}{L}\right)^2\right)}, \qquad (n=1,2,\ldots). \tag{5.1.5}$$

The denominator in (5.1.4) is $\approx L$ for $h/L \ll 1$. Thus the interval between two wave periods of resonant oscillation T_n and T_{n+1} is $\approx T_n/(n+1)$. Steady-state condition is considered to have been established when the amplitude of the transient excitation has decreased to less than 5% of its initial value, that is, $e^{\Re[s_n t]} < 0.05$ in (5.1.1) where $\Re$ denotes the real part of a complex number. From (5.1.3)–(5.1.5) the number of oscillations required to establish steady-state condition near resonance is found to be:

$$\frac{t}{T_n} \geq \frac{3h\left(1+\frac{1}{3}\left(\frac{n\pi h}{L}\right)^2\right)}{\pi\left(\frac{\nu}{2\sigma}\right)^{1/2}\left(1+\frac{h}{b}\right)}. \tag{5.1.6}$$

Because the trench dimensions were much smaller than the wavelength of surface waves in the wave tank, addition of the trench was not deemed to change the surface wave condition in the wave tank significantly. This was confirmed by both theory and experiment, which will be presented later. For an estimate of the time required to establish a steady-state condition in the wave tank we may neglect the change in water depth in the trench region and consider the entire working section of the wave tank between the mean position of the wave plate, and the end wall, to be of constant depth h, that is, $L = 19.75\,\mathrm{m}$. In the experiments with stratified fluid in the trench there were approximately two surface wavelengths in the constant-depth channel. From (5.1.4), the wave period of resonant oscillation of the constant-depth

channel corresponding to $n = 4$, with $L = 19.75\,\mathrm{m}$ and $h = 0.152\,\mathrm{m}$, is $\approx 8.1\,\mathrm{sec}$. With $2b = 0.394\,\mathrm{m}$ and $\nu = 1.0 \times 10^{-6}\,\mathrm{m^2 sec^{-1}}$ this implies ≈ 100 oscillations of the wave generator to establish a steady-state condition in the wave tank. This result is independent of the length of the channel L for a given value of σ_n. However, surface waves of the same wave period correspond to a smaller modal number n in a shorter channel. Because the time interval between successive modes of resonant oscillation of the main channel given by $(T_n - T_{n+1})$ increases with decreasing n, with a shorter channel a resonant condition for the internal waves in the trench that corresponds to an off-resonant condition for the surface waves in the constant-depth channel may be found. With this arrangement, the internal wave will be much more sensitive to variations of wave period than the surface wave. This is important because the major objective in this study is to investigate the frequency dependence of the internal motions in the trench due to surface waves.

5.2 Comparison of Theoretical Results with Experiments

A general description of all the experiments conducted in this study is given in table 5.2.1, and a summary of the nominal experimental conditions is given in table 5.2.2; the exact conditions for these experiments will be presented later. To illustrate the different physical effects involved in wave-trench interaction, the presentation and discussion of the results of the laboratory investigation are divided into five sub-sections. The results of surface wave motion in a constant-depth channel filled with fresh water without the trench at the end of the channel are presented in § 5.2.1. In these experiments (Series H) the rectangular cavity in the trench region was filled in by a plywood false bottom. Thus the length of the constant-depth channel was $L = 19.75\,\mathrm{m}$ measured from the mean position of the wave plate to the end wall. These experiments were conducted because the motion of the strati-

Experiment Series	Description
G	fresh water in the constant-depth channel and trench
H	fresh water in the constant-depth channel without the trench
I	fresh water in the constant-depth channel, and a deep layer of salt water in the trench with a thin diffuse salinity interface
J	same as Series I, but with a larger thickness of the diffuse salinity interface
K	fresh water in the constant-depth channel, and a shallow layer of salt water in the trench with a thin diffuse salinity interface
L	damping of standing internal wave in a rectangular basin partially filled with a stratified fluid of water and salt water
M	same as Series K, but with a larger thickness of the diffuse salinity interface

Table 5.2.1. General description of experiments performed.

Experiment Series	T (sec)	S (mm)	L (m)	ℓ (m)	d (cm)	h (cm)	h_1 (cm)	h_2 (cm)	δ (cm)	ρ_1 (g/cm^3)	ρ_2 (g/cm^3)
G	7.0-9.0	4.8-5.0	19.15	0.6	15.2	15.2	30.4	0.0		1.0	
H	7.0-9.0	4.6-5.0	19.75			15.2				1.0	
I	7.3-8.2	4.6-29.5	19.15	0.6	15.2	15.2	22.8	7.6	1.3	1.0	1.05
J	7.8-8.4	3.3-14.0	19.15	0.6	15.2	15.2	22.8	7.6	2.5	1.0	1.05
K	9.6-10.8	4.8-114.3	19.15	0.6	15.2	15.2	26.6	3.8	1.3	1.0	1.05
L	7.8, 10.0			0.6			22.8, 26.6	7.6, 3.8		1.0	1.05
M	10.0-11.2	4.9-50.0	19.15	0.6	15.2	15.2	26.6	3.8	2.5	1.0	1.05

Table 5.2.2. Summary of experimental conditions. The numbers presented in the table are nominal values.

fied fluid in the trench is directly related to the conditions of the surface waves in the fresh water filled constant-depth channel. Hence, it is important to investigate first the surface wave motion in the constant-depth channel without the trench. By comparing these measurements with the results of the experiments with the trench, we could determine the effects of the trench on the surface wave. The results of the experiments with fresh water in both the trench and the constant-depth channel (Series G) are presented next in § 5.2.2. The experimental set-up was as shown in figure 5.1.1 except that fresh water filled the trench in these experiments. The distance between the mean position of the wave plate and the upstream edge of the trench was $L = 19.15\,\mathrm{m}$, and the width of the trench was $\ell = 0.6\,\mathrm{m}$. In § 5.2.3 the results of the experiments with a fresh water–salt water fluid in the trench and

fresh water in the constant-depth channel are presented. The density difference between the two fluids was $\approx 5\%$ in these experiments. The depth of the upper fluid (water) was $h_1 = 22.8\,\text{cm}$, and the depth of the lower fluid (salt water) was $h_2 = 7.6\,\text{cm}$. The depths h_1 and h_2 respectively, were measured from the undisturbed water surface and the trench bottom to the center of the diffuse salinity interface. Two sets of experiments were conducted with the above conditions in the trench: (i) $\delta \approx 1.3\,\text{cm}$ (Series *I*); and (ii) $\delta \approx 2.5\,\text{cm}$ (Series *J*), where δ is the thickness of the diffuse salinity interface defined as the ratio of the maximum density difference between the two fluids to the maximum density gradient in the diffuse salinity interface. From the results of these experiments we could determine the effects of a density transition region on the internal wave motion. In § 5.2.4 we present the results of those experiments where the total depth of the stratified fluid in the trench region was kept the same (i.e., $h_1 + h_2 = 30.4\,\text{cm}$), whereas the depth of the lower fluid (salt water) was reduced to $h_2 = 3.8\,\text{cm}$. Two sets of experiments were conducted, with $\delta \approx 1.3\,\text{cm}$ (Series K), and with $\delta \approx 2.5\,\text{cm}$ (Series M), respectively. A major objective of these experiments was to determine whether non-linear processes are important in the generation of internal waves in a submarine trench by surface waves, or whether the linear models developed in Chapter 3 were sufficient. In § 5.2.5 the results of the decay of standing internal waves in a rectangular basin are presented. In these experiments a standing internal wave was generated in the trench as before. After the internal wave motions in the trench had attained steady-state conditions, a gate was lowered at the upstream edge of the trench to separate the trench region from the constant-depth channel. In this manner, the effects of boundary friction on internal wave motions in the trench could be studied separately.

5.2.1 Experiments with Fresh Water in a Constant-Depth Channel

In these experiments, the rectangular trench as shown in figure 5.1.1 was filled in by a plywood false bottom; the gaps between this section and the adjacent false bottom and the side walls of the wave tank were sealed by polyethylene rope. The length of the constant-depth channel L was 19.75 m, with a water depth h of 15.2 cm. Note that L is defined as the length of the constant-depth region measured from the mean position of the wave plate to the upstream edge of the trench, therefore without the trench L is the length of the constant-depth region between the mean position of the wave plate and the end wall, that is, $L = 19.75$ m. Waves were generated by a bulkhead wave generator that moved in simple-harmonic motion with a constant stroke $S = 4.8$ mm. A series of experiments were conducted for wave periods varying from 7.0 sec to 9.0 sec.

The response of the surface waves is shown in figure 5.2.1 where the wave height at the end wall of the channel, H_3, normalized by the stroke of the wave machine, S, is plotted as a function of the product of the wave number, k, and the length of the channel, L. The wave height is defined as the distance between the positive and the negative extrema of the surface elevation at steady-state condition. The wave number k is calculated using the dispersion relation for a homogeneous fluid (equation 3.1.25a) with the wave period T measured in the experiments. The linear inviscid solution shown in figure 5.2.1 is constructed using potential function formulation in a similar manner to the wavemaker problem of Ursell, Dean and Yu (1960). The only difference between the two problems is that the horizontal velocity must vanish at the end wall in this case, while in the wavemaker problem the channel extends from the oscillating plane of the wave generator to infinity. The surface elevation of the standing wave at the end wall is given by:

$$\eta_3 = \frac{\rho_1 S \sigma^2}{4g} \left[\frac{(\Lambda^h)^{-1}}{k^2} \frac{\sinh 2kh}{\sin kL} - \sum_n^{\infty} \frac{(\Lambda_n^h)^{-1}}{\hat{k}_n^2} \frac{\sin 2\hat{k}_n h}{\sinh \hat{k}_n L} \right] \cos \sigma t \qquad (5.2.1)$$

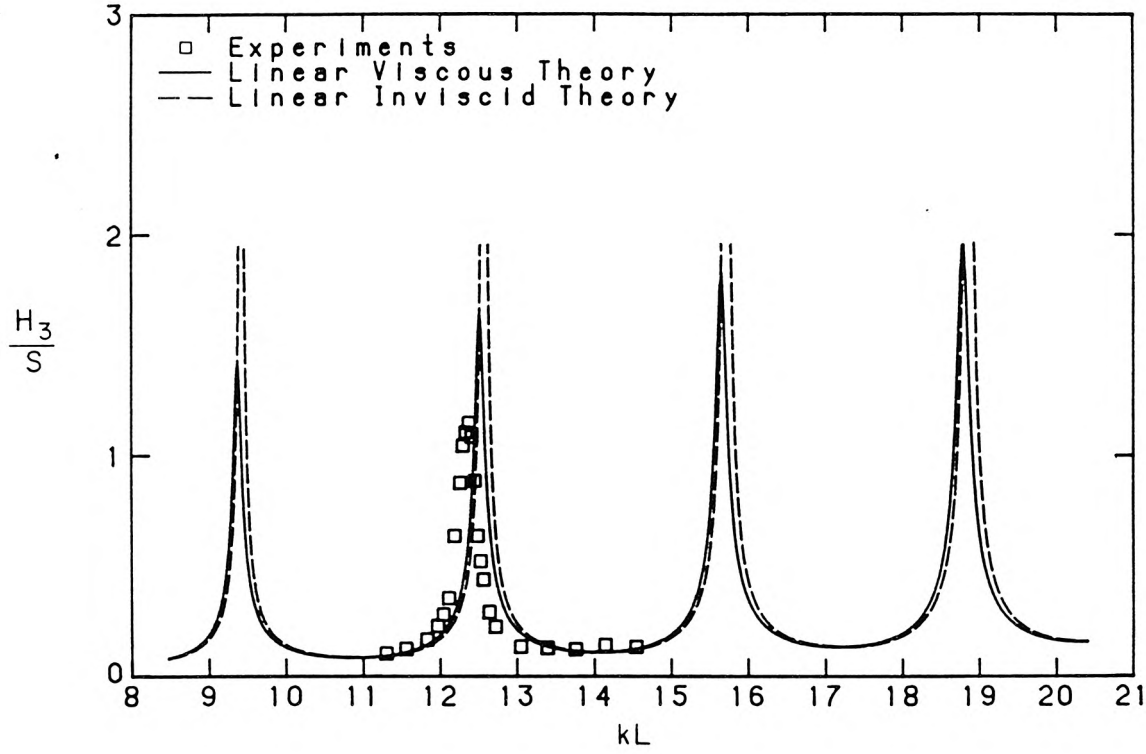

Figure 5.2.1. Variation of normalized wave height at the end wall with relative wave number for constant-depth channel conditions; $h = 15.2\,\mathrm{cm}$, $L = 19.75\,\mathrm{m}$.

wherein k, Λ^h, and $\hat{k}_n$, Λ^h_n, $(n = 1, 2, \ldots)$ are given by (3.1.23) and (3.1.25). Equation 5.2.1 is the inviscid solution; notice that the solution is singular when $kL = n\pi$, $(n = 1, 2, \ldots)$. The comparable expression for η_3 with energy dissipation is the same as (5.2.1) but the determined wave number k using the inviscid theory (equation 3.1.25a) in the denominator term of $\sin kL$ should be replaced by the complex wave number, which includes both the attenuation rate and the shift in wave number due to viscosity. The wave number including the viscous effects is given by (3.3.45c) with (3.3.49) and (3.3.78). It is recalled from § 3.3 that energy dissipation in the homogeneous fluid is considered to take place in the boundary layers adjacent to the side walls and at the channel bottom. In addition, the flows in the boundary layers are assumed to be laminar.

At resonance, the wavelength of the standing waves in the channel is given by $\lambda = 2L/n$, thus $kL = n\pi$, $(n = 1, 2, \ldots)$. Using the inviscid theory, the wave period for the resonant mode shown at $kL = 4\pi$ is found to be $T_0 \approx 8.1$ sec, which is about 0.3 sec greater than the wave period corresponding to the lowest mode of oscillation of the internal waves in the trench for the experimental conditions of Series I shown in table 5.2.2. The measured amplitude response is somewhat smaller than the theoretical curve for the damped case, and the measured resonant peak at $T = 8.226$ sec $(kL = 12.37)$ is shifted from the inviscid natural period of oscillation of the channel by approximately 6%, and from the viscous prediction by a somewhat smaller amount; these are compared to the interval between adjacent resonant peaks. These results indicate that energy dissipation in the channel was larger in the actual fluid, though the difference between experiments and theory was small.

In figure 5.2.2, the variation of the wave extrema, normalized by S, is plotted as a function of kL near the inviscid natural resonant wave period of 8.1 sec. Because of small amounts of drifting in the wave gage analog output during the experiment, the mean water level obtained from the wave records was not necessarily equal to zero. Thus, the amplitudes of the wave crest and the wave trough at steady-state conditions were evaluated with respect to the computed mean water level. Nonlinear effects are evident in these results, the maximum ratio of the positive extremum to the negative extremum measured at the end wall was about 1.9 at a wave period of $T = 8.2$ sec $(kL = 12.41)$. For standing surface waves in a fluid of depth h, Tadjbakhsh and Keller (1960) developed a finite amplitude wave theory to the third order. The equation of the standing wave profile to second order is:

$$\eta = a \sin \sigma t \cos kx + \frac{1}{8} a^2 k \left(T - T^{-1} + T^{-3} \left(T^2 - 3 \right) \cos 2\sigma t \right) \cos 2kx \qquad (5.2.2)$$

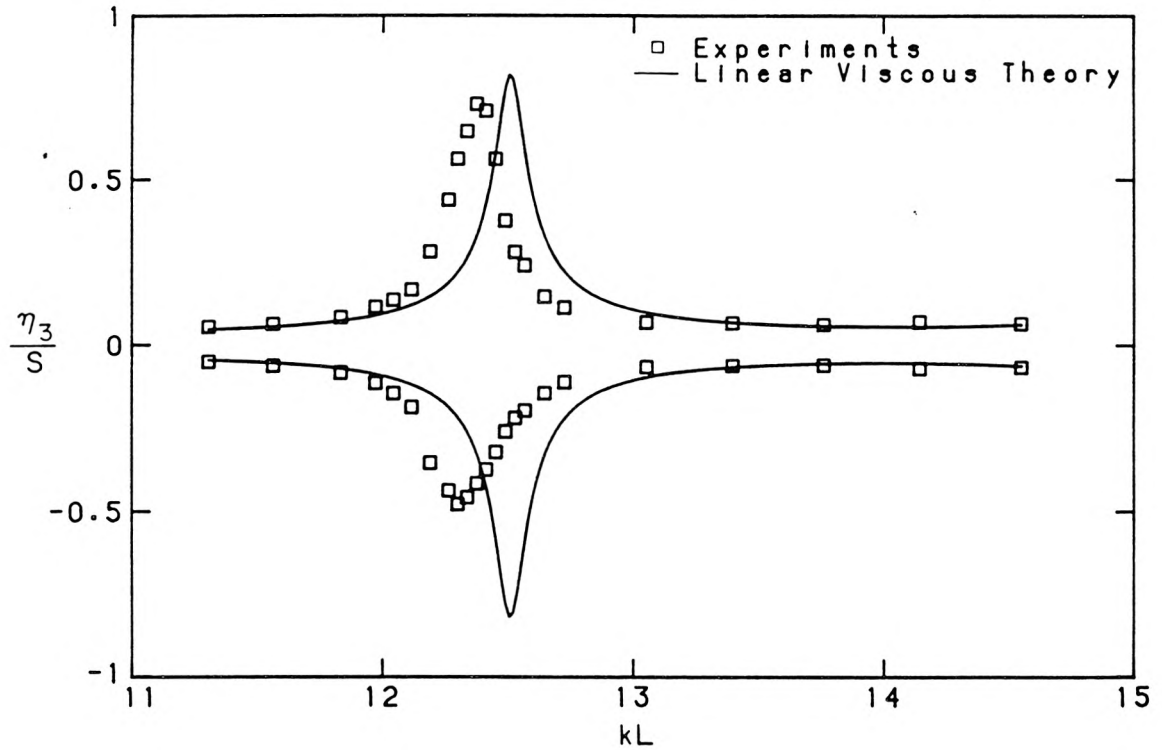

Figure 5.2.2. Variation of wave extrema at the end wall with relative wave number near resonance at $kL = 4\pi$; $h = 15.2\,\text{cm}$, $L = 19.75\,\text{m}$.

and the dispersion relation to third order is:

$$\sigma^2 = gk\mathcal{T}\left(1 - \frac{a^2k^2}{32\mathcal{T}^4}\left(2\mathcal{T}^6 + 3\mathcal{T}^4 + 12\mathcal{T}^2 - 9\right)\right) \tag{5.2.3}$$

where a is the wave amplitude of the linear solution, k is the wave number, σ is the circular frequency, h is the fluid depth, and $\mathcal{T}$ is written for $\tanh kh$. The above expansion is valid if the ratio of the coefficient of the second order term to that of the first is much less than unity, that is, if:

$$\left|\frac{ak\left(\mathcal{T} - \mathcal{T}^{-1} + \mathcal{T}^{-3}\left(\mathcal{T}^2 - 3\right)\right)}{8}\right| \ll 1. \tag{5.2.4}$$

If $kh \ll 1$, equation (5.2.4) reduces to:

$$\frac{3H}{16k^2h^3} \ll 1 \tag{5.2.5}$$

where $H = 2a$ is the wave height of the linear solution.

The difference between the dimensionless parameter, H/k^2h^3, and the Ursell number is of some importance. The Ursell number is defined as $Ur = Hl^2/h_0^3$, where H, l, and h_0 refer to a characteristic wave height, wavelength and depth. Equation 5.2.2 is obtained by expanding the standing wave profile in the form of a power series taking the wave slope ka as the perturbation parameter. The analysis is similar to the expansion technique used by Stokes for progressive waves of finite amplitudes. When $kh \ll 1$, the dimensionless parameter H/k^2h^3 is proportional to the ratio of the coefficient of the second order term in (5.2.2) to that of the first. However, when the value of kh is so small that H/k^2h^3 is of order unity (5.2.2) must become invalid, and a different expansion procedure that assumes long waves is necessary. It is well known that for long waves whose wavelengths are large compared to the water depth the magnitude of the nonlinear terms is given by the wave height parameter, H/h_0, and the magnitude of the vertical acceleration is indicated by the dispersive parameter, h_0^2/l^2. Nonlinear effects result in the wave crest moving faster than the leading edge, hence wave breaking will eventually occur. On the other hand, vertical acceleration results in long waves travelling faster than short waves, hence a non-sinusoidal wave will disperse into its spectral components as the wave propagates. The Boussinesq equations (see, for example, Whitham, 1974) are derived by taking both the values of H/h_0 and h_0^2/l^2 small but of an equal order of magnitude, hence including the effects of finite amplitude and vertical acceleration as a first approximation, whose opposing effects allow waves of permanent form. Thus, the Ursell number measures the relative importance of the nonlinear effects to the dispersive effects. The dimensionless parameter H/k^2h^3 may be regarded as another form of Ursell number when $kh \ll 1$ (with $H/k^2h^3 \ll 1$).

From (5.2.5), with $h = 15.2\,\text{cm}$, $L = 19.75\,\text{m}$, and $k = 4\pi/L$ for the resonant

mode of $n = 4$, the condition that second order effects are negligible is found to be:

$$\frac{H}{h} \ll 0.05. \tag{5.2.6}$$

The measured value of H/h at the end wall for $T = 8.2\,\text{sec}$ ($kL = 12.41$) was about 0.034, thus it is not surprising that second order effects were important in these experiments near resonance, where the wave heights were large compared to the water depth. Away from resonance the agreement between the experimental results and the linear theory is good.

To further illustrate the characteristics of the surface waves near resonance the steady-state portion of the time history of the surface elevation at the end wall is shown in figure 5.2.3 for a range of relative wave frequency σ/σ_0, where $\sigma_0 = 2\pi/T_0$ with $T_0 = 8.1\,\text{sec}$ corresponding to the predicted wave period for the resonant mode of $kL = 4\pi$ using the linear inviscid theory. The ordinate is normalized surface elevation with respect to the stroke of the wave generator, and the abscissa is a dimensionless time. Note that $L/\sqrt{gh}$ is the time for a surface wave to travel from the wave plate to the end wall. Because $L \approx 2\lambda$ for this resonant mode, the abscissa is approximately equal to $t/2T$, which is half the number of oscillations generated by the wave machine. It is seen in figure 5.2.3 that the surface waves are almost sinusoidal away from resonance (see, for example, $\sigma/\sigma_0 = 1.006$). As σ decreases, the crest to trough ratio of amplitude increases, a secondary oscillation appears behind the main wave before the frequency for the peak amplitude response ($\sigma/\sigma_0 = 0.985$) is reached. This secondary oscillation grows in amplitude as σ is further decreased past the resonant peak until it becomes equal in amplitude to the main wave. The two waves then merge together and eventually a nearly sinusoidal wave appears. This behaviour is similar to that observed by Lepelletier (1980); in that study the waves were those generated in a rectangular tank by moving the tank in an oscillatory manner.

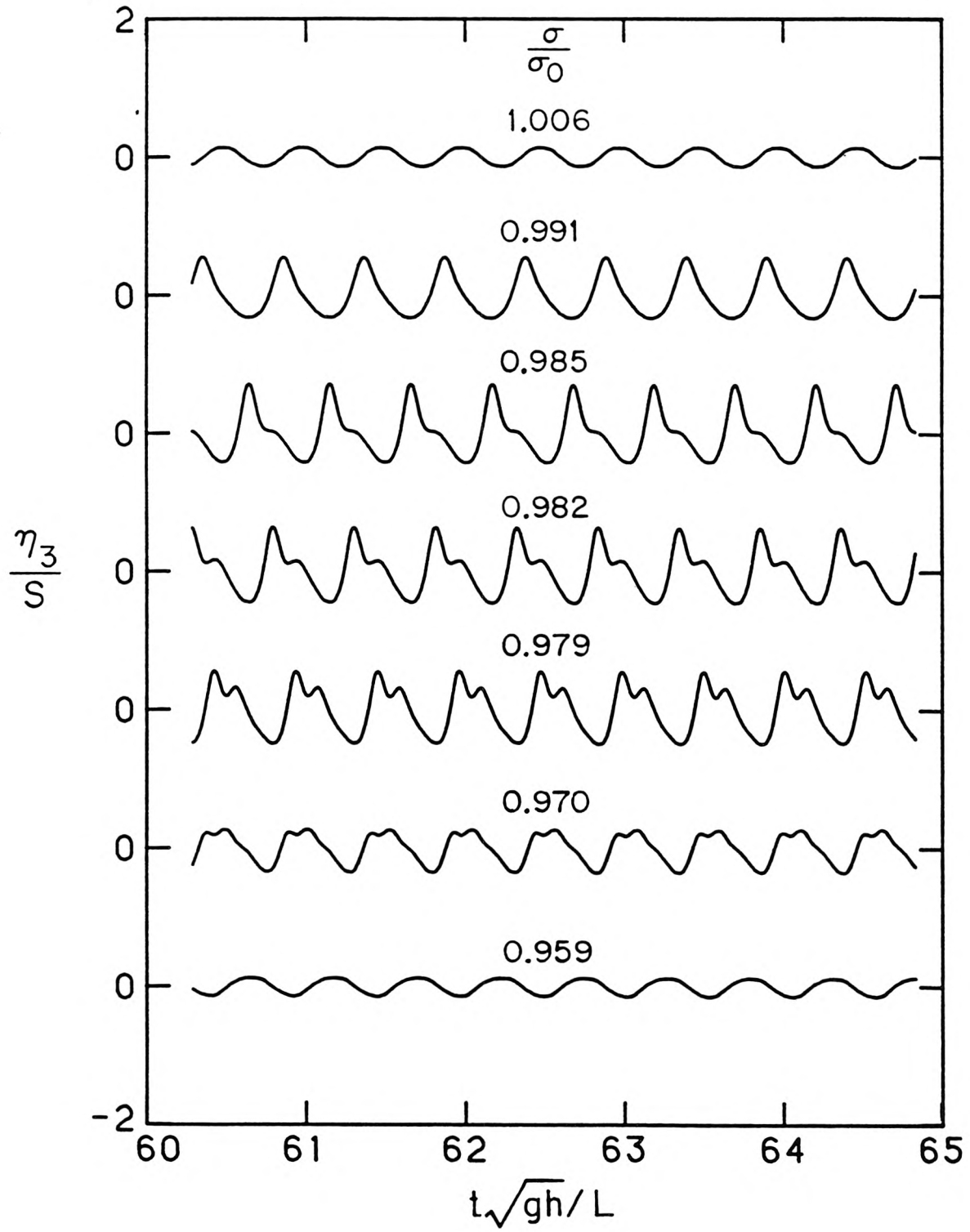

Figure 5.2.3. Steady-state free surface motions at the end wall for relative circular frequencies near resonance at $kL = 4\pi$; $h = 15.2\,\text{cm}$, $L = 19.75\,\text{m}$, $S = 4.8\,\text{mm}$.

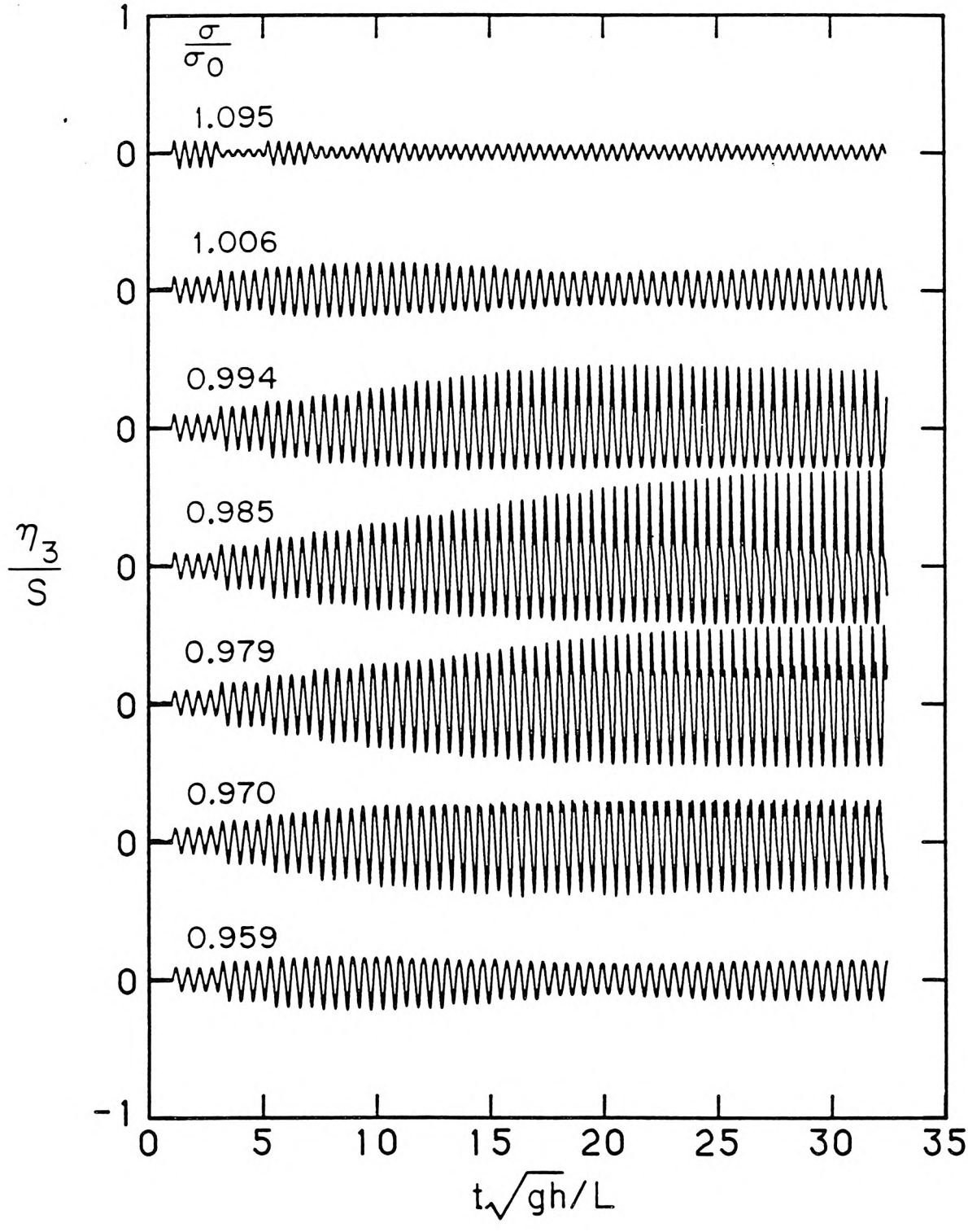

Figure 5.2.4. Time histories of free surface motion at the end wall as recorded experimentally for relative circular frequencies near resonance at $kL = 4\pi$; $h = 15.2\,\text{cm}$, $L = 19.75\,\text{m}$, $S = 4.8\,\text{mm}$.

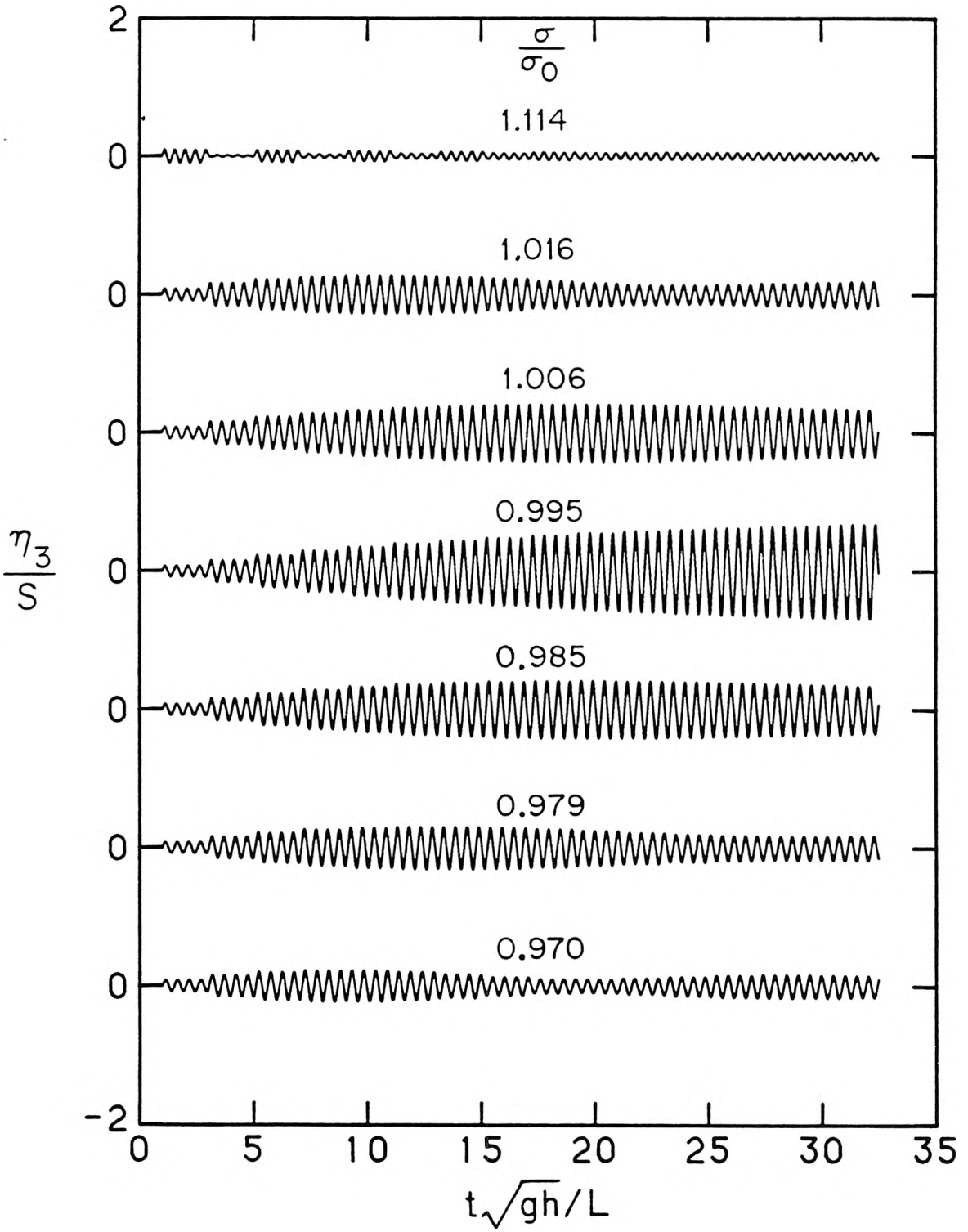

Figure 5.2.5. Time histories of free surface motion at the end wall for relative circular frequencies near resonance at $kL = 4\pi$, computed using (5.1.1); $h = 15.2\,\mathrm{cm}$, $L = 19.75\,\mathrm{m}$.

To illustrate the evolution of the standing surface waves in the wave tank the complete water surface time histories at the end wall from the start of the wave generator are presented in figure 5.2.4 as recorded experimentally for several wave frequencies near resonance. It is helpful to compare this figure with the theoretical time histories obtained using the linear theory, which can be computed from the steady-state solution of (5.2.1) by Fourier superposition. However, the effort is much reduced if long waves are assumed in the wave tank. An analytical solution of the time history of the surface motion is given by (5.1.1); the solution is constructed using linear dispersive dissipative theory. Some computed time histories are shown in figure 5.2.5. Note that the scale of the ordinate is twice as large in figure 5.2.4 as in figure 5.2.5. It is seen that the amplitude of the surface waves increases about every four oscillations initially. This is because near the resonant mode of $kL = 4\pi$ there are approximately two wavelengths in the constant-depth channel. Thus, when the wave generator is first started, it takes approximately a time of $2T$ for the first wave of the progressive wave train (primary incident wave) to reach the end wall. There the wave train is nearly fully reflected (primary reflected wave); the reflection process preserves the phase of the incident wave. The primary reflected wave is reflected from the wave plate a time of $2T$ later (secondary incident wave). At resonance, the length of the channel is an integral multiple of half wavelength ($L/\lambda = n/2$, $n = 1, 2, \ldots$) hence the primary incident wave and the secondary incident wave are in phase, and the two waves superimpose to increase the wave amplitude. But the combined wave does not arrive at the end wall until a time of $2T$ later, when the wave record at the end wall shows a distinct change in the wave amplitude. In time, the tertiary and the higher order incident waves are also superimposed in phase, hence the wave amplitude at the end wall increases every four oscillations. However, the higher order incident waves have progressively smaller amplitudes due to viscous dissipation; thus, the wave motion eventually attains a

steady-state condition. Because at resonance the incident waves are always in phase at the end wall, beat effects are absent. When off resonance the wavelengths of the incident waves are not an integral multiple of $\lambda/2$, thus the higher order incident waves superimpose at different phase angles (either constructively or destructively) with the primary incident wave, therefore changing the wave amplitude at the end wall each time a new train of reflected waves arrives. The period of the beat is longer for smaller phase shifts between the incident waves, and this period becomes infinite at resonance. An interesting situation is shown in the top time traces of figures 5.2.4 and 5.2.5, respectively, for $\sigma/\sigma_0 = 1.095$ and $\sigma/\sigma_0 = 1.114$. In these cases, there are approximately two and a quarter wavelengths in the constant-depth channel. The secondary incident wave is 180° out of phase with the primary incident wave. Because viscous effects take time to develop, the amplitude of the secondary incident wave is almost the same as that of the primary incident wave, hence the surface elevation at the end wall drops to nearly zero, four oscillations after the start of the wave generator. The tertiary incident wave is in phase with the primary incident wave, and the wave amplitude at the end wall increases again after another four oscillations. This process repeats itself but the higher order incident waves have progressively smaller amplitudes due to viscous dissipation, thus the wave motion eventually attains a steady-state condition.

In figure 5.2.4, $\sigma/\sigma_0 = 0.985$ ($kL = 12.37$) corresponds to the maximum amplitude response measured in these experiments. The surface elevation is almost symmetrical about the mean water level initially. Then the front face of the wave steepens as the amplitude increases, and the amplitude of the wave crest becomes increasingly larger than the amplitude of the wave trough. Eventually, a secondary oscillation emerges behind the main wave and grows with the main wave as wave motions in the wave tank approach steady-state conditions.

It should be noted that long wave theory can be used to model the surface

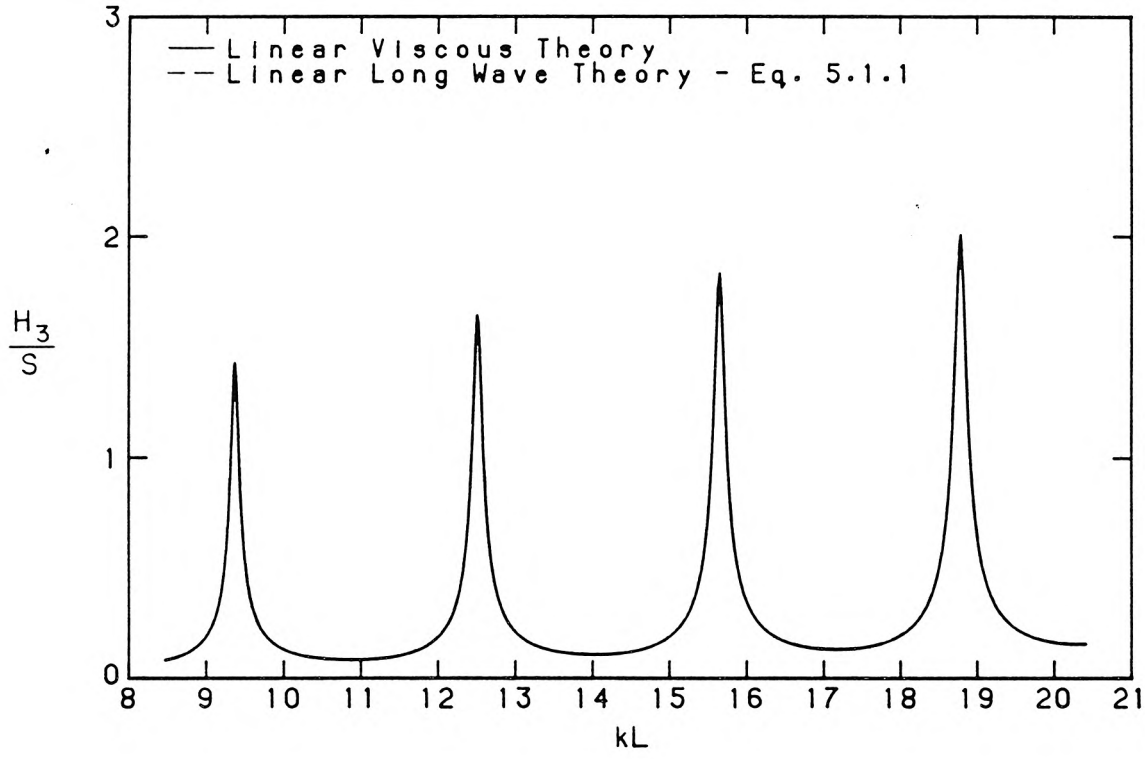

Figure 5.2.6. Comparison between the predicted normalized surface wave heights at the end wall obtained using the linear viscous theory (equation 5.2.1), and the long wave theory (equation 5.1.1); $h = 15.2\,\text{cm}$, $L = 19.75\,\text{m}$.

wave motion in the wave tank for the conditions in our experiments. The common criteria used to specify long waves is that the water depth to wavelength ratio h/λ is less than 0.05. For the water depth of 15.2 cm used in this study, this implies a wavelength larger than about 3.0 m ($kL < 40$), which is actually much smaller than the wavelengths of the surface waves in these experiments ($\approx 10\,\text{m}$). Indeed, a comparison of the normalized wave heights at the end wall (figure 5.2.6) obtained using the linear viscous theory (equation 5.2.1), which is valid for all ranges of relative water depth h/λ, and the long wave theory (equation 5.1.1), shows no difference in the theoretical results from the two theories for the range of kL of interest to this study. Notice that the amplitude response of the surface wave H_3/S increases as the relative wave number kL increases. This is because the amplitude of

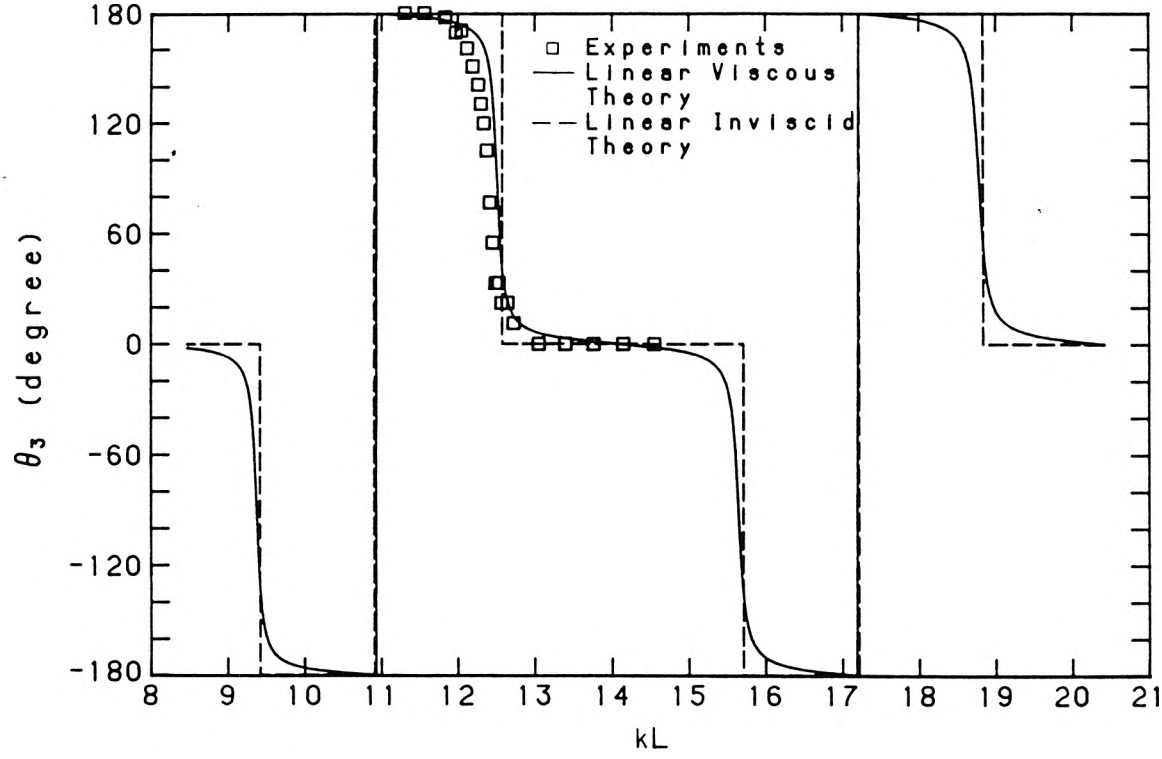

Figure 5.2.7. Variation of the relative phase angle between surface motion at the end wall and wave plate motion with relative wave number; $h = 15.2\,\text{cm}$, $L = 19.75\,\text{m}$.

the incident wave generated by the bulkhead wave generator increases as the value of kh increases. This result is most easily understood by considering the incident waves generated by an oscillating vertical plate that moves in simple-harmonic motion in a constant-depth channel that extends from the wave plate to infinity (see, Ursell, Dean and Yu, 1960).

Finally, the variation of the relative phase angle between the surface motion at the end wall and the wave plate motion, θ_3, with relative wave number, kL, is shown in figure 5.2.7. The relative phase angle is defined between $-180°$ and $180°$. For example, if the phase angle of the surface motion at the end wall leads the phase angle of the wave plate motion by $270°$, the relative phase angle between the surface motion at the end wall and the wave plate motion is equal to $-90°$. When a

secondary oscillation such as those shown in figure 5.2.3 appeared, the wave record was filtered to eliminate the secondary wave, and the phase angle was obtained from the filtered wave record. Several features in figure 5.2.7 are characteristic of the wave motion in this wave generator–closed channel configuration. These are discussed here to help the reader to interpret the results of the trench experiments. First let us consider the linear inviscid theory. In this case the phase angle between the surface motion at the end wall and the wave plate motion must be either in phase or 180° out of phase. This is because the net work done on the fluid by the wave generator over one complete oscillation must be zero, because there is no energy dissipation in the channel in the inviscid theory. As a result, the fluid motion in the channel is a true standing wave; the end wall is always an antinode, the location of the wave plate cannot be an antinode because the horizontal velocity would then be zero, and the boundary condition on the oscillating plate cannot be satisfied. Because the length of the channel is an integral multiple of half wavelength ($L/\lambda = n/2$, $n = 1, 2, \ldots$) at resonance, and the standing wave is an antinode at the end wall, the boundary condition at the wave plate cannot be satisfied at resonance, hence the solution is singular. In the linear viscous theory, the wave motion in the channel is also represented by two sinusoidal progressive waves travelling in opposite directions, but the wave amplitude of each progressive wave is attenuated in its direction of wave propagation. The left- and right-going progressive waves must have the same amplitude and phase at the end wall, where the horizontal velocity vanishes. Moving away from the end wall, and in the direction towards the wave generator, the amplitude of the left-going wave is attenuated due to viscous damping, whereas the amplitude of the right-going wave increases at the same rate in this direction opposite to its direction of wave propagation. Thus, the wave motion in the channel is not a true standing wave, in that the envelope of the wave amplitude of the combined wave has no nodes and antinodes besides the

antinode at the end wall. Because of this, the conclusion, which is predicted by the linear inviscid theory, that an antinode occurs at the wave plate at resonance, cannot occur if based on the linear viscous theory. The surface motion at the end wall is 90° out of phase with the motion of the wave plate at the frequency of the resonant peak, because the net work done by the wave generator on the fluid is then a maximum. This condition is required to balance the maximum rate of energy dissipation in the channel at resonance. When off resonance, the relative phase angle varies continuously with the frequency of the wave generator to adjust for the energy balance between viscous dissipation in the channel and energy input from the wave generator. The variation of the relative phase angle with frequency is directly related to the fluid state at the wave plate.

In summary, surface wave motions in a constant-depth channel with a vertical wall at one end and a bulkhead wave generator that moves in simple-harmonic motion with a constant stroke at the opposite end were studied experimentally, and theoretically using linear wave theory, for conditions near a mode of resonant oscillation of the surface waves in the constant-depth channel. Surface wave measurements were obtained that would be compared with the results of the experiments with the trench to determine the effects of the trench on the surface waves. The experimental results indicate that the response curve is very steep near resonance, and a secondary oscillation develops in the main wave when the wave amplitude is sufficiently large. Thus, the characteristics of the surface waves are very sensitive to variations of wave period near a resonant mode of oscillation of the surface waves in the constant-depth channel. For this reason, in studying the generation of internal waves in the trench, it is desirable to have a near-resonant condition of the internal waves in the trench and an off-resonant condition of the surface waves in the constant-depth channel, then the motions of the internal waves will be much more sensitive to variations of wave period than the motions of the surface waves.

5.2.2 Experiments with Fresh Water in a Rectangular Trench

The objectives of these experiments were: (i) to determine the effects of change in water depth on the surface waves; and (ii) to obtain surface wave measurements for comparison with results of the experiments that used a stratified trench. In these experiments, the width of the trench was $\ell = 60\,\text{cm}$, and the depth of the trench was $d = 15.2\,\text{cm}$. The rectangular trench was connected to the end of a constant-depth channel of length $L = 19.15\,\text{m}$ filled with fresh water to a depth of $h = 15.2\,\text{cm}$ (figure 5.1.1). Thus the water depth in the trench region was $h_1 = 30.4\,\text{cm}$. A vertical wall was located at the downstream end of the trench, at the other end of the constant-depth channel a bulkhead wave generator consisting of a vertical plate moved in simple-harmonic motion with a constant stroke $S = 4.8\,\text{mm}$. Surface wave motion in the wave tank was investigated for wave periods varying from 7.0 sec to 9.0 sec, that is, near the resonant mode of $kL = 4\pi$, where k is the wave number of the surface wave obtained in the constant-depth channel using the linear inviscid theory.

The studies by Lee and Ayer (1981), Miles (1982), and Kirby and Dalrymple (1983) indicate that the effects of a trench on surface waves are significant only when the wavelength of the surface waves is of the same order as the trench width and depth. For the stratified trench problem, we are interested in surface waves of wavelength much longer than the trench width. This is because density differences in navigation trenches are usually small. In a study by the Marine Board of the National Research Council (1983) on criteria for the depths of dredged navigational channels it was reported that, at Europort (Holland) the bottom was defined as a region where the specific gravity of the fluid was greater than 1.2. A result of small density ratio is that the wavelength of the surface waves is much longer than the wavelength of the internal waves in the trench for the same wave period; this will be discussed more fully in § 5 3. Therefore, a trench in a homogeneous

fluid generally would have little effect on the surface waves for the range of surface wavelengths that would produce large internal oscillations in the corresponding stratified trench problem. In figure 5.2.8*a*, the normalized wave height at the end wall is obtained theoretically for the case where there is a trench and for the case where there is only the constant-depth channel. The trench solution is obtained using the potential formulation of Kirby and Dalrymple (1983) with correction for boundary layer dissipation as described in § 3.3.3. The abscissa is normalized with respect to the trench width ℓ, but k is the wavelength of the surface waves in the constant-depth channel. Indeed, there are little differences between the two solutions for the range of experimental conditions considered in this study, that is, near the predicted resonant peak of $k\ell = 0.380$. The variation of the relative phase angle between the surface motion at the end wall and the wave plate motion with $k\ell$ is shown in figure 5.2.8*b*. It is seen that the two theories give almost identical results. These results are expected because the ratio of the trench width to the wavelength of the surface wave in the constant-depth channel, ℓ/λ, corresponding to the relative wave number of the predicted resonant peak of $k\ell = 0.380$, is only about 0.06.

The above results are based on the assumption that the wave motion is dominated by inviscid flows, and viscous dissipation is important only within very thin boundary layers adjacent to the solid surfaces. In particular, the effects of flow separation at the edge of the trench are ignored. Therefore, it is important to compare these results with experiments. The normalized surface wave height at the end wall ($x/\ell = 1$), H_3/S, is plotted as a function of the relative wave number, $k\ell$, in figure 5.2.9. The variation of wave extrema with $k\ell$ at two locations above the trench ($x/\ell = 0$ and $x/\ell = 1$) is plotted in figures 5.2.10*a* and 5.2.10*b*. The relative wave number of the resonant peak as measured experimentally was $k\ell = 0.376$ at a wave period of $T = 8.226$ sec. In figures 5.2.9 and 5.2.10 the measured response curves

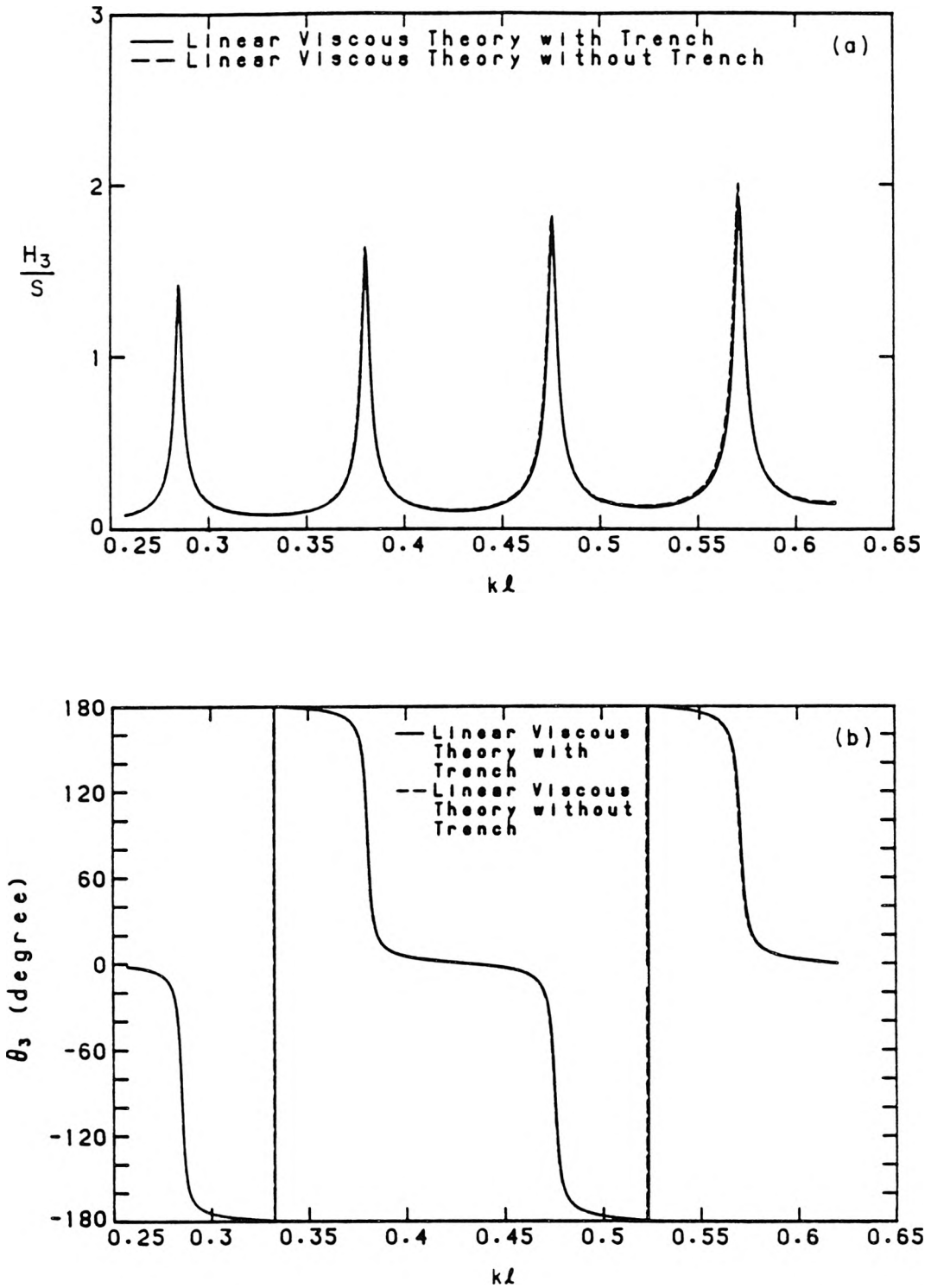

Figure 5.2.8. Variation of (a) normalized wave height, and (b) relative phase angle, at the end wall with relative wave number, computed for constant-depth channel with trench conditions; $h = 15.2\,\text{cm}$, $L = 19.15\,\text{m}$, $\ell = 60.0\,\text{cm}$, $d = 15.2\,\text{cm}$, and for constant-depth channel conditions; $h = 15.2\,\text{cm}$, $L = 19.75\,\text{m}$.

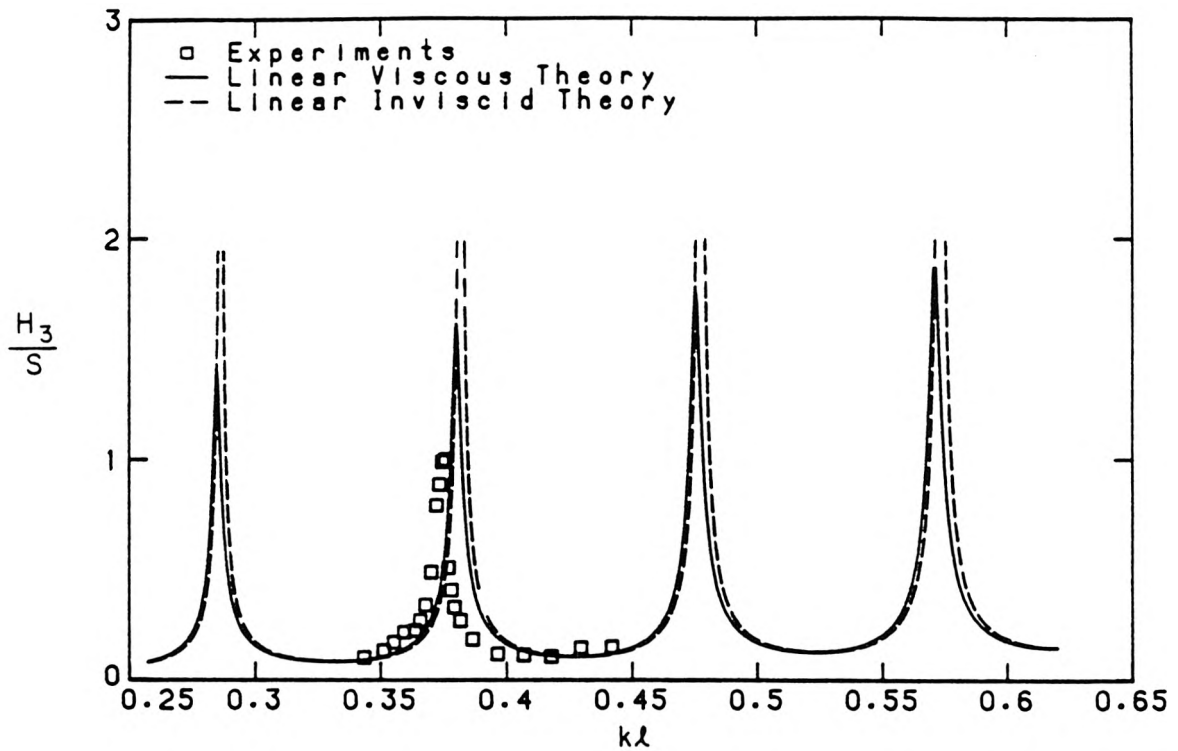

Figure 5.2.9. Variation of normalized wave height at the end wall with relative wave number for constant-depth channel with trench conditions; $h = 15.2\,\text{cm}$, $L = 19.15\,\text{m}$, $\ell = 60.0\,\text{m}$, $d = 15.2\,\text{cm}$.

near the resonant peak of $k\ell = 0.376$ exhibit a distinct jump that is not observed in the experiments with the constant-depth channel (figures 5.2.1 and 5.2.2). The nature of this sudden jump in the measured response curve is not clear and this could have been the result of experimental variation, because the response curve is very steep near resonance. Also, in comparison with the response curves for the constant-depth channel, the maximum wave height is smaller by about 13%. Note that in figure 5.2.9, the difference in the relative wave number between the measured resonant peak at $k\ell = 0.376$ and the predicted resonant peak at $k\ell = 0.380$ when compared to the interval between adjacent resonant peaks is only about 4%. In figure 5.2.11 the variation of the relative phase angle at the end wall with $k\ell$ is shown, the discontinuity in the measured relative phase angle between the surface

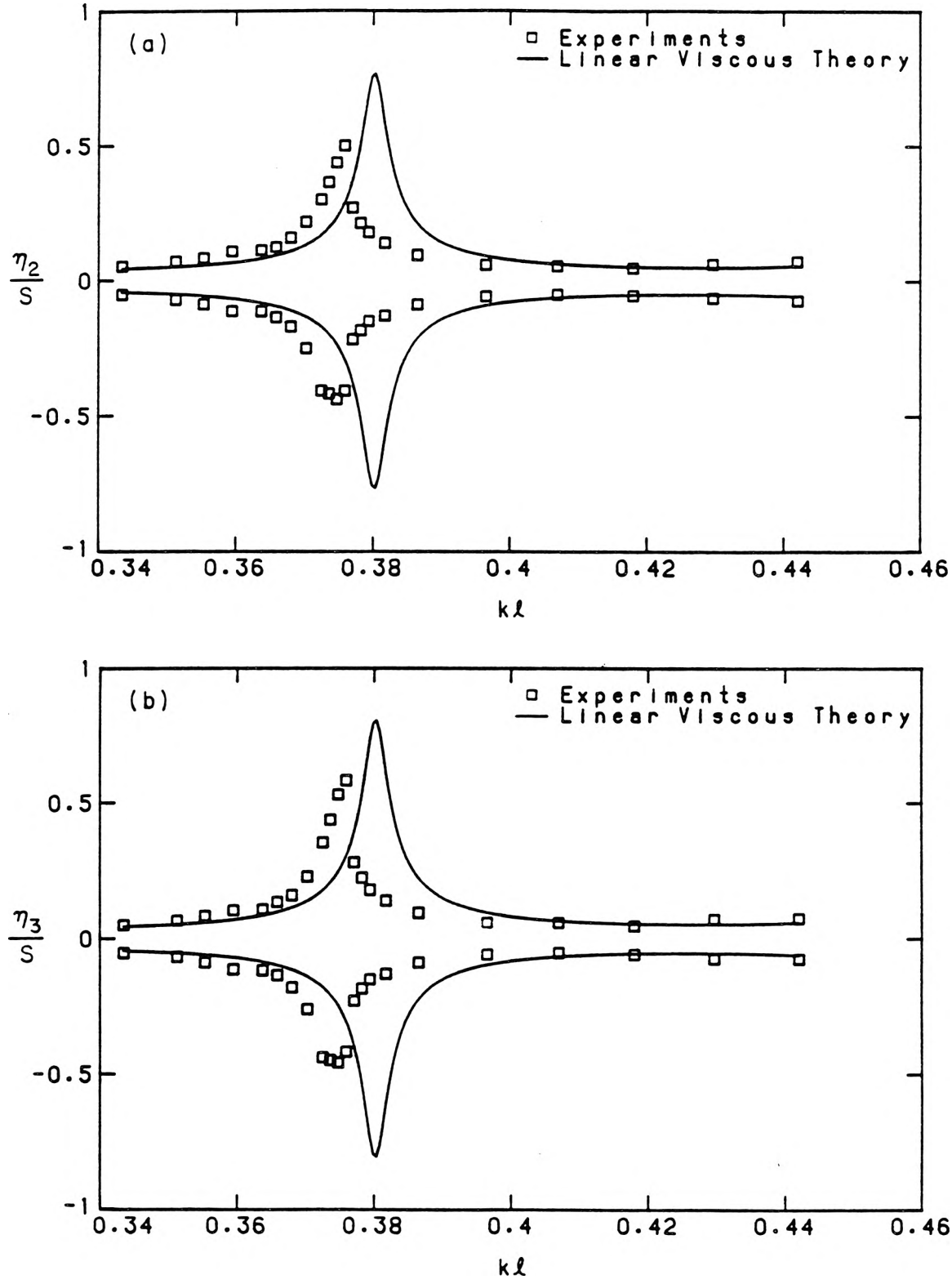

Figure 5.2.10. Variation of wave extrema at two locations above the trench with the relative wave number for a resonant mode of oscillation of the surface waves in the constant-depth channel and trench: (*a*) $x/\ell = 0$, (*b*) $x/\ell = 1$; $h = 15.2\,\text{cm}$, $L = 19.15\,\text{m}$, $\ell = 60.0\,\text{cm}$, $d = 15.2\,\text{cm}$.

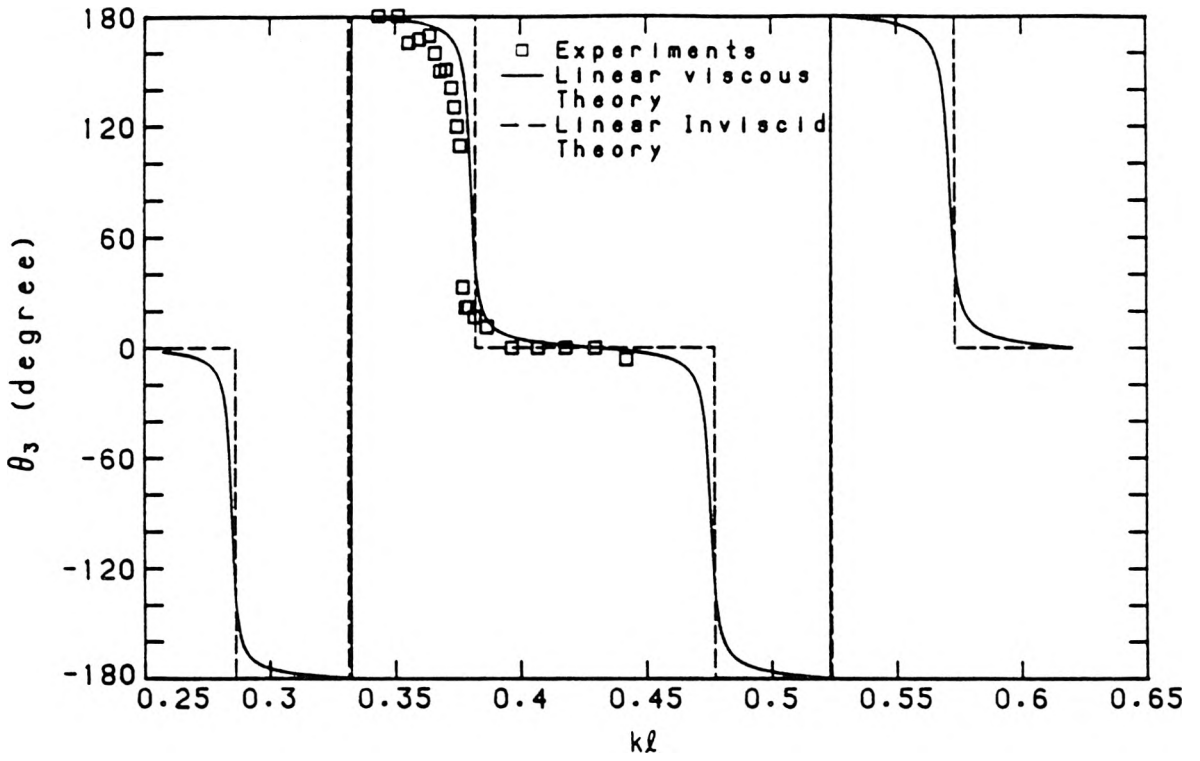

Figure 5.2.11. Variation of the relative phase angle between surface motion at the end wall and wave plate motion with relative wave number, for constant-depth channel with trench conditions; $h = 15.2\,\text{cm}$, $L = 19.15\,\text{m}$, $\ell = 60.0\,\text{cm}$, $d = 15.2\,\text{cm}$.

motion at the end wall and the wave plate motion is clearly seen.

The time histories of the steady-state motion at the end wall are shown in figure 5.2.12 for a range of relative wave frequencies σ/σ_0, where $\sigma_0 = 2\pi/T_0$, and $T_0 = 8.1\,\text{sec}$ ($k\ell = 0.382$) is the determined wave period of resonant oscillation of the surface waves for the constant-depth channel with trench conditions using the linear inviscid theory. The wave profiles are almost sinusoidal before the wave frequency reaches the frequency of the sudden jump in the response curve (figure 5.2.9) at $\sigma/\sigma_0 = 0.985$ ($k\ell = 0.376$). After the jump, a secondary oscillation appears behind the main wave, the secondary wave eventually grows to the same amplitude as the main wave as σ decreases. The two waves then merge together. As σ decreases the wave amplitudes become progressively smaller due to an off-resonant condition for

the surface waves in the constant-depth channel and trench. The surface elevation becomes nearly symmetrical about the mean water level. The behaviour of the secondary wave after the sudden jump in the response curve is very similar to the experiments with the constant-depth channel. The water surface time histories measured at the end wall from the start of the wave generator are presented in figure 5.2.13. It is seen that from $\sigma/\sigma_0 = 0.988$ to $\sigma/\sigma_0 = 0.985$ the water surface time history at the the end wall changes suddenly from a characteristic "beat" pattern of off-resonant oscillation to a resonant condition that is characterized by the absence of the "beat" pattern. This sudden change in the water surface time history at the end wall was not observed in the experiments with the constant-depth channel (figure 5.2.4). In figure 5.2.13, after the sudden jump in wave amplitude at $\sigma/\sigma_0 = 0.985$, the growth of the surface wave and the evolution of a secondary wave behind the main wave follow the same general pattern as shown in figure 5.2.4 for the experiments with the constant-depth channel.

The experimental results for the constant-depth channel and for the constant-depth channel with trench conditions both indicate larger energy dissipation in the wave tank than the theoretical predictions. Because a simple-harmonic motion of the wave generator is assumed in the theoretical formulation, it is important to compare the generated incident waves with the predictions of the linear wavemaker theory (Ursell, Dean and Yu, 1960). The primary incident wave was measured at a point about 5.0 m from the mean position of the wave plate (figure 5.1.1), which corresponds to a relative distance of $x/h \approx 30$. There were approximately four waves passing this location before the first wave reflected from the end of the channel arrived. The second and the third waves were not affected by transient effects at the leading edge of the first wave (see, for example, figure 5.2.4), hence the wave height of the primary incident waves was obtained from the average of the wave heights of the second and the third waves. In figure 5.2.14 the wave height of

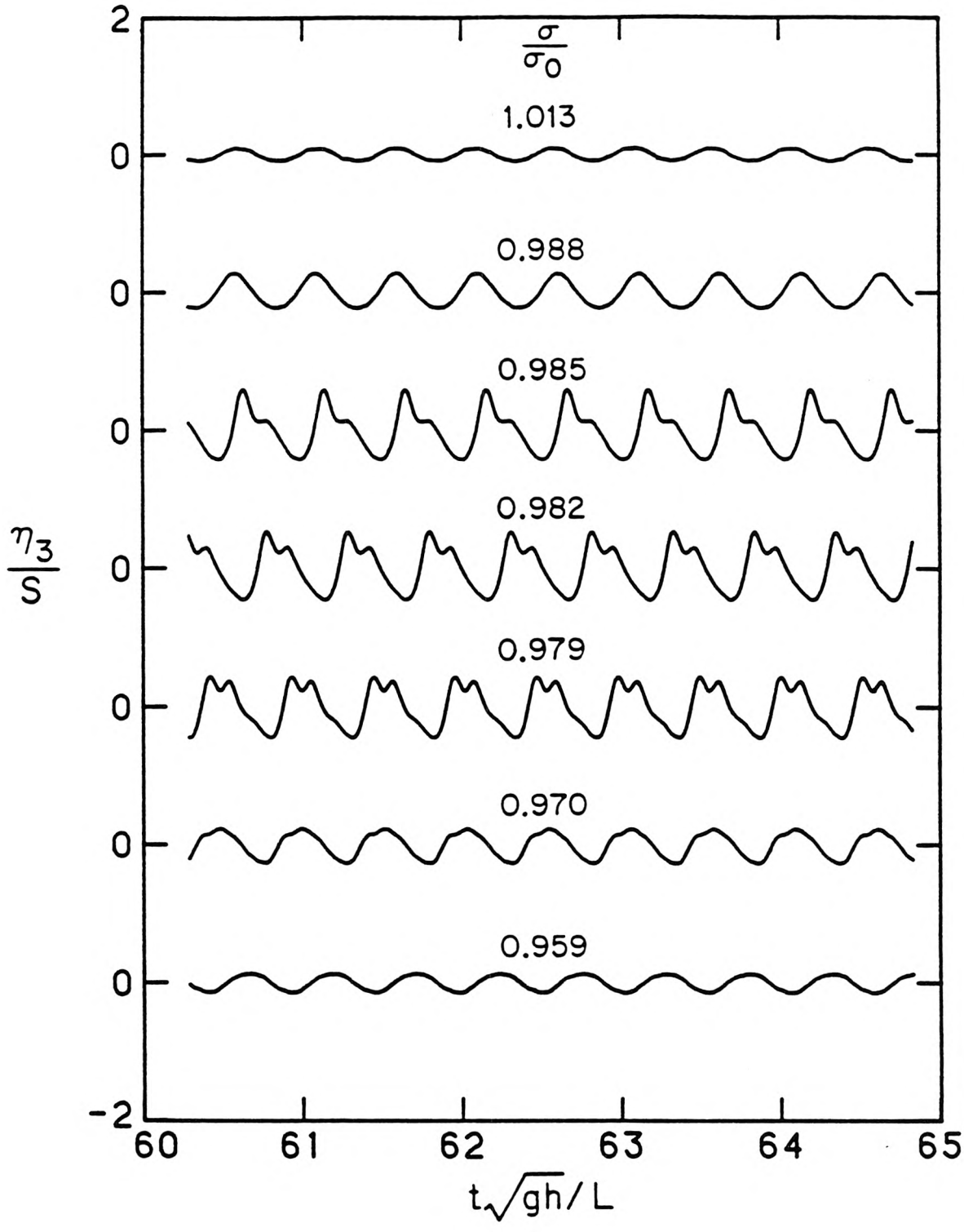

Figure 5.2.12. Steady-state free surface motions at the end wall for relative circular frequencies near a resonant mode of oscillation of the surface waves in the constant-depth channel and trench; $h = 15.2\,\text{cm}$, $L = 19.15\,\text{m}$, $\ell = 60.0\,\text{cm}$, $d = 15.2\,\text{cm}$.

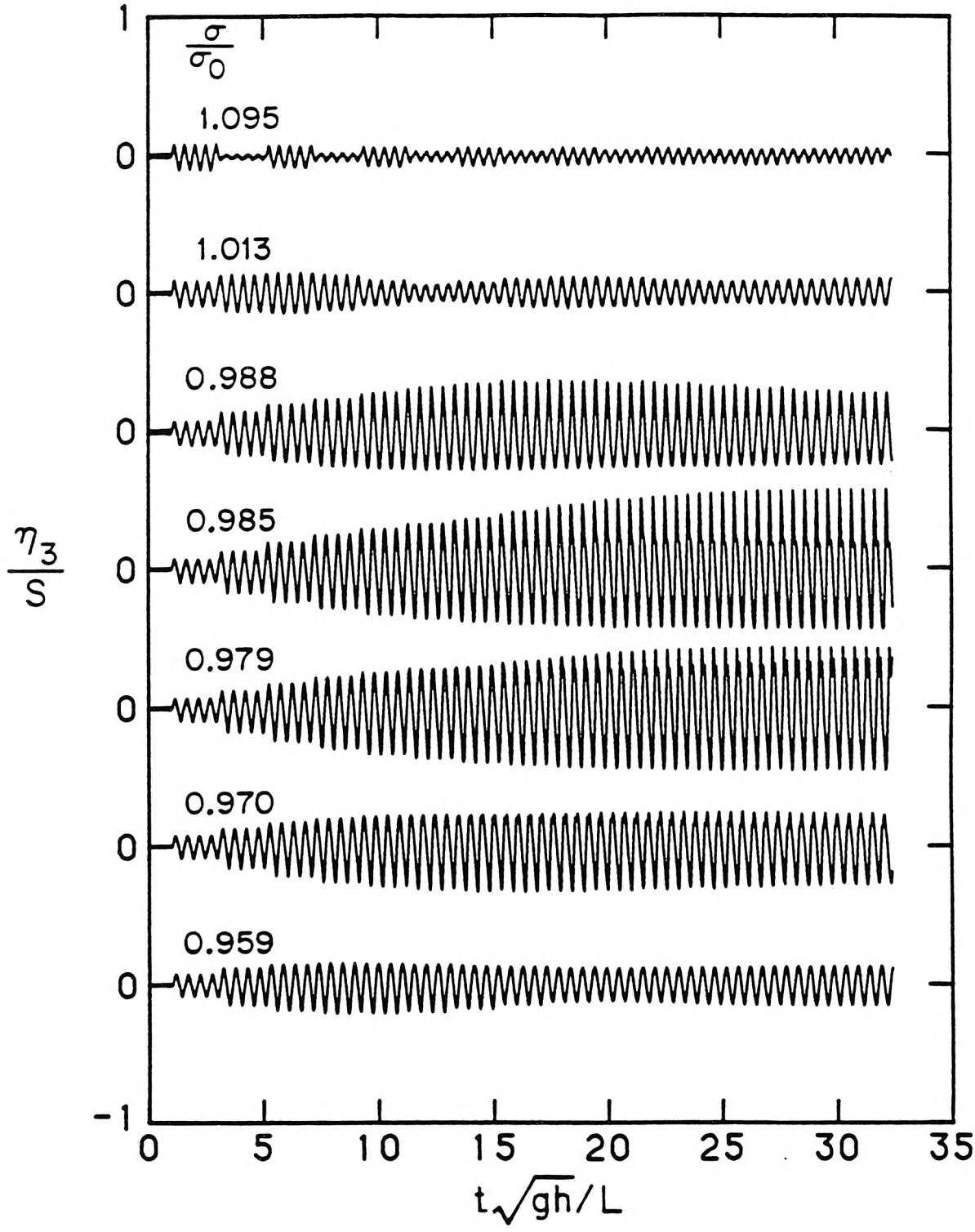

Figure 5.2.13. Time histories of free surface motion at the end wall for relative circular frequencies near a resonant mode of oscillation of the surface waves in the constant-depth channel and trench; $h = 15.2\,\text{cm}$, $L = 19.15\,\text{m}$, $\ell = 60.0\,\text{cm}$, $d = 15.2\,\text{cm}$.

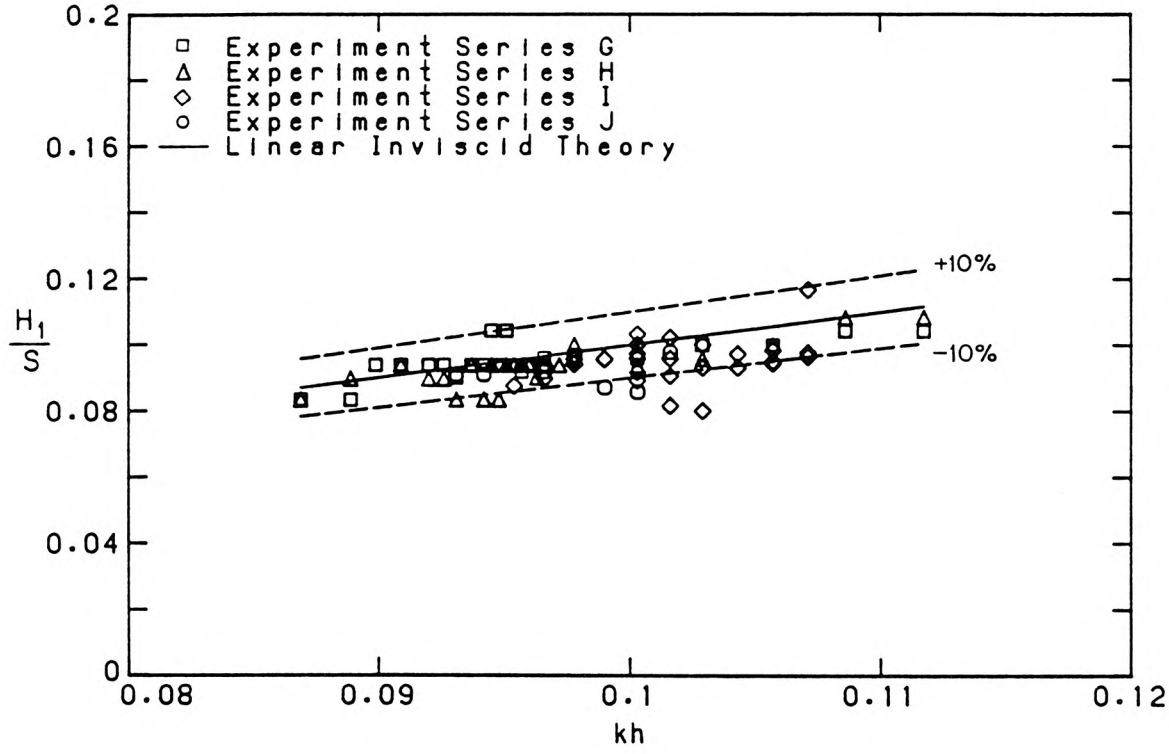

Figure 5.2.14. Variation of normalized incident wave with relative wave number. The waves were generated by a bulkhead wave generator that moved in simple-harmonic motion in water of a constant depth of $h = 15.2\,\text{cm}$.

the primary incident waves, H_1, normalized by the stroke of the wave generator, S, is plotted as a function of the relative wave number kh using the data from four sets of experiments. The agreement between the experimental results and the theory is reasonably good ($\pm 10\%$) indicating that the linear wavemaker theory is adequate in describing the wave generation process for these experiments.

In summary, surface wave motions in a rectangular trench that is connected at one end to a constant-depth channel and closed at the other end by a vertical wall, were studied experimentally, and theoretically using linear wave theory, for conditions near a mode of resonant oscillation of the surface waves in the constant-depth channel and trench. Surface waves were generated by a bulkhead wave generator that moved in simple-harmonic motion with a constant stroke at the opposite end

of the constant-depth channel. The major objective of the experiment was to look for physical effects not included in the theoretical models, such as flow separation, and to obtain surface wave measurements for comparison with results of the experiments with the constant-depth channel and the experiments with the stratified trench. The experiments conducted with fresh water in the trench indicate small but positive differences compared to the results of the experiments conducted in the constant-depth channel. Further studies on this topic are warranted. It is noted that the constant-depth channel and trench arrangement used in this study (figure 5.1.1) is not very suitable for the investigation of flow separation. In particular, the standing surface wave had an antinode at the end wall. Hence the horizontal component of the fluid velocity above the trench was much smaller than the horizontal component of the fluid velocity at some other locations along the wave tank. To study the effects of flow separation around the edges of the trench, it is more effective to put the end wall one quarter of a wavelength downstream from the trench, then the location of the trench is near the node of a standing surface wave where the horizontal component of the fluid velocity is the largest. This has not been done in this study and is recommended for future work.

5.2.3 Experiments with a Deep Lower Fluid in a Stratified Trench

A series of experiments were conducted with a stratified fluid of water and salt water in the rectangular trench and fresh water in the constant-depth channel. The experimental arrangement is shown in figure 5.1.1. The water depth in the constant-depth channel was $h = 15.2\,\text{cm}$. In the trench region, the depth of the upper fluid (fresh water) was $h_1 = 22.8\,\text{cm}$, and the depth of the lower fluid (salt water) was $h_2 = 7.6\,\text{cm}$. The depths h_1 and h_2 were measured from the water surface and the trench bottom, respectively, to the center of the diffuse salinity

interface. Experiments were conducted using two nominal thicknesses of the diffuse salinity interface: (i) $\delta = 1.3\,\text{cm}$ (Series I), and (ii) $\delta = 2.5\,\text{cm}$ (Series J). The thickness of the diffuse salinity interface is defined as the ratio of the maximum density difference between water and salt water to the maximum density gradient in the diffuse salinity interface, that is:

$$\delta = -\Delta\rho \left(\frac{d\rho}{dz}\right)^{-1}_{\max} \tag{5.2.7}$$

where $\Delta\rho = \rho_2 - \rho_1$. Because the internal wave motion in the trench is directly related to the density stratification, it is important to determine the exact thickness of the diffuse salinity interface in these experiments. The trench was stratified by first filling the wave tank with fresh water to a depth of $h = 15.2\,\text{cm}$. Salt water was then introduced through a port in the bottom of the trench. The filling process created a diffuse salinity interface of thickness of about 2.5 cm; this was reduced to about 0.5 cm by selective withdrawal of fluid from the diffuse salinity interface. The density profile was determined from conductivity measurements made at a location 2.0 cm from the upstream wall of the trench immediately after the thickness of the diffuse salinity interface was reduced and about 15 minutes after the experiment was completed. In Series I the experiments were conducted within two hours after the interface was reduced. In Series J the stratified fluid in the trench was left undisturbed for 6 to 7 hours, then the density profile in the trench was measured again before the experiment was conducted. The thickness of the diffuse salinity interface for these experiments was determined from the density profiles obtained after the experiments; the actual experiments took about 17 minutes. Hence, these values correspond to steady-state conditions in the trench. The same procedure was followed in the experiments with the shallower lower fluid (Series K and Series M).

In Series I, the mean value of the thickness of the diffuse salinity interface was 1.32 cm, with a standard deviation of 0.12 cm. The mean density of salt water was

$1.0497\,\mathrm{gcm}^{-3}$, with a standard deviation of $0.00084\,\mathrm{gcm}^{-3}$. In Series J, the mean thickness of the diffuse salinity interface was 2.46 cm, with a standard deviation of 0.06 cm. The mean density of salt water was $1.0507\,\mathrm{gcm}^{-3}$, with a standard deviation of $0.0005\,\mathrm{gcm}^{-3}$.

In experiments Series J and Series M the density profiles in the trench were measured after the thickness of the interface was reduced and also before the experiments were conducted; the time period in between varied from 6 to 8 hours. Thus, we can determine the molecular diffusion coefficient of salt in water from these measurements. Assuming a surface of density discontinuity at $z = -h_1$ at some initial time $t = 0$, the density profile in the trench region at a subsequent time t due to molecular diffusion is given by the following diffusion equation:

$$\rho = \rho_1 + \Delta\rho\,\mathrm{erfc}\left(\frac{z - h_1}{\sqrt{4D_m t}}\right) \tag{5.2.8}$$

where D_m is the molecular diffusion coefficient, and "erfc" is the complimentary error function. Substitution of (5.2.8) in (5.2.7) yields the following relationship for the thickness of the diffuse salinity interface and the molecular diffusion coefficient:

$$\delta = (4\pi D_m t)^{\frac{1}{2}} \tag{5.2.9}$$

Hence, the molecular diffusion coefficient D_m can be calculated for the time interval $(t_2 - t_1)$ by:

$$D_m = \frac{1}{4\pi}\left(\frac{{\delta_{t_2}}^2 - {\delta_{t_1}}^2}{t_2 - t_1}\right). \tag{5.2.10}$$

Using (5.2.10), the molecular diffusion coefficient D_m was obtained from thirteen experiments, the mean is $1.31 \times 10^{-5}\,\mathrm{cm^2sec^{-1}}$, and the standard deviation is $0.07 \times 10^{-5}\,\mathrm{cm^2sec^{-1}}$. Hammack (1980) quoted a molecular diffusion coefficient D_m of salt in water of $1.5 \times 10^{-5}\,\mathrm{cm^2sec^{-1}}$.

Some typical density profiles in the trench are presented in figures 5.2.15*a* and 5.2.15*b*; the wave periods of these experiments correspond to resonant conditions

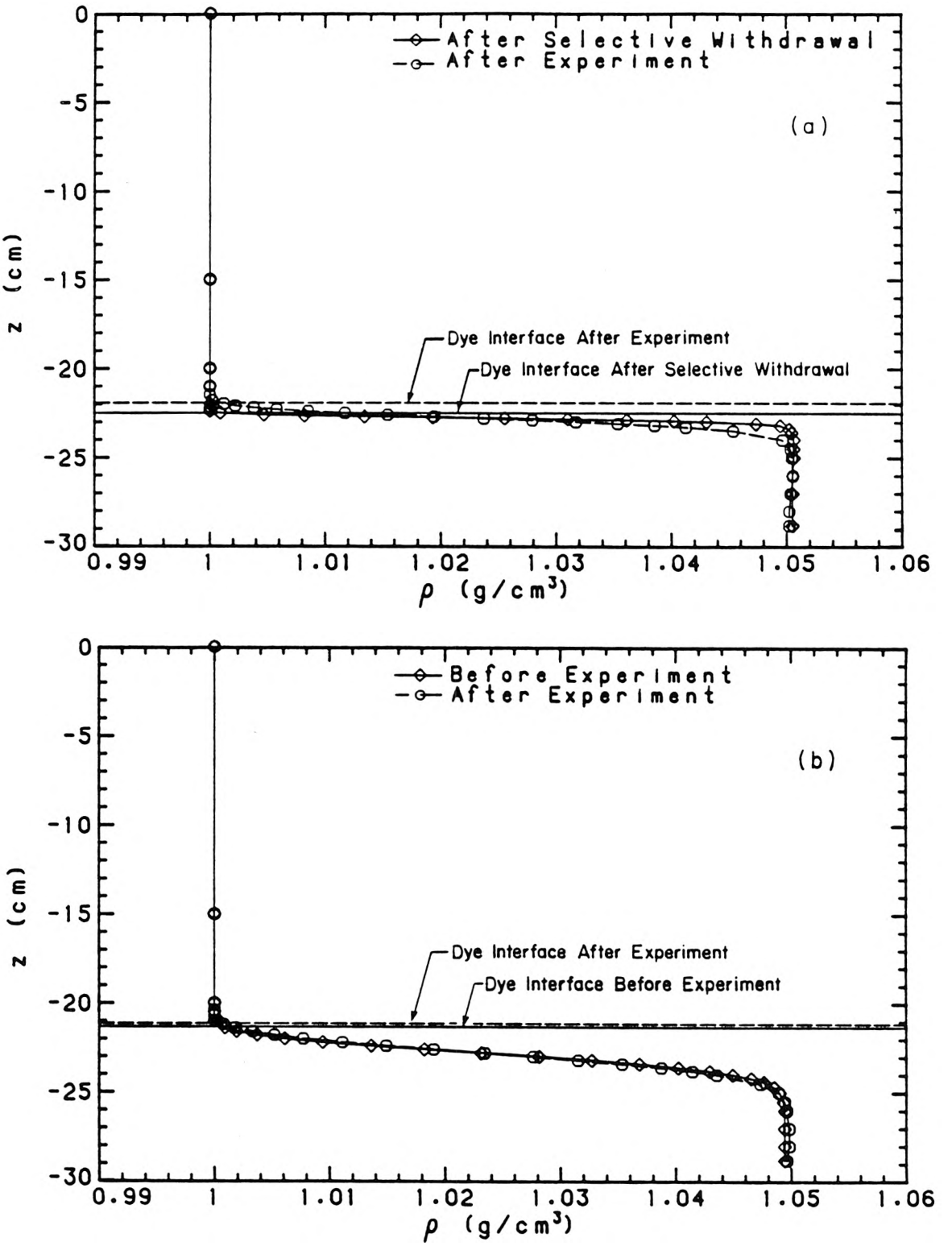

Figure 5.2.15. Density Profiles before and after experiments for wave periods corresponding to resonant conditions of internal waves in the trench: (*a*) $T = 7.8\,\text{sec}$, and (*b*) $T = 8.0\,\text{sec}$; $h_1 = 22.8\,\text{cm}$, $h_2 = 7.6\,\text{cm}$, $\Delta\rho \approx 0.05\,\text{gcm}^{-3}$. The density profiles were obtained at a location 2.0 cm from the upstream wall of the trench.

of internal waves in the trench for the experimental conditions of Series I and Series J, respectively. The ordinate is the vertical distance below the water surface; the "mouth" of the trench and the trench bottom, respectively, are located at $z = -15.2\,\text{cm}$ and at $z = -30.4\,\text{cm}$, and the center of the diffuse salinity interface is located at $z = -22.8\,\text{cm}$. For figure 5.2.15*a*, the thickness of the diffuse salinity interface increased from 0.54 cm after the interface was reduced, to 1.41 cm after the experiment was completed, during a time interval of 116 minutes. Using (5.2.10), with $\delta_{t_2} = 1.41\,\text{cm}$, $\delta_{t_1} = 0.54\,\text{cm}$, and $(t_2 - t_1) = 116$ minutes, the apparent diffusion coefficient D_a is found to be $1.94 \times 10^{-5}\,\text{cm}^2\text{sec}^{-1}$. For figure 5.2.15*b* the thickness of the diffuse salinity interface before and after the experiment was 2.22 cm and 2.61 cm, respectively. The time interval between measurement of the density profiles was 115 minutes. Using these values, the apparent diffusion coefficient is found to be $2.17 \times 10^{-5}\,\text{cm}^2\text{sec}^{-1}$. The larger values of the apparent diffusion coefficient were attributed to mixing of the fluids by internal wave motions; the internal waves in the trench were "at resonance" in these experiments. The values of the apparent diffusion coefficient in most experiments were smaller than the above values.

Experiments were conducted for a range of wave periods near the lowest mode of oscillation of the internal waves in the trench. In Series I, internal waves for a wide range of surface wave heights above the trench were studied. Hence, the results of these experiments are presented first.

When the trench was first installed, the length of the rectangular cavity was almost exactly equal to 60.0 cm (± 1.0 mm). This length decreased to 59.5 cm after a short period of use, due to swelling of the plywood false bottom in the wave tank, and then remained constant. Nevertheless, the original trench width of 60.0 cm has been used in § 5.2.1 and § 5.2.2 for the evaluation of the theoretical results. This small difference in the trench width had negligible effects on the surface waves in the constant-density case, because the wavelength of the surface wave was large

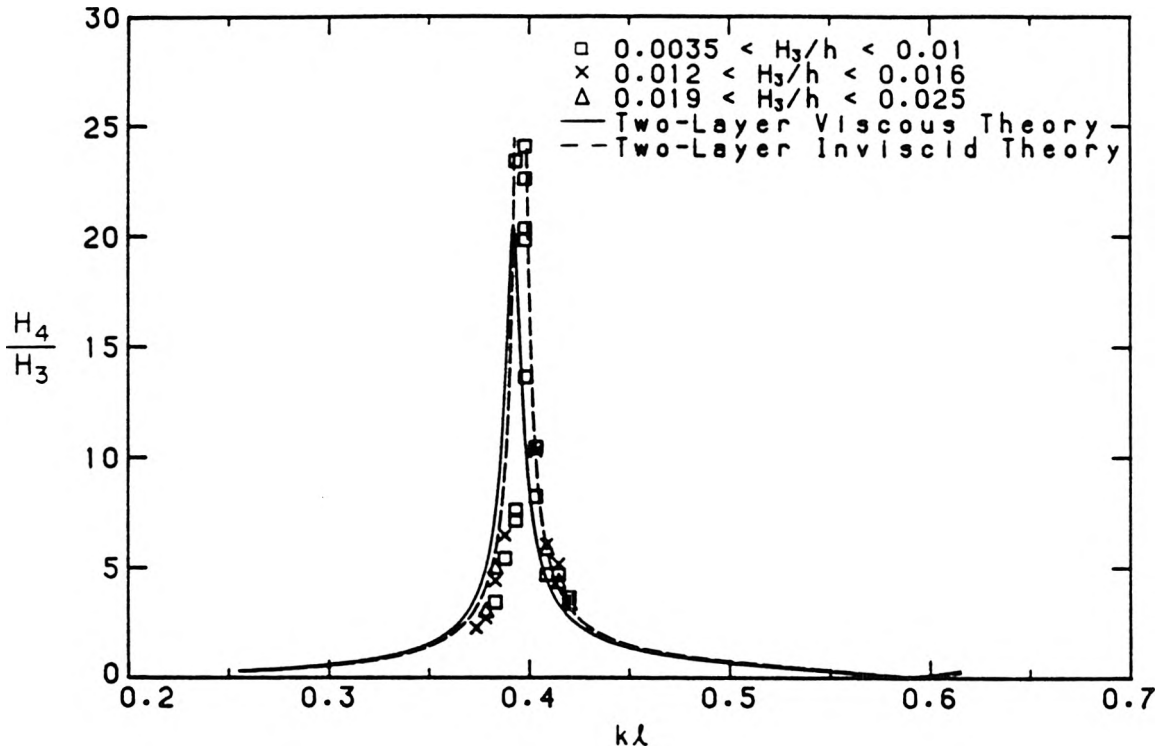

Figure 5.2.16. Variation of normalized internal wave height at the upstream wall of the trench with relative wave number. The theoretical results are obtained using the two-layer viscous theory and the two-layer inviscid theory; $h = 15.2\,\text{cm}$, $h_1 = 22.8\,\text{cm}$, $h_2 = 7.6\,\text{cm}$, $L = 19.15\,\text{m}$, $\ell = 59.5\,\text{cm}$, $d = 15.2\,\text{cm}$, $b = 19.7\,\text{cm}$, $\rho_2/\rho_1 = 1.05$.

compared to the trench dimensions. However, the wavelengths of internal waves in the trench were only about twice the trench width for the lowest mode of oscillation. Therefore, the exact length of 59.5 cm will be used in the following analysis of internal waves.

In figure 5.2.16, the internal wave height at the upstream wall of the trench, H_4, normalized by wave height of the surface wave at the end wall, H_3, is plotted as a function of $k\ell$, where k is the wave number of the surface wave in the constant-depth channel obtained using (3.1.25a). From the two-layer inviscid theory, the wave period corresponding to the lowest mode of oscillation of the internal waves in the trench is found to be 7.75 sec ($k\ell = 0.396$), and the wave period for a mode

of the resonant oscillation of the surface waves in the constant-depth channel is 8.1 sec ($k\ell = 0.379$). As seen in figue 5.2.16 the response curve obtained from the experiments is extremely peaked and H_4/H_3 (this ratio will be termed the amplification factor R) attains a magnitude of about twenty-four at resonance while, of course, the response from the linear inviscid theory tends to infinity at resonance. To either side of resonance the response decreases rapidly. The linear viscous theory, with $\nu = 1.0 \times 10^{-6}\,\mathrm{m^2 sec^{-1}}$ for both layers, predicts a smaller amplification factor ($H_4/H_3 = 20.49$) than the experiments, and the wave period of resonant oscillation of the internal waves in the trench is shifted to 7.82 sec ($k\ell = 0.392$). It appears that the two-layer viscous theory has overestimated energy dissipation in the trench. The excessive energy loss is due to dissipation in the interfacial boundary layers built into the two-layer viscous theory. Interfacial boundary layers do not exist in the real fluids that are miscible. A detailed discussion of energy loss in various regions of the fluid is presented in § 5.2.5.

The wave period corresponding to the second resonant mode of the internal waves in the trench is about 4.4 sec from the two-layer inviscid theory. Thus, the difference between the wave periods of the resonant peaks predicted by the two-layer viscous theory and the two-layer inviscid theory when compared to the difference between the wave periods of the first and second resonant modes is only about 2%.

The relative phase angle between internal wave motion at the upstream wall of the trench and surface wave motion at the end wall, θ_{43}, is plotted as a function of the relative wave number, $k\ell$, in figure 5.2.17. The results of the theories and experiments show a shift from in phase to out of phase through resonance. The experimental data show a more rapid change in the relative phase angle than the prediction of the two-layer viscous theory, which again indicates smaller viscous dissipation in the experiments compared to the theories.

In figure 5.2.18 the same experiments are compared to predictions obtained

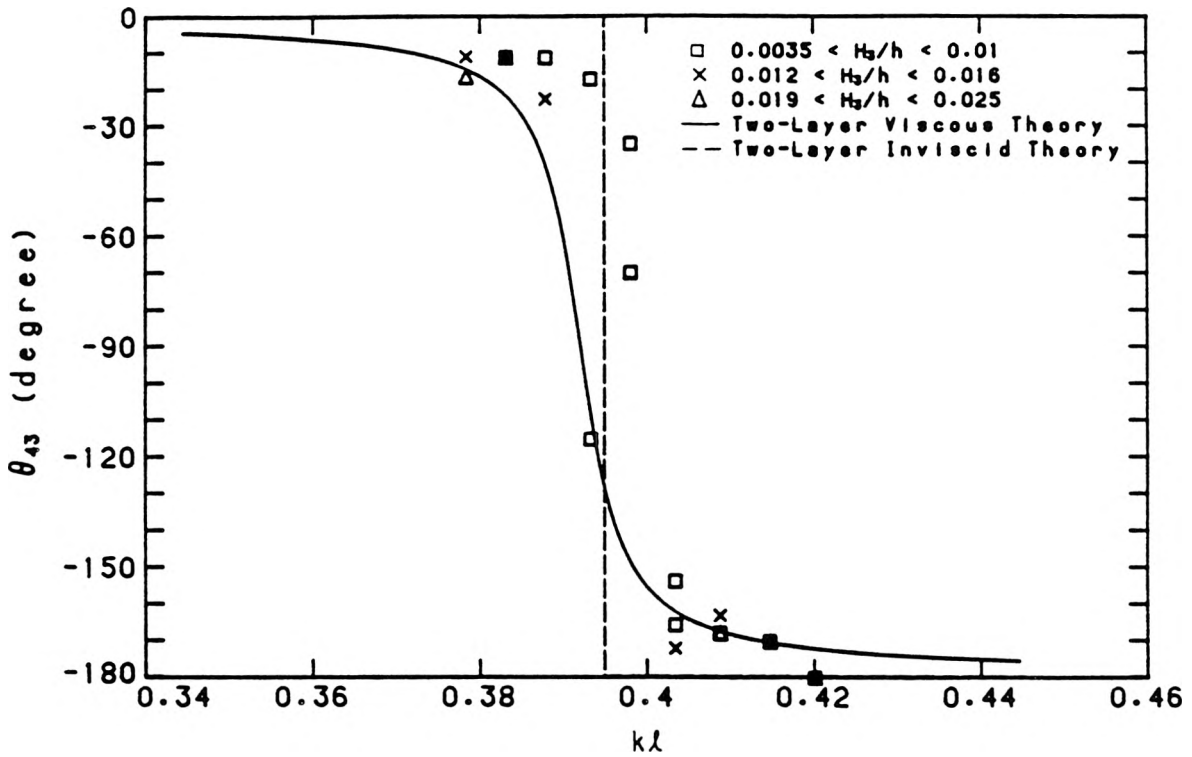

Figure 5.2.17. Variation of the relative phase angle between internal wave motion at the upstream wall of the trench and surface wave motion at the end wall with relative wave number. The theoretical results are obtained using the two-layer viscous theory and the two-layer inviscid theory; $h = 15.2\,\text{cm}$, $h_1 = 22.8\,\text{cm}$, $h_2 = 7.6\,\text{cm}$, $L = 19.15\,\text{m}$, $\ell = 59.5\,\text{cm}$, $d = 15.2\,\text{cm}$, $b = 19.7\,\text{cm}$, $\rho_2/\rho_1 = 1.05$.

using the three-layer viscous theory and the three-layer inviscid theory, computed for a value of $\delta = 1.3\,\text{cm}$. The theoretical response curves are computed for the internal wave height at the top of the density transition region, that is, at $z = -22.15\,\text{cm}$, where z is measured positive upwards from the still water surface. It is recalled from § 4.1.3 that the interfacial wave gage measures wave motion at a location close to the top of the diffuse salinity interface. The wave period for the lowest mode of resonant oscillation of the internal waves in the trench is found to be 7.80 sec ($k\ell = 0.393$) using the three-layer inviscid theory. In figure 5.2.19 the trench responses obtained using the two-layer inviscid theory and the three-layer

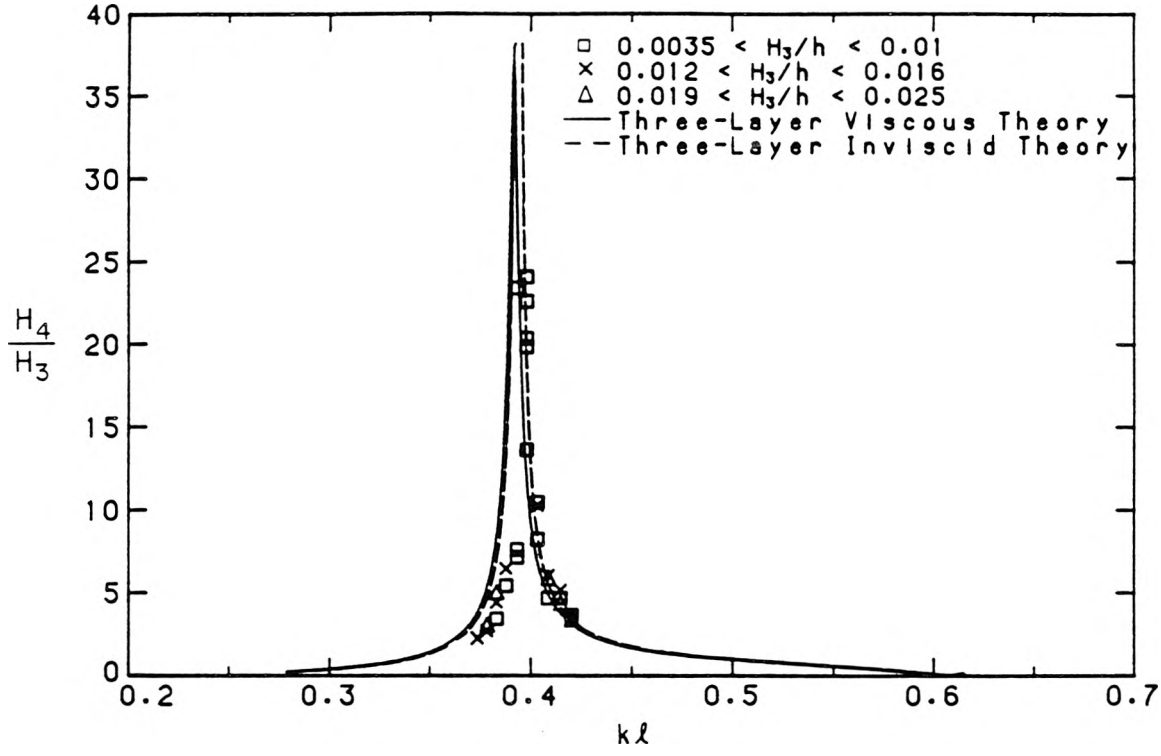

Figure 5.2.18. Variation of normalized internal wave height at the upstream wall of the trench with relative wave number. The theoretical results are obtained using the three-layer viscous theory and the three-layer inviscid theory, computed for the internal wave height at the top of the density transition region; $h = 15.2\,\text{cm}$, $h_1 = 22.15\,\text{cm}$, $h_2 = 6.95\,\text{cm}$, $\delta = 1.3\,\text{cm}$, $L = 19.15\,\text{m}$, $\ell = 59.5\,\text{cm}$, $d = 15.2\,\text{cm}$, $b = 19.7\,\text{cm}$, $\rho_2/\rho_1 = 1.05$.

inviscid theory are compared. It is seen that the effects of the density transition region on the invisicd results are very small for these conditions; the difference between the wave periods of resonance obtained using the two-layer inviscid theory and the three-layer inviscid theory when compared to the difference between the wave periods of the first and the second resonant modes of internal oscillations in the trench is less than 2%. With damping, the wave period of the resonant peak is found to be 7.83 sec ($k\ell = 0.392$) using the three-layer viscous theory. The corresponding amplification factor is $H_4/H_3 = 37.17$, which is almost twice that predicted by the two-layer viscous theory (figure 5.2.16); this is attributed to

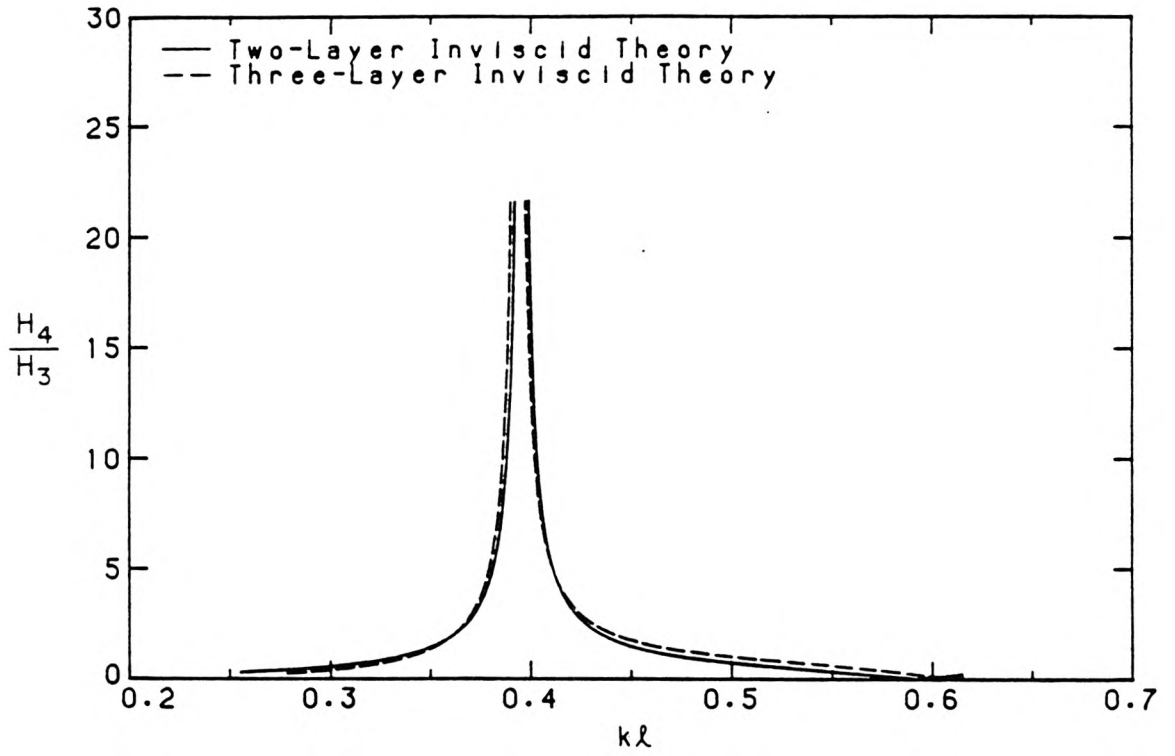

Figure 5.2.19. Comparison between the trench responses obtained using the two-layer inviscid theory and the three-layer inviscid theory for the lowest mode of oscillation of internal waves in the trench.

the absence of the interfacial boundary layer damping in the three-layer viscous theory. It is recalled from § 3.3.2 that in the three-layer viscous theory, viscous dissipation is considered to take place in the boundary layers adjacent to the solid surfaces only. In fact, the three-layer model is a closer realization of the actual conditions in the trench, provided that the density differences between the two fluids remain small (Boussinesq approximation). The comparison of the predictions of the three-layer viscous theory to the experimental measurements (figure 5.2.18) indicates that laminar boundary layer damping near the solid surfaces alone tends to underestimate energy loss in the trench; a similar conclusion is also reached in § 5.2.1 and § 5.2.2 for the experiments with fresh water. The variation of relative phase angle, θ_{43}, with relative wave number, $k\ell$, is shown in figure 5.2.20 for the

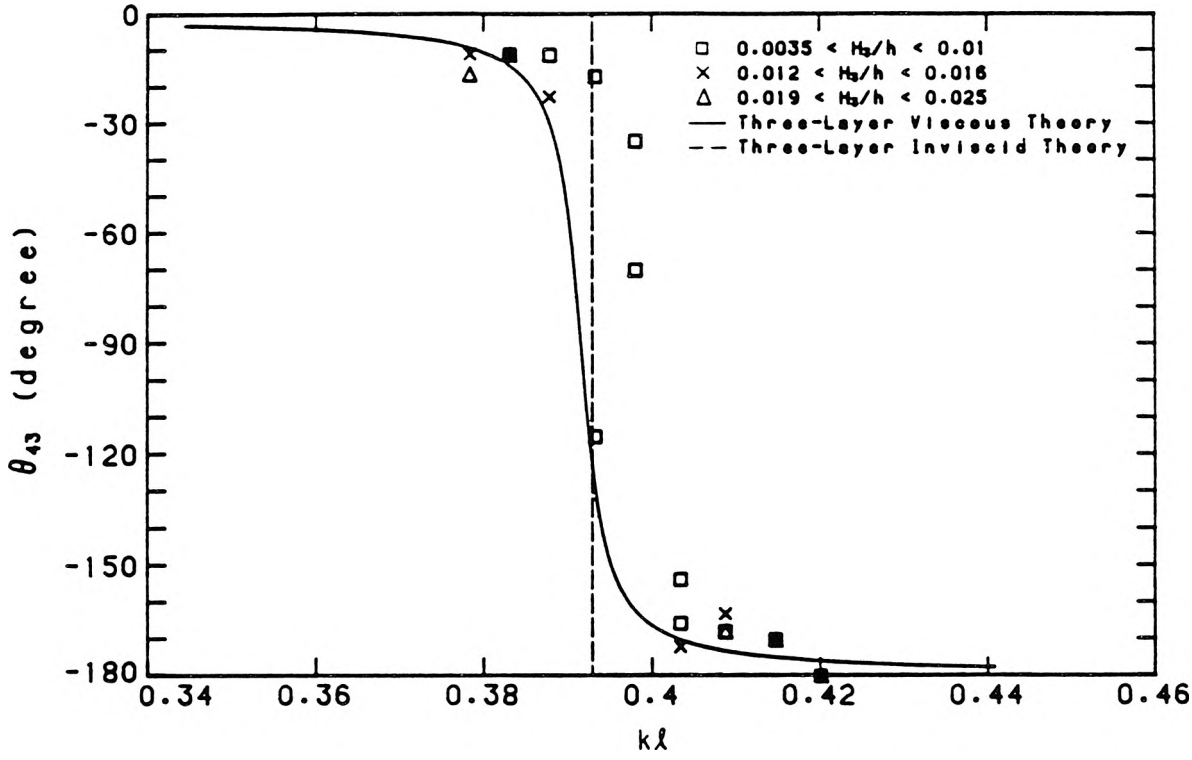

Figure 5.2.20. Variation of the relative phase angle between internal wave motion at the upstream wall of the trench and surface wave motion at the end wall with relative wave number. The theoretical results are obtained using the three-layer viscous theory and the three-layer inviscid theory, computed for the internal wave motion at the top of the density transition region; $h = 15.2\,\text{cm}$. $h_1 = 22.15\,\text{cm}$, $h_2 = 6.95\,\text{cm}$, $\delta = 1.3\,\text{cm}$. $L = 19.15\,\text{m}$, $\ell = 59.5\,\text{cm}$, $d = 15.2\,\text{cm}$, $b = 19.7\,\text{cm}$, $\rho_2/\rho_1 = 1.05$.

results of experiments and three-layer theories.

In figure 5.2.21, the wave extrema of internal wave at the upstream wall of the trench, η_4, normalized by the surface wave height at the end wall, H_3, is plotted as a function of the relative wave number, $k\ell$, for the lowest mode of oscillation of the internal waves in the trench. The amplitudes of the wave crest and the wave trough are evaluated with respect to the mean dye interface, which changes with time due to molecular diffusion. The spread of data near $k\ell = 0.4$ is due to steepness of the response curve near resonance. Thus, the trench response was very sensitive to

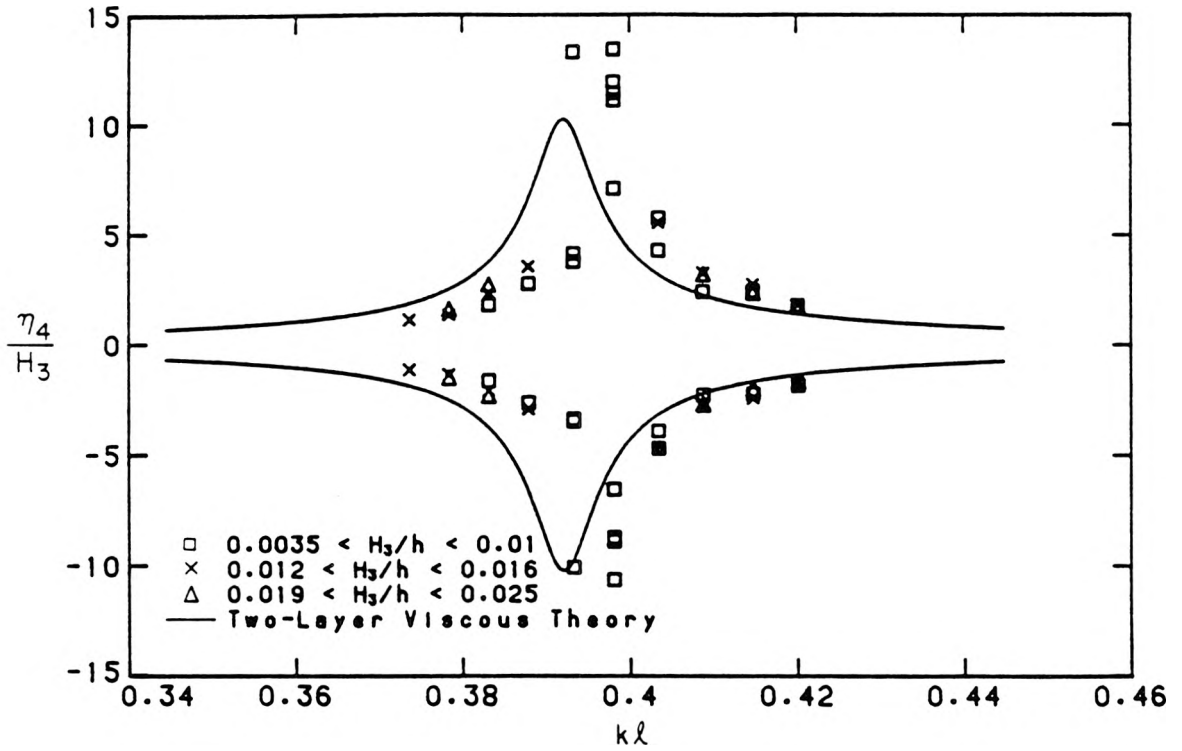

Figure 5.2.21. Variation of internal wave extrema at the upstream wall of the trench with relative wave number, for the lowest mode of oscillation of the internal waves in the trench. The theoretical results are obtained using the two-layer viscous theory; $h = 15.2\,\text{cm}$, $h_1 = 22.8\,\text{cm}$, $h_2 = 7.6\,\text{cm}$, $L = 19.15\,\text{m}$, $\ell = 59.5\,\text{cm}$, $d = 15.2\,\text{cm}$, $b = 19.7\,\text{cm}$, $\rho_2/\rho_1 = 1.05$.

variations in experimental conditions. Note that the scale of the ordinate is much smaller than the scale of the abscissa. The important feature in this figure is the symmetry of the internal wave motions about the quiescent level for a wide range of surface wave heights. The corresponding surface wave extrema at two locations ($x/\ell = 0$ and $x/\ell = 1$) above the trench are shown in figures 5.2.22*a* and 5.2.22*b*. The maximum value of H_3/h in these experiments was 0.0247. It is recalled from (5.2.6) that second order effects in the surface wave profile are negligible if the ratio of the wave height of the standing surface wave to the water depth, H_3/h, is much less than 0.05. Indeed, the free surface elevation above the trench appears to be

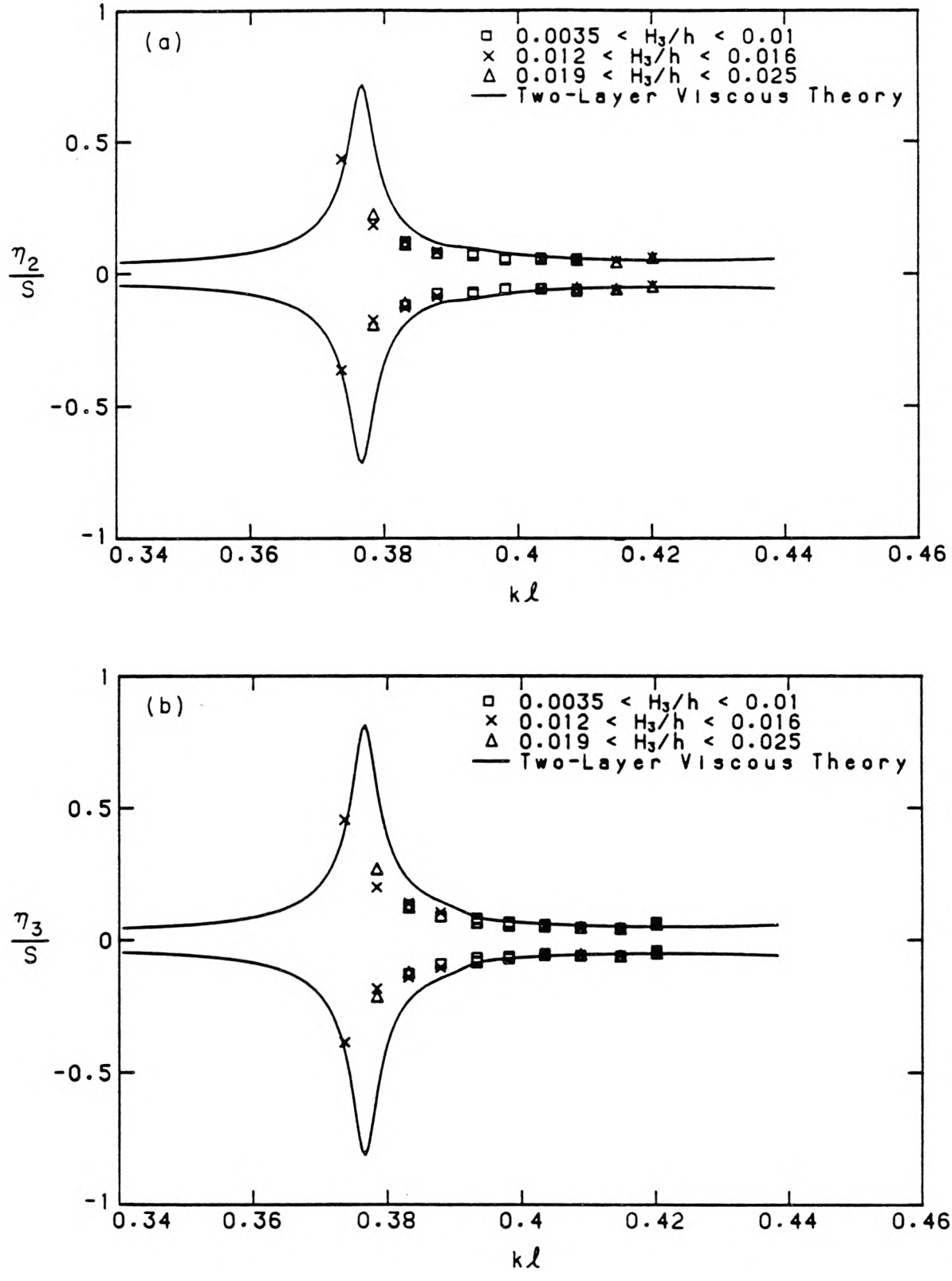

Figure 5.2.22. Variation of surface wave extrema at two locations above the trench with relative wave number: (*a*) $x/\ell = 0$, and (*b*) $x/\ell = 1$.

reasonably symmetric about the mean water level.

It should be noted that in computing the theoretical response curves, a nominal density ratio of $\rho_2/\rho_1 = 1.05$ has been used. The mean value of the density of salt water for these experiments was $1.0497\,\mathrm{gcm}^{-3}$. The density of fresh water was $0.9982\,\mathrm{gcm}^{-3}$ at the room temperature of 20°C. This implies a value of ρ_2/ρ_1 of 1.0516, which is 3.2% larger than the nonimal density ratio of 1.05 when compared to 0.05. Because the frequency of internal oscillation varies as $\sqrt{\Delta\rho/\rho_2}$, where $\Delta\rho = \rho_2 - \rho_1$, the difference in the predicted resonant frequency of the internal waves in the trench as the result of using the nominal density ratio is less than 2%.

Nonlinear standing internal waves had been studied by Thorpe (1968). For a two-layer fluid that completely fills a rectangular tank, the equation of the interface to second order for small density difference is:

$$\eta(x,t) = a\sin\sigma t\cos Kx + \frac{a^2K}{8T_1^2T_2^2}(T_1 - T_2)(T_1T_2 - 3\cos 2\sigma t)\cos 2Kx \qquad (5.2.11)$$

and the dispersion relation to third order is:

$$\sigma^2 = \frac{gK(\rho_2-\rho_1)T_1T_2}{(\rho_1T_2+\rho_2T_1)}\left[1 + \frac{a^2K^2}{32T_1^3T_2^3}(9T_1^2 + 9T_2^2 - 18T_1T_2 - 6T_1^3T_2 - 6T_2^3T_1 + 8T_1^2T_2^2)\right] \qquad (5.2.12)$$

where h_1, h_2 are the depths of the upper and the lower fluid, respectively, a is the wave amplitude, K is the wave number, and $T_i = \tanh Kh_i$, $(i = 1,2)$. The second order term in (5.2.11) distorts the symmetric waveform of the linear solution given by the first order term; the distance from trough to crest remains constant for second order approximation. Equation 5.2.11 is valid if the ratio of the coefficient of the second order term to that of the first is much less unity, that is, if:

$$\left|\frac{aK(T_1 - T_2)(3 + T_1T_2)}{8T_1^2T_2^2}\right| \ll 1. \qquad (5.2.13)$$

If one of the fluids is deep and the other shallow of depth h, equation (5.2.13) reduces to:

$$\frac{3H}{16Kh^2} \ll 1 \tag{5.2.14}$$

where $H = 2a$.

For standing surface waves in water of depth h, the relevant condition is given by (5.2.5). Thus, the presence of the upper fluid reduces the amplitude of the second order term by a factor of Kh. It is seen that the left hand side of (5.2.14) is not in the form of the Ursell number, defined as $Ur = Hl^2/h_0^3$ for long waves in a homogeneous fluid, where H, l, and h_0 refer to a characteristic wave height, wavelength and depth. Because the Ursell number measures the relative importance of the nonlinear effects to the dispersive effects, it is important to examine the physical meaning of the dimensionless parameter H/Kh^2 with regard to internal waves.

Equation 5.2.11 is valid only when the density difference between the upper fluid and the lower fluid is very small compared to the fluid densities; the full equation, which takes no account of small density difference, is given in Thorpe (1968). For this condition, equation 5.2.14 is the limiting result for standing internal waves at the interface of a deep fluid overlying a shallow fluid, or vice versa. As in (5.2.2), equation 5.2.11 must become invalid when the value of Kh is so small that H/Kh^2 is of order unity, and a different expansion procedure is necessary. The theory of long waves of finite amplitude and permanent form in a stratified fluid had been studied by Benjamin (1966, 1967). Benjamin (1966) considered internal waves whose wavelengths are very large compared to the total fluid depth. Fixing his attention on the first mode of the infinite number of internal wave modes in a continuously stratified fluid, Benjamin (1966) demonstrated that a non-sinusoidal internal wave suffers dispersion of its steepest parts at a rate depending on the difference between the phase and group velocities of its predominant spectral components, which for long

waves is proportional to h_0^2/l^2 times the phase velocity obtained using infinitesimal wave theory. However, nonlinear effects result in the local wave speed at the wave crest exceeding the phase velocity of infinitesimal waves by an amount proportional to $(H/h_0)(\Delta\rho/\rho_0)$ times the phase velocity, where $\Delta\rho/\rho_0$ represents the fractional change in density over the total depth of the fluid. Hence, the relative importance of the nonlinear effects to the dispersive effects is rated by the ratio $(\Delta\rho/\rho_0)(Hl^2/h_0^3)$ for internal waves compared to Hl^2/h_0^3 for surface waves.

Benjamin (1967) considered a different situation in which the density of the fluid varies only within a layer whose thickness is much smaller than the wavelength of the internal wave, while the total depth of the stratified fluid is infinite. Benjamin's solution for a solitary wave at the interface of two homogeneous fluids clearly brought out the results that $Hl/h_0^2 = O(1)$ for the internal wave. This result is consistent with (5.2.14). The dimensionless parameter H/kh^2 is a measure of the relative importance of the nonlinear effects to the dispersive effects for standing internal waves at the interface of a deep fluid overlying a shallow fluid, or vice versa.

The wave extrema of internal waves, η_4, normalized by the depth of the lower fluid, h_2, are plotted as a function of K_2h_2 in figure 5.2.23 for all the experiments in Series I, where K_2 is the wave number of the internal waves in the trench. In these experiments, the wave periods were measured and the wave numbers of the internal waves K_2 were calculated using the two-layer dispersion relation (equation 3.1.18a). In figure 5.2.23, the theoretical predictions are obtained using (5.2.11), with the wave number K given by K_2, and the wave amplitude a given by the mean of the positive and negative wave extrema measured at the upstream wall of the trench, that is, $a = H_4/2$. The good agreement between experiments and second order theory (equation 5.2.11) suggests that second order effects in the internal waves were very weak. From figure 5.2.23, an estimate of the second order effects in the internal wave profiles can be obtained using (5.2.13). The maximum value of

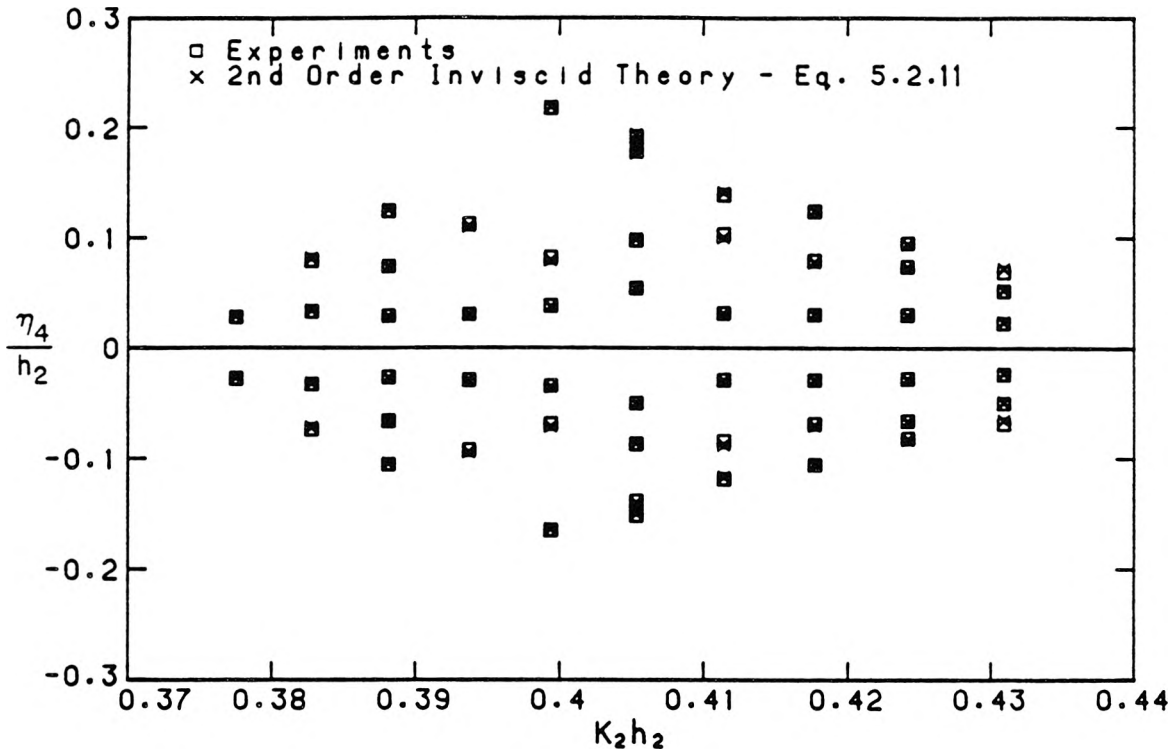

Figure 5.2.23. Comparison between the internal wave extrema at the upstream wall of the trench for experiments, and second order theory (equation 5.2.11); $h_1 = 22.8\,\text{cm}$, $h_2 = 7.6\,\text{cm}$, $\rho_2/\rho_1 = 1.05$.

H_4/h_2 in these experiments was 0.382 at $K_2h_2 = 0.399$ ($K_2h_1 = 1.197$, $k\ell = 0.393$), the corresponding ratio of the amplitude of the second order terms in (5.2.11) to that of the first is found to be 0.144 which indeed is much less than unity. The corresponding value of the dimensionless parameter, $H_4/K_2h_2^2$, is 0.96.

The profiles of the density interface for two different wave heights of the internal wave for a wave period of 7.7 sec are shown in figures 5.2.24*a* and 5.2.24*b*. For this wave period the internal waves were near resonance for the lowest mode of oscillation. The ordinate is normalized by the mean of the internal wave heights measured at the two vertical walls of the trench. The abscissa is normalized by the trench width. The agreement between the results of the experiments and the

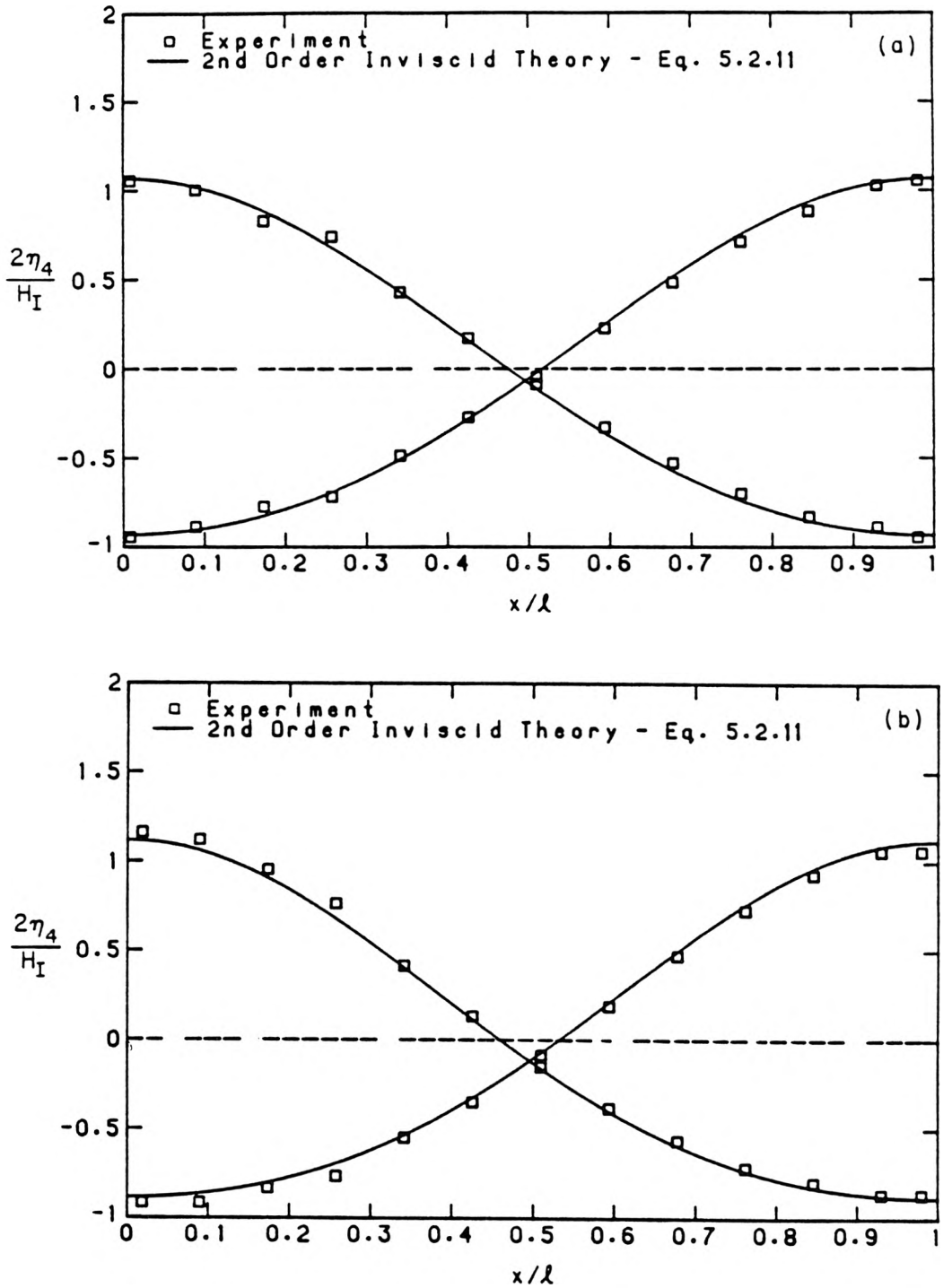

Figure 5.2.24. Standing internal wave profiles for the lowest mode of oscillation of the internal waves in the trench: (*a*) $H_4/h_2 = 0.184$, and (*b*) $H_4/h_2 = 0.317$. The wave period is 7.7 sec ($k\ell = 0.398$). The experimental data are obtained from steady-state wave records taken at intervals of 5.0 cm along the trench. The theoretical curve is computed using (5.2.11), with $h_1 = 22.8$ cm, $h_2 = 7.6$ cm, and $T = 7.7$ sec.

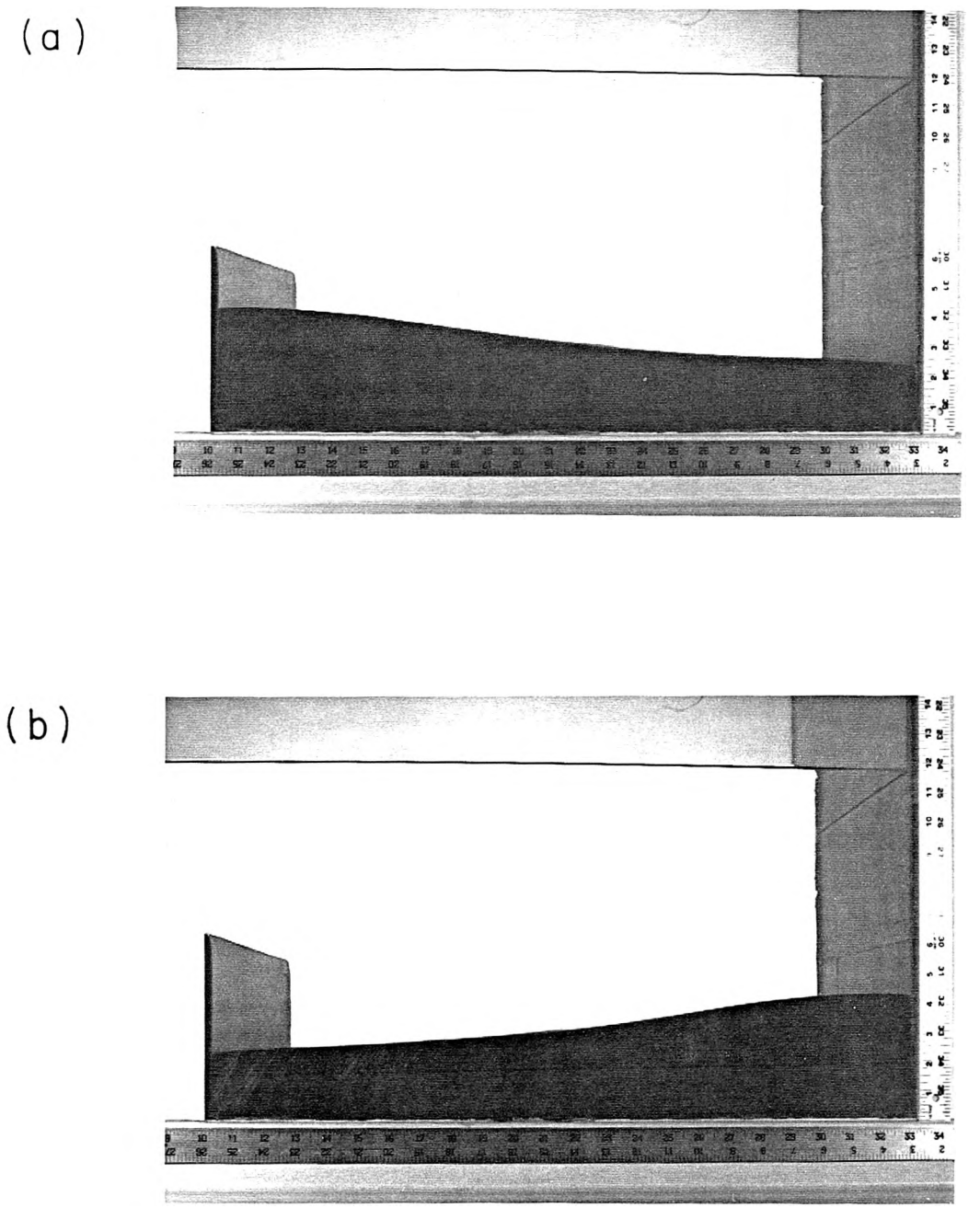

Figure 5.2.25. Standing internal waves in a deep lower fluid in the trench for the 1st mode of resonant oscillation ($K_2\ell = \pi$): (a) maximum upward displacement at $x/\ell = 0$, and (b) maximum downward displacement at $x = 0$; $h_1 = 22.8\,\mathrm{cm}$, $h_2 = 7.6\,\mathrm{cm}$, $\Delta\rho \approx 0.05\,\mathrm{gcm}^{-3}$, $T = 7.8\,\mathrm{sec}$.

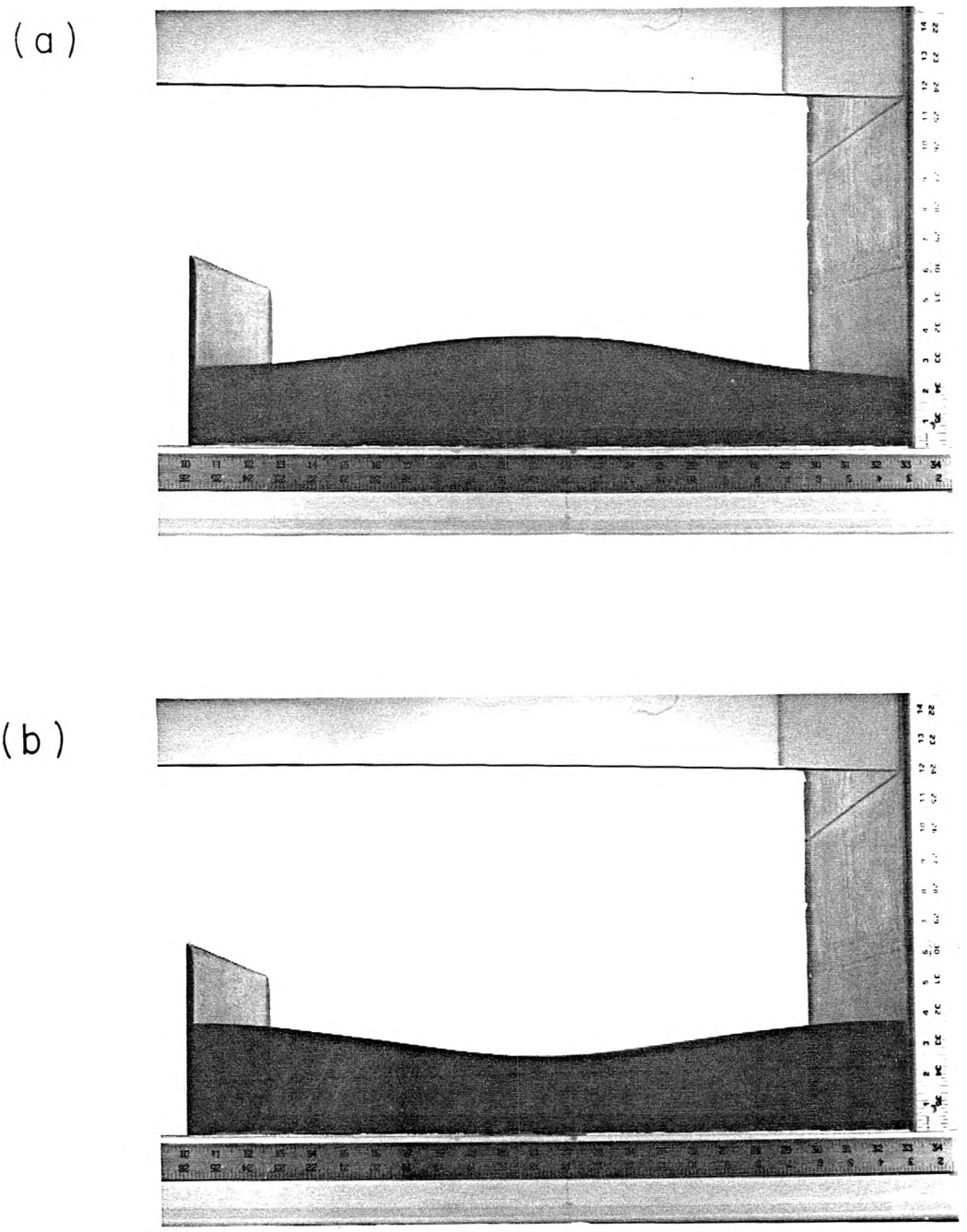

Figure 5.2.26. Standing internal waves in a deep lower fluid in the trench for the 2nd mode of resonant oscillation ($K_2\ell = 2\pi$) (a) maximum upward displacement at $x/\ell = 0.5$, and (b) maximum downward displacement at $x/\ell = 0.5$; $h_1 = 22.8\,\mathrm{cm}$, $h_2 = 7.6\,\mathrm{cm}$, $\Delta\rho \approx 0.05\,\mathrm{gcm}^{-3}$, $T = 4.5\,\mathrm{sec}$.

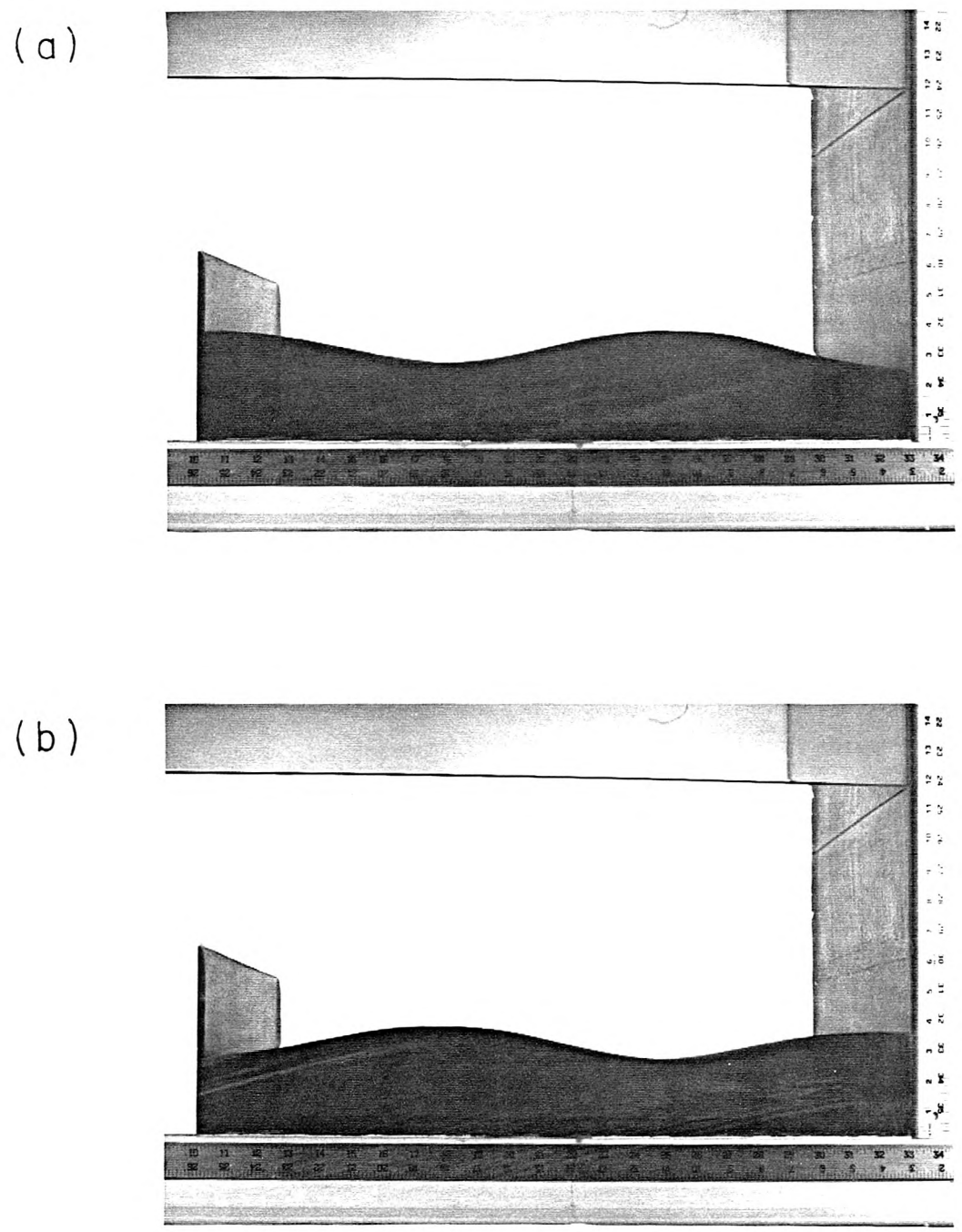

Figure 5.2.27. Standing internal waves in a deep lower fluid in the trench for the 3rd mode of resonant oscillation ($K_2\ell = 3\pi$): (a) maximum upward displacement at $x/\ell = 0$, and (b) maximum downward displacement at $x/\ell = 0$; $h_1 = 22.8\,\mathrm{cm}$, $h_2 = 7.6\,\mathrm{cm}$, $\Delta\rho \approx 0.05\,\mathrm{gcm}^{-3}$, $T = 3.4\,\mathrm{sec}$.

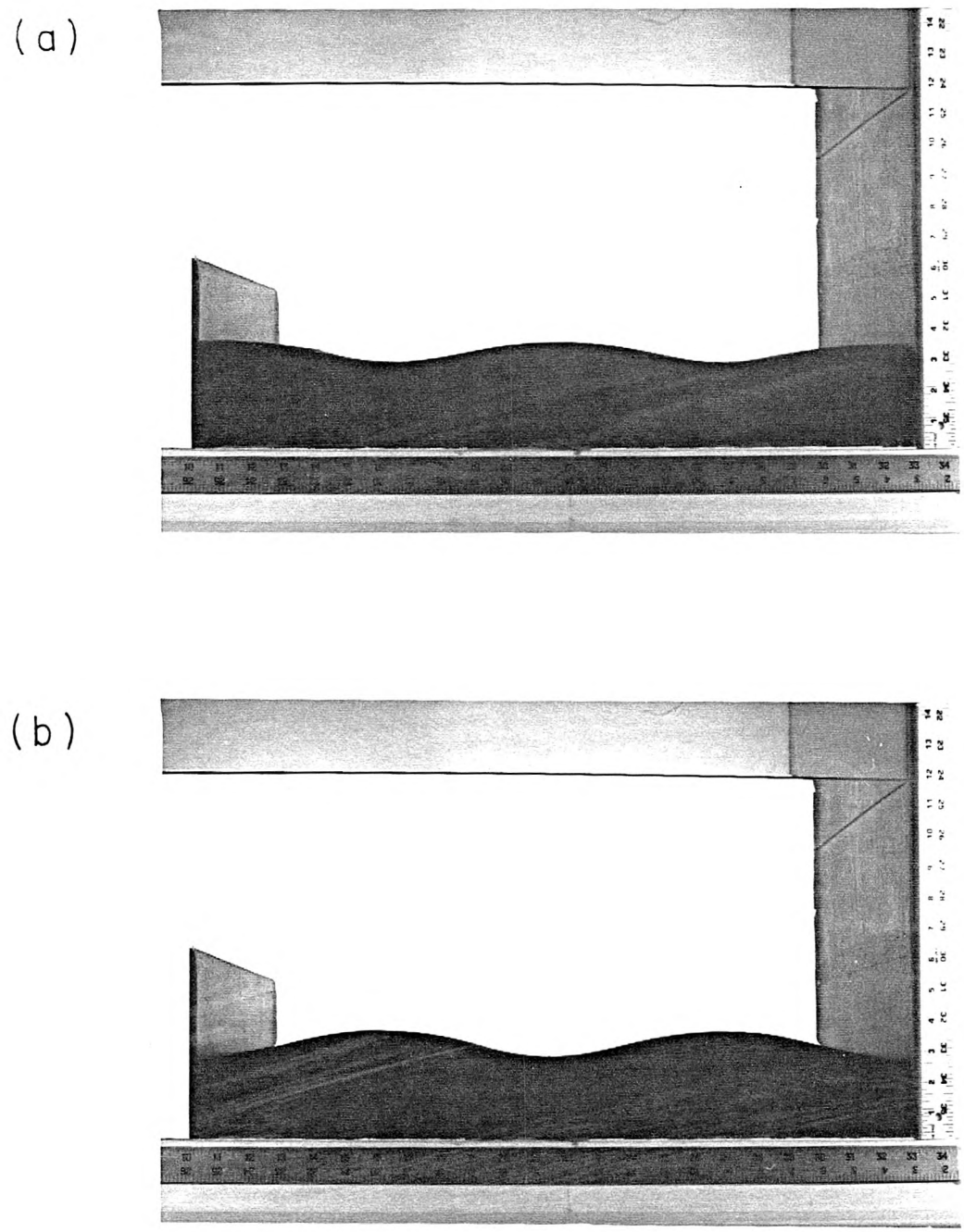

Figure 5.2.28. Standing internal waves in a deep lower fluid in the trench for the 4th mode of resonant oscillation ($K_2\ell = 4\pi$): (a) maximum upward displacement at $x/\ell = 0.5$, and (b) maximum downward displacement at $x/\ell = 0.5$; $h_1 = 22.8\,\mathrm{cm}$, $h_2 = 7.6\,\mathrm{cm}$, $\Delta\rho \approx 0.05\,\mathrm{gcm}^{-3}$, $T = 2.9\,\mathrm{sec}$.

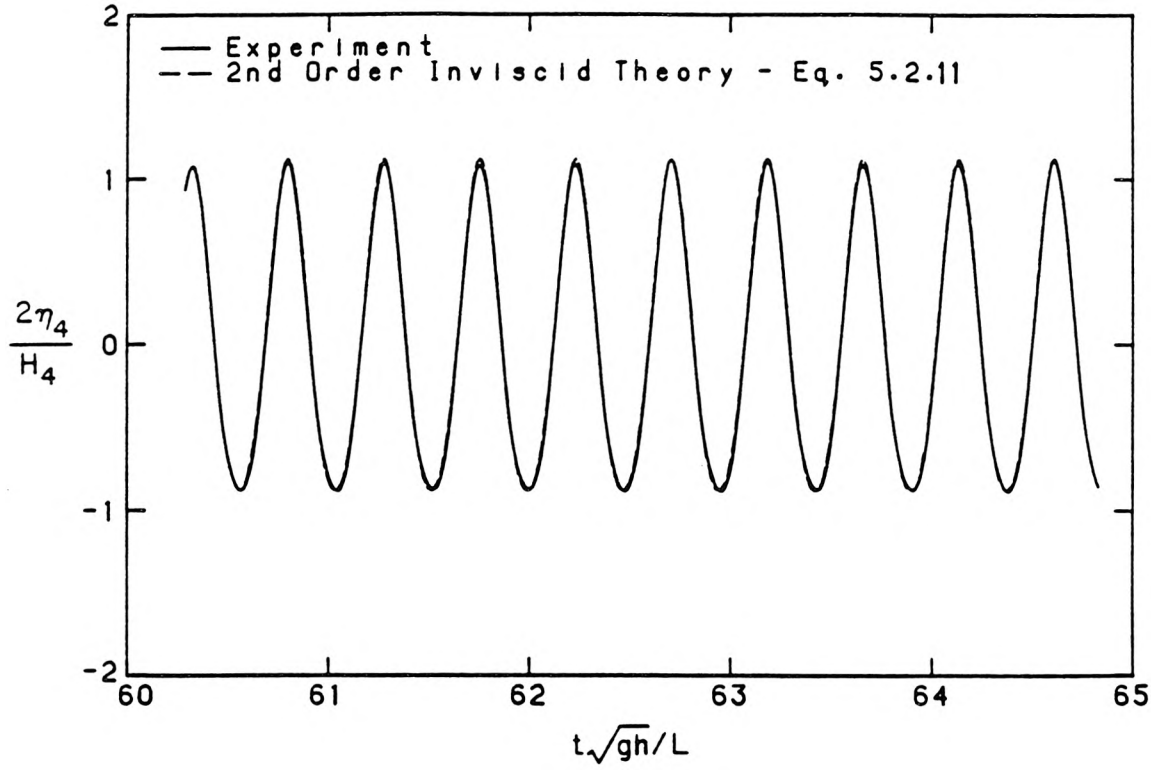

Figure 5.2.29. Comparison between the steady-state internal wave time histories at the upstream wall of the trench for experiment and second order theory (equation 5.2.11); $h_1 = 22.8\,\text{cm}$, $h_2 = 7.6\,\text{cm}$, $H_4 = 2.4\,\text{cm}$, $T = 7.7\,\text{sec}$, $\rho_2/\rho_1 = 1.05$.

second order theory (equation 5.2.11) is excellent. Notice that the standing internal waves do not have a true node at $x/\ell = 0.5$ due to second order effects in the wave profiles. The internal oscillations were observed to be two-dimensional; no cross-waves were seen in the direction across the wave tank. Photographs of standing internal waves in the trench for the first four modes of resonant oscillation are shown in figures 5.2.25–5.2.28. Notice that in these figures the motion of the free surface are very small compared to the motion of the dye interface. It is seen in figures 5.2.25*a* and 5.2.25*b* that the internal wave profiles for the lowest mode of oscillation are similar to those shown in figure 5.2.24*b*. In figure 5.2.29, the steady-state portion of the time history of internal wave motion at the upstream wall of the trench is compared to second order theory (equation 5.2.11) for a wave period

of 7.7 sec. The ordinate is normalized by $H_4/2$, where H_4 is the wave height of the internal waves measured at the upstream wall of the trench. The abscissa is dimensionless time measured from the start of the wave generator. The phase of the computed wave has been matched to coincide with the phase of the measured wave.

To further illustrate the characteristics of internal waves near resonance, the steady-state portion of the time histories of motion at the upstream wall of the trench are presented in figure 5.2.30 for a range of relative circular frequencies, σ/σ_0, where $\sigma_0 = 2\pi/7.75$ is the resonant frequency for the lowest mode of oscillation of the internal waves in the trench obtained using the two-layer inviscid theory. It is seen that the internal wave motions are weakly nonlinear, and the ratio of crest amplitude to trough amplitude increases with the internal wave height. No secondary oscillation is seen in the internal waves, in contrast to the surface wave motions near a resonant mode of oscillation of the surface waves in the constant-depth channel (figure 5.2.3). This may simply be explained by the effects of density stratification; the presence of the upper fluid reduces the amplitude of the second order term in the wave profile (see equations 5.2.5 and 5.2.14). The spurious signals seen for $\sigma/\sigma_0 = 0.969$ in figure 5.2.30 are due to electronic problems in the interfacial wave gage. The corresponding steady-state portion of the surface wave time histories at the end wall are shown in figure 5.2.31. The high frequency components seen in some of the surface wave records are not secondary oscillations due to nonlinear effects as discussed in § 5.2.1 and § 5.2.2, but are due to irregular motions of the wave generator. After close examination, the problem was found to be in the servo-valve of the wave generator. The servo-valve directs the flow of oil to either end of a double-acting hydraulic cylinder and thus controls the motion of the wave plate. The deflective servo-valve was replaced and the high frequency components in the surface waves disappeared. It is important to note that the high

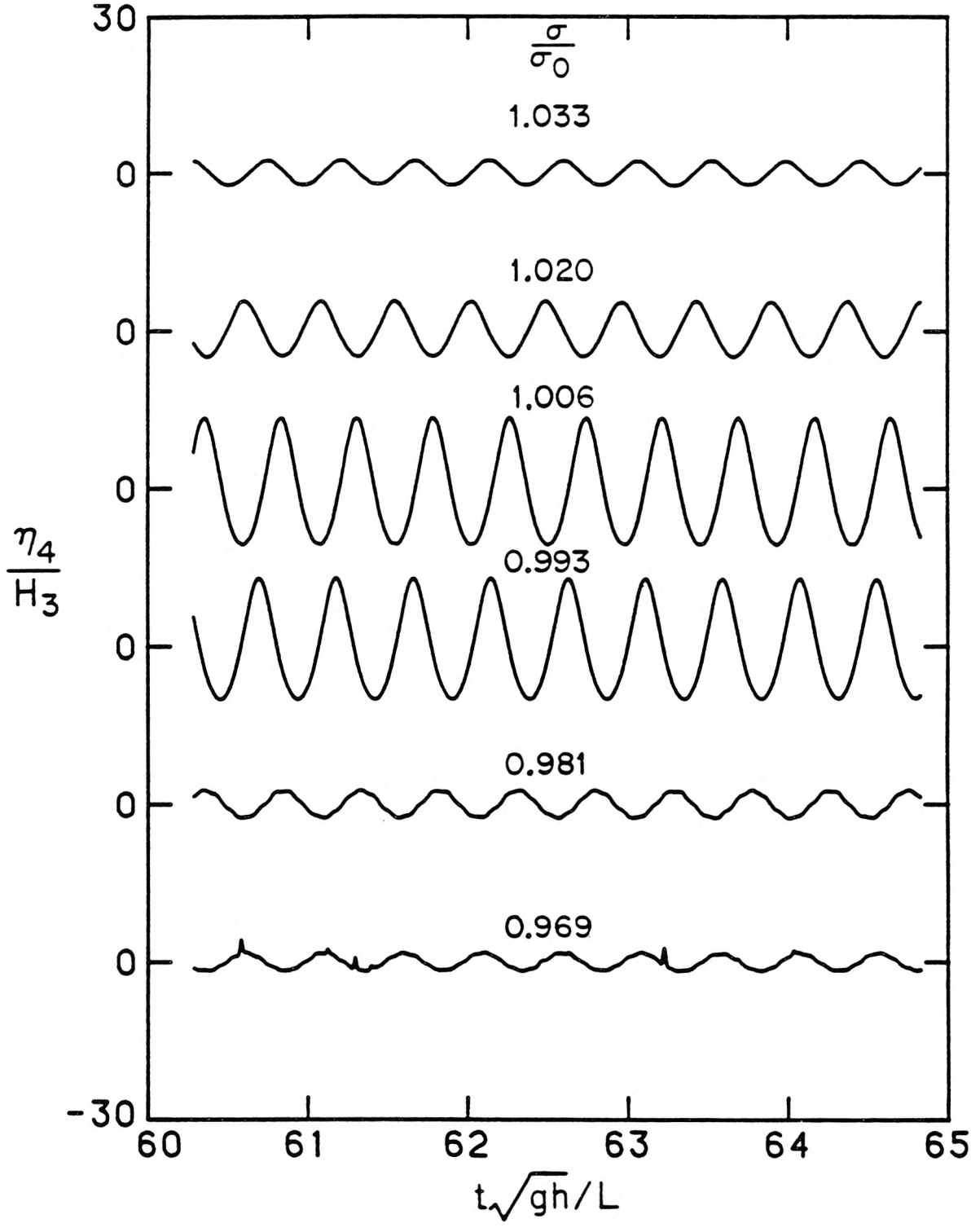

Figure 5.2.30. Steady-state internal wave motions at the upstream wall of the trench for relative circular frequencies near the lowest mode of internal oscillation in the trench; $h_1 = 22.8\,\text{cm}$, $h_2 = 7.6\,\text{cm}$, $\Delta\rho \approx 0.05\,\text{gcm}^{-3}$.

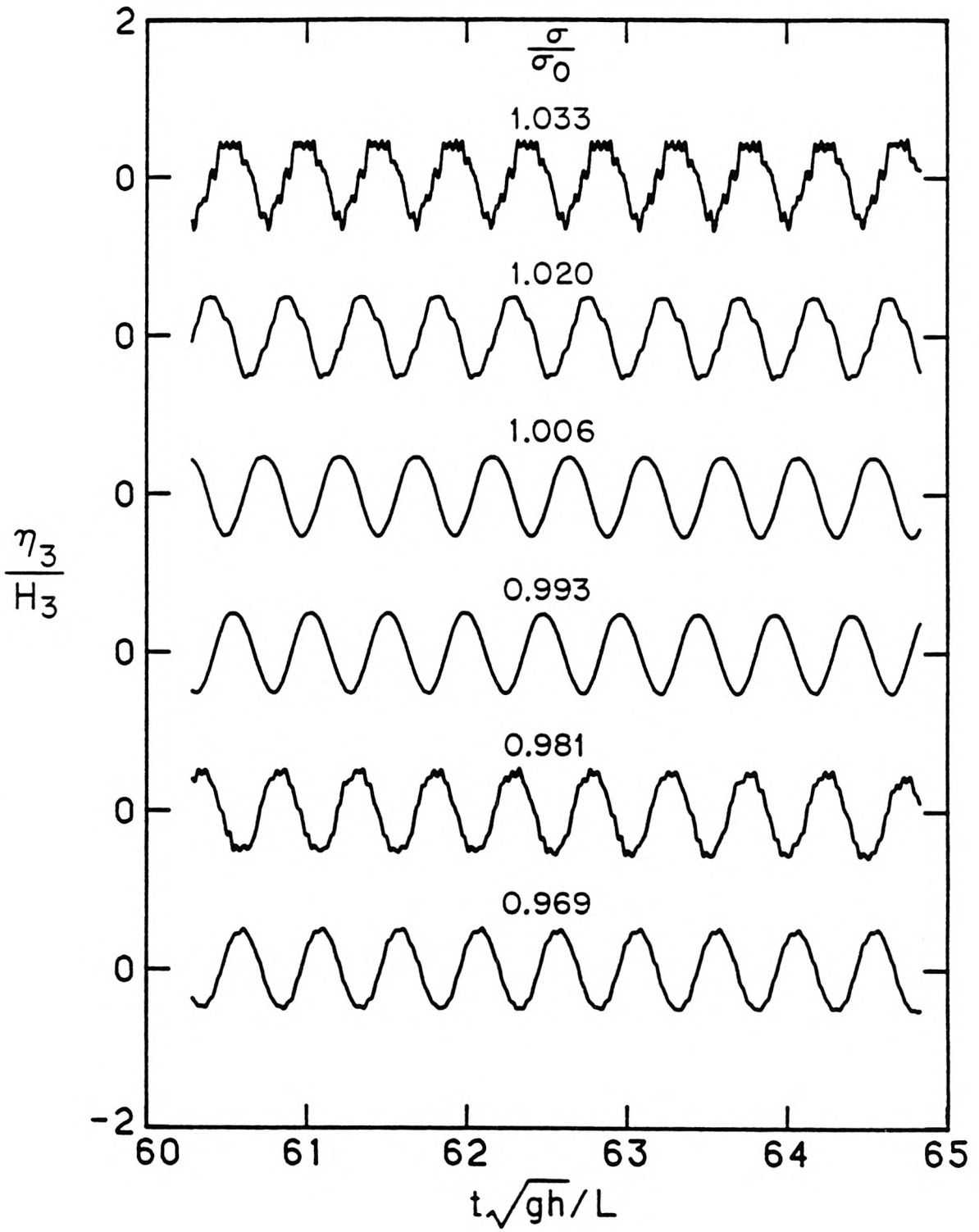

Figure 5.2.31. Steady-state water surface motions at the end wall for relative circular frequencies near the lowest mode of internal oscillation in the trench; $h_1 = 22.8\,\text{cm}$, $h_2 = 7.6\,\text{cm}$, $\Delta\rho \approx 0.05\,\text{gcm}^{-3}$.

frequency components apparent in the surface wave records are not observed in the internal wave records. This may be because the peakedness of the response curve of figure 5.2.16 results in an efficient filter for the frequencies away from resonance.

The complete time histories of the internal waves at the upstream wall of the trench and of the surface waves at the end wall, from the start of the wave generator, are presented in figure 5.2.32 for a wave period of 7.7 sec ($\sigma/\sigma_0 = 1.006$). Note that the scale of the ordinate for the internal waves is a factor of ten smaller than that of the surface waves, that is, the internal waves would appear ten times larger than those shown if plotted to the same scale as the surface waves. This wave period corresponds to the lowest mode of oscillation of internal waves in the trench and an off-resonant condition for surface waves in the constant-depth channel. Notice the absence of a beat pattern in the internal wave record due a resonant condition in the trench; the growth of internal waves are retarded temporarily after the first few oscillations due to a decrease in amplitude of the surface waves above the trench.

Surface and internal wave time histories are presented in figure 5.2.33 for a wave period of 7.6 sec ($\sigma/\sigma_0 = 1.02$), which corresponds to off-resonant conditions in both the constant-depth channel and the trench. The internal wave record is characterized by a beat pattern, and amplitude modulation due to changing amplitude of the surface waves. From these figures, one can obtain an idea of the time required to establish steady-state conditions in the trench. Further off-resonance, the beat period of the internal waves becomes still shorter. This situation is shown in figure 5.2.34 for a wave period of 7.4 sec ($\sigma/\sigma_0 = 1.047$).

The time histories of motion of the surface and internal waves are shown in figure 5.2.35 for a wave period of 8.2 sec ($\sigma/\sigma_0 = 0.945$). This wave period corresponds to a resonant mode of oscillation for the surface waves in the constant-depth channel and an off-resonant condition for the internal waves in the trench. However, the internal wave record does not show a beat pattern, because at this off-resonant con-

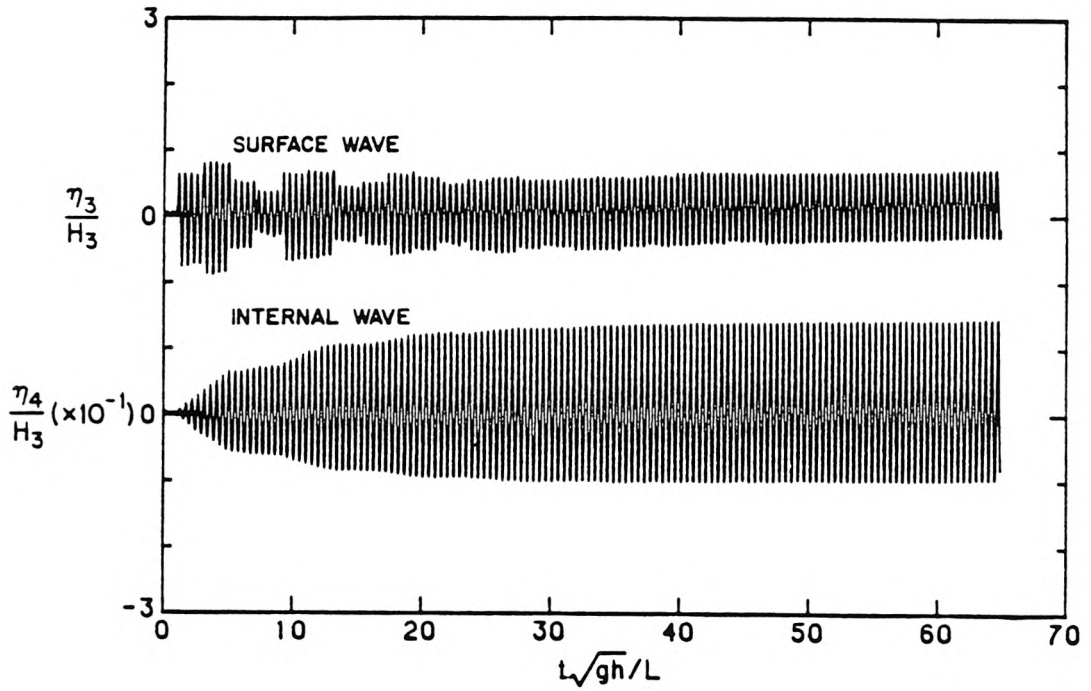

Figure 5.2.32. Surface and internal waves for experiment at $T = 7.7$ sec ($k\ell = 0.398$) and $H_3 = 1.08$ mm.

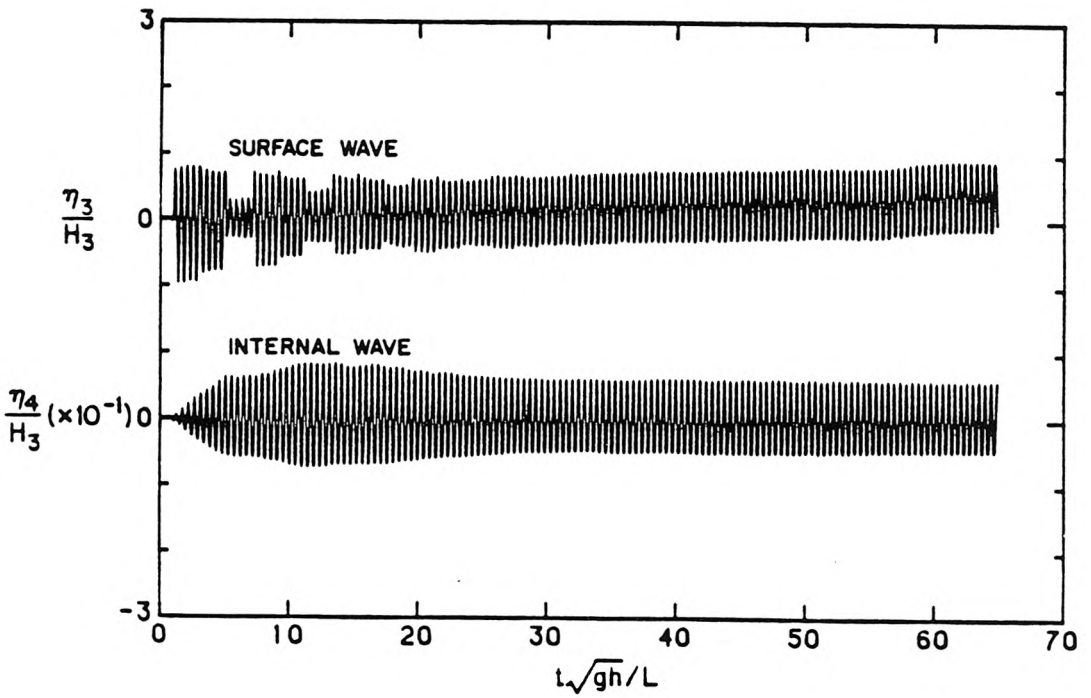

Figure 5.2.33. Surface and internal waves for experiment at $T = 7.6$ sec ($k\ell = 0.404$) and $H_3 = 1.36$ mm.

dition for the internal waves the effects of the surface waves are more pronounced. As seen in figure 5.2.16, the measured amplification factor, H_4/H_3, is only about 2.3 for $k\ell = 0.374$ ($\sigma/\sigma_0 = 0.945$). Indeed, the internal wave motion appears to follow the growth of the surface waves.

We concluded in § 5.2.2 that a trench in a homogeneous fluid has little effect on the surface waves if the dimensions of the trench are small compared to the wavelength of the surface wave. Internal oscillation in a stratified trench can change the above conclusion in important ways. The effects of internal waves on the waves on the water surface will be discussed now. It is noted that in calculating the amplification factor, H_4/H_3, for the response curves, the wave height H_3 is taken to be the wave height on the water surface at the end wall. In linear two-layer theory, the fluid motion is composed of the contributions of the surface mode and interfacial mode (see equation 3.1.20). These two modes have the same wave period but different wavelengths. The surface mode and the interfacial mode, respectively, are generated at the water surface and at the density interface, where the density differences between the fluid above and the fluid below provide the restoring force responsible for the existence of wave motions. Hence, the effects of the interfacial mode are most pronounced at the density interface whereas the effects of the surface mode are most pronounced at the water surface. For the lowest mode of oscillation of the internal wave in the trench the wavelength of the interfacial mode is very close to twice the trench width. For the same wave period, the wavelength of the surface mode is much longer than the wavelength of the interfacial mode. The wave motion observed on the water surface may be regarded as the sum of the effects of the surface mode and the interfacial mode, and likewise on the density interface. However, we shall demonstrate that the surface effect of the interfacial mode is very small compared to that of the surface mode, if density differences between the two fluids are small. Thus, in most circumstances the water surface motion

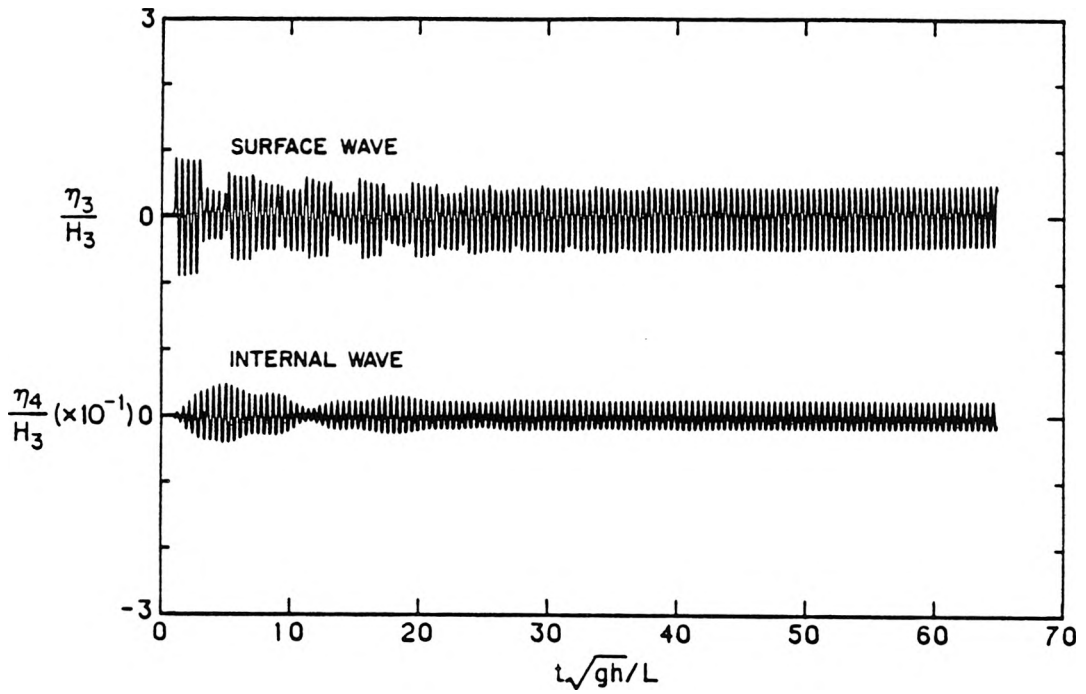

Figure 5.2.34. Surface and internal waves for experiment at $T = 7.4\,\text{sec}$ ($k\ell = 0.414$) and $H_3 = 3.05\,\text{mm}$.

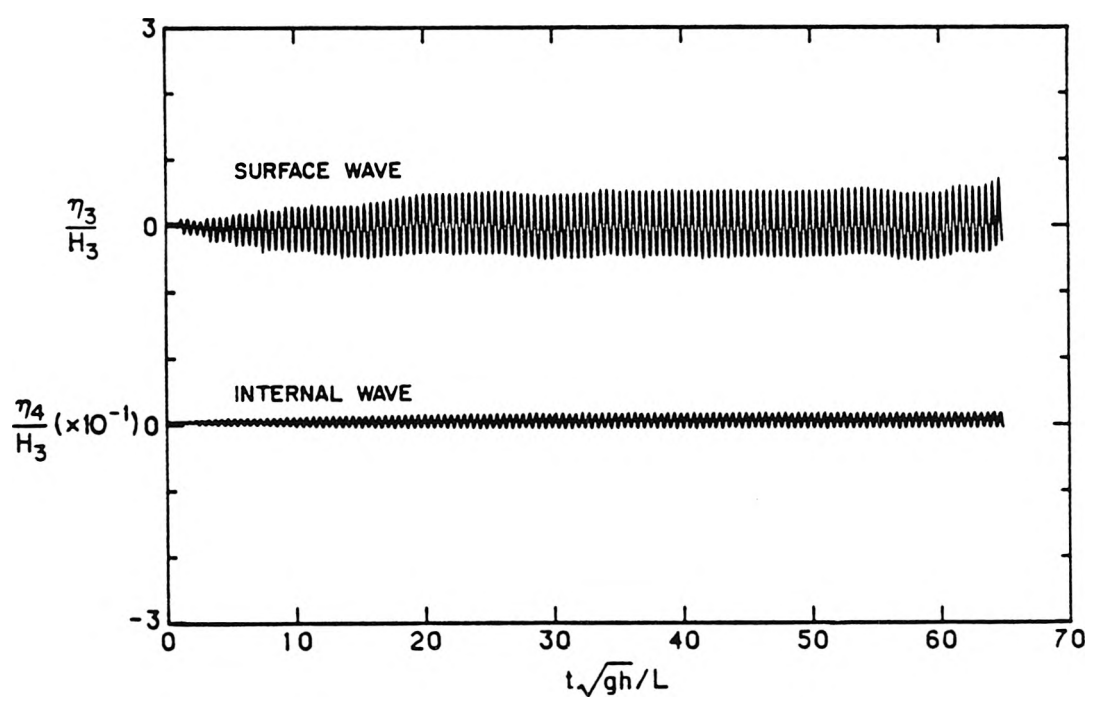

Figure 5.2.35. Surface and internal waves for experiment at $T = 8.2\,\text{sec}$ ($k\ell = 0.374$) and $H_3 = 1.85\,\text{mm}$.

above the trench can be represented reasonably well by the surface mode alone. When the effects of the internal oscillations cannot be felt on the water surface, the fluid motion above the trench would behave as if there had been no density variation in the trench. Therefore, an incident surface wave whose wavelength is large compared to the trench dimensions will not be affected by the presence of the stratified trench. On the other hand, the internal oscillations of the density interface will be noticeable due to comparatively small potential energy involved in a given deformation of the density interface. The above situation may change when a resonant condition develops in the trench. The amplitude of the internal motions at the interface may become large enough to be noticeable on the water surface. Then the fluid state above the trench must adjust to this new condition, thus changing the surface waves scattered by the trench in important ways. To illustrate this, let us consider the motion of a time-periodic plane progressive wave in a two-layer fluid, that is, the problem treated in § 3.3.1.1. The upper fluid is of depth h_1 and of density ρ_1, and the lower fluid is of depth h_2 and of density ρ_2. The velocity potentials Φ_1 for the upper layer and Φ_2 for the lower layer are given by:

$$\Phi_1(x,z,t) = C\left(\cosh Kz + \frac{\sigma^2}{gK}\sinh Kz\right)\cos(Kx-\sigma t), \tag{5.2.15a}$$

$$\Phi_2(x,z,t) = C\left(\frac{\sigma^2}{gK}\cosh Kh_1 - \sinh Kh_1\right)\frac{\cosh K(z+h_1+h_2)}{\sinh Kh_2} \cdot \cos(Kx-\sigma t) \tag{5.2.15b}$$

wherein C is an arbitrary constant, and K is the wave number given by the two-layer dispersion relation (3.1.18a), which is written here for convenience to the readers:

$$\sigma^4\left(\frac{\rho_2}{\rho_1}\coth Kh_1\coth Kh_2 + 1\right) - \sigma^2\frac{\rho_2}{\rho_1}(\coth Kh_1 + \coth Kh_2)\,gK + \left(\frac{\rho_2}{\rho_1} - 1\right)g^2K^2 = 0. \tag{5.2.16}$$

The displacement of the water surface ($z = 0$) and of the density interface ($z = -h_1$)

can be found from the following relationship:

$$\eta = \int \frac{\partial \Phi}{\partial z} dt. \tag{5.2.17}$$

From (5.2.15) and (5.2.17), the ratio of the amplitude of displacement of the density interface to that of the water surface is found to be:

$$R^* = \left(\cosh Kh_1 - \frac{gK}{\sigma^2} \sinh Kh_1 \right) \tag{5.2.18}$$

Note that R^* is different from the amplification factor R; R is the ratio of the amplitude of the internal waves in the trench to the amplitude of the surface waves due to wave-trench interaction, whereas R^* represents the ratio of the amplitude of the vertical displacement of a fluid particle at the density interface to that on the free surface in a two-layer fluid of constant-depth, due to the wave motion of the surface mode or the interfacial mode. Equations 5.2.15 and 5.2.18 are the same for the surface mode and the interfacial mode, but the wave number K is different in each case. The wave numbers are given by the two real roots of (5.2.16), which we designate by K_1 for the surface mode and by K_2 for the interfacial mode. Using (5.2.16), with $h_1 = 22.8\,\text{cm}$, $h_2 = 7.6\,\text{cm}$, $T = 2\pi/\sigma = 7.75\,\text{sec}$, and $\rho_2/\rho_1 = 1.05$, the values of K_1 and K_2 are found to be $0.473\,\text{m}^{-1}$ and $5.294\,\text{m}^{-1}$, respectively. Substituting K_2 for K in (5.2.18) and using the above flow conditions yield a value of $R^* = -118.45$. The minus sign indicates that the wave at the water surface is 180° out of phase with the wave at the interface, for the interfacial mode. It is seen that the effects of the interfacial mode on the water surface are indeed very small for the above conditions.

For the surface mode, we substitute the determined value of K_1 for K in (5.2.18), which yields a value of $R^* = 0.24$, thus the wave motion at the interface is diminished, compared to the wave motion on the water surface. Let us compare this result with the fluid motion in a time-periodic progressive wave in a homogeneous fluid of

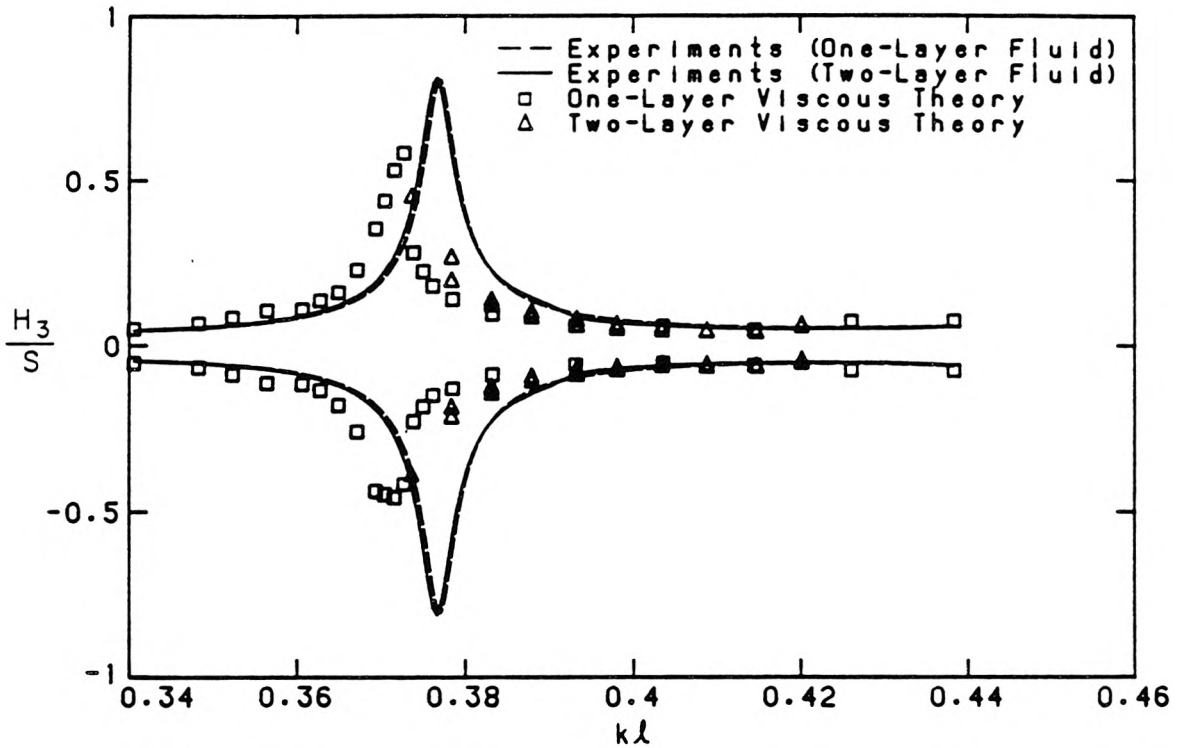

Figure 5.2.36. Variation of surface wave extrema at the end wall with relative wave number. Comparison between the results for fresh water in trench and a two-layer fluid in trench.

the same total depth $h = h_1 + h_2$. From linear theory (see, for example, Dean and Dalrymple, 1984), the ratio of the amplitude of the vertical displacement of a fluid particle at a depth z to that on the water surface is given by $\sinh k(h+z)/\sinh kh$, where z is measured positive upwards from the still water surface, and k denotes the wave number in homogeneous fluid. Putting $k = K_1$ and using the previously stated flow conditions yield an amplitude ratio of 0.25. Thus, for the surface mode, the wave motion at the interface is in phase with the wave motion at the water surface and has been decreased in amplitude by almost the same amount that the particle oscillations would have been decreased in amplitude if there had been no variation in density with depth.

Seen in this light, we expect that the effects of internal oscillations due to wave-

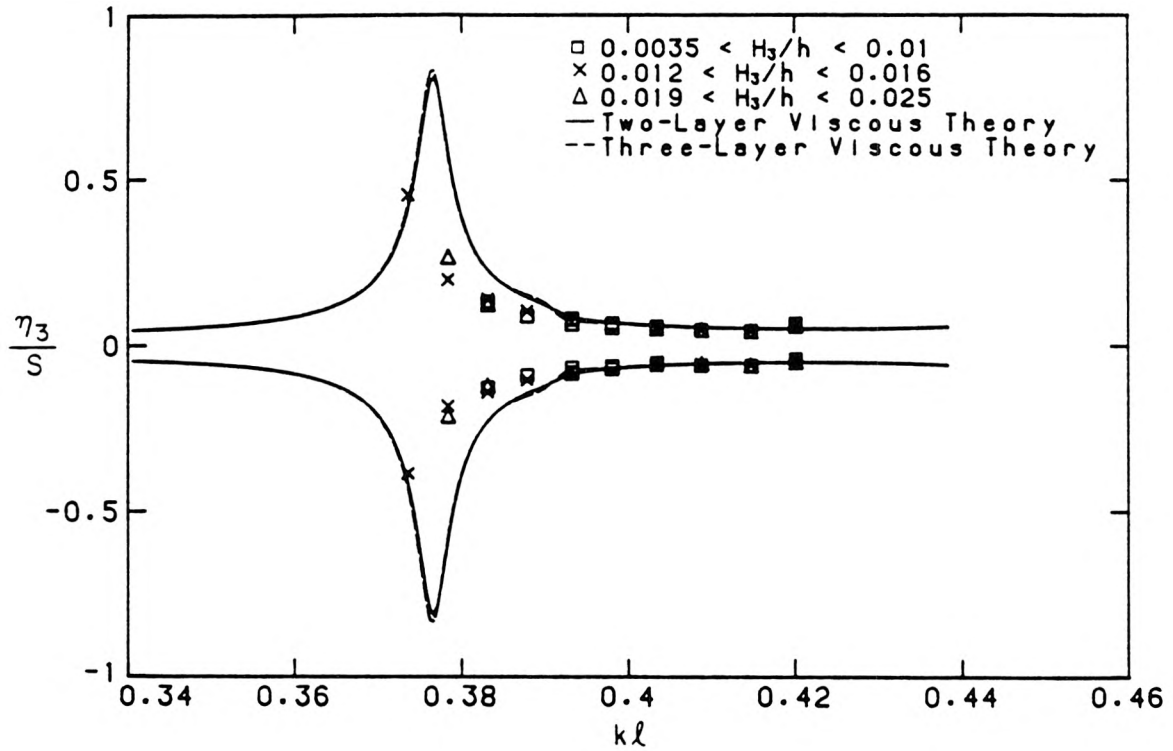

Figure 5.2.37. Variation of surface wave extrema at the end wall with relative wave number. The experimental results for stratified fluid in trench with a mean thickness of the diffuse salinity interface of 1.32 cm (Series *I*) are compared to the predictions of the two-layer viscous theory; $h_1 = 22.8\,\text{cm}$, $h_2 = 7.6\,\text{cm}$, and the three-layer viscous theory; $h_1 = 22.15\,\text{cm}$, $h_2 = 6.95\,\text{cm}$, $\delta = 1.3\,\text{cm}$.

trench interaction on the water surface will be small if $|R/R^*| \ll 1$. In other words, because the amplitude of the internal motion decays rapidly with distance from the density interface toward the free surface, the effects of internal oscillation cannot be felt on the free surface unless the motion at the density interface is sufficiently large. This appears to be the case in our experiments. The variation of surface wave extrema at two locations above the trench with relative wave number was presented in figures 5.2.10*a* and 5.2.10*b* for the condition that fresh water fills both the constant-depth channel and the trench, and in figures 5.2.22*a* and 5.2.22*b* for the case of a stratified fluid in the trench. The experimental and theoretical results

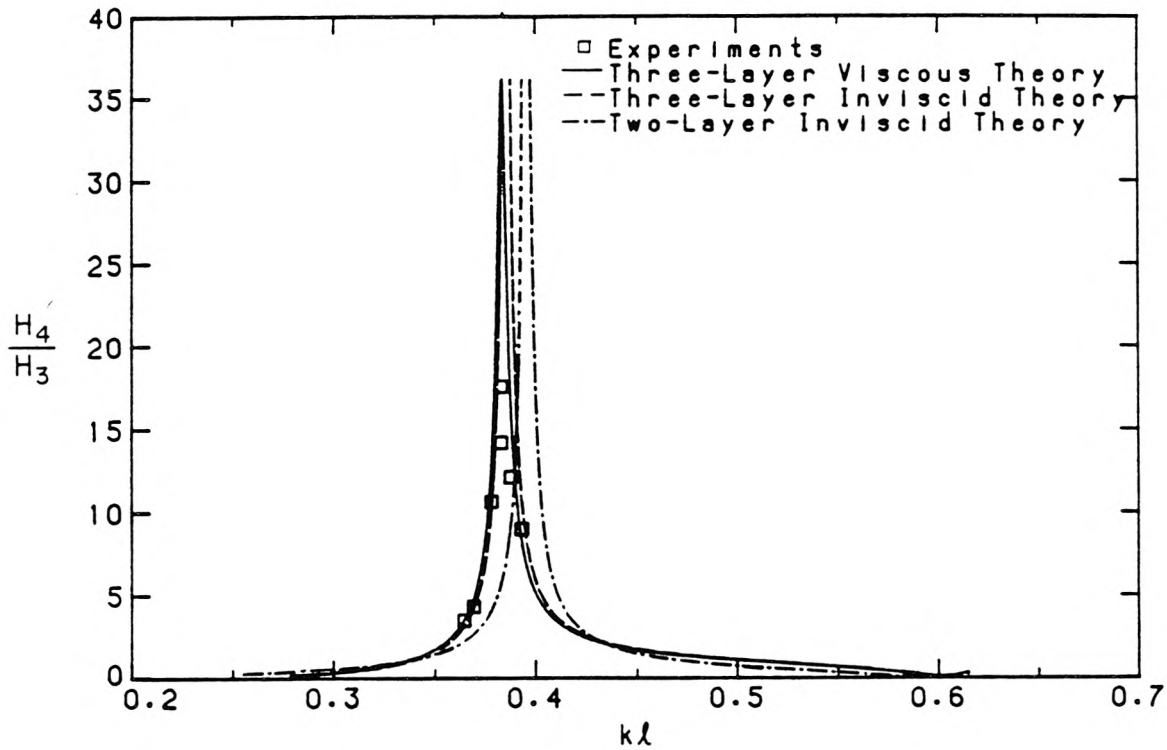

Figure 5.2.38. Variation of normalized internal wave height at the upstream wall of the trench with relative wave number for a diffuse salinity interface thickness of 2.5 cm. Comparison between the results of the experiments, the two-layer inviscid theory, the three-layer viscous theory, and the three-layer inviscid theory.

shown in figures 5.2.10*b* and 5.2.22*b* are plotted together in figure 5.2.36. It is seen in figure 5.2.36 that the differences in the surface wave height for the two cases are small for both experiment and theory. The lowest mode of oscillation of the internal waves in the trench occurs at $k\ell = 0.392$. The amplification factor R obtained using the two-layer viscous theory is 20.49 at $k\ell = 0.392$, and R^* is about -120 from the previous calculation, thus $|R/R^*| \approx 0.17$. Hence, the effects of the internal oscillations on the waves on the water surface are small.

The theoretical results shown in figures 5.2.22*a* and 5.2.22*b* were obtained using the two-layer viscous theory. A comparison of the surface wave extrema at the end wall for the results of the same experiments, and the predictions of the two-layer viscous theory and the three-layer viscous theory, is presented in figure 5.2.37. In

computing the theoretical solution using the three-layer viscous theory, the thickness of the diffuse salinity interface was taken to be 1.3 cm. It is seen that the two-layer viscous theory and the three-layer viscous theory yield nearly identical results, but the three-layer viscous theory predicts somewhat larger effects on the water surface near the relative wave number for the lowest mode of resonant oscillation of the internal wave in the trench, that is, near $k\ell = 0.392$. This is because the three-layer viscous theory does not include interfacial boundary layer damping, consequently, the amplification factor as predicted by the three-layer viscous theory is larger than that predicted by the two-layer viscous theory (see figures 5.2.16 and 5.2.18). Thus, the effects of the internal oscillations on the water surface as predicted by three-layer viscous theory are also more pronounced near resonance. Also seen in figure 5.2.37, the theoretical predictions of the two-layer viscous theory and the three-layer viscous theory agree resonably well with the experimental measurements at off-resonant conditions of the surface waves in the constant-depth channel and trench.

Finally, in figure 5.2.38 we present the response of the internal wave motion for those experiments where the thickness of the diffuse salinity interface was increased to a mean value of 2.46 cm (Series J). The theoretical predictions obtained using the three-layer theories (with $\delta = 2.5$ cm) and the two-layer inviscid theory are also shown. There is a small but definite shift in the resonant frequency of the internal waves in the trench relative to that predicted by the two-layer inviscid theory; the difference between the wave periods of resonance for the lowest mode obtained using the two-layer inviscid theory and the three-layer inviscid theory when compared to the difference between the wave periods of the first and second resonant modes is about 6%. The relative wave number $k\ell$ corresponding to the lowest mode of oscillation of the internal waves in the trench as predicted by the two-layer inviscid theory, the three-layer inviscid theory, and the three-layer viscous

theory, respectively, are 0.396, 0.386, and 0.383. The corresponding wave periods are 7.75 sec, 7.95 sec, and 7.99 sec. The effect of increasing the thickness of the diffuse salinity interface is to decrease the resonant frequency. This is quite understandable from the physical point of view, because the density of the quiescent fluid, $\overline{\rho}$, which represents the inertia of the fluid, is almost unchanged by increasing the thickness of the diffuse salinity interface, whereas the restoring force responsible for the existence of wave motion, represented by $g\eta d\overline{\rho}/dz$, where η is the vertical displacement of a fluid element from its undisturbed position, decreases as δ increases. The frequency of the motion will decrease with smaller restoring force, which is the case shown here. Nevertheless, the effects of the thickness of the diffuse salinity interface on the response of the internal wave are still small. Comparing figure 5.2.38 ($\delta = 2.5\,\mathrm{cm}$) to figure 5.2.18 ($\delta = 1.3\,\mathrm{cm}$), it is seen that the maximum values of the amplification factor, H_4/H_3, which were obtained using the three-layer viscous theory, are about the same for the two different thicknesses of the diffuse salinity interface.

In summary, the responses of a two-layer stratified fluid in a rectangular trench to time-periodic surface waves were studied experimentally and theoretically for wave periods near the lowest mode of resonant oscillation of the internal waves in the trench. A constant-depth channel and trench arrangement allowed definitive experiments to be conducted and compared to the theoretical predictions. Density stratification in the trench was created using fresh water and salt water. For these experiments the depth of fresh water in the constant-depth channel and the depths of fresh water and salt water in the trench region were held fixed and experiments were conducted with two different thicknesses of the diffuse salinity interface. The experimental results indicate that when the ratio of the internal wave height to the depth of the lower fluid, H_4/h_2, is small compared to the relative internal wave number, K_2h_2, second order effects in the internal wave profiles are small. The dimensionless parameter $H_4/K_2h_2^2$ is proportional to the amplitude of the second

order term in the internal wave profile. It is also a measure of the relative importance of the nonlinear effects to the dispersive effects. The measured response curves for the internal waves in the trench were compared to the theoretical predictions obtained using a linear two-layer theory and a linear three-layer theory. Satisfactory agreement between the measured and the predicted responses was obtained for these experiemnts where the values of the dimensionless parameter, $H_4/K_2h_2^2$, were small. The measured profiles of the interface also compared well with the finite amplitude standing internal wave solutions of Thorpe (1968); the standing internal waves did not have a true node due to second order effects in the wave profiles. The experimental results indicate that the response characteristics of the trench for wave periods near internal resonance tend to be an effective filter for higher frequency components in the surface waves. The results of the linear viscous theories show that the frequencies of resonant oscillation of the internal waves in the trench are smaller compared to the predictions of the linear inviscid theories, but the differences are small for these experimental conditions. This is because a relatively deep lower fluid ($K_2h_2 \approx 0.4$) was used in these experiments, thus internal wave damping due to shearing motions in the boundary layer adjacent to the trench bottom were substantially reduced compared to wave motions in a shallower lower fluid in the trench. It was found that the three-layer viscous theory underestimated energy dissipation in the actual fluid, whereas the two-layer viscous theory overestimated the damping significantly. The three-layer viscous theory considers the effects of continuous density variation at the density interface and assumes that the entire loss of the energy of waves is localized in laminar boundary layers adjacent to the solid surfaces. The two-layer viscous theory assumes a surface of density discontinuity at the density interface and consequently energy dissipation takes place in the boundary layers adjacent to the density interface as well as at the solid surfaces. Thus, the three-layer model should be a closer realization of the

real fluid conditions. The experimental results therefore suggest that extra energy loss not accounted for by the linear viscous theories existed in the real fluids. The thickness of the diffuse salinity interface affects the density gradient and hence the buoyancy force responsible for the existence of internal waves. The measured and the predicted frequencies of resonant oscillation of the internal waves in the trench decrease as the thickness of the interface increases. Finally, theoretical analysis suggests that the effects of the internal waves on the waves on the water surface can be related to the amplification factor R and an amplitude ratio R^*. The effects of internal oscillations on waves on the water surface are small when $R/R^* \ll 1$, which appears to be the case in these experiments.

5.2.4 Experiments with a Shallow Lower Fluid in a Stratified Trench

In § 5.2.3, internal wave motion in a deep lower fluid ($K_2 h_2 \approx 0.4$) in a rectangular trench was investigated for a range of wave periods near the lowest mode of internal oscillation. The linear theories predicted the motion in the trench quite well for the conditions of weakly nonlinear internal motions and small dissipative effects. It is the intent in this section to study internal oscillations in the same trench for conditions where these effects are more important. The objective is to establish a range of validity of the linear theories, and hence determine their usefulness in predicting internal resonance in submarine trenches under other flow conditions.

We have seen in (5.2.14) that second order nonlinear effects in standing internal waves at the interface of a two-layer fluid where one of the fluids is deep and the other shallow of depth h are characterized by the dimensionless parameter H/Kh^2, where H is the wave height and K is the wave number. In our experiments the wavelengths of the internal waves in the trench were large compared to the depth of the lower fluid (salt water), but the total fluid depth was not large enough in

comparison with the wavelength to be considered as infinite. Thus, the dimensionless parameter H/Kh^2 gives only an estimate of the magnitude of the second order effects in the internal wave profiles (see equations 5.2.13 and 5.2.14). Nevertheless, this parameter is seen to vary inversely as the square of the shallow fluid h. Hence, it is expected that nonlinear effects in the standing internal waves in the trench will be more important as the depth of the lower fluid h_2 decreases. However, the gradient of horizontal velocity near the bottom, for fixed internal wave height at the upstream wall of the trench H_4 and internal wave number K_2, increases as h_2 decreases (this may be deduced from the boundary layer solutions in § 3.3, the details are discussed more fully in § 5.2.5); thus, viscous dissipation in the boundary layer adjacent to the trench bottom increases as h_2 decreases. In a shallow lower fluid, the effects of nonlinearity and dissipation may compete with each other and thus produce a much more complicated behaviour. Motivated by the above conclusion, a series of experiments were conducted using the experimental arrangement shown in figure 5.1.1, with $h_1 = 26.6\,\text{cm}$, and $h_2 = 3.8\,\text{cm}$. Hence, the value of h_2 in these experiments was reduced by half from the value of h_2 of 7.6 cm used in the experiments which were discussed in § 5.2.3. The value of the dimensionless parameter $H_4/K_2h_2^2$ would be increased by four times for the same wave height and wave number of the internal wave. The density difference between water and salt water in these experiments was kept about the same, that is, $\Delta\rho \approx 0.05\,\text{gcm}^{-3}$.

Experiments were conducted using two nominal thicknesses of the diffuse salinity interface: (i) $\delta \approx 1.3\,\text{cm}$ (Series K), and (ii) $\delta = 2.5\,\text{cm}$ (Series M). In Series K the mean thickness of the diffuse salinity interface was 1.31 cm, with a standard deviation of 0.09 cm. The mean density of the lower fluid (salt water) was $1.0506\,\text{gcm}^{-3}$, with a standard deviation of $0.0008\,\text{gcm}^{-3}$. Internal oscillations for a wide range of surface wave heights above the trench were studied; the results of this case will be discussed now.

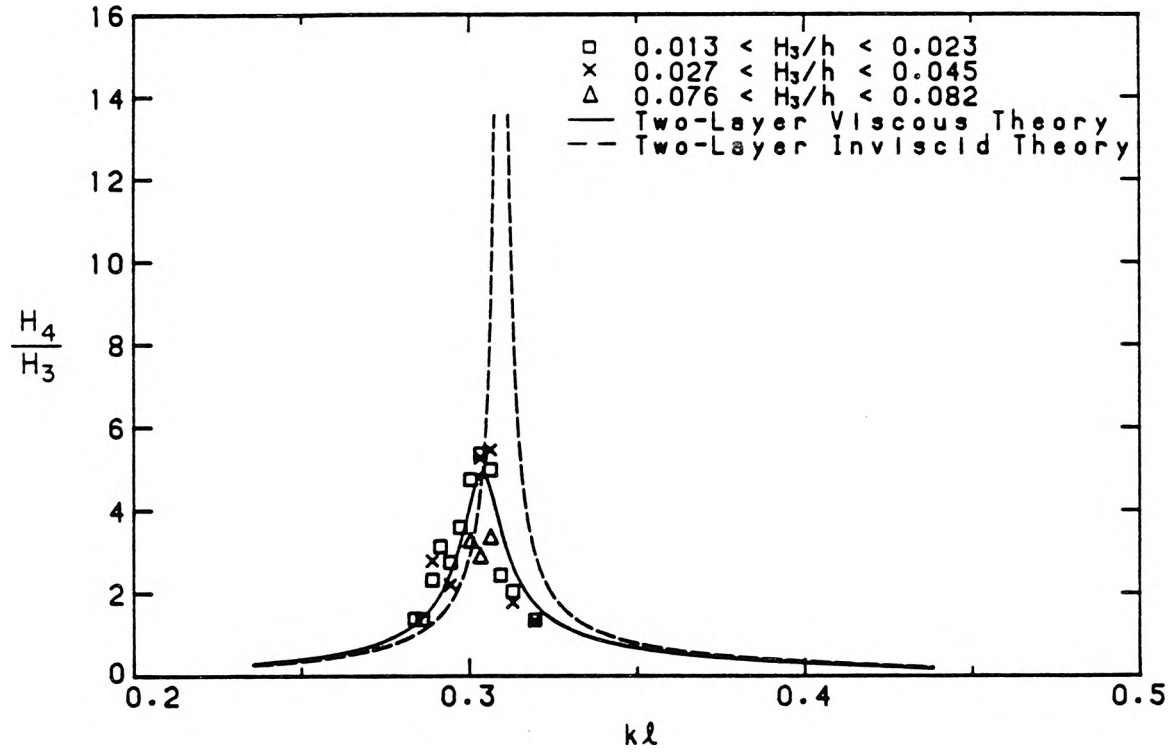

Figure 5.2.39. Variation of normalized internal wave height at the upstream wall of the trench with relative wave number. The theoretical results are obtained using the two-layer viscous theory and the two-layer inviscid theory; $h = 15.2\,\text{cm}$, $h_1 = 26.6\,\text{cm}$, $h_2 = 3.8\,\text{cm}$, $L = 19.15\,\text{m}$, $\ell = 59.5\,\text{cm}$, $b = 19.7\,\text{cm}$, $\rho_2/\rho_1 = 1.05$.

In figure 5.2.39, the internal wave height at the upstream wall of the trench, H_4, normalized by the wave height of the surface wave at the end wall, H_3, is plotted as a function of $k\ell$, where k is the wave number of the surface wave in the constant-depth channel obtained using the linear inviscid theory. From the two-layer inviscid theory, the wave period corresponding to the lowest mode of oscillation of the internal waves in the trench is found to be 9.9 sec ($k\ell = 0.31$). It is seen that the linear inviscid theory is inadequate in predicting the response of the internal oscillation because in addition to nonlinear effects, viscous dissipation is significant in this shallow region. The linear viscous theory, with a kinematic viscosity $\nu = 1.0 \times 10^{-6}\,\text{m}^2\text{sec}^{-1}$ for both layers, predicts a resonant wave period of internal oscillation in the trench of

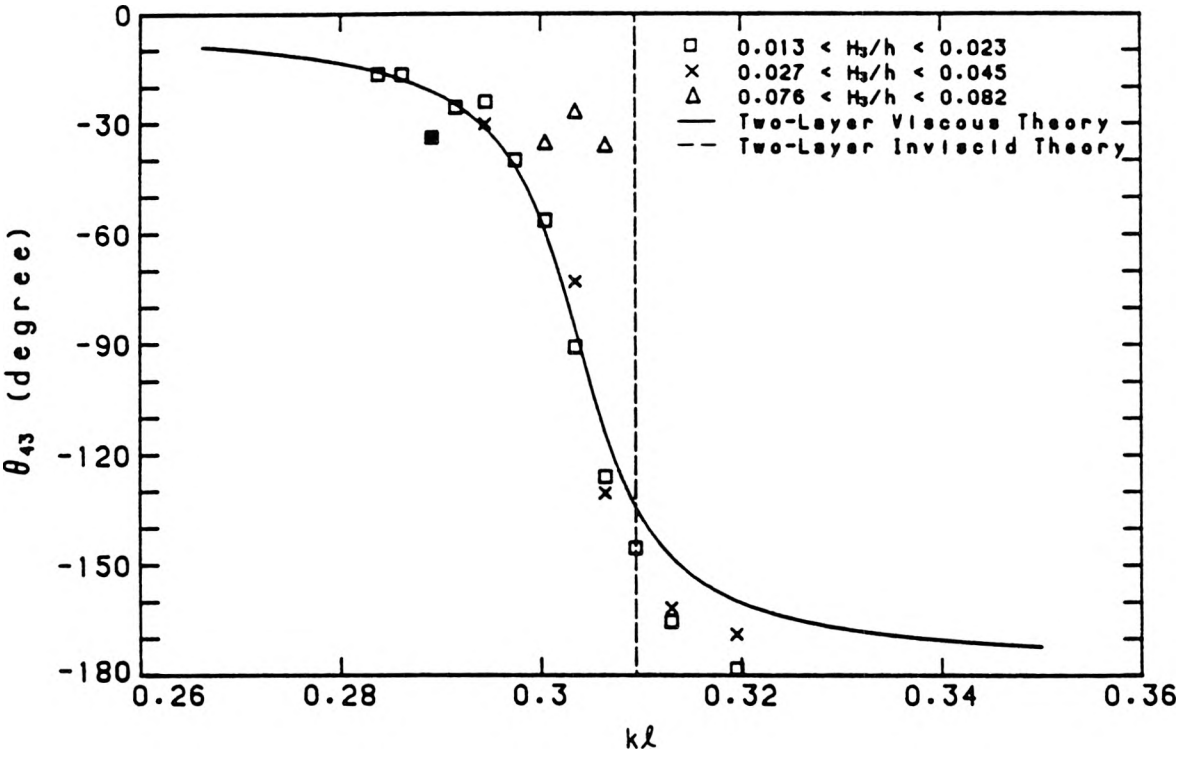

Figure 5.2.40. Variation of the relative phase angle between internal wave motion at the upstream wall of the trench and surface wave motion at the end wall with relative wave number. The theoretical results are obtained using the two-layer viscous theory and the two-layer inviscid theory; $h = 15.2\,\text{cm}$, $h_1 = 26.6\,\text{cm}$, $h_2 = 3.8\,\text{cm}$, $L = 19.15\,\text{m}$, $\ell = 59.5\,\text{cm}$, $b = 19.7\,\text{cm}$, $\rho_2/\rho_1 = 1.05$.

10.08 sec ($k\ell = 0.304$) and an amplification factor, H_4/H_3, of 4.9. The agreement between experiment and linear viscous theory is good, even though nonlinear effects are significant in this problem. The wave period of resonance for the second resonant mode is about 5.4 sec from the two-layer inviscid theory. The difference between the wave periods of resonance for the lowest mode predicted by the two-layer viscous theory and the two-layer inviscid theory when compared to the interval between the first and second resonant modes is about 4%. This compares to 2% for the case of the deep lower fluid (i.e., $h_2 = 7.6\,\text{cm}$) reflecting this increase in viscous effect on the internal wave motions in the trench. The relative phase angle between internal

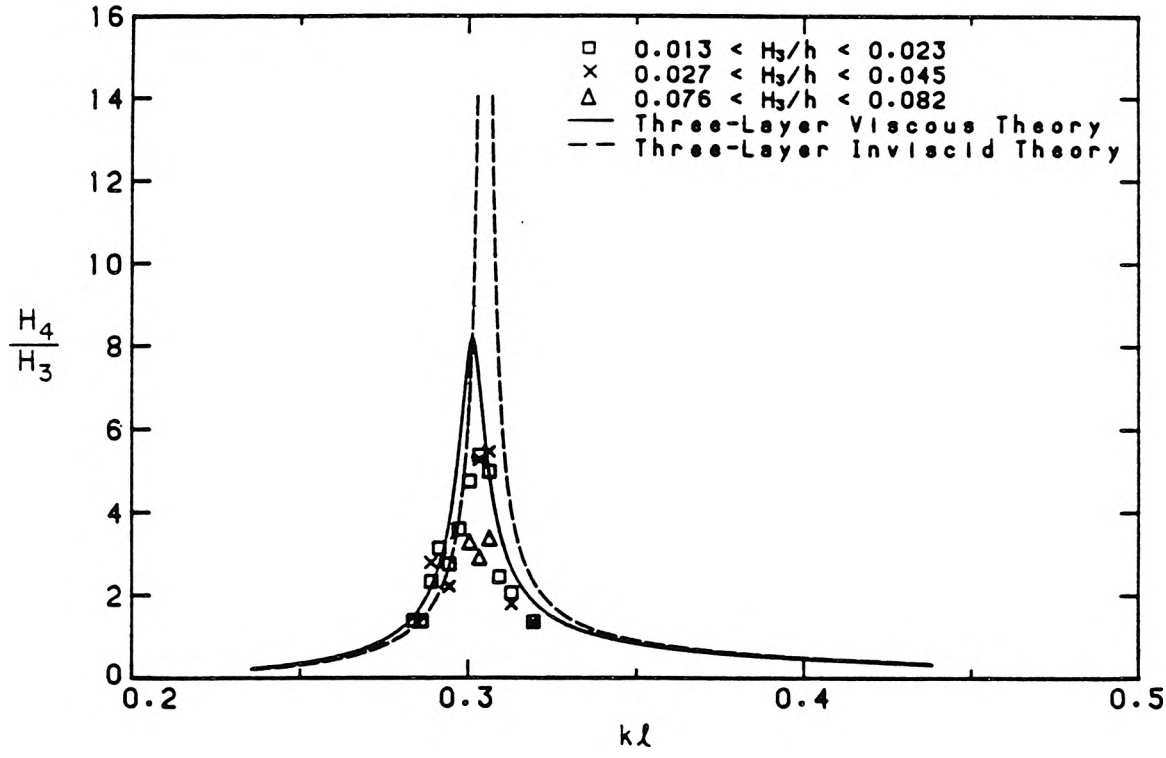

Figure 5.2.41. Variation of normalized internal wave height at the upstream wall of the trench with relative wave number. The theoretical results are obtained using the three-layer viscous theory and the three-layer inviscid theory, computed for the internal wave height at the top of the density transition region; $h = 15.2\,\text{cm}$, $h_1 = 25.95\,\text{cm}$, $h_2 = 3.15\,\text{cm}$, $\delta = 1.3\,\text{cm}$, $L = 19.15\,\text{m}$, $\ell = 59.5\,\text{cm}$, $d = 15.2\,\text{cm}$, $b = 19.7\,\text{cm}$, $\rho_2/\rho_1 = 1.05$.

wave motion at the upstream wall of the trench and surface wave motion at the end wall, θ_{43}, is plotted as a function of the relative wave number, $k\ell$, in figure 5.2.40. The shift in θ_{43} from in phase to 180° out of phase through trench resonance is also predicted well by the linear viscous theory.

In figure 5.2.41 the results of the same experiments are compared with the predictions of the three-layer viscous theory and the three-layer inviscid theory, computed using $\delta = 1.3\,\text{cm}$. The theoretical response curves are computed for the internal wave height at the top of the density transition region, that is, at $z = -25.95\,\text{cm}$, where z is measured positive upwards from the still water surface.

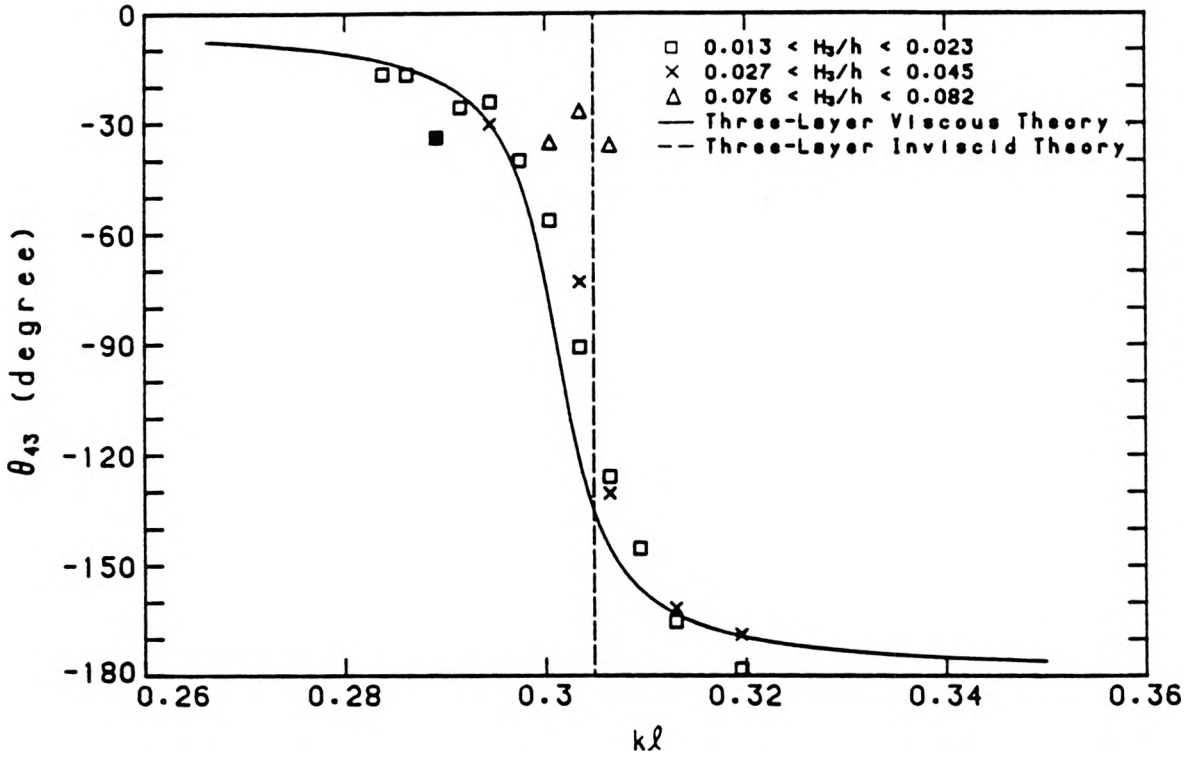

Figure 5.2.42. Variation of the relative phase angle between internal wave motion at the upstream wall of the trench and surface wave motion at the end wall with relative wave number. The theoretical results are obtained using the three-layer viscous theory and the three-layer inviscid theory, computed for the internal wave motion at the top of the density transition region; $h = 15.2\,\text{cm}$, $h_1 = 25.95\,\text{cm}$, $h_2 = 3.15\,\text{cm}$, $\delta = 1.3\,\text{cm}$, $L = 19.15\,\text{m}$, $\ell = 59.5\,\text{cm}$, $d = 15.2\,\text{cm}$, $b = 19.7\,\text{cm}$, $\rho_2/\rho_1 = 1.05$.

The wave period of resonant oscillation of the internal waves in the trench is found to be 10.05 sec ($k\ell = 0.306$) using the three-layer inviscid theory. In comparison with the deep fluid, that is, $h_2 = 7.6\,\text{cm}$, the density transition region has a more pronounced effect on the response curve in this case. The difference between the wave periods of resonance predicted by the two-layer inviscid theory and the three-layer inviscid theory when compared to the interval between the first and second resonant modes is about 3.3%. Note that the total depth in the trench region ($h_1 + h_2$) and the thickness of the diffuse salinity interface were about the same

in these two sets of experiments. However, the fractional change in h_2 was greater in the shallow lower fluid by the inclusion of the density transition region, hence the shift in the response curve is more pronounced (see equation 3.2.48). The wave period of the resonant peak predicted by the three-layer viscous theory is 10.17 sec ($k\ell = 0.301$). The corresponding theoretical amplification factor is 8.2, compared to a value of 4.9 from the two-layer viscous theory. This difference is attributed to interfacial boundary layer damping built into the two-layer viscous theory, and is not included in the three-layer viscous theory. It is recalled that for the deep lower fluid, that is, $h_2 = 7.6$ cm, the two viscous theories predicted somewhat larger differences ($\approx$ 8% larger) in the amplification factor. These results suggest that viscous dissipation in the boundary layer adjacent to the trench bottom increases more rapidly than that in the boundary layers adjacent to the density interface, as the depth of the lower fluid decreases. This point will be further elucidated in § 5.2.5. Figure 5.2.41 also indicates that viscous dissipation in the actual fluid was larger than that predicted by laminar boundary layer damping near the solid surfaces. The variation of relative phase angle with relative wave number is shown in figure 5.2.42.

In figure 5.2.43, the wave extrema of internal wave motion at the upstream wall of the trench, η_4, normalized by the surface wave height at the end wall, H_3, is plotted as a function of the relative wave number, $k\ell$, for the lowest mode of oscillation of internal waves in the trench. In comparison with figure 5.2.21, nonlinear effects are clearly seen in the internal waves in the shallow lower fluid. The ratio of the crest amplitude to the trough amplitude of the internal wave in these experiments reached a maximum value of 3.1 at $k\ell = 0.306$, the corresponding value of H_3/h was 0.0803. It is interesting to compute the ratio of the second order term in (5.2.11) to that of the first, even though the solution given by (5.2.11) is clearly invalid in this case. We have $H_4/h_2 = 1.079$, $K_2h_1 = 1.393$, $K_2h_2 = 0.199$. From

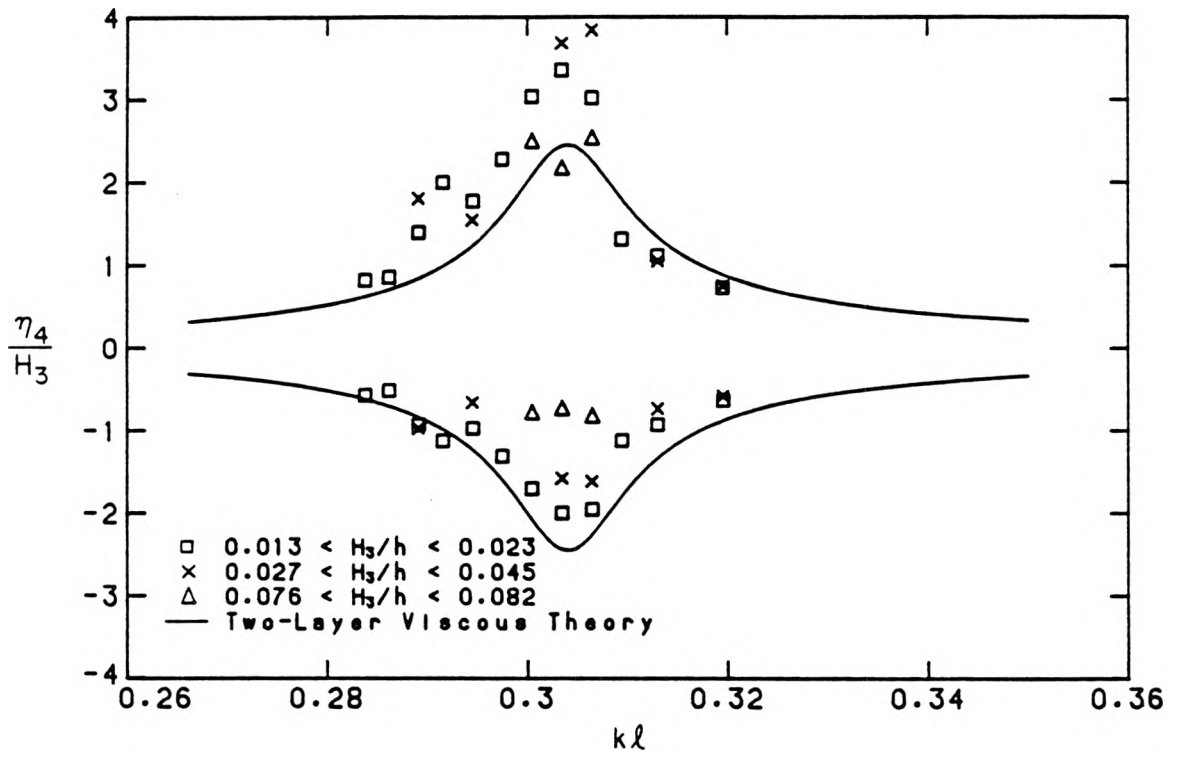

Figure 5.2.43. Variation of wave extrema of internal waves at the upstream wall of the trench with relative wave number, for the lowest mode of oscillation of internal waves in the trench. The theoretical results are obtained using the two-layer viscous theory; $h = 15.2\,\text{cm}$, $h_2 = 26.6\,\text{cm}$, $h_2 = 3.8\,\text{cm}$, $L = 19.15\,\text{m}$, $\ell = 59.5\,\text{cm}$, $b = 19.7\,\text{cm}$, $\rho_2/\rho_1 = 1.05$.

(5.2.13) this implies an amplitude ratio of 0.972, which is indeed large, indicating that nonlinear effects are important. The corresponding value of the dimensionless parameter, $H_4/K_2h_2^2$, is 5.422. The internal wave heights are also large compared to the depth of the lower fluid.

The corresponding surface wave extrema at two locations above the trench ($x/\ell = 0$ and $x/\ell = 1$) are shown in figures 5.2.44*a* and 5.2.44*b*, where η_2/S corresponds to the normalized amplitude of the free surface elevation at $x/\ell = 0$, and η_3/S corresponds to the normalized amplitude of the free surface elevation at $x/\ell = 1$. The values of H_3/h that were used in these experiments were considerably larger

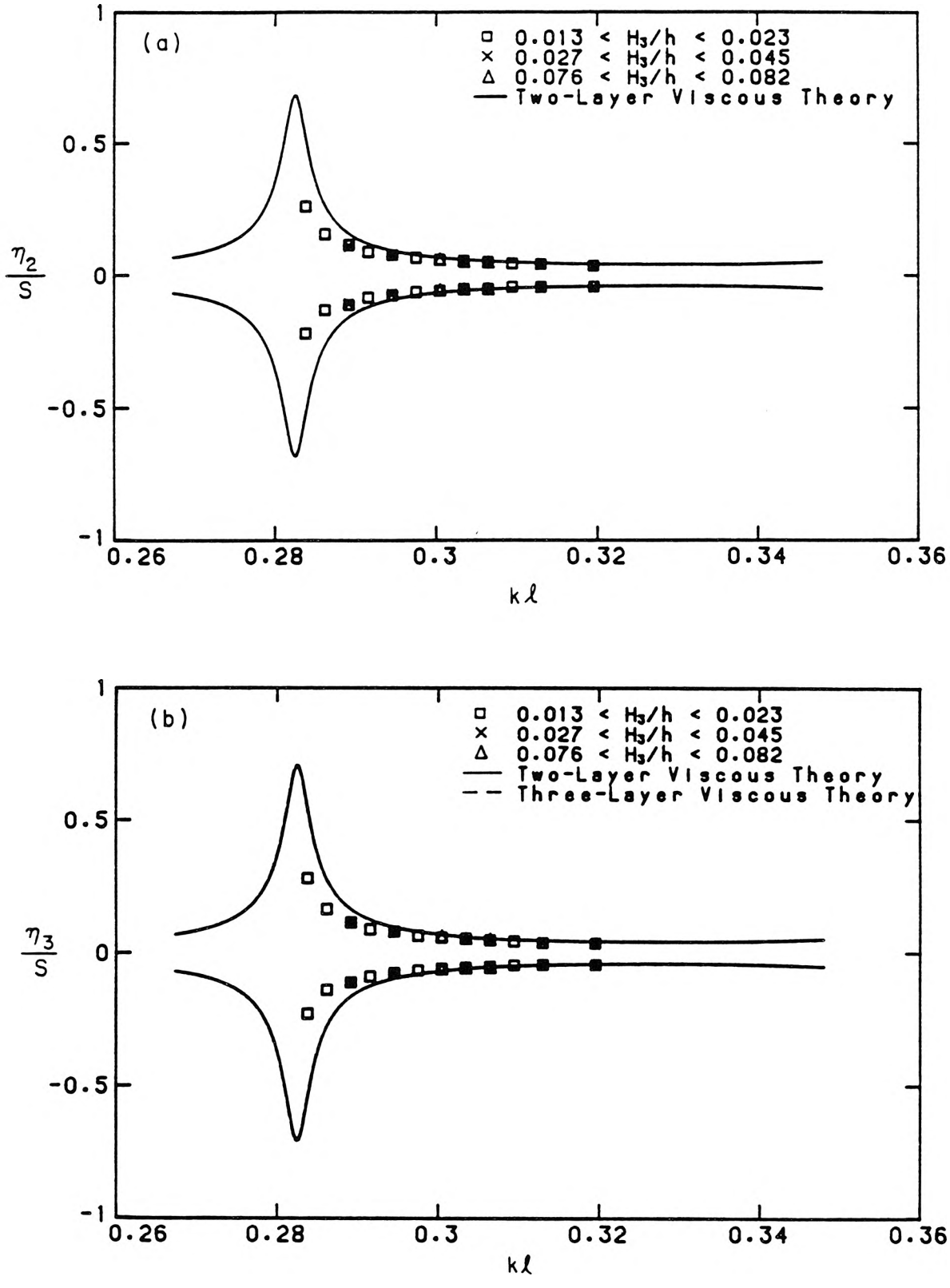

Figure 5.2.44. Variation of surface wave extrema at two locations above the trench with relative wave number: (*a*) $x/\ell = 0$, and (*b*) $x/\ell = 1$.

than those used in the experiments with the deep lower fluid, that is, $h_2 = 7.6\,\text{cm}$. This is because the amplification factor for the internal waves was small in the shallow lower fluid, hence larger surface wave amplitudes were needed to generate the internal waves. It is seen in figures 5.2.44*a* and 5.2.44*b* that the free surface motions above the trench correspond to an off-resonant condition in the main channel. The wave period for the nearest resonant mode of oscillation of the surface waves in the main channel is found to be 10.85 sec ($k\ell = 0.282$) using the two-layer viscous theory. Hence, using (5.2.5), with $kh = k\ell \cdot h/\ell = 0.282 \times 0.152/0.595 = 0.072$, the condition that second order effects are negligible in the standing surface wave profile is:

$$\frac{H_3}{h} \ll \frac{16k^2h^2}{3} \approx 0.028. \tag{5.2.19}$$

Considering the relatively large values of H_3/h in these experiments, the good symmetry shown by the surface waves about the mean water level is somewhat surprising. In figure 5.2.44*b* the theoretical curves obtained using the three-layer viscous theory (with $\delta = 1.3\,\text{cm}$) are also shown. It is seen that the two-layer viscous theory and the three-layer viscous theory yield identical results. These results indicate that the effects of internal oscillations on the motion of the free surface are small for these experimental conditions. These may be simply because the amplification factor of the internal wave in the trench is substantially less in the shallow lower fluid ($h_2 = 3.8\,\text{cm}$). Because the effects of density variations in the trench are not pronounced on the water surface, the two-layer viscous theory and the three-layer viscous theory yield the same results for the surface motion above the trench.

The steady-state portion of the time histories of internal wave motion as measured at the upstream wall of the trench for three different wave heights and a wave period of 10.0 sec are presented in figure 5.2.45. The ordinate is normalized by the internal wave height H_4 and the abscissa is a dimensionless time measured from

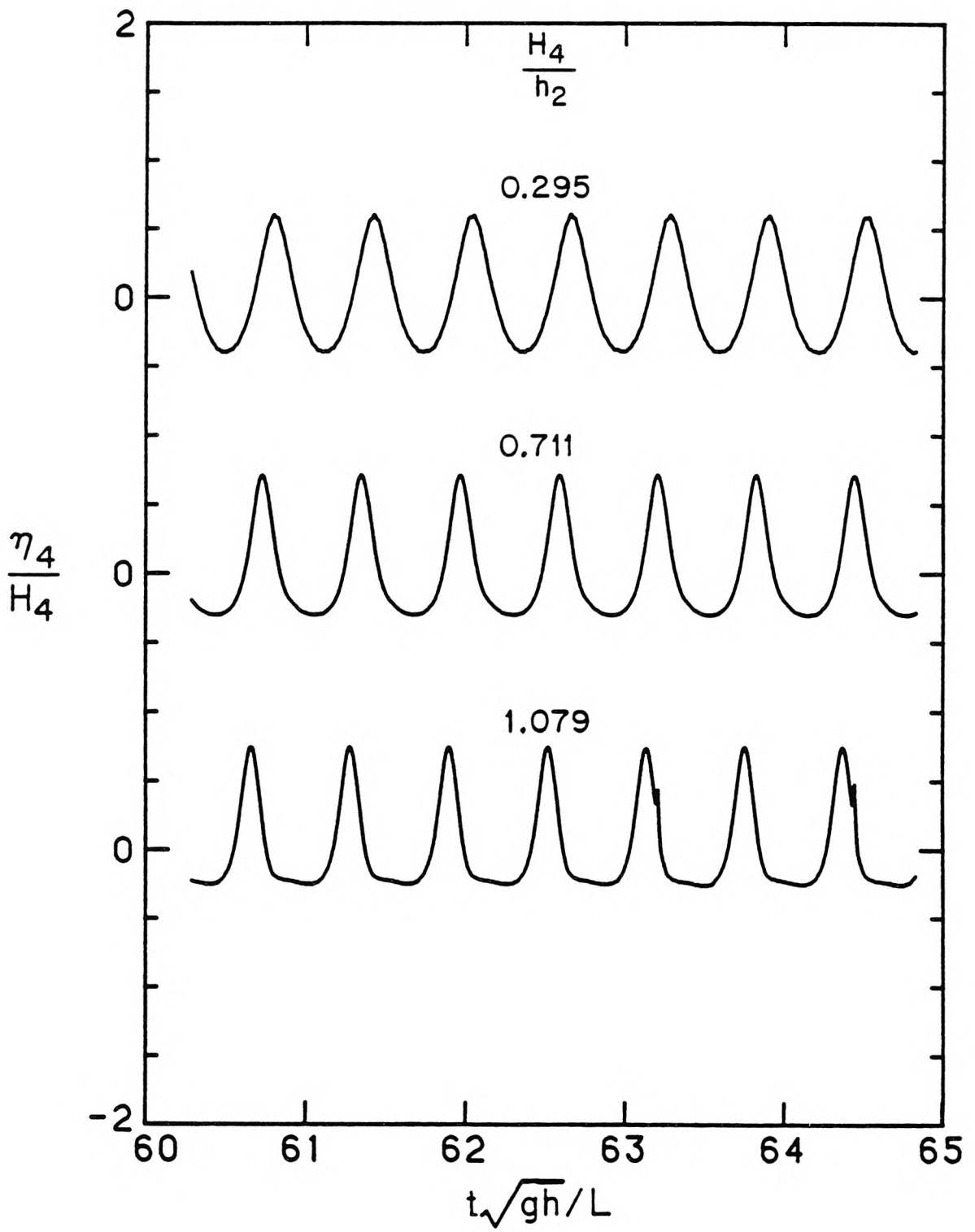

Figure 5.2.45. Steady-state internal wave time histories at the upstream wall of the trench for a wave period of 10.0 sec ($k\ell = 0.306$); $h_1 = 26.6$ cm, $h_2 = 3.8$ cm, $\Delta\rho \approx 0.05\,\mathrm{gcm}^{-3}$.

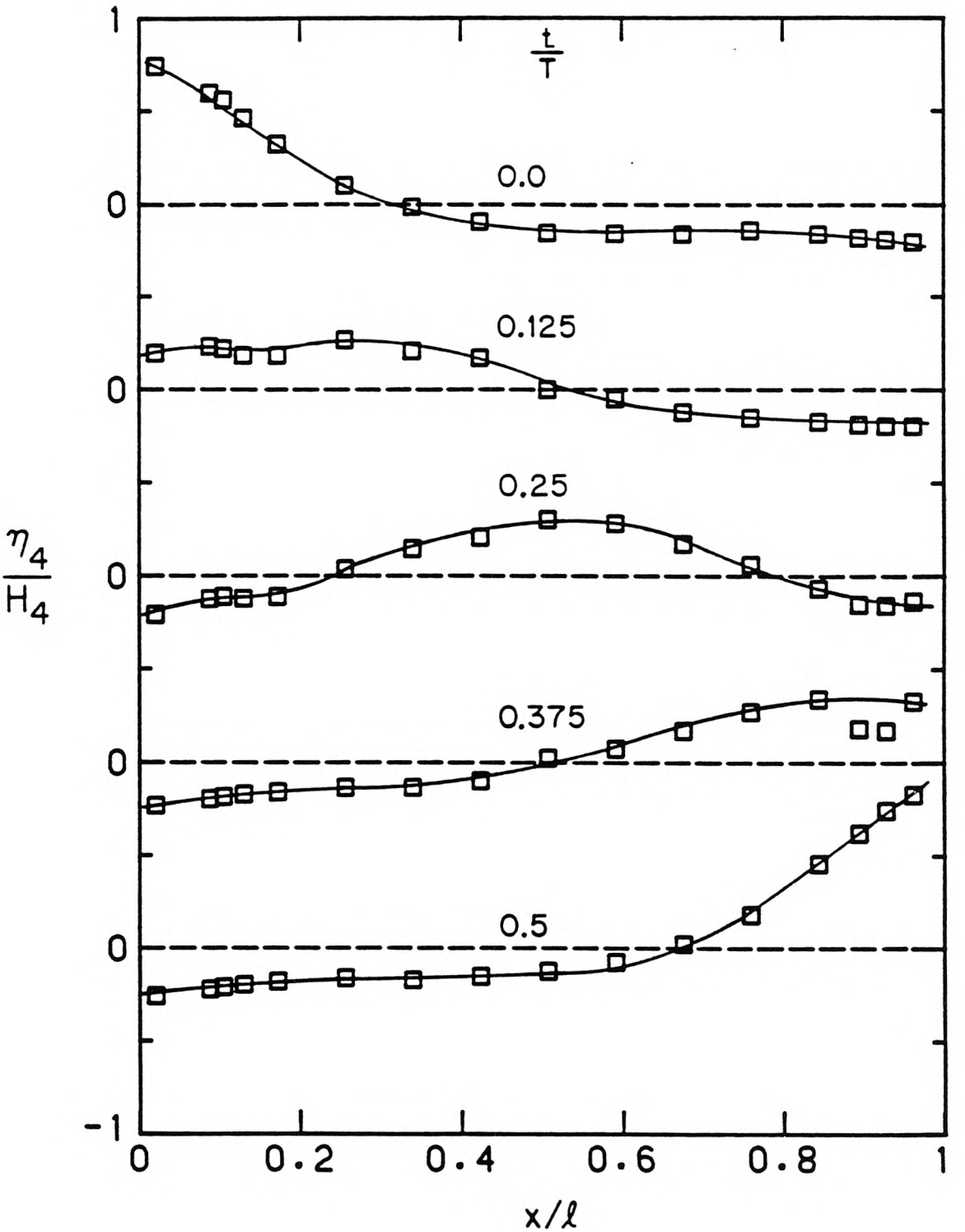

Figure 5.2.46. Profiles of density interface at various times within half a wave period for $T = 10.0\,\text{sec}$ and $H_4/h_2 = 1.079$; $h_1 = 26.6\,\text{cm}$, $h_2 = 3.8\,\text{cm}$, $\Delta\rho \approx 0.05\,\text{gcm}^{-3}$.

(a)

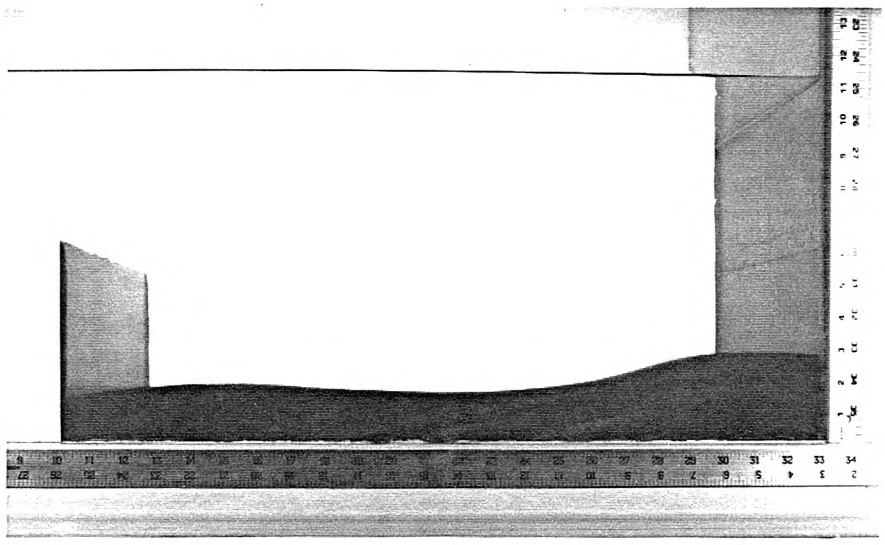

(b)

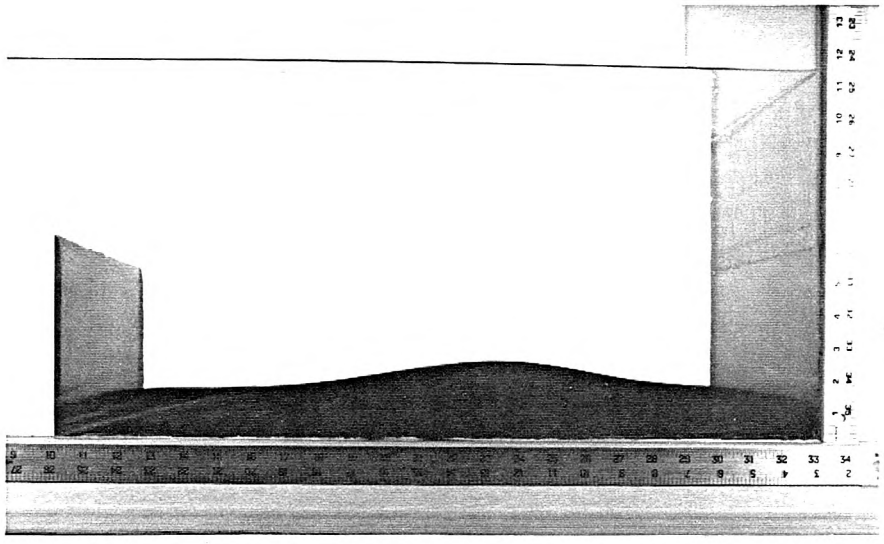

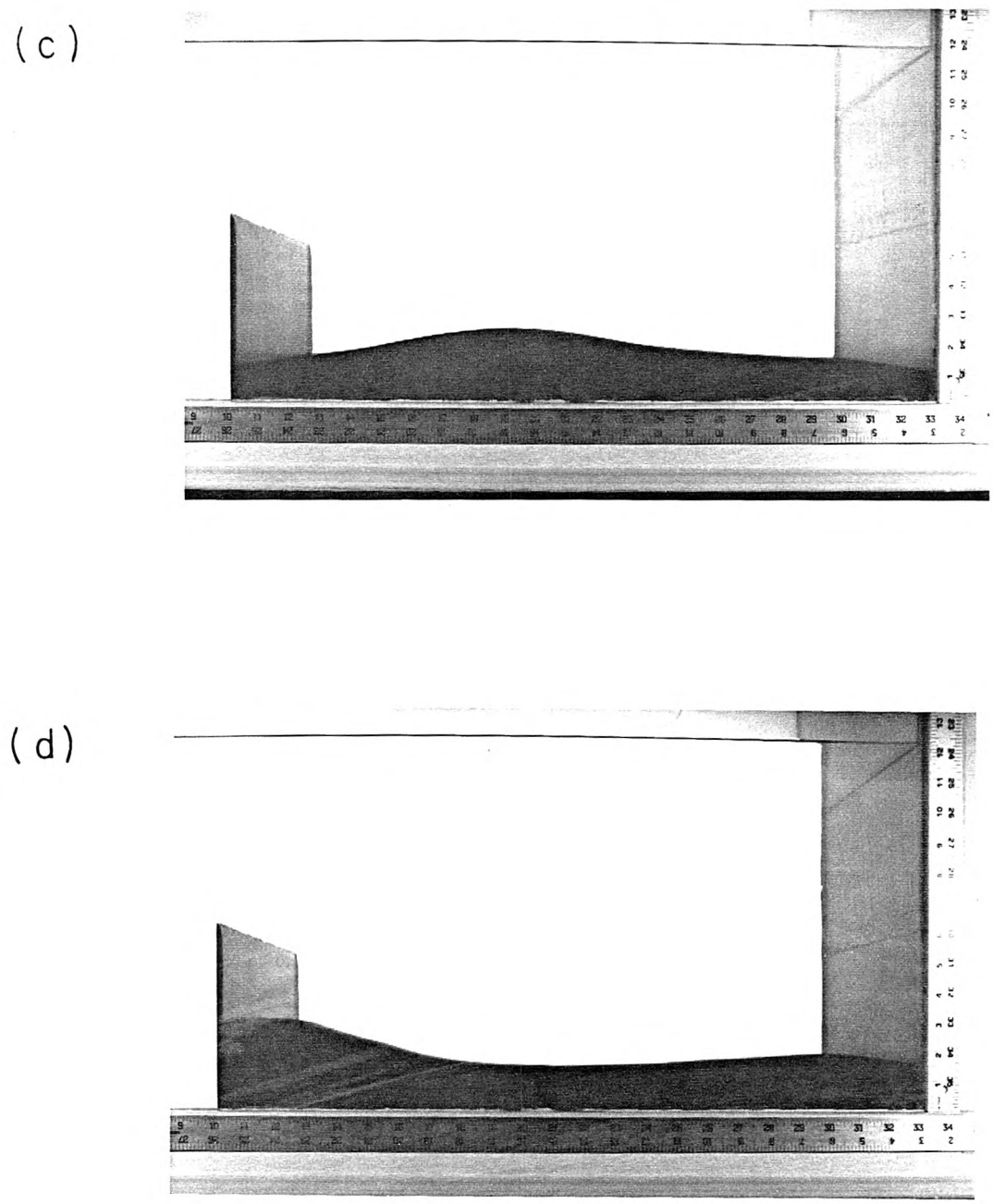

Figure 5.2.47. Internal waves in a shallow lower fluid in the trench for the lowest mode of resonant oscillation: (a) maximum upward displacement at $x/\ell = 1$, (b) and (c) internal wave travelling from right to left, and (d) maximum upward displacement at $x/\ell = 0$; $h_1 = 26.6\,\mathrm{cm}$, $h_2 = 3.8\,\mathrm{cm}$, $\Delta\rho \approx 0.05\,\mathrm{gcm}^{-3}$, $T = 10.2\,\mathrm{sec}$.

the start of the wave generator. For this wave period the internal waves are at resonance for the lowest mode of oscillation. The ratio of the crest amplitude to the trough amplitude for $H_4/h_2 = 0.295$, 0.711 and 1.079 are 1.55, 2.38 and 3.10, respectively. The spurious signals seen in the wave record for $H_4/h_2 = 1.079$ are due to the effect of mixing at the interface. The variation of the normalized elevation of the density interface with relative distance along the trench is presented in figure 5.2.46 for $H_4/h_2 = 1.079$ for several different phases of an internal oscillation. The data points were obtained from steady-state wave records taken at intervals of 5.0 cm along the trench. To construct the plots shown in figure 5.2.46 from individual internal wave records, the surface motions at the end wall were recorded at the same time as the internal motions, then the elevations of the density interface at different locations along the trench were obtained for the same phase of the surface motions. The travelling wave pattern is clearly seen, the internal wave looks like a single "hump" travelling back and forth in the trench almost entirely above the quiescent density interface. Steady-state conditions in the trench were still reached in this case; the thickness of the diffuse salinity interface after the experiment was about 10% larger than the mean.

Lepelletier (1980) conducted experiments in a rectangular tank, which was filled with water to a shallow depth when compared to the length of the tank. Lepelletier generated standing waves by oscillating the tank horizontally in a sinusoidal manner at the resonant frequencies of the surface waves in the rectangular tank. Wave motions were measured near one end of the tank by a resistance wave gage, which was stationary. Lepelletier represented the wave motions in the rectangular tank as the sum of two cnoidal waves, which have the same amplitude and travel in opposite directions. Appreciable discrepancies were found between the measured and the cnoidal wave shapes in some cases. Helal and Molines (1981) conducted similar experiments in an oscillating rectangular tank, which was partially filled

with a two-layer stratified fluid of water and salt water. The motions of the standing internal waves were also obtained in the form of two internal cnoidal waves of the same amplitude travelling in opposite directions. Helal and Molines showed experimentally that the waves in the oscillating tank as measured by a stationary wave gage could be represented by a linear superposition of a cnoidal shape wave and a sine shape wave; the sine wave component was due to the oscillatory motion of the tank. Thus the experimental measurements could not be compared directly to a standing wave in a stationary frame. The constant-depth channel and trench arrangement used in this study (figure 5.1.1) has eliminated the difficulty stated above. Our experiments showed that standing internal waves of various characteristics can be generated in the trench by moving a vertical plate in the fresh water filled constant-depth channel sinusoidally and by carefully controlling the depths and the density stratifications in the trench region. The experimental results are directly comparable to the theoretical predictions.

Photographs of a travelling internal wave are shown in figure 5.2.47. This wave is about 60% larger in amplitude than the one shown in figure 5.2.46 and the wave profiles as seen could be maintained for only a few oscillations. This is because the density stratifications in the trench were constantly changing due to intense mixing of the two fluids at the interface. Hence, a steady-state condition could not be realized in this case.

The steady-state portion of the time histories of internal motion at the upstream wall of the trench, and of free surface motion at the end wall, are presented in figures 5.2.48 and 5.2.49, respectively, for a range of relative circular frequencies, σ/σ_0, near the lowest mode of oscillation of the internal waves in the trench; σ_0 is the circular frequency of resonant oscillation, which is $2\pi/9.9$ rad/sec from the two-layer inviscid theory. As seen in figure 5.2.49 the surface waves are symmetrical about the mean water level for the range of frequencies of these experiments. The

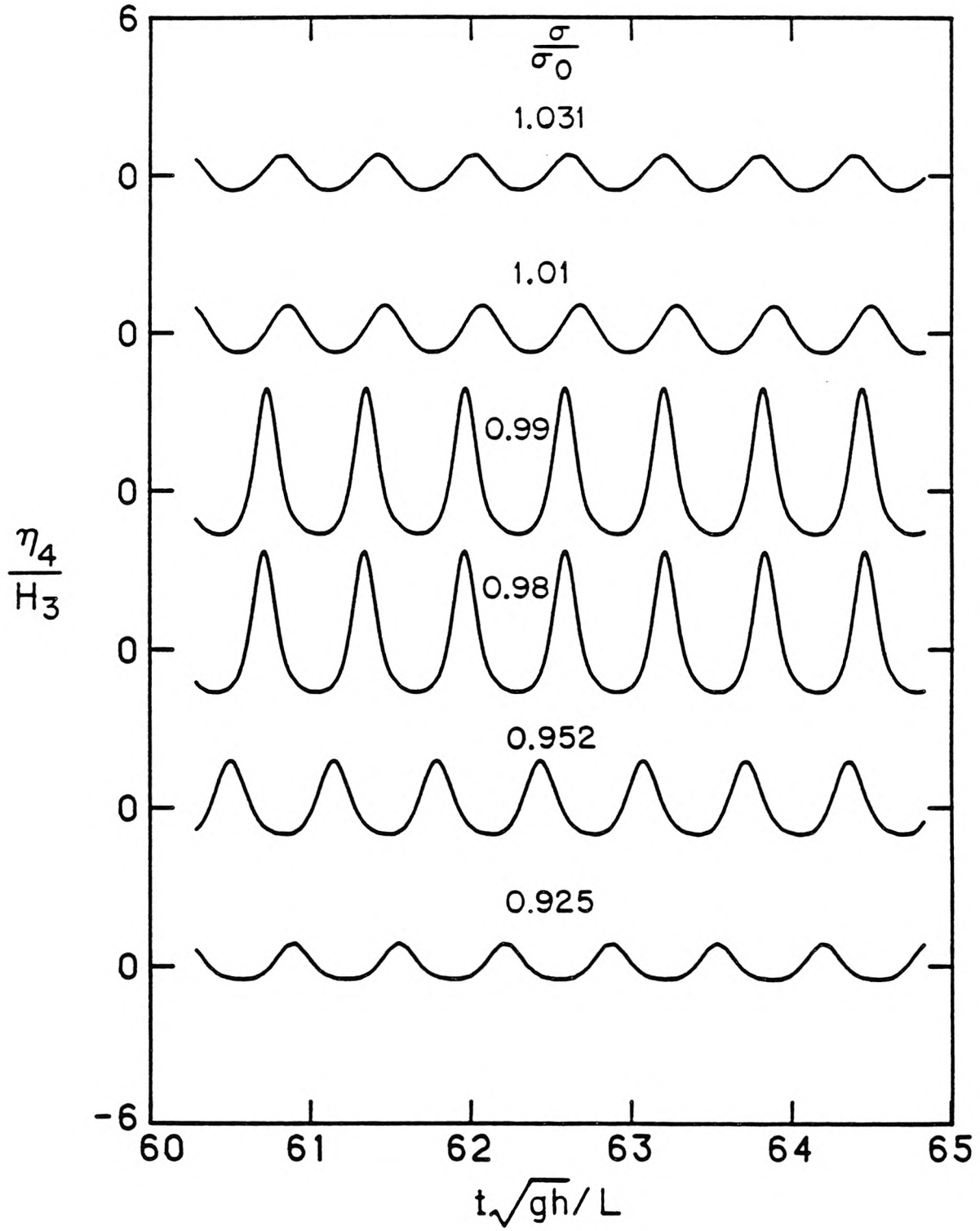

Figure 5.2.48. Steady-state internal wave motions at the upstream of the trench for relative circular frequencies near the lowest mode of internal oscillation in the trench; $h_1 = 26.6\,\text{cm}$, $h_2 = 3.8\,\text{cm}$, $\Delta\rho \approx 0.05\,\text{gcm}^{-3}$.

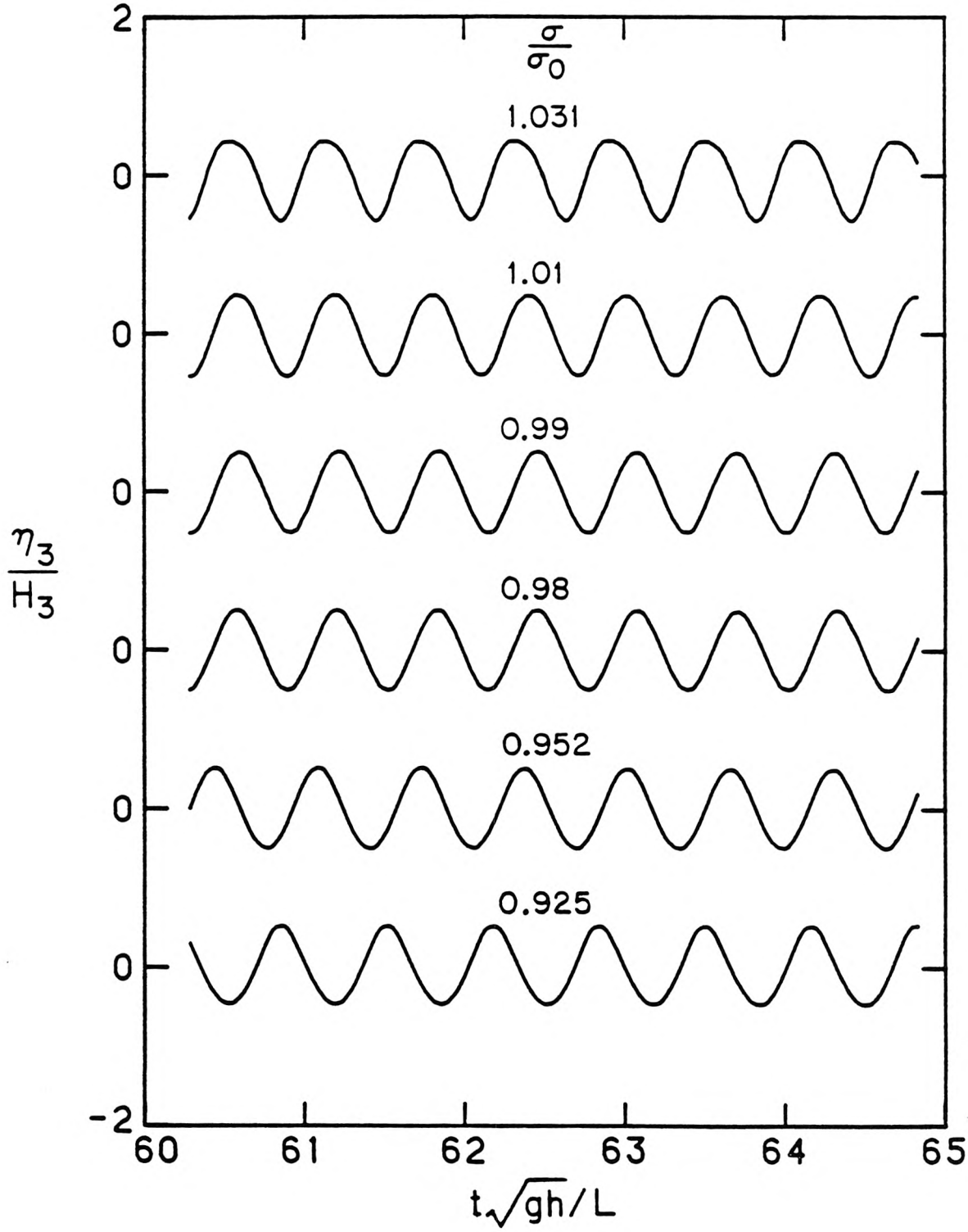

Figure 5.2.49. Steady-state free surface motions at the end wall for relative circular frequencies near the lowest mode of internal oscillation in the trench; $h_1 = 26.6\,\text{cm}$, $h_2 = 3.8\,\text{cm}$, $\Delta\rho \approx 0.05\,\text{gcm}^{-3}$.

wave period corresponding to the nearest resonant mode of oscillation of the surface waves in the constant-depth channel is 10.79 sec ($\sigma/\sigma_0 = 0.918$) obtained using the two-layer inviscid theory. No secondary oscillation is observed in these off-resonant conditions for the free surface motions in the main channel, hence the pressure force exerted by the surface waves on the internal waves was nearly sinusoidal for these experiments. The complete time histories of the internal waves and of the surface waves are presented in figures 5.2.50–5.2.53 for several typical wave periods near the lowest mode of trench resonance. Note that the surface and internal waves are plotted to a different scale. Beat patterns, which diminish with time, can be seen in each wave record. The waveforms of the internal motions as shown in these figures are non-symmetrical about the quiescent density (dye) interface. However, no secondary oscillations are seen in the internal waves. From these internal wave records one also gets an idea that mixing at the interface must be small, otherwise the density stratifications in the trench would be constantly changing, hence the internal motions would approach steady-state condition in a more complicated fashion.

Finally, we present in figure 5.2.54 the response curve obtained from those experiments where the thickness of the diffuse salinity interface was increased to a mean value of 2.44 cm, with a standard deviation of 0.04 cm. The mean density of the lower fluid (salt water) was 1.0496 gcm^{-3}, with a standard deviation of 0.0017 gcm^{-3}. The predictions of the internal wave height using the three-layer viscous theory and three-layer inviscid theory were computed at the top of the density transition region, that is, at $z = -25.35$ cm, with $\delta = 2.5$ cm. The relative wave number $k\ell$ corresponding to the lowest mode of oscillation of the internal waves in the trench as predicted by the two-layer inviscid theory, the three-layer inviscid theory, and the three-layer viscous theory are 0.31, 0.295 and 0.292, respectively. The corresponding wave periods are 9.9 sec, 10.38 sec, and 10.51 sec. Thus, the difference between the wave periods of resonance for the lowest mode predicted by the

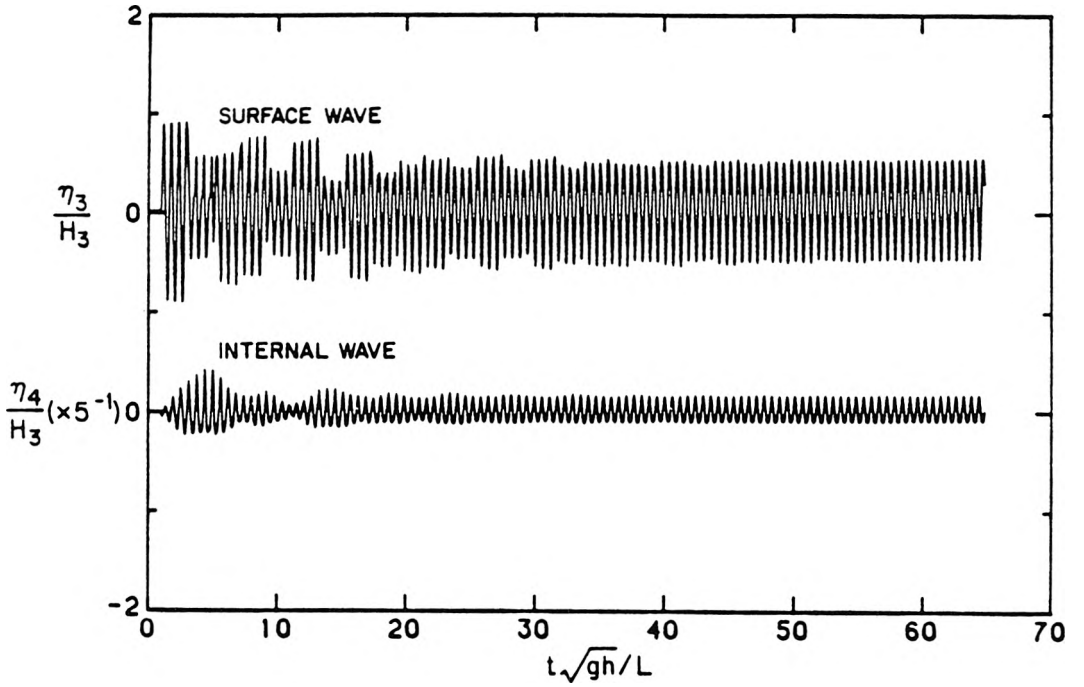

Figure 5.2.50. Surface and internal waves for experiment at $T = 9.6\,\text{sec}$ ($k\ell = 0.319$) and $H_3 = 4.95\,\text{mm}$.

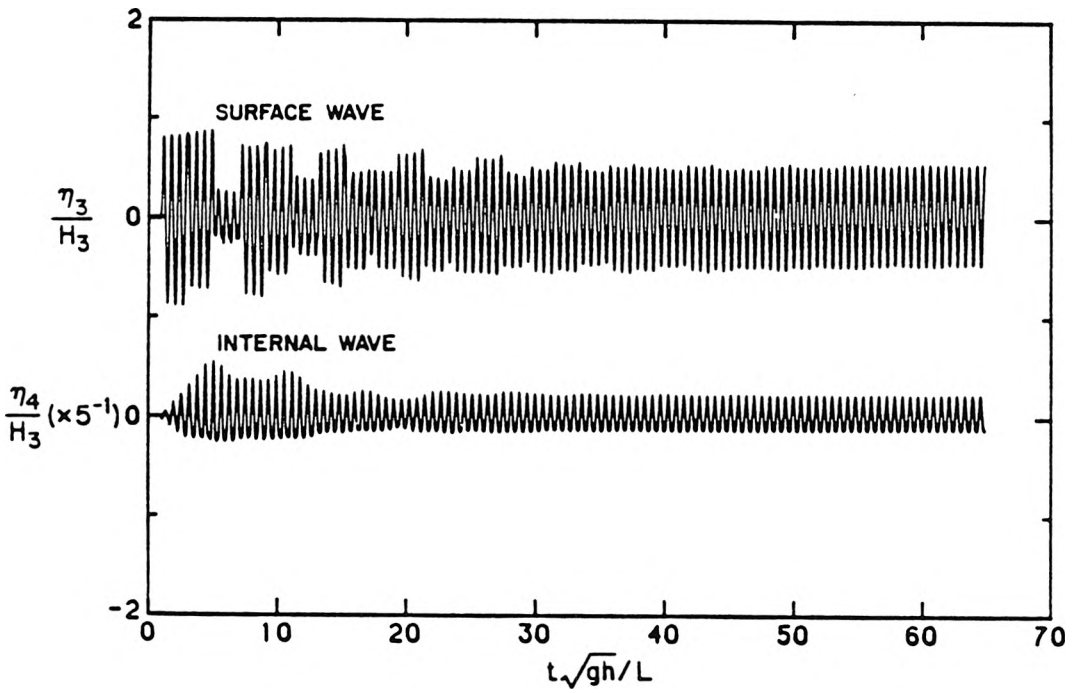

Figure 5.2.51. Surface and internal waves for experiment at $T = 9.8\,\text{sec}$ ($k\ell = 0.313$) and $H_3 = 5.15\,\text{mm}$.

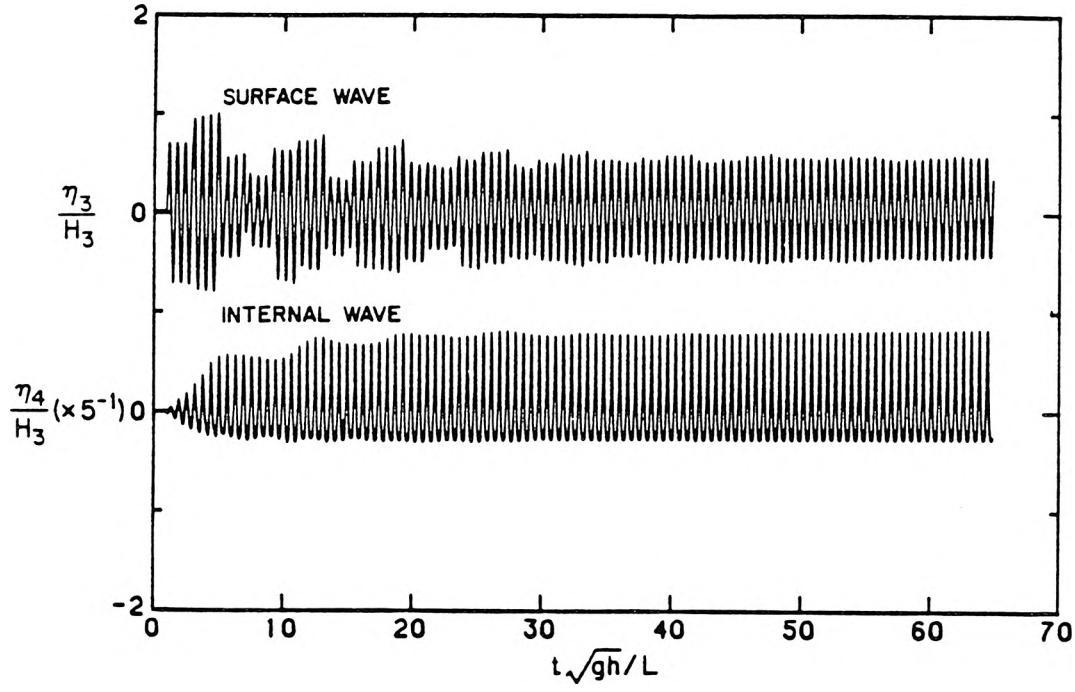

Figure 5.2.52. Surface and internal waves for experiment at $T = 10.0\,\text{sec}$ ($k\ell = 0.306$) and $H_3 = 4.95\,\text{mm}$.

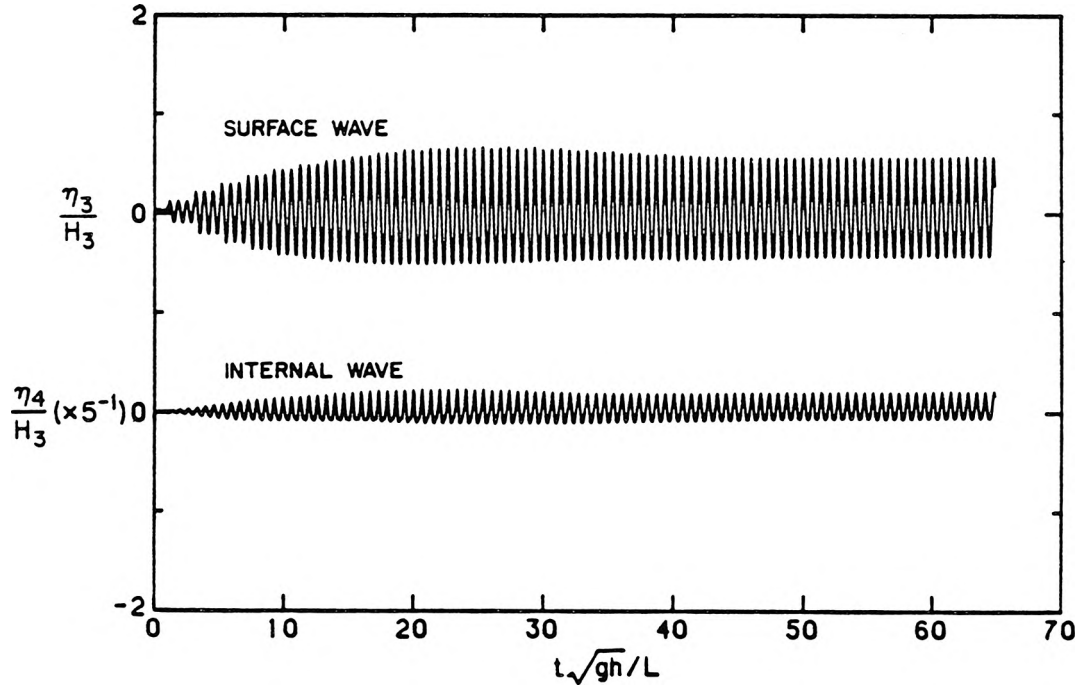

Figure 5.2.53. Surface and internal waves for experiment at $T = 10.8\,\text{sec}$ ($k\ell = 0.284$) and $H_3 = 2.45\,\text{mm}$.

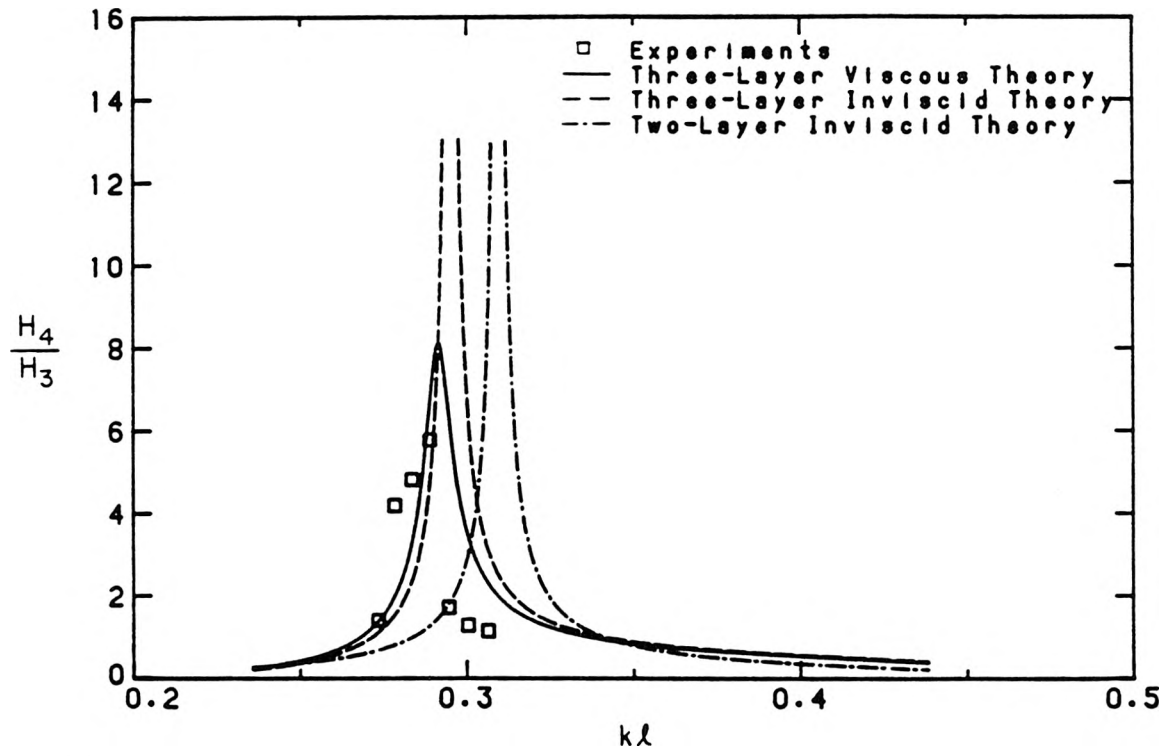

Figure 5.2.54. Variation of normalized internal wave height at the upstream wall of the trench with relative wave number for diffuse salinity interface thickness of 2.5 cm. Comparison between the results of the experiments, the two-layer inviscid theory, the three-layer viscous theory, and the three-layer inviscid theory.

two-layer inviscid theory and the three-layer inviscid theory when compared to the interval between the first and second resonant modes is about 11%, reflecting the increase in the effect of the density transition region on the response curve in the shallow lower fluid compared to that in the deep lower fluid (i.e., $h_2 = 7.6\,\text{cm}$). The experimental data are too limited to give anything more than a general picture of the response curve, which appears to agree with the predictions of the three-layer viscous theory and the three-layer inviscid theory.

In summary, the internal motions in a two-layer stratified rectangular trench due to time-periodic surface waves were studied experimentally and theoretically for the condition that the depth of the lower fluid (salt water) in the trench was reduced

by half from the depth used in the experiments that were discussed in § 5.2.3. The trench responses were obtained for a range of wave periods near the lowest mode of oscillation of the internal waves in the trench for two different thicknesses of the diffuse salinity interface. In this case, the depth of the lower fluid in the rectangular trench was small compared to the wavelength of the internal waves ($K_2 h_2 \approx 0.2$). The inviscid theory could not predict the response of the stratified fluid in the trench as good as in the case of the deep lower fluid (i.e., $h_2 = 7.6\,\text{cm}$). This was due to the proximity of the density interface to the trench bottom, and hence the increased importance of viscous effects and/or the influence of nonlinearities in the shallow region. The two-layer and three-layer viscous theories predicted the internal wave heights in the trench satisfactorily, even though nonlinear effects were important for these experimental conditions. The linear theories did not do so well in predicting the amplitudes of the wave crest and wave trough, due to nonlinear effects in these experiments. The effects of the density transition region on the internal motions in the trench were also more pronounced in this case because the thickness of the diffuse salinity interface was comparable to the depth of the lower fluid. The dimensionless parameter, $H_4/K_2 h_2^2$, increases as the depth of the lower fluid , h_2, decreases. The effects of viscosity also increase as h_2 increases. Comparing the results of these experiments to those for the deep lower fluid (i.e., $h_2 = 7.6\,\text{cm}$), the amplitude responses of the internal waves in the shallow lower fluid (i.e., $h_2 = 3.8\,\text{cm}$) were substantially smaller. In addition, the internal wave in the shallow lower fluid behaved more like a travelling wave than a standing wave as observed in the deep lower fluid. The waveforms of the internal motions were non-symmetrical about the still density interface. At resonance, the internal wave looked like a single "hump" travelling back and forth between the vertical walls of the trench almost entirely above the still density interface.

5.2.5 Damping of Standing Internal Waves in a Rectangular Basin

The experiments that were discussed in § 5.2.3 and § 5.2.4 for the oscillation of internal waves in a rectangular trench showed that the two-layer viscous theory overestimated energy dissipation in the actual fluid, whereas the three-layer viscous theory underestimated the damping significantly. The two-layer viscous theory assumes that the entire loss of energy of waves is localized in very thin laminar boundary layers adjacent to the density interface and at the solid surfaces. This follows from the treatment of two immiscible fluids. Thus, if the effects of viscosity are neglected the horizontal components of the fluid velocity across the density interface are discontinuous; the density interface is a surface of infinite velocity gradient, that is, a vortex sheet. Viscosity, however small, will instantaneously even out such a discontinuity by the diffusion of momentum, but the gradient of velocity is still very large within thin layers of fluids (boundary layers) adjacent to the density interface. Indeed, it was found in § 3.3.1.1 and § 3.3.1.2 for progressive waves and for standing waves in a two-layer fluid that energy dissipation in the boundary layers adjacent to the solid surfaces and at the density interface are both proportional to $\nu^{1/2}$, where ν is a characteristic kinematic viscosity of the fluids. However, a miscible fluid (water and salt water) was used in the experiments, and the gradient of fluid velocity in the diffuse salinity interface is substantially less than that at the density interface of two immiscible fluids. It can be deduced from (3.3.131) that energy dissipation in the diffuse salinity interface is only proportional to ν. In the three-layer viscous theory, the density variation and the velocity distribution in the density transition region are continuous, and energy dissipation is considered to take place only in the laminar boundary layers adjacent to the solid surfaces. Hence, the three-layer viscous theory should be a closer realization of the actual fluid state than the two-layer viscous theory. It follows that the observed discrepancies between theoretical predictions and experimental observation might be due to other sources

of damping not included in the linear viscous theories.

To further investigate the various aspects of internal wave damping, the attenuation of standing internal waves was studied experimentally in a rectangular basin, which was partially filled with a stratified fluid of water and salt water. A theoretical treatment of the two-layer problem is given in § 3.3.1.2. As in previous experiments, the arrangement shown in figure 5.1.1 was used to generate the internal waves in the trench. The wave period was chosen to correspond to the lowest mode of oscillation of the internal waves in the trench. After a steady-state condition was established in the wave tank, a gate constructed of lucite was lowered at the upstream edge of the trench ($x = 0$) to separate the trench region ($0 < x < \ell$) from the region of the constant-depth channel ($-L < x < 0$). The gate was held in place by vertical guides fastened to the side walls of the wave tank. To reduce leakage around the gate, rubber seals were used against the glass walls and the false bottom. The mounting arrangement for the rubber seals was similar to that for the wave plate. The motion of the decaying standing internal wave in the trench was measured by the interfacial wave gage at a location close to the upstream wall of the trench.

For the study of internal wave damping, the above arrangement had at least two advantages over the constant-depth channel and trench combinations used in the previous experiments. First, flow separation at the upstream edge of the trench was eliminated in this problem. Second, the effects of the surface waves were kept to a minimum. Note that without the gate the fluid at $x = 0$ acts as a wave generator for the fluid motion in the trench. Closing the gate instantly brought the fluid motion at this location to zero; thus, the pressure force exerted by the surface waves on the density interface disappeared. It is recalled that the forced internal wave motion in the trench was due to action of a surface wave whose wavelength was large compared to the width of the trench. After the gate was closed the surface motions

in the trench region no longer corresponded to the conditions for the forced resonant oscillations of the internal waves. Hence, the internal wave amplitude continued to decrease due to viscous effects alone.

The rectangular basin created in the manner described above was 59.5 cm long and 39.4 cm wide. One objective of the investigation was to test the validity of the linear viscous theory. Hence, conditions were chosen in which nonlinear effects related to the internal waves were either small, or large. As mentioned earlier, we have obtained the former conditions with a deep lower fluid, that is, the depth of the upper fluid (water) in the trench region was $h_1 = 22.8\,\text{cm}$, and the depth of the lower fluid (salt water) was $h_2 = 7.6\,\text{cm}$. Three experiments were conducted with different thicknesses of the diffuse salinity interface: $\delta = 1.03\,\text{cm}$, $1.41\,\text{cm}$, and $2.61\,\text{cm}$. The corresponding wave periods for the lowest mode of oscillation of the internal waves as measured experimentally were 7.8 sec, 7.8 sec, and 8.0 sec, respectively. The wave periods for the first two experiments were the same because the difference in the thickness of the diffuse salinity interface was small. Though a much larger thickness of the interface was used in the third experiment, the wave period of resonant oscillation had only increased slightly for these experimental conditions. The density of salt water in these three experiments were, respectively, $1.0513\,\text{gcm}^{-3}$, $1.0505\,\text{gcm}^{-3}$, and $1.0494\,\text{gcm}^{-3}$.

A fourth experiment was conducted with a shallow lower fluid in the trench ($h_1 = 26.6\,\text{cm}$, $h_2 = 3.8\,\text{cm}$). These conditions were used in the experiments that were discussed in § 5.2.4, where it was shown that nonlinear effects related to the internal oscillations were very important in the shallow region. Hence, it is interesting to see how the decay of the internal wave as recorded experimentally compared to the theoretical predictions of the linear viscous theory. The thickness of the diffuse salinity interface was 0.94 cm, and the density of salt water was $1.0506\,\text{gcm}^{-3}$. The wave period measured was 10.0 sec.

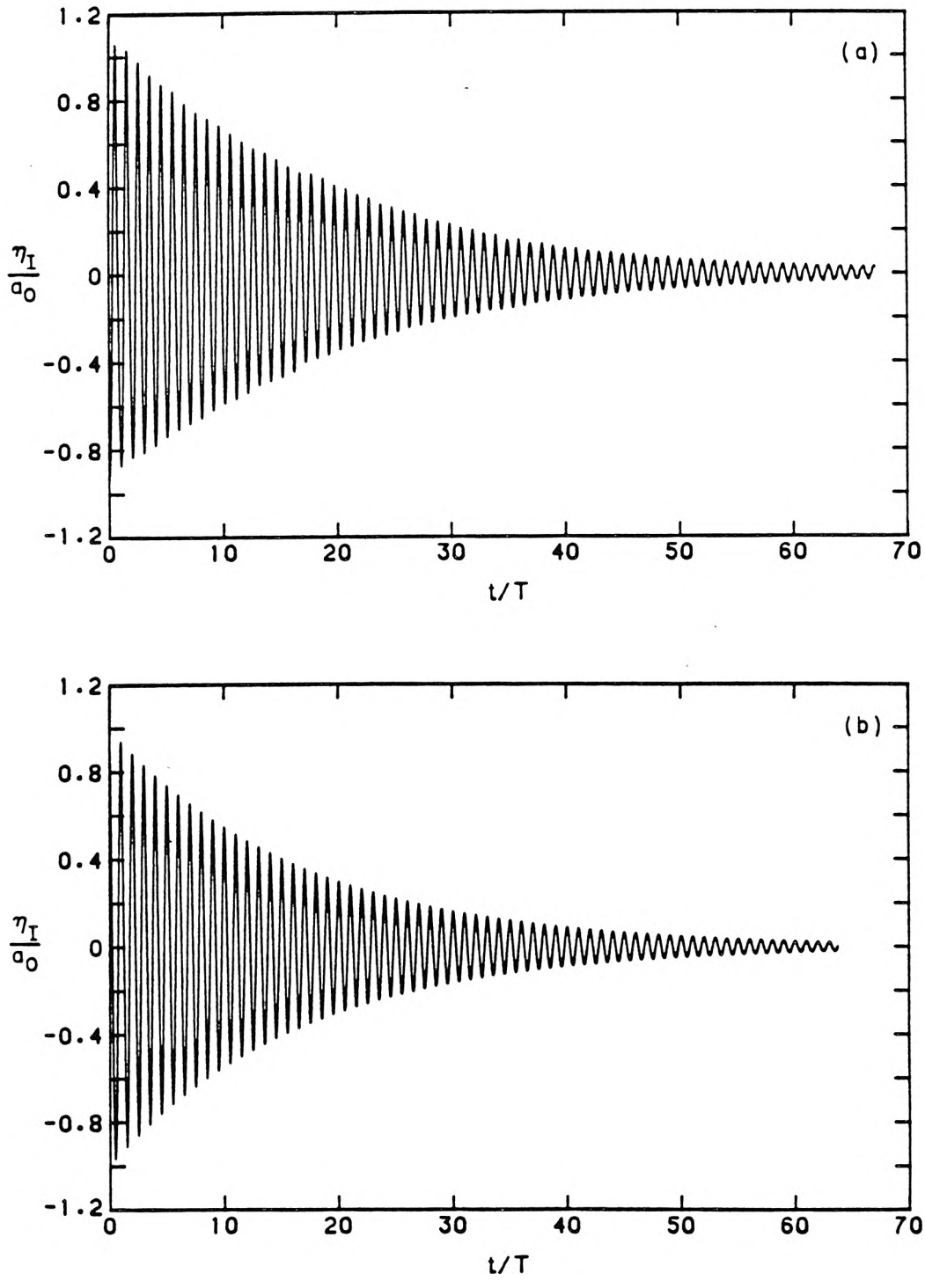

Figure 5.2.55. Time histories of decay of internal oscillations at the upstream wall of the rectangular basin for the lowest mode of resonant oscillation in the deep lower fluid ($h_1 = 22.8\,\text{cm}$, $h_2 = 7.6\,\text{cm}$): (a) experiment; $T = 7.8\,\text{sec}$, $a_0 = 1.12\,\text{cm}$, $\delta = 1.41\,\text{cm}$, $\rho_2 = 1.0505\,\text{gcm}^{-3}$, and ($b$) two-layer viscous theory; $T = 7.843\,\text{sec}$, $\rho_2/\rho_1 = 1.05$.

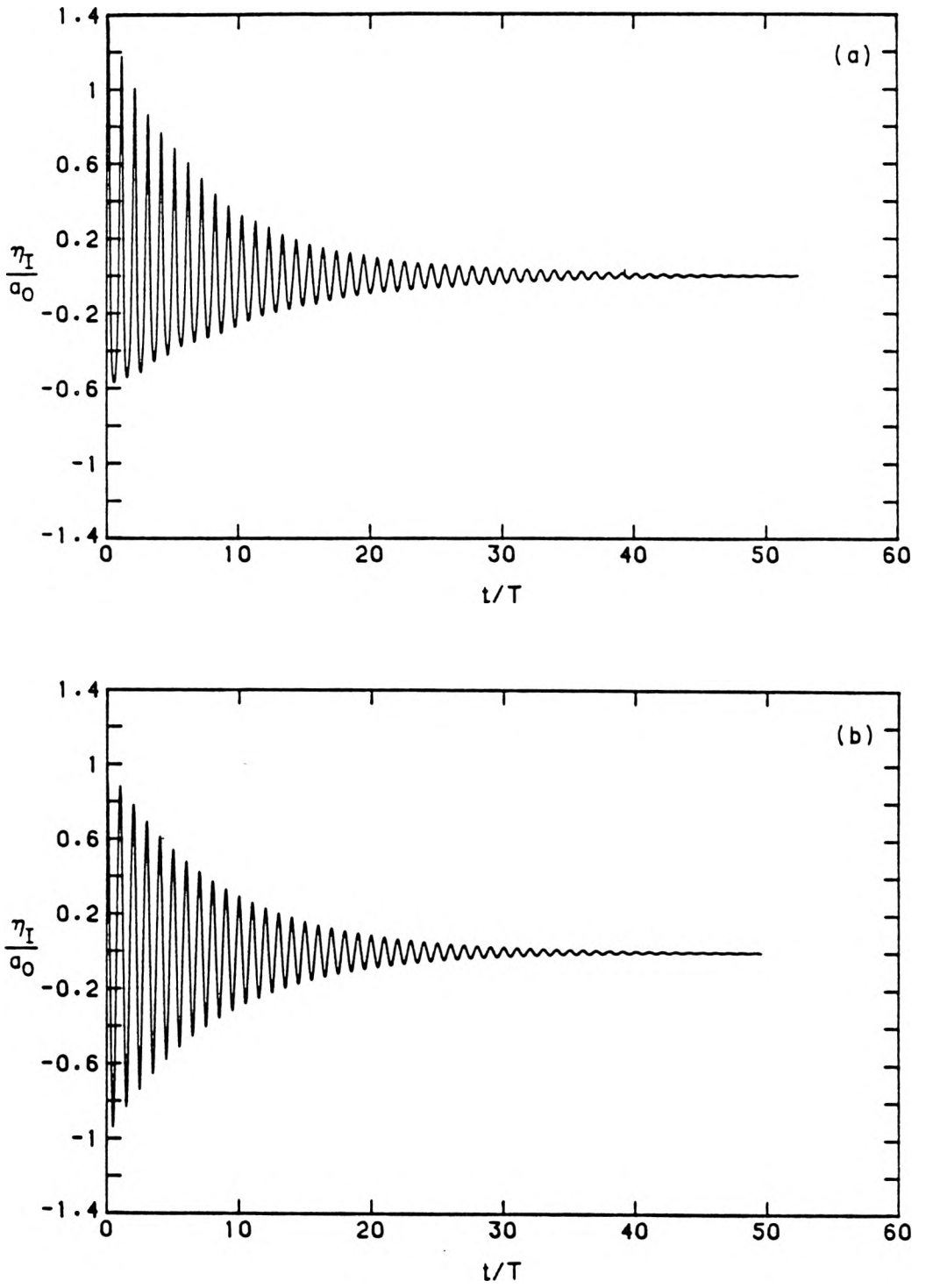

Figure 5.2.56. Time histories of decay of internal oscillations at the upstream wall of the rectangular basin for the lowest mode of resonant oscillation in the shallow lower fluid ($h_1 = 26.6$ cm, $h_2 = 3.8$ cm): (a) experiment; $T = 10.0$ sec, $a_0 = 1.07$ cm, $\delta = 9.4$ cm, $\rho_2 = 1.0506\,\mathrm{gcm}^{-3}$, and ($b$) two-layer viscous theory; $T = 10.095$ sec, $\rho_2/\rho_1 = 1.05$.

The experimental and theoretical results for the time history of the decay of the internal oscillations at the upstream wall are presented in figures 5.2.55*a* and 5.2.55*b*, respectively. The experiment was conducted in the deep lower fluid, that is, $h_2 = 7.6\,\text{cm}$ for a wave period of 7.8 sec, which corresponded to the lowest mode of oscillation of the internal waves in the rectangular basin. The density of salt water was $1.0505\,\text{gcm}^{-3}$, and the thickness of the diffuse salinity interface was 1.41 cm. In figure 5.2.55*a*, η_I and a_0 are, respectively, the time-dependent displacement of the density interface and the average of the crest amplitude and the trough amplitude measured at the upstream wall at an initial time $t = 0$, and T is the measured wave period of 7.8 sec. The abscissa of the theoretical curve in figure 5.2.55*b* is normalized by the predicted wave period of the resonant oscillation which, from the two-layer viscous theory, is 7.843 sec. At $t/T = 0$, the ratio of the experimentally observed crest amplitude to trough amplitude of the internal oscillation is about 1.2. This ratio decreases as the amplitude of the standing internal wave a decreases with time. The theoretical time history includes damping in the boundary layers adjacent to the density interface and at the solid surfaces. Considering the sensitivity of damping to the conditions of the solid surfaces in the experiment, the linear viscous theory does a good job in predicting the decaying internal oscillations for this weakly nonlinear case.

The measured and the predicted time histories of the decay of the internal oscillations for $h_2 = 3.8\,\text{cm}$ are presented in figures 5.2.56*a* and 5.2.56*b*, respectively. This is the fourth experiment discussed earlier. The wave period of resonant oscillation measured was 10.0 sec, and the wave period predicted by the two-layer viscous theory was 10.095 sec. The experimentally observed time decay of oscillation of the internal wave is highly non-symmetrical about the quiescent density interface in this shallow lower fluid.

The results of three experiments in the deep lower fluid ($h_2 = 7.6\,\text{cm}$) are

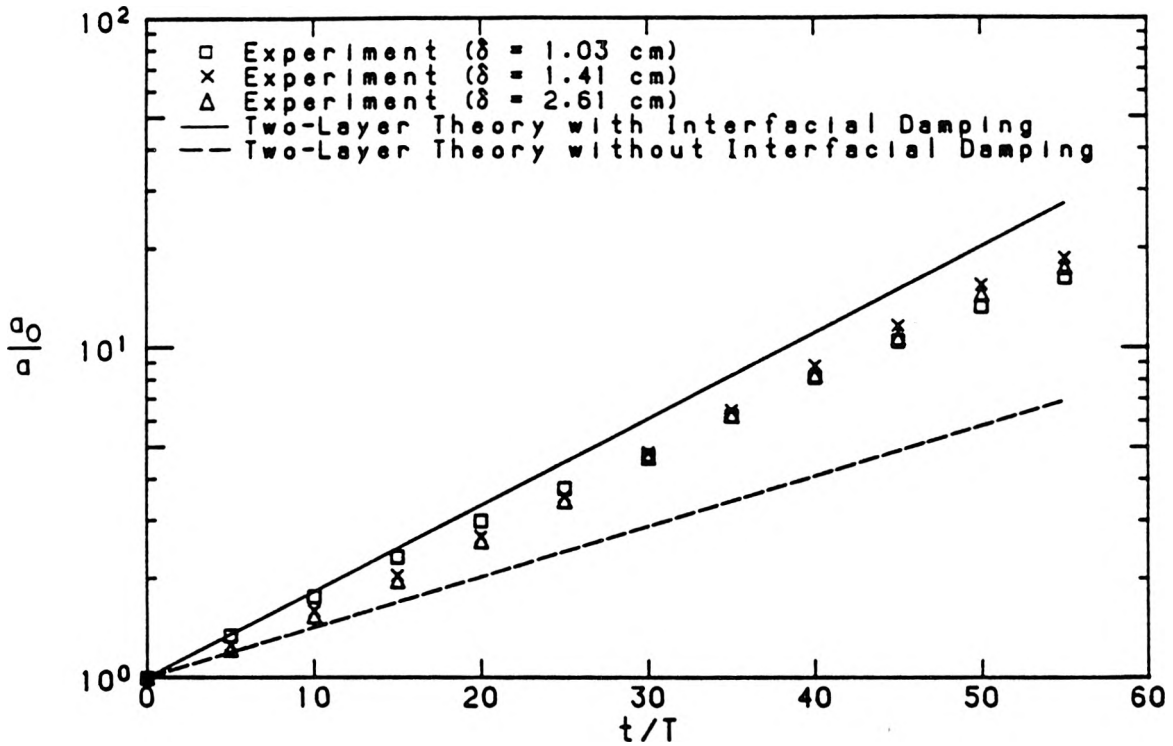

Figure 5.2.57. Amplitude envelopes of the decay of internal oscillations in the deep lower fluid; $h_1 = 22.8\,\text{cm}$, $h_2 = 7.6\,\text{cm}$.

presented in figure 5.2.57. The ordinate is a_0/a where a_0 is an initial wave amplitude, and a is the wave amplitude at a subsequent time t taken from the average of the crest amplitude and the trough amplitude. The abscissa is the number of oscillations t/T, where T is the wave period measured. Thus figure 5.2.57 shows the amplitude envelopes of the decay of the internal waves. From (3.3.120), a/a_0 and t/T are related to the modulus of decay α^* by:

$$\alpha^* = \frac{T}{t} \ln\left(\frac{a_0}{a}\right) \tag{5.2.20}$$

where "ln" is the natural logarithm. Also shown in figure 5.2.57 are the predictions of the two-layer viscous theory. These are found using (3.3.111)–(3.3.113), (3.3.121) and (5.2.20), with $h_1 = 22.8\,\text{cm}$, $h_2 = 7.6\,\text{cm}$, $b = 19.7\,\text{cm}$, $\rho_2/\rho_1 = 1.05$, $\nu_1 = \nu_2 = 1.0 \times 10^{-6}\,\text{m}^2\text{sec}^{-1}$, and an internal wavelength of twice the trench width, that is,

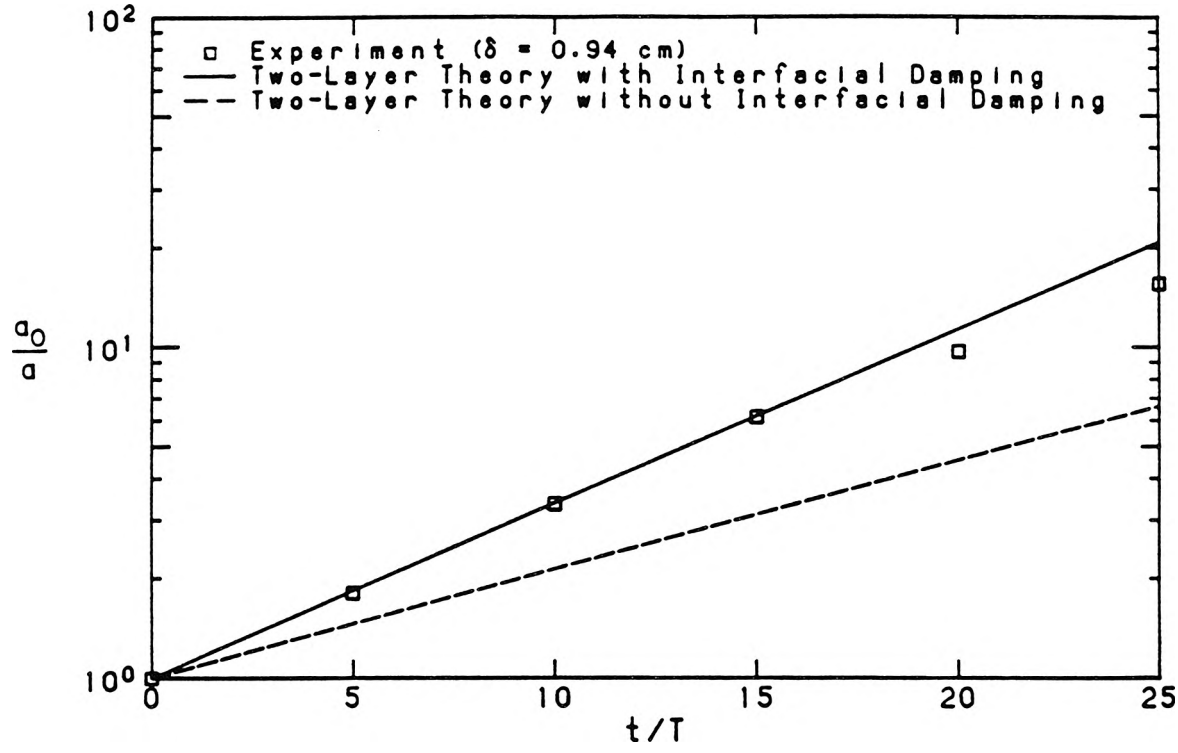

Figure 5.2.58. Amplitude envelopes of the decay of internal oscillations in the shallow lower fluid; $h_1 = 26.6\,\text{cm}$, $h_2 = 3.8\,\text{cm}$.

1.2 m for the lowest mode of resonant oscillation. The full line is the result including energy dissipation in all the boundary layers, that is, the boundary layers adjacent to the solid surfaces and at the density interface. According to (3.3.111) we may break the modulus of decay into two parts: that part due to the solid surfaces and that part due to the density interface. The dashed line in figure 5.2.57 is a plot of (5.2.20) with the modulus of decay given by that due to the solid surfaces only.

Several conclusions may be obtained from figure 5.2.57. First, the damping of the internal wave in these experiments is characterized by a constant value of the modulus of decay. Second, the measured modulus of decay is nearly the same for different thicknesses of the diffuse salinity interface δ. This indicates that energy dissipation in the diffuse salinity interface is not sensitive to the thickness of the

interface in the real fluid. This may be simply because wave damping in the density transition region is small compared to the total energy loss in the fluid for these experimental conditions. Last, the modulus of decay given by the full line overestimates the energy dissipation, whereas the dashed line underestimates the damping significantly. The former is attributed to damping at the density interface, which does not exist in the miscible fluids. The latter suggests that other sources of energy dissipation not included in the two-layer model existed in the experiment. The excessive energy loss could not be due to flow separation or surface action, because these effects were negligible in the rectangular basin that had been isolated from the constant-depth channel. It is possible that the linear viscous theories, which assume the ideal conditions of a very smooth surface, have underestimated the energy dissipation near the solid surfaces. The effects of these on the internal oscillations were not studied.

The amplitude envelopes of the decay of internal waves in the shallow lower fluid ($h_2 = 3.8\,\mathrm{cm}$) for the lowest mode of resonant oscillation are presented in figure 5.2.58. The experimental and theoretical time histories of the internal wave have been shown in figures 5.2.56*a* and 5.2.56*b*, respectively. In figure 5.2.58 the wave amplitude a is given by the average value of the crest amplitude and the trough amplitude. It is surprising that even though the waveform as seen in figure 5.2.56*a* is highly non-symmetrical about the quiescent density interface, the internal wave amplitude measured can still be related to a constant value of the modulus of decay.

It is constructive to examine the energy loss in various parts of the fluid in the rectangular basin. A comparison is made in table 5.2.3 between the attenuation rates for standing internal waves in the deep lower fluid ($h_2 = 7.6\,\mathrm{cm}$) and in the shallow lower fluid ($h_2 = 3.8\,\mathrm{cm}$), for the lowest resonant mode in the rectangular basin. These results are obtained using the two-layer viscous theory. The

T (sec)	7.843	10.095
h_1 (cm)	22.8	26.6
h_2 (cm)	7.6	3.8
α (sec^{-1})	0.00766	0.01203
α_B(sec^{-1})	0.00262	0.00595
α_I(sec^{-1})	0.00318	0.00452
α_{W1}(sec^{-1})	0.00018	0.00011
α_{W2}(sec^{-1})	0.00049	0.00025
α_{W3}(sec^{-1})	0.00007	0.00002
α_{W4}(sec^{-1})	0.00112	0.00118

Table 5.2.3. Comparison between the attenuation rates for standing internal waves in the deep lower fluid and in the shallow lower fluid for the lowest resonant mode in the rectangular basin; $\ell = 59.5$ cm, $b = 19.7$ cm.

attenuation rate α is related to the wave amplitude a by:

$$a = a_0 e^{-\alpha t} \tag{5.2.21}$$

where a_0 is the wave amplitude at an initial time $t = 0$. Hence $\alpha = \alpha^*/T$ from (3.3.120) and (5.2.21). From (3.3.111), the attenuation rate may be divided into the following parts (see figure 3.3.4):

$$\alpha = \alpha_B + \alpha_I + \alpha_{W1} + \alpha_{W2} + \alpha_{W3} + \alpha_{W4} \tag{5.2.22}$$

where the subscript B denotes the basin bottom, I denotes the density interface, $W1$ denotes the end walls for $-b < y < b$ at $x = 0$ and $x = \ell$ in the upper layer, $W2$ denotes the side walls for $0 < x < \ell$ at $y = -b$ and $y = b$ in the upper layer,

$W3$ denotes the end walls for $-b < y < b$ at $x = 0$ and $x = \ell$ in the lower layer, and $W4$ denotes the side walls for $0 < x < \ell$ at $y = -b$ and $y = b$ in the lower layer. Notice that the energy loss is concentrated in three regions: in the boundary layers adjacent to the density interface, at the basin bottom, and at the side walls at $y = -b$ and $y = b$, whereas the fraction of energy loss due to the end walls at $x = 0$ and $x = \ell$ is very small. The latter is because the horizontal component of the fluid velocity is much larger than the vertical component for the lowest mode of resonant oscillation, hence viscous dissipation in the boundary layers adjacent to the end walls at $x = 0$ and $x = \ell$ is much smaller than those at the basin bottom and the side walls at $y = -b$ and $y = b$. It is seen that the total energy loss in the upper fluid is smaller than that in the lower fluid. This is understandable because in the internal wave mode, the water particle velocities decrease rapidly with distance from the density interface in the upper layer but they decrease much more slowly in the lower layer. The former can be deduced from (5.2.18) and has been discussed in § 5.2.3; the latter can be seen in (3.3.83*b*), from which the horizontal component of the fluid velocity in the lower fluid u_2 can be obtained. This is given for the inviscid case in dimensional form as:

$$u_2 = a_0\sigma_0 \frac{\cosh K(z + h_1 + h_2)}{\sinh Kh_2} \sin Kx \sin \sigma_0 t \tag{5.2.23}$$

where a_0 is the amplitude of the internal wave. From (5.2.23), the ratio of u_2 on the bottom, $z = -(h_1 + h_2)$, to that at the interface, $z = -h_1$, is given by $1/\cosh Kh_2$. Using $h_2 = 7.6$ cm, and the wave number of the internal wave $K = K_2 = \pi/\ell$ for the lowest mode of oscillation, the ratio of the horizontal velocity on the basin bottom to that at the density interface is found to be 0.925. Hence, equation 5.2.23 predicts that the amplitude of the horizontal velocity is almost uniform in the lower layer, therefore the energy loss due to the bottom at $z = -(h_1 + h_2)$ and the side walls at $y = -b$ and $y = b$ should be approximately proportional to their surface areas. Indeed, it is seen in table 5.2.3 that α_B is approximately equal to $(b/h_2)\alpha_{W4}$.

Using (5.2.23) and table 5.2.3, the ratio of u_2 on the basin bottom for the shallow lower fluid to that for the deep lower fluid, for the same internal wave amplitude at the density interface, is found to be about 1.6. The ratio of the attenuation rate for the bottom (α_B) for these two cases is about 2.3, reflecting the effect of this increase in the horizontal velocity near the bottom. Note that these comments are only of an approximate nature because the waves in the lower fluid for the shallow layer are nonlinear. Hence, damping in the boundary layer adjacent to the basin bottom increases as h_2 decreases. The density interface is an important source of energy loss in immiscible fluids but its contribution is greatly reduced in miscible fluids such as water and salt water.

In summary, the damping of the standing internal waves was studied in the same rectangular trench used in previous experiments; a vertical partition was used to separate the trench region from the constant-depth channel after steady-state conditions were established in the trench. Hence, in these experiments the effects of surface motions on the internal waves were negligible. The time histories of the decay of the internal oscillations in the trench were obtained for two different depths of the lower fluid to examine the effects of bottom dissipation and nonlinearity on the damping of internal waves. The amplitude envelopes of the decay of internal oscillations obtained from these experiments could be related to constant values of the modulus of decay, even for the case of the shallow lower fluid where the internal motions were highly non-symmetrical about the quiescent density interface. The excessive energy loss observed in the experiments which were discussed in § 5.2.3 and § 5.2.4 for the constant-depth channel and trench arrangement was also observed in these experiments. Hence, it appears that the excessive energy loss could not be attributed to flow separation and/or surface wave damping. Roughness of the solid surfaces could increase energy dissipation substantially but the effects of this on the internal wave were not studied. Experiments with different thicknesses of

the diffuse salinity interface and theoretical analysis of damping in various parts of the fluid indicate that the density interface is an important source of energy loss in immiscible fluids but its significance in miscible fluids such as water and salt water is substantially reduced. Both experiment and theory show that, if the total depth of the stratified fluid is held fixed, energy dissipation increases as the depth of the lower fluid decreases due to the increase in fluid velocity adjacent to the bottom.

5.3 Wave Interaction with a Rectangular Trench in an Infinite Region

In the experimental phase of this investigation, because of wave reflection from the ends of the wave tank, the problem of surface wave propagation over a trench in an infinite region could not be studied in the laboratory. Therefore, a different experimental set-up (figure 5.1.1) was adopted where the problem could be formulated theoretically and the results compared directly to the experimental measurements. The objective of the experimental investigation was to determine if the linear models developed are adequate or if it is necessary to use more complicated models. The results of theory and experiment dealing with this arrangement have been discussed in § 5.2. Hence, when we use the same theoretical approach for the case of a trench in an infinite region, we already have some knowledge of the range of validity of the linear solutions.

In this section we present the linear steady-state solutions for a time-periodic progressive surface wave, which propagates over a rectangular trench in an infinite region; the direction of wave propagation is perpendicular to the longitudinal axis of the trench. The theoretical treatment of this problem is given in § 3.4. As shown in figure 3.4.1, the fluid in the trench region is represented by a two-layer system with the heavier fluid confined within the trench; the fluid outside the trench is homogeneous. The regions before and after the trench are of a constant depth and

of infinite lateral extent. It is assumed that energy dissipation takes place in the boundary layers adjacent to the density interface, and next to the trench bottom as discussed in § 3.3; the flows in the boundary layers are laminar. We also ignore damping due to the vertical walls at $x = 0$ and $x = \ell$, this contribution has been shown earlier to be relatively small in a trench where the ratio of the trench width to the depth of the lower fluid is large. As mentioned earlier, this is because for shallow water conditions the amplitude of the horizontal component of the fluid velocities is large compared to the amplitude of the vertical component, hence the shear stress developed adjacent to the trench bottom is substantially larger than that developed adjacent to the vertical walls at $x = 0$ and $x = \ell$. This situation was illustrated in § 5.2.5 for the decay of a standing internal wave in a rectangular basin. However, we caution that for internal waves in a deep lower fluid in the trench, the shearing motions near the vertical walls may become a dominant cause of wave attenuation instead of that at the bottom. In addition, we also ignore wave damping in the infinite region ($x < 0$ and $x > \ell$), that is, the homogeneous fluid outside the trench region ($0 < x < \ell$) is assumed to be inviscid. Hence, viscous effects are considered to be due solely to the fluid motion in the trench.

For the problem shown in figure 3.4.1, the quantities of interest are the wave height of the standing internal wave H_I, the wave height of the reflected surface wave H_{S_r}, and the wave height of the transmitted surface wave H_{S_t}. Each of the above three quantities can be related functionally to the independent variables of the problem as follows:

$$H_{sub} = f(H_{S_i}, \sigma, g, h, h_1, h_2, \ell, \rho_1, \rho_2, \mu_1, \mu_2) \tag{5.3.1}$$

wherein the dependent variable H_{sub} can be used to denote any one of the three quantities H_I, H_{S_r}, and H_{S_t}. In (5.3.1), H_{S_i} is the wave height of the incident surface wave, σ is its circular wave frequency ($2\pi/T$ with T the wave period), g is

the acceleration of gravity, ρ_1 is the density of the upper fluid, ρ_2 is the density of the lower fluid, μ_1 is the dynamic viscosity of the upper fluid, μ_2 is the dynamic viscosity of the lower fluid, and h, h_1, h_2, and ℓ are defined in figure 3.4.1. The twelve variables involve three physical dimensions: mass, length and time, thus physical reasoning leads to one particular choice of dimensionless groups:

$$\frac{H_{sub}}{H_{S_i}} = f\left(\frac{H_{S_i}}{h}, \frac{\sigma^2 h}{g}, \frac{h_1}{h}, \frac{h_2}{h}, \frac{\ell}{h}, \frac{\rho_1}{\rho_2}, \varepsilon_1, \varepsilon_2\right) \tag{5.3.2}$$

where

$$\varepsilon_i = \frac{\sigma^2}{g}\left(\frac{\nu_i}{\sigma}\right)^{1/2}, \qquad (i = 1, 2). \tag{5.3.3}$$

In (5.3.3), $\nu_i = \mu_i/\rho_i$, $(i = 1, 2)$ is the kinematic viscosity of the fluid. The dimensionless quantity ε_i, $(i = 1, 2)$ is a boundary layer parameter. For fresh water and salt water we assume that $\nu_1 = \nu_2 = 1.0 \times 10^{-6}\,\mathrm{m^2 sec^{-1}}$. In the following analysis, we shall be interested in the case where H_{S_i}/h is held fixed, and H_{sub}/H_{S_i} varies with the frequency parameter $\sigma^2 h/g$ for conditions determined by the four dimensionless groups h_1/h, h_2/h, ℓ/h, and ρ_1/ρ_2, which define the trench geometry and the density ratio. A summary of the conditions for the cases that will be discussed is presented in table 5.3.1. Note that from the dispersion relation of a homogeneous fluid (equation 3.1.25a) we have $\sigma^2 h/g = kh \tanh kh$, where k is the wave number of the surface wave in the infinite region, thus we may use kh instead of $\sigma^2 h/g$ as the frequency parameter.

Before we present the results of the two-layer theory treated in § 3.4, let us consider a simple method for finding the value of kh corresponding to a mode of oscillation of the internal waves in the trench. This method, though not as precise as the numerical approach, would still be very useful to engineers who design navigation channels, to reduce the potential of wave-induced internal resonance.

It has been shown that for long waves with infinitesimal amplitude in a two-layer fluid with small density difference, the phase speed of the surface mode C_1 is

Case	$\frac{h_1}{h}$	$\frac{h_2}{h}$	$\frac{\ell}{h}$	$\frac{\rho_2}{\rho_1}$
a	1.5	0.5	3.95	1.05
b	1.5	0.5	3.95	1.1
c	1.5	0.5	10.0	1.05
d	1.75	0.25	3.95	1.05
e	1.5	3.5	3.95	1.05

Table 5.3.1. Summary of conditions for a time-periodic surface wave that propagates over a two-layer stratified rectangular trench in an infinite region.

given by (see, for example, Gill, 1982):

$$C_1^2 = g(h_1 + h_2) + O(\epsilon) \tag{5.3.4}$$

where $\epsilon = (\rho_2 - \rho_1)/\rho_2$, and the phase speed of the internal mode C_2 is given by:

$$C_2^2 = \frac{g\epsilon h_1 h_2}{(h_1 + h_2)} + O(\epsilon^2). \tag{5.3.5}$$

To a first order approximation, the wave number of the internal mode corresponding to a resonant mode of oscillation of the internal waves in the trench is given by $K_2 = n\pi/\ell$, $(n = 1, 2, \ldots)$. Then the resonant frequency is given by $\sigma = K_2 C_2$, with C_2 given by (5.3.5). For long waves, the phase speed of the surface wave in the infinite region is equal to $\sqrt{gh}$. Hence the relative wave number kh of the incident

wave is found to be:

$$kh \approx \frac{n\pi}{\ell}\sqrt{\frac{\epsilon h h_1 h_2}{(h_1+h_2)}}, \qquad (n=1,2,\ldots). \tag{5.3.6}$$

In addition, we have $K_1/K_2 = C_2/C_1$ for the same wave period, hence the wave number of the surface mode is given by:

$$K_1 \approx \frac{n\pi}{\ell}\frac{\sqrt{\epsilon h_1 h_2}}{(h_1+h_2)}, \qquad (n=1,2,\ldots). \tag{5.3.7}$$

For the constant density problem, Kirby and Dalrymple (1983) showed that total reflection of the surface wave by a rectangular trench occurs for $K_1\ell = (n-\frac{1}{2})\pi$, $(n=1,2,\ldots)$. But from (5.3.7) $K_1\ell = O(\sqrt{\epsilon})$, $\epsilon \ll 1$ for resonant oscillation of internal waves, hence for the problem of internal resonance we are interested in incident waves whose wavelength is much longer than that which would produce large surface reflection in the corresponding constant density problem.

Equation 5.3.5 is expected to work well when $K_2 h_2$ is small compared to unity. An appropriate situation may be the lowest mode of oscillation of internal waves in a trench where $\ell/h_2 \gg 1$. For the higher modes we should use the dispersion relation for a two-layer fluid (equation 3.1.18a) to find the resonant frequency σ; equation 3.1.18a is valid for all ranges of relative fluid depths $K_i h_1$ and $K_i h_2$, $(i=1,2)$. The surface waves, however, generally would fall in the range of long waves for at least the first few modes of oscillation of the internal waves. Hence, equation (5.3.4) is still a very good approximation for this problem.

In the following sections, the responses of a two-layer fluid in a rectangular trench to a time-periodic surface wave for various trench aspect ratios and density ratios of the lower fluid to the upper fluid will be presented. This is done to show the sensitivity of the internal oscillations to variations in these quantities.

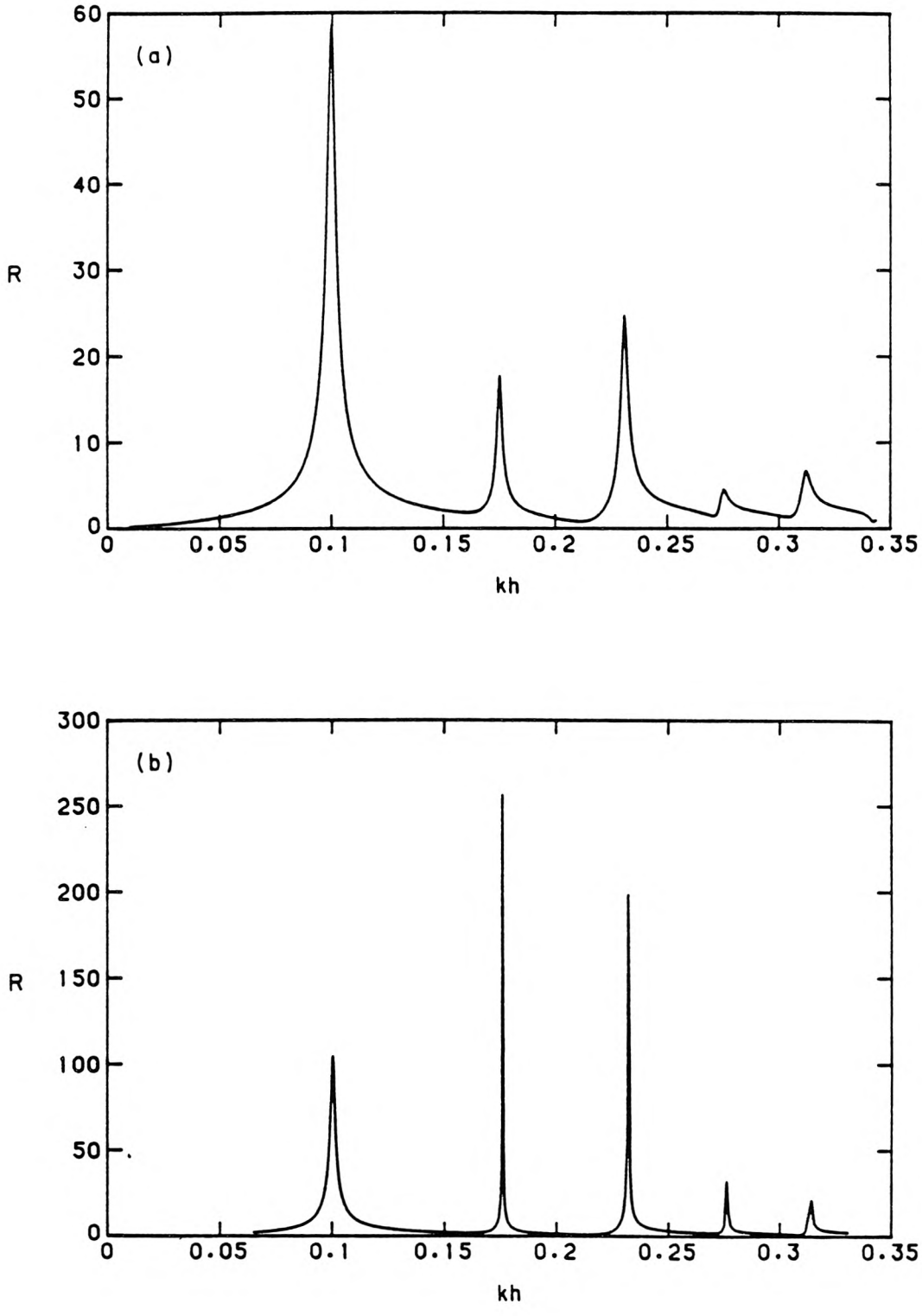

Figure 5.3.1. Variation of amplification factor, R, with relative wave number, kh: (a) two-layer viscous theory, and (b) two-layer inviscid theory; $h_1/h = 1.5$, $h_2/h = 0.5$, $\ell/h = 3.95$, $\rho_2/\rho_1 = 1.05$.

5.3.1 Case a ($h_1/h = 1.5$, $h_2/h = 0.5$, $\ell/h = 3.95$, $\rho_2/\rho_1 = 1.05$)

In figure 5.3.1*a*, the amplification factor of internal wave R, is plotted as a function of relative wave number for the surface waves in the infinite region kh. The amplification factor is defined as the ratio of the amplitude of the internal wave at $x = 0$ to the amplitude of the incident surface wave, that is, $R = H_I/H_{S_i}$. The above chosen conditions are similar to the constant-depth channel and trench arrangement in the wave tank (figure 5.1.1), except that the constant-depth regions before and after the rectangular trench have now been extended to infinity. In addition, there are at least two major differences between the two problems. First, the water surface above the trench in the wave tank was always near an antinode of a standing wave, due to the proximity of the end wall at $x = \ell$. Hence, above the trench the amplitude of the horizontal component of the fluid velocity was much less than the amplitude of the vertical component of the fluid velocity. For a trench in an infinite region, the fluid state in the trench region is not so dictated. Thus, the velocity distribution above the trench can be very different from that in the wave tank. Second, damping due to the side walls of the wave tank does not exist in this two-dimensional problem.

From (5.3.6) the value of kh for the first three modes of oscillation of the internal waves is found to be 0.106, 0.213, and 0.319. The value of kh for the lowest mode of oscillation agrees quite well with the more accurate numerical method of § 3.4; the corresponding value of K_2h_2 is about 0.4. For the second and the third modes of oscillation, equation 5.3.6 poorly predicts the frequencies of resonant oscillation. This is because the wavelength of the internal wave is not necessarily long compared to the fluid depths for the higher modes of oscillation of the internal waves, even though the surface waves are long waves. Note that even for this relatively short trench ($\ell/h = 3.95$), the surface waves that excite the first five modes of oscillation of the internal waves in the trench all are long waves, that is, $kh/2\pi < 0.05$. The

values of the relative wave number, kh, for the first five resonant peaks as shown in figure 5.3.1a are: 0.0997, 0.175, 0.231, 0.275, and 0.312, and the corresponding values of $K_2\ell$ are: 0.995π, 1.99π, 2.98π, 3.98π, and 4.96π, which are very close to the values of $K_2\ell = n\pi$, $(n = 1, 2, \ldots)$. Hence, instead of using the two-layer viscous theory of § 3.4, we may determine the frequencies of resonant oscillation from the two-layer dispersion relation (3.1.18a) by substituting for K the wave numbers of resonant oscillation of the internal waves in the trench, that is, $K = K_2 = n\pi/\ell$, $(n = 1, 2, \ldots)$. This method, of course, does not yield the amplification factor R, but it is still useful in the design of navigation channels to avoid the conditions that would lead to internal resonance. It is seen in figure 5.3.1a that the amplification factor for the lowest mode of oscillation reaches a value of almost 60, whereas for the laboratory conditions with the end wall at the downstream edge of the trench the predicted value of the amplification factor is about 20 (figure 5.2.16). But it is noted that in the laboratory problem, the wave height of internal wave is normalized by the wave height of surface waves above the trench.

Figure 5.3.1a indicates that the lowest mode of oscillation has the largest response. The computation steps in kh near the resonant peaks have been refined to ensure that the maximum value of R is reached. The maximum response of the internal wave is very sensitive to the damping rate, which is a function of the depth ratios and the density ratio, as well as the frequency parameter. To illustrate this, the corresponding inviscid solution for the case of a trench in an infinite region is shown in figure 5.3.1b. In the inviscid problem, the amplitude of the response curve is limited only by radiation loss from the trench. It is seen that the higher modes of oscillation have larger responses than the lowest mode but the resonant peaks of the higher modes have such a small frequency bandwidth that a small degree of damping reduces the amplification factor substantially. The more important result is that the lowest mode of oscillation has the largest frequency bandwidth. Figures 5.3.1a and

5.3.1*b* indicate that the asymmetric modes ($n = 1, 3, 5, \ldots$) have larger frequency bandwidths than the symmetric modes ($n = 2, 4, 6, \ldots$), which is no doubt related to the velocity and pressure distributions in the trench region. Although this case is shown for comparison, in this section we present primarily the results of the viscous problem and this is implied unless specifically stated otherwise. It should be noted that laminar viscous boundary dissipation is used herein.

The variation of the transmission and reflection coefficients of the surface waves with relative wave number is presented in figures 5.3.2*a* and 5.3.2*b*, respectively. The transmission coefficient K_t is defined as the ratio of the amplitude of the transmitted wave to the amplitude of the incident wave, that is, $K_t = H_{S_t}/H_{S_i}$. In a similar manner, the reflection coefficient K_r is defined as the ratio of the amplitude of the reflected wave to the amplitude of the incident wave, that is, $K_r = H_{S_r}/H_{S_i}$. It is seen that the transmission and reflection coefficients of the surface wave are closely related to the amplification factor of the internal wave. Large reflections of the surface waves take place at approximately the same relative wave numbers that correspond to resonant conditions of the internal waves in the trench. When the internal waves are "off-resonance," the incident wave is little affected by the trench because the wavelength of the surface wave is very large compared to the trench width. This result is apparent in the transmission coefficient. Large reflection also occurs when the wave number of the surface wave in the trench region is given by $K_1\ell = (n - \frac{1}{2})\pi$, ($n = 1, 2, \ldots$). However, the latter condition is generally outside the range of surface waves of interest to the problem of internal resonance. The corresponding inviscid solution for the transmission and reflection coefficients are shown in figures 5.3.3*a* and 5.3.3*b*, respectively.

The variation of the dimensionless quantity, $(K_r^2 + K_t^2)$, with kh, is presented in figure 5.3.4. The quantity $(1 - K_r^2 - K_t^2)$ is a measure of the energy loss in the trench (equal to zero for an inviscid fluid). As expected, the variation of energy loss in

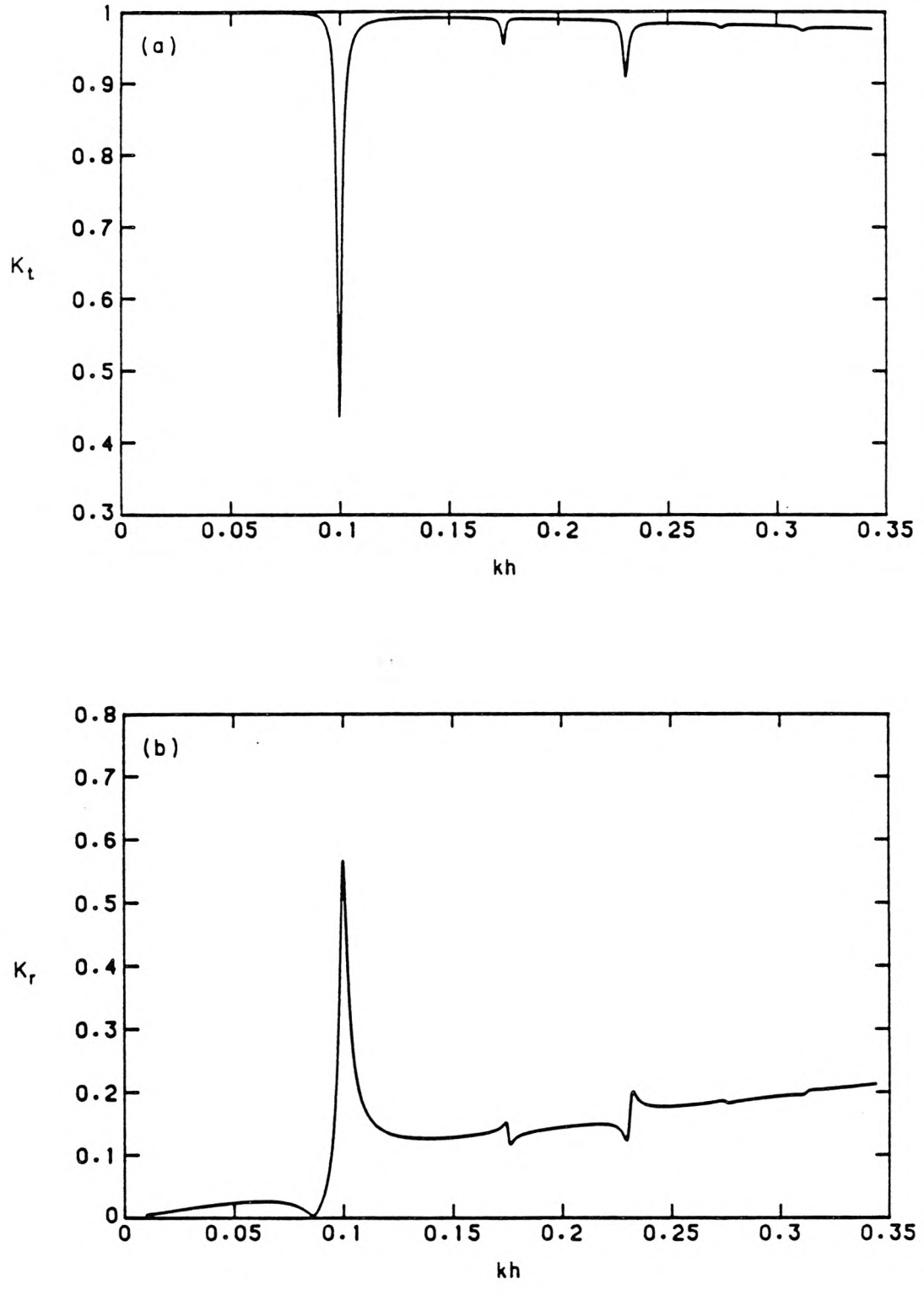

Figure 5.3.2. Variation of (a) transmission coefficient, and (b) reflection coefficient, with relative wave number—two-layer viscous theory; $h_1/h_2 = 1.5$, $h_2/h = 0.5$, $\ell/h = 3.95$, $\rho_2/\rho_1 = 1.05$.

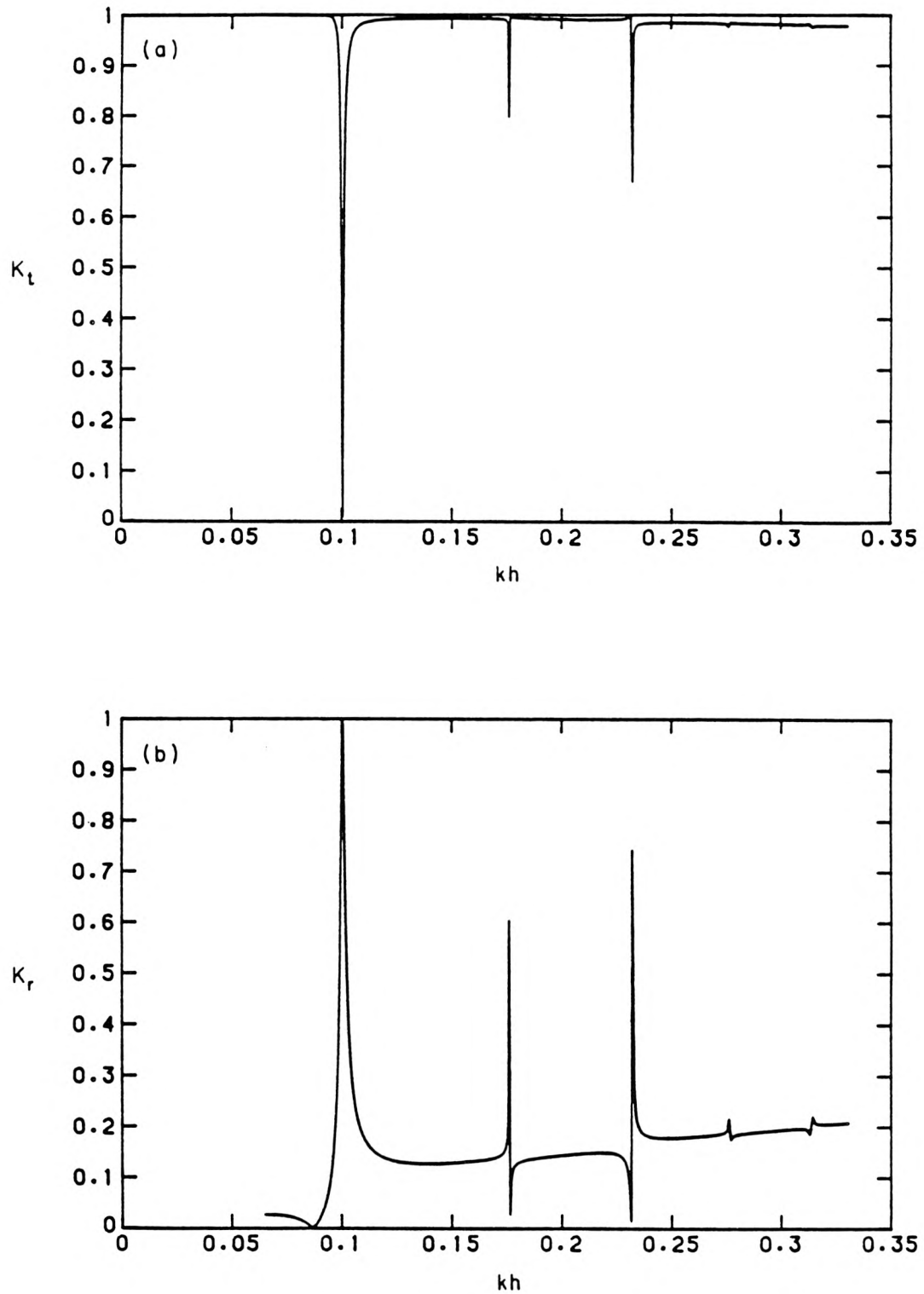

Figure 5.3.3. Variation of (a) transmission coefficient, and (b) reflection coefficient, with relative wave number—two-layer inviscid theory; $h_1/h = 1.5$, $h_2/h = 0.5$, $\ell/h = 3.95$, $\rho_2/\rho_1 = 1.05$.

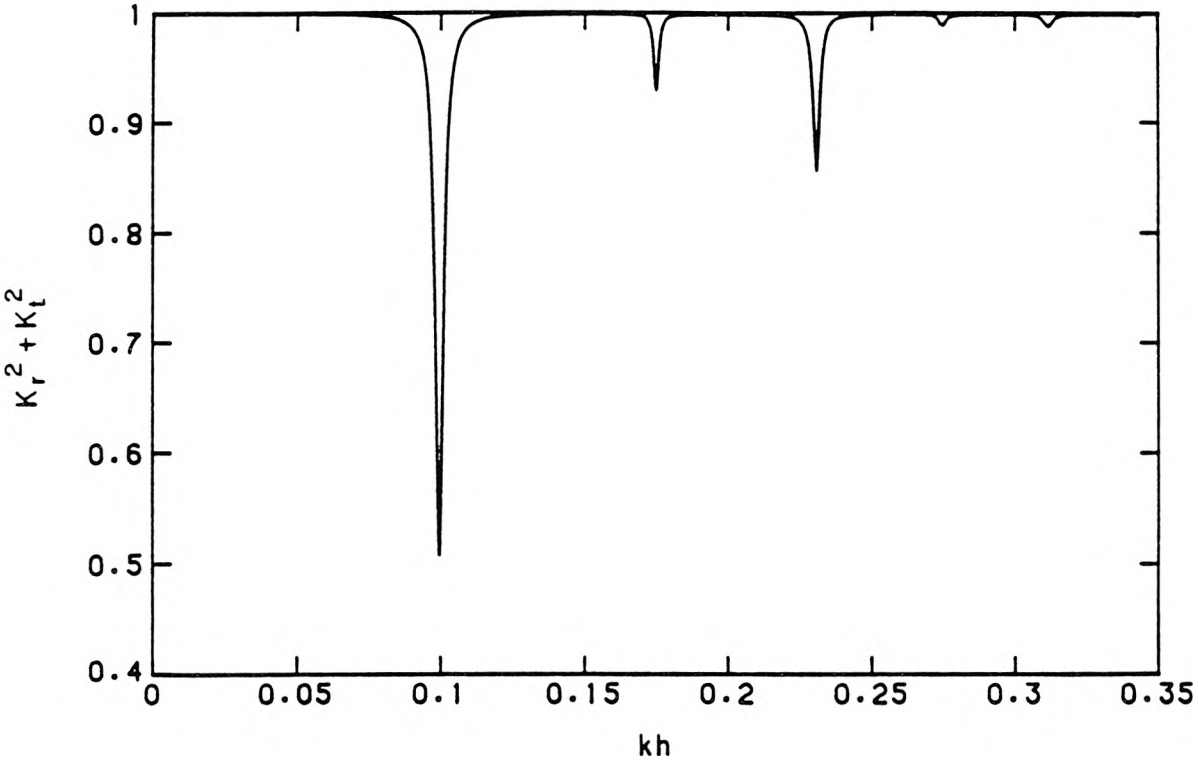

Figure 5.3.4. Variation of incident wave energy conserved in wave-trench interaction with relative wave number; $h_1/h = 1.5$, $h_2/h = 0.5$, $\ell/h = 3.95$, $\rho_2/\rho_1 = 1.05$.

the trench with relative wave number closely follows the trend of the amplification factor. Notice that the energy of the incident wave is nearly completely conserved when the period of the internal wave is "off-resonance."

5.3.2 Case b ($h_1/h = 1.5$, $h_2/h = 0.5$, $\ell/h = 3.95$, $\rho_2/\rho_1 = 1.1$)

Next we keep the same length and depth ratios but change the density ratio ρ_2/ρ_1 to 1.1. The variation of R, and $(K_r^2 + K_t^2)$, with kh are shown in figures 5.3.5*a* and 5.3.5*b*, respectively. The values of kh for the first five resonant peaks are found to be: 0.139, 0.245, 0.325, 0.389, and 0.443. The corresponding values of $K_2\ell$ are: 0.998π, 1.99π, 2.99π, 3.98π, and 4.97π. In comparison to figure 5.3.1*a*, it is seen that the magnitude of the resonant frequencies has increased due to this increase in density of the lower layer. The effect of increasing the density of the lower fluid is

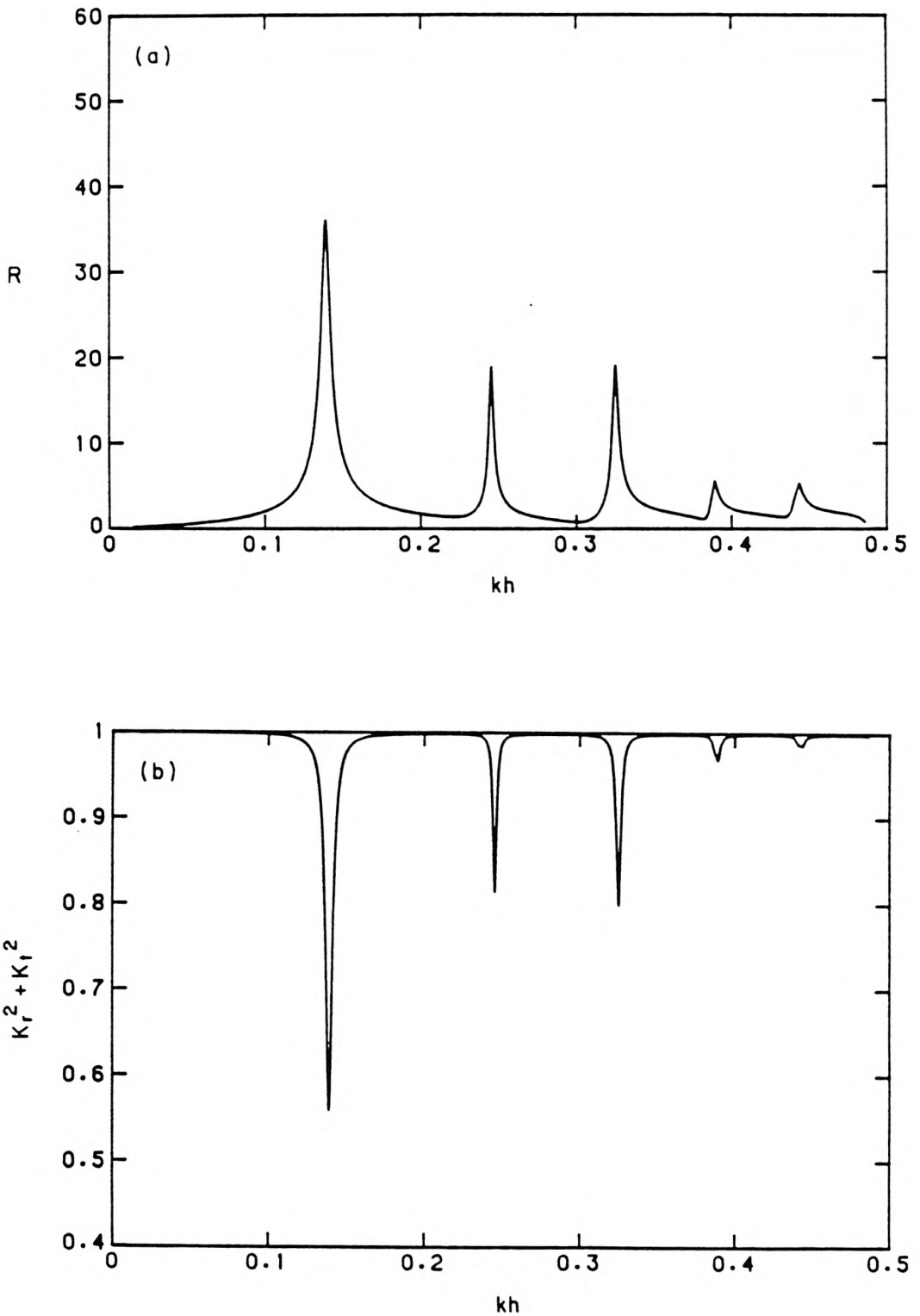

Figure 5.3.5. Variation of (a) amplification factor, and (b) incident wave energy conserved in wave-trench interaction, with relative wave number; $h_1/h = 1.5$, $h_2/h = 0.5$, $\ell/h = 3.95$, $\rho_2/\rho_1 = 1.1$.

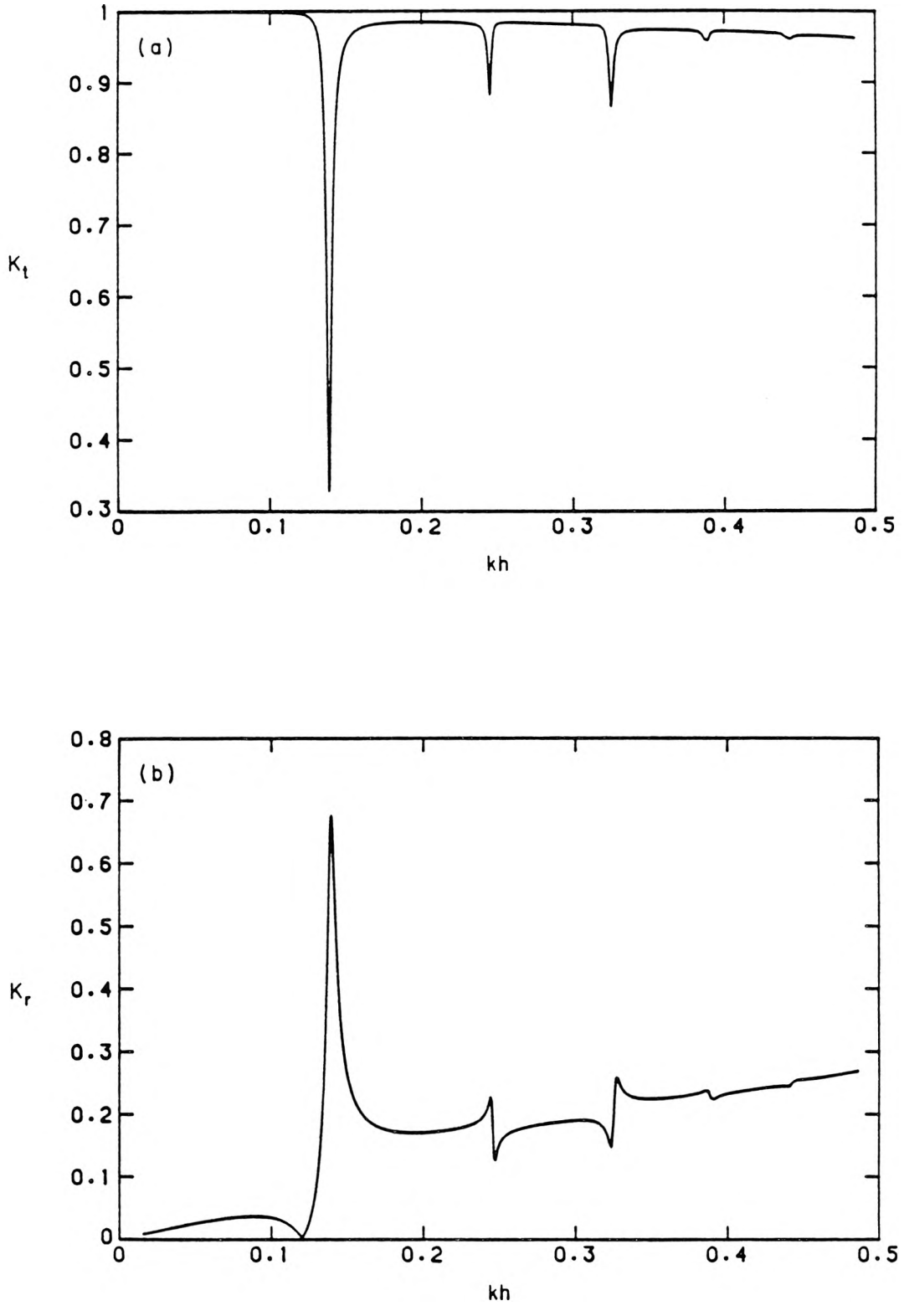

Figure 5.3.6. Variation of (a) transmission coefficient, and (b) reflection coefficient. with relative wave number; $h_1/h = 1.5$, $h_2/h = 0.5$, $\ell/h = 3.95$, $\rho_2/\rho_1 = 1.1$.

to increase both the inertia of the lower fluid and the restoring force responsible for the internal wave motion. If the wavelength is held fixed, the effect is to increase the frequency of oscillation. Hence, the response curve is shifted in the direction of higher frequencies, that is, larger kh. The effect on the amplification factor of changing the density ratio is more difficult to interpret because the amplification factor depends on the velocity distribution in the trench region and on the damping rate, which are both functions of ρ_2/ρ_1. Figure 5.3.5*a* indicates that the maximum amplitude responses in general have decreased. This is quite understandable from the physical point of view, for more potential energy would be involved in a given deformation of the density interface. The frequency bandwidths of the resonant peaks appear to be about the same for the two conditions; note that the scales of the abscissa in figures 5.3.1*a* and 5.3.5*a* are different. Again energy loss in the trench is closely related to the amplification factor. The transmission and reflection coefficients are presented in figures 5.3.6*a* and 5.3.6*b*, which follow a trend similar to figures 5.3.2*a* and 5.3.2*b*, respectively.

5.3.3 Case c ($h_1/h = 1.5$, $h_2/h = 0.5$, $\ell/h = 10.0$, $\rho_2/\rho_1 = 1.05$)

In figures 5.3.7*a* and 5.3.7*b* the variations of R and $(K_r^2 + K_t^2)$, respectively, with kh, are presented for the same conditions as Case a except that the relative trench width is increased to $\ell/h = 10.0$. As the width of the trench is increased, the resonant modes of oscillation of the internal waves occur at still larger wave periods. The values of kh for the first five resonant peaks are found to be: 0.0413, 0.0801, 0.115, 0.146, and 0.173. The corresponding values of $K_2\ell$ are: 0.99π, 1.98π, 2.98π, 3.97π, and 4.97π. The first three resonant peaks are also predicted well by the long wave approximation (equation 5.3.6); the corresponding values of kh are: 0.0420, 0.0840, and 0.0126. Comparing figures 5.3.1*a* and 5.3.7*a*, it is seen that the interval between adjacent resonant peaks decreases as ℓ/h increases, thus a wide

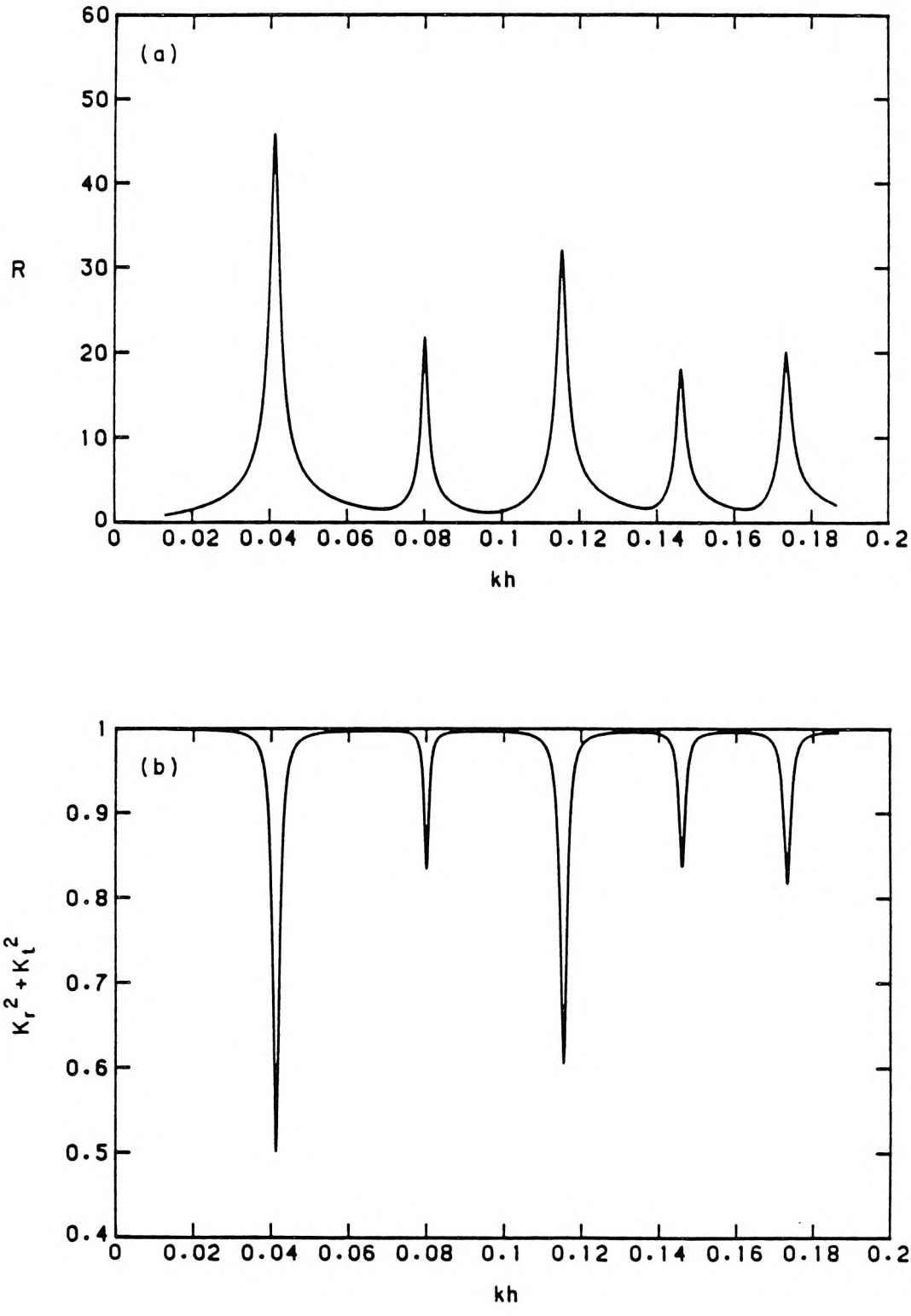

Figure 5.3.7. Variation of (a) amplification factor, and (b) incident wave energy conserved in wave-trench interaction, with relative wave number; $h_1/h = 1.5$, $h_2/h = 0.5$, $\ell/h = 10.0$, $\rho_2/\rho_1 = 1.05$.

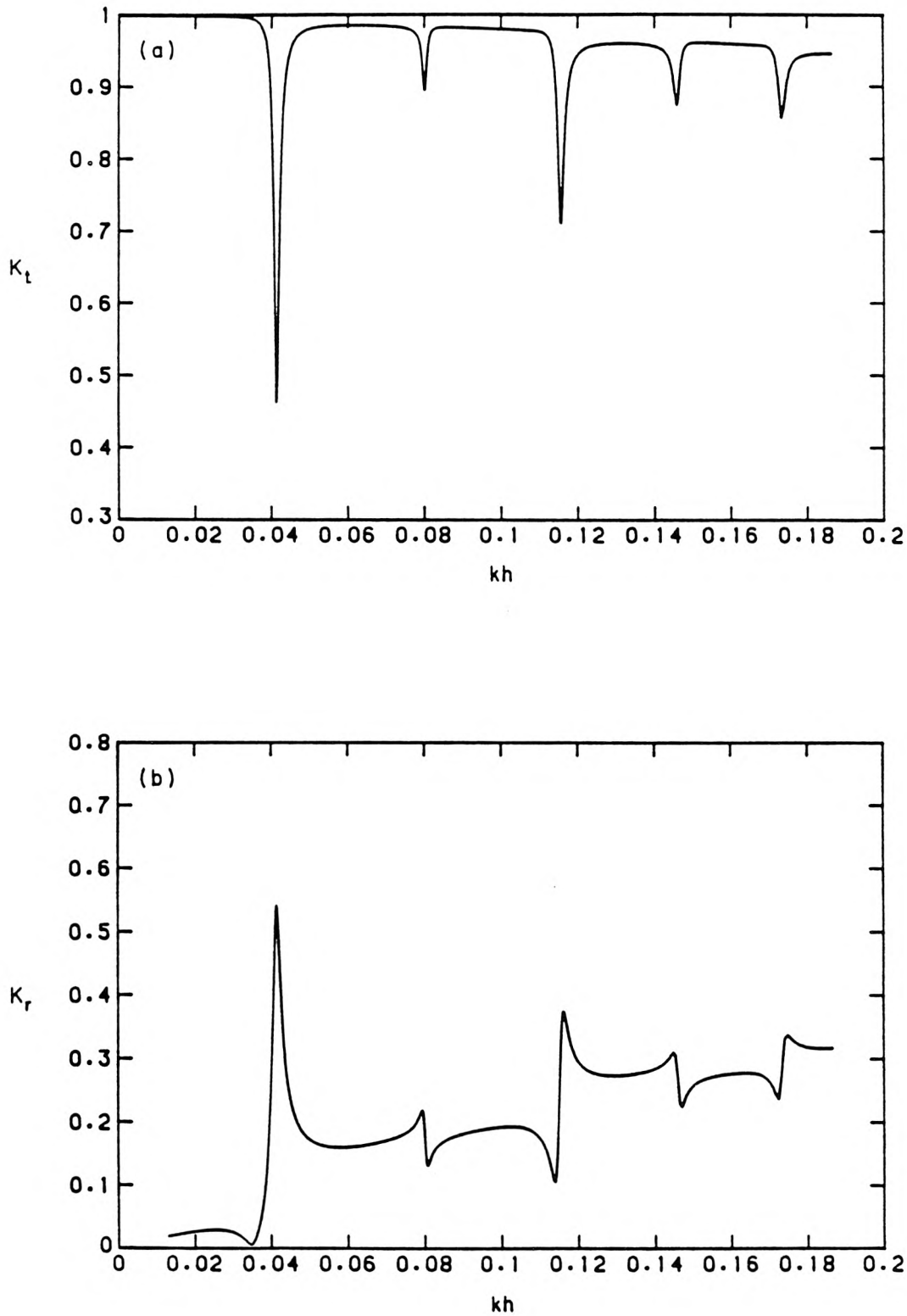

Figure 5.3.8. Variation of (a) transmission coefficient, and (b) reflection coefficient, with relative wave number; $h_1/h = 1.5$, $h_2/h = 0.5$, $\ell/h = 10.0$, $\rho_2/\rho_1 = 1.05$.

trench is more susceptible to internal resonance than a narrow trench for the same range of incident wave conditions. The transmission and reflection coefficients are presented in figure 5.3.8*a* and 5.3.8*b*, respectively. The effects of the oscillation of internal waves on surface wave transmission is apparent, and it is seen that large reflections of the incident wave occur for $K_2\ell = n\pi$, $(n = 1, 2, \ldots)$. Minimum values of the the transmission coefficient also occur for $K_1\ell = (n - \frac{1}{2}\pi)$, $(n = 1, 2, \ldots)$, which are the resonant conditions for the surface waves. However, the latter occur at much higher frequencies than the resonant frequencies of the internal waves; hence, its effects are not apparent. Nevertheless, if in figure 5.3.8*a* the spikes in the transmission coefficient due to the resonant oscillation of the internal waves are ignored, K_t is seen to vary slowly with kh due to the periodic behaviour of the transmission coefficient. This effect becomes more pronounced in a wide trench, because the resonant conditions for the surface waves occur at longer wave periods.

5.3.4 Case d ($h_1/h = 1.75$, $h_2/h = 0.25$, $\ell/h = 3.95$, $\rho_2/\rho_1 = 1.05$)

The result of reducing h_2/h to 0.25 while the trench geometry and the density ratio are held fixed are presented in figure 5.3.9*a* for the trench response. Comparing figure 5.3.9*a* to figure 5.3.1*a*, the response curve is seen to have shifted towards longer wave periods. This is because, for the same value of kh, the value of $K_2\ell$ is larger for the case with the shallow lower fluid, thus the resonant frequencies of the internal waves decrease. The values of kh for the first five resonant peaks are found to be: 0.0772, 0.144, 0.20, 0.252, and 0.292. The corresponding values of $K_2\ell$ are: 0.98π, 1.98π, 2.97π, 4.02π, and 4.96π. We can deduce from figures 5.3.9*a* and 5.3.9*b* that the damping rate increases as a result of the decrease in the relative depth of the lower fluid h_2/h; the damping rate for a progressive wave is defined in (3.3.45*c*). Comparing figure 5.3.9*a* to figure 5.3.1*a*, it is seen that the amplification factor for the lowest mode of oscillation is reduced by about half from the deep

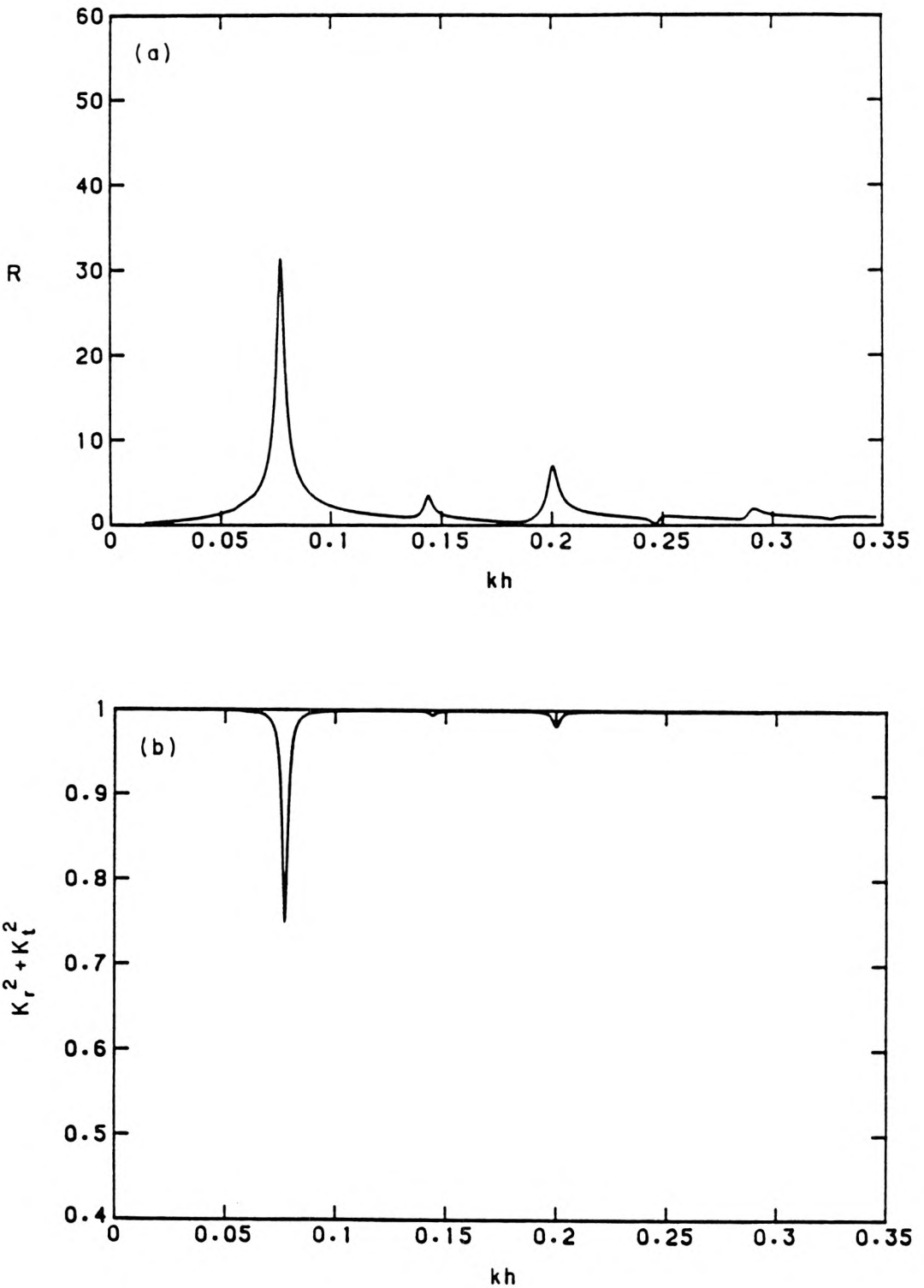

Figure 5.3.9. Variation of (a) amplification factor, and (b) incident wave energy conserved in wave-trench interaction, with relative wave number; $h_1/h = 1.75$, $h_2/h = 0.25$, $\ell/h = 3.95$, $\rho_2/\rho_1 = 1.05$.

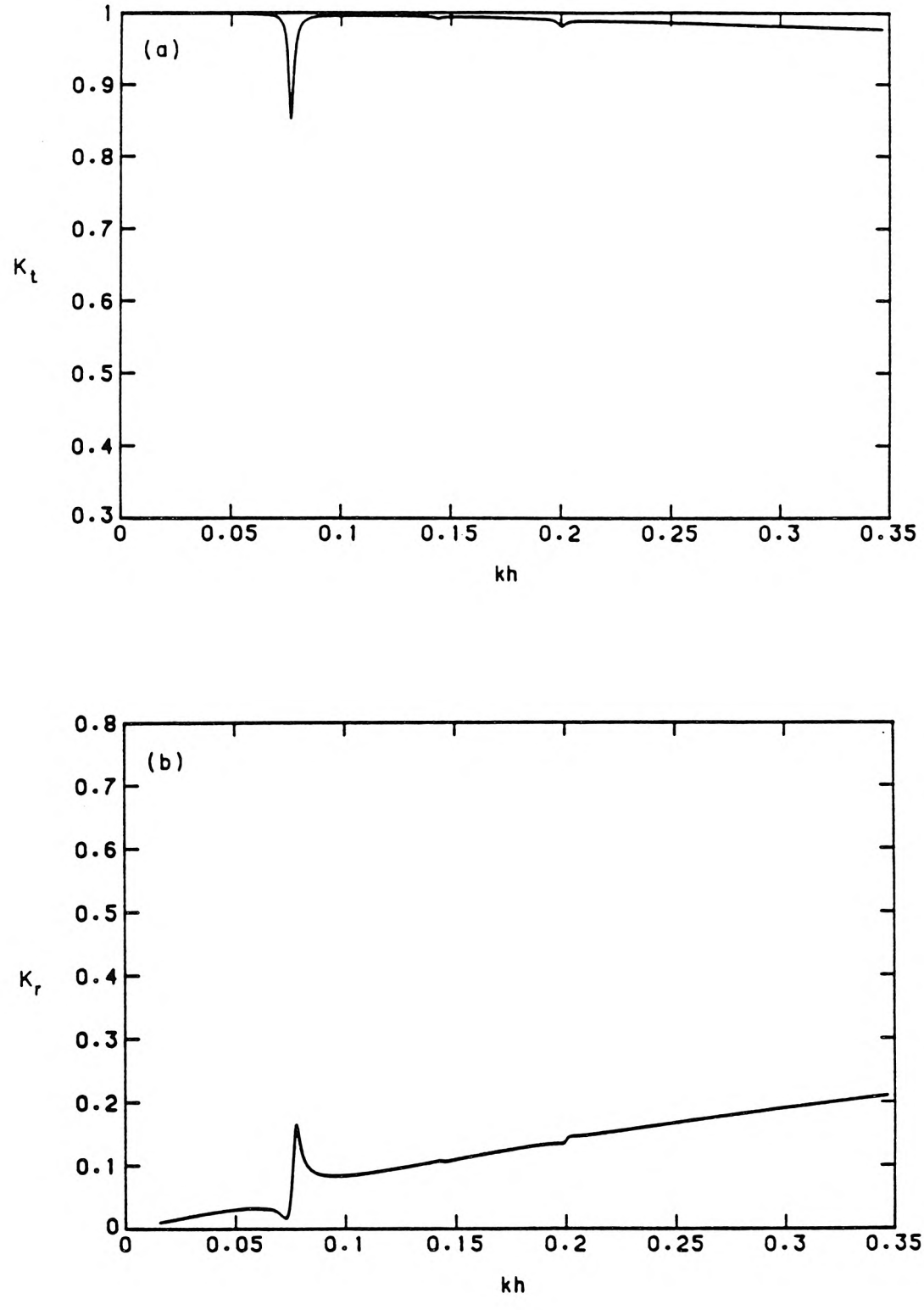

Figure 5.3.10. Variation of (a) transmission coefficient, and (b) reflection coefficient, with relative wave number; $h_1/h = 1.75$, $h_2/h = 0.25$, $\ell/h = 3.95$, $\rho_2/\rho_1 = 1.05$.

lower fluid to the shallow lower fluid, thus if the damping rates were the same in both cases, the energy loss in Case a should be about four times of the energy loss in Case d. The energy loss in the trench region is proportional to $(1 - K_r^2 + K_t^2)$. It is seen in figures 5.3.4 and 5.3.9*b* that the energy loss in the shallow lower fluid is equal to nearly half of that in the deep lower fluid, thus the damping rate must have increased substantially. This is no doubt due to larger shear stress developed near the bottom in the shallow lower fluid, that is, Case d compared to Case a. For the transmission and reflection coefficients presented in figures 5.3.10*a* and 5.3.10*b*, it is seen that the effects of the internal waves on the incident waves are reduced substantially as the relative depth of the upper layer is increased from $h_1/h = 1.5$ (Case a) to $h_1/h = 1.75$ (Case d).

5.3.5 Case e ($h_1/h = 1.5$, $h_2/h = 3.5$, $\ell/h = 3.95$, $\rho_2/\rho_1 = 1.05$)

To demonstrate the effect of a deep lower fluid, the value of h_2/h is increased to 3.5 while the other aspect ratios are held fixed. Comparing figure 5.3.11*a* with figure 5.3.1*a*, it is seen that the resonant peaks of the first three modes of oscillation are shifted towards higher frequencies, indicating that for the same value of kh the wavelength of the internal wave is longer in the deep lower fluid. The values of kh for the first five resonant peaks are found to be: 0.133, 0.197, 0.243, 0.281, and 0.315. The corresponding values of $K_2\ell$ are: 1.01π, 2.0π, 2.99π, 3.97π, and 4.95π. A striking feature in figure 5.3.11*a* is the substantial increase in the bandwidth of the lowest mode of oscillation. Comparing figure 5.3.11*a* to 5.3.1*a*, it is seen that the effect of increasing the depth of the lower fluid on the response curve is decreasingly smaller for larger values of kh. This is reasonable because, as the value of kh increases, the wavelength of the internal wave decreases, therefore the actual depth of the lower fluid becomes less significant. The large reduction in energy loss for the lowest mode of oscillation shown in figure 5.3.11*b* is no doubt due to the

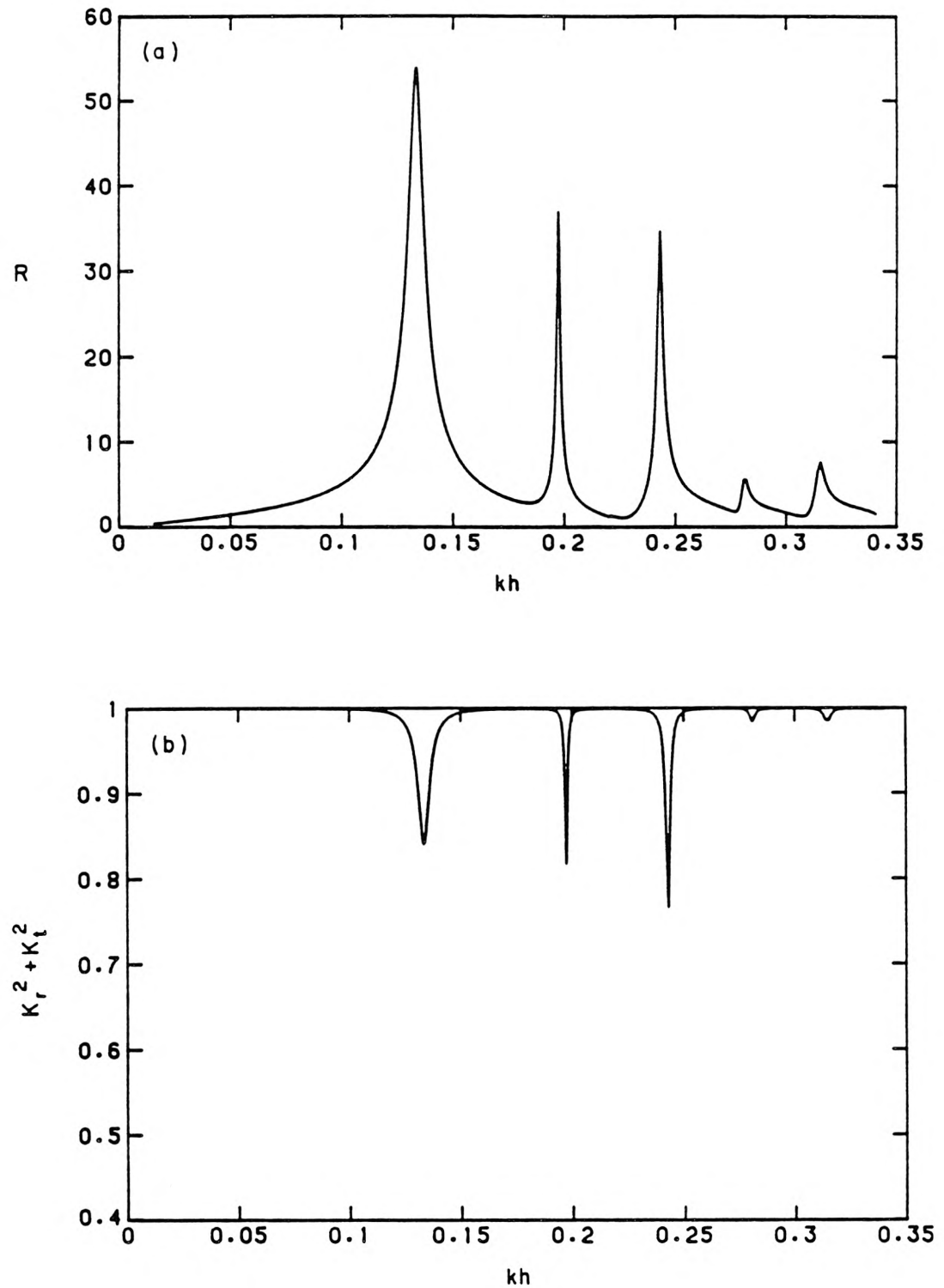

Figure 5.3.11. Variation of (a) amplification factor, and (b) incident wave energy conserved in wave-trench interaction, with relative wave number; $h_1/h = 1.5$, $h_2/h = 3.5$, $\ell/h = 3.95$, $\rho_2/\rho_1 = 1.05$.

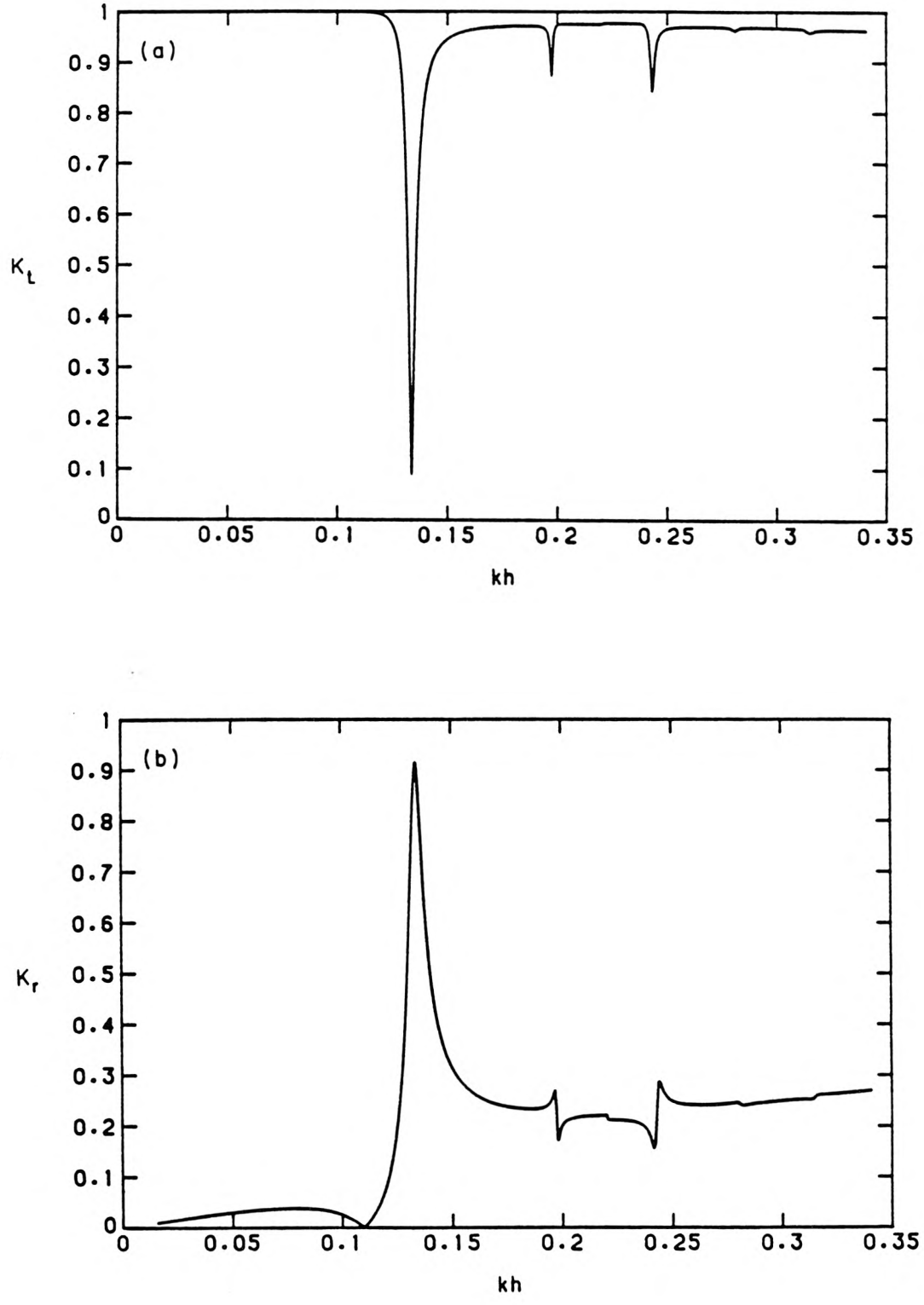

Figure 5.3.12. Variation of (a) transmission coefficient, and (b) reflection coefficient, with relative wave number; $h_1/h = 1.5$, $h_2/h = 3.5$, $\ell/h = 3.95$, $\rho_2/\rho_1 = 1.05$.

lack of significant attenuation by bottom friction. The internal waves in the deep lower fluid do not induce near the trench bottom any motions that can lead to large shear stress in the bottom boundary layer. Consequently, the dominant cause of wave attenuation is energy dissipation in shearing motions in the boundary layers adjacent to the density interface. We caution that damping due to the vertical walls at $x = 0$ and $x = \ell$, which is ignored in the present analysis, may be important in this situation. It is interesting to see that the energy loss is actually larger for the second and the third modes of oscillation, even though the value of the amplification factor for the higher modes is smaller. These results suggest that the damping rate due to the interfacial boundary layers increases as the modal number increases, for these flow conditions. The transmission and reflection coefficients are presented in figures 5.3.12*a* and 5.3.12*b*, respectively.

5.3.6 Application of the Two-Layer Theory to Prototype Situations

In the previous discussion we have demonstrated that the surface wave conditions responsible for the oscillation of internal waves in a trench generally would fall in the range of long waves, that is $h/\lambda < 0.05$, where λ is the wavelength of the incident wave. This was demonstrated experimentally in § 5.2 for a relatively narrow trench compared to the fluid depths. Thus, long waves that might produce resonant conditions in a harbor could also be responsible for the oscillation of internal waves in a navigation channel. To further illustrate the importance of internal resonance in stratified trenches, we consider a typical navigation trench as shown in figure 5.3.13. The depth of the homogeneous fluid in the infinite region is $h = 6\,\mathrm{m}$ (20 ft), the depth of the trench is $d = 9\,\mathrm{m}$ (30 ft), and the width of the trench is $\ell = 300\,\mathrm{m}$ (1000 ft). A layer of heavier fluid of depth $h_2 = 3\,\mathrm{m}$ (10 ft) lies next to the trench bottom. Let us consider the situations where the heavier fluid is due to sedimentation of suspended sediments, as discussed in Chapter 1. In a study by the

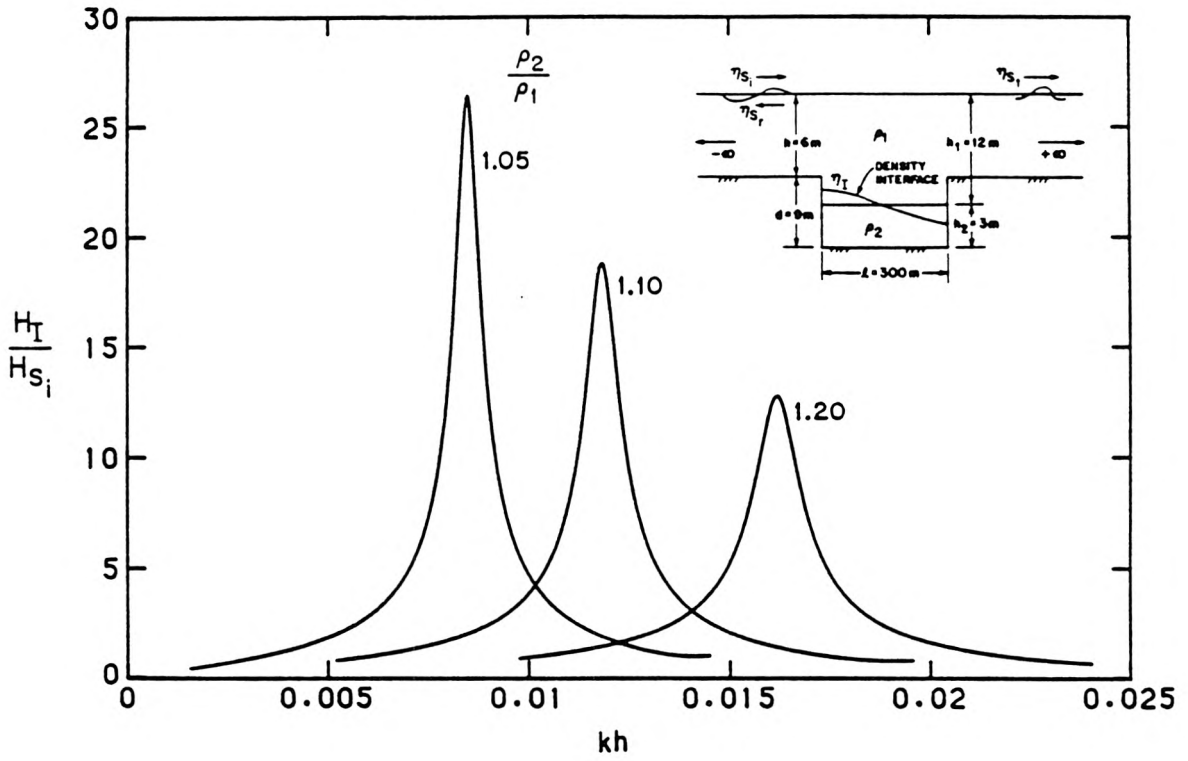

Figure 5.3.13. Variation of amplification factor with relative wave number for the lowest mode of internal resonance in a navigation channel for different values of the density ratio ρ_2/ρ_1.

Marine Board of the National Research Council (1983) on criteria for the depths of dredged navigational channels it was reported that at Europort (Holland) the bottom was defined as a region where the specific gravity of the fluid was larger than 1.2. Hence, let us examine the responses of the trench for three different density ratios of the lower fluid to the upper fluid ρ_2/ρ_1, these are given as: 1.05, 1.1, and 1.2, respectively. The response curves for the lowest mode of oscillation for the three cases are presented in figure 5.3.13. For $\rho_2/\rho_1 = 1.05$, the relative wave number kh of resonant oscillation is found to be 0.0085, the corresponding value of the amplification factor is 26.44. As ρ_2/ρ_1 increases, the resonant frequency also increases, whereas the amplification factor decreases. The former is due to the effects of the increase in the restoring force at the density interface, and the latter is

related to the increase in the potential energy required for a given deformation of the density interface, as the density difference between the two fluids increases. The relative wave number kh of resonant oscillation is 0.0118 for $\rho_2/\rho_1 = 1.10$, the corresponding value of the amplification factor is 18.81. For $\rho_2/\rho_1 = 1.2$, the relative wave number kh of resonant oscillation is increased to 0.0162, and the amplification factor of the resonant peak is reduced to 12.79. The wave periods of the lowest mode of resonant oscillation for the above three cases are, respectively, 9.6 minutes, 6.9 minutes, and 5.2 minutes. These wave periods are commonly observed in harbor resonance. As the relative length ℓ/h increases, the resonant modes of oscillation of the internal waves occur at increasingly larger wave periods for the same modal number n, whereas the number of resonant modes of oscillation increases within a given range of wave periods. Hence, the fluid motion in a wide trench is more susceptible to internal resonance than in a narrow trench.

The above examples illustrate that, for a resonant condition of the internal waves in the navigation channel, the internal waves can attain large amplitudes relative to the amplitude of the incident surface waves.

It is expected that internal waves at resonance may induce large shearing motions near the trench boundaries compared to a trench of the same geometry in a homogeneous fluid, for the same incident wave conditions. This result may be obtained by comparing the horizontal velocity on the trench bottom due to the internal wave, to that due to the surface wave. Assuming long waves and small density difference, an estimate for the horizontal velocities in the lower layer is given by (3.3.5a) and (3.3.5b), respectively, for the surface wave and the internal wave. The ratio of the horizontal velocities is:

$$\frac{U_I}{U_S} = \frac{H_I}{H_S}\sqrt{\left(1 - \frac{\rho_1}{\rho_2}\right)\frac{h_1}{h_2}} \tag{5.3.8}$$

where the subscripts S and I denote the surface wave and the internal wave, re-

spectively. Notice that in (5.3.8), if the wave height of the surface wave and the wave height of the internal wave are the same, the internal wave has much smaller particle velocity than the surface wave because the phase speed of the internal wave is only a fraction of that of the surface wave. However, for a resonant condition of the internal wave in the trench, the amplitude of the internal wave is substantially larger than the amplitude of the wave on the water surface, hence the ratio U_I/U_S is much larger than unity. For the vertical velocity, in a homogeneous fluid the amplitude of the vertical velocity decreases with distance from the water surface, whereas in a two-layer fluid the amplitude of the vertical velocity is the largest at the density interface for the internal wave. Hence, for a resonant condition of the internal waves in the trench, the internal waves can attain large amplitudes relative to those of the surface waves, which result in local velocities near the trench boundaries that may be significantly larger than those corresponding to a non-stratified fluid, leading to more serious bottom erosion.

We have discussed that long surface waves are generally responsible for internal resonance in navigational channels. Is it possible for "packets" of much shorter waves, which have a long period of amplitude modulation, to excite the resonant oscillation of internal waves in the trench? The answer to this question is negative within the framework of a linear theory. This is because we can consider the wave groups to be made up of two progressive waves of slightly different frequencies σ_1 and σ_2 travelling in the same direction. Then the period of amplitude modulation of the wave groups is given by $\sigma = (\sigma_2 - \sigma_1)/2$. This is the familar problem of "beat effect" in linear wave theory. If σ is the resonant frequency for the oscillation of internal waves in the trench, then the two periodic wave components (of frequencies σ_1 and σ_2) both lead to off-resonant conditions in the trench. Therefore, by linear superposition, the amplitude of the resulting internal wave motion due to the wave groups will also be small.

It should be noted that the theoretical results presented in § 5.3.1–§ 5.3.5 are based on the assumption of laminar flow in the boundary layers. These results are presented to show the sensitivity of the internal oscillations to viscous effects. Indeed, dissipation of internal wave energy due to boundary friction is found to significantly reduce the amplitude of the internal waves in the trench. The boundary layers are probably turbulent in prototype conditions, and the damping rates for the surface and internal waves should be determined based on turbulent flows in the boundary layers. For turbulent flow a theoretical analysis of the velocity distribution within an oscillatory boundary layer had been carried out by Kajiura (1964). This assumes a turbulent eddy viscosity which is a function of space and time. The analysis leads to a quadratic drag law, which relates the bottom shear stress to the amplitude of the inviscid velocity on the bottom by a drag coefficient. The drag coefficient is a function of the wave Reynolds number $\mathrm{Re} = u_B A_B/\nu$, and the relative bottom roughness A_B/k_S, where u_B is the inviscid velocity on the bottom, A_B is the amplitude of the bottom fluid particle displacement based on inviscid theory, and k_S is the equivalent roughness. This relationship is analogous to the dependency of the friction factor for unidirectional steady flow. The wave friction factor diagram, which is similar to the Moody chart, was given by Jonsson (1966). Once the bottom shear stress is known, the attenuation rate can be found using the method of energy balance in a similar manner to the treatment presented in § 3.3.2 for laminar flow. In reality, it is not easy to determine the roughness length scale because of sand ripples and other roughness elements that may be found on a natural sea bottom.

So far we have only considered steady-state wave motions. As a final comment it should be noted that because surface waves in the ocean may be assumed steady for only a short duration, it is important to know the time required for the internal waves in the trench to reach steady-state conditions for a time-periodic surface

wave that propagates over the trench. The theoretical time history of the internal oscillations in the trench can be computed from the steady-state solutions by Fourier superposition. Because this has not been done we will discuss the transient motion only qualitatively.

The forced internal oscillations in the trench are due to the pressure force exerted by the surface waves on the density interface that displaces the heavier fluid and brings buoyancy effects into action. The simple-harmonic motion produced by the restoring force as a result of the displacement of the interface from its quiescent position has a circular frequency equal to the buoyancy frequency $\mathcal{N}$. Therefore, a characteristic time for the interface to adjust to a vertical displacement is given by $1/\mathcal{N}$. The surface waves propagate past the trench in a time of order ℓ/C_1, where ℓ is trench width and C_1 is the wave speed due to the surface wave. Hence, the ratio of the adjustment time to the displacement time is given by:

$$F_I = \frac{C_1}{\mathcal{N}\ell} \tag{5.3.9}$$

where F_I is the internal Froude number. The internal Froude number is a measure of the relative importance of the advective effect to the buoyancy effect. If $F_I < 1$ the density interface can adjust to the advective motion of the surface wave and maintain the internal oscillation. If $F_I > 1$ the stratified fluid will have sufficient momentum to overcome the buoyancy forces and the fluid will behave as if it were homogeneous.

Assuming long waves in a two-layer fluid, the frequency of resonant oscillation of the internal waves in the trench is given by $\sigma_n = (n\pi/\ell)C_2$, $(n = 1, 2, \ldots)$ with C_2 given by (5.3.5). Hence, the internal Froude number is proportional to $C_1/\sqrt{\epsilon}$, where $\epsilon = (\rho_2 - \rho_1)/\rho_2$, and C_1 is given by (5.3.4).

If the density difference between the upper fluid and the lower fluid is small compared to unity, the phase speed of the surface wave is much larger than that of

the internal wave in the trench for the same wave period. It follows from the above discussion that appreciable internal motions cannot be developed in the trench within a few oscillations. Similar reasoning also leads to the conclusion that a solitary wave will have a negligible effect on the density interface, because $F_I \gg 1$ for $\epsilon \ll 1$. For a steady train of time-periodic progressive waves with a frequency close to the resonant frequency of the internal waves in the trench, the time required to establish steady-state conditions in the trench will be primarily controlled by friction. The number of transient oscillations will be smaller for internal waves in a shallower lower fluid, due to the larger shearing motions adjacent to the trench bottom. The initial growth of the amplitudes of the internal waves at the trench walls at $x = 0$ and $x = \ell$ will be approximately linear with time for the lowest mode of internal oscillation. This can be seen from the results of the experiments for wave motions in the water filled constant-depth channel discussed in § 5.2.1. In those experiments, the wave amplitude at the end wall increased about every four oscillations initially because it took the primary reflected wave from the end wall a time of four wave periods to travel twice the length of the channel and superimpose constructively on the primary incident wave; there were about two wavelengths in the constant-depth channel. A similar situation will happen for internal waves in a trench during transient oscillations. For the lowest resonant mode, it takes only one wave period for the internal wave to travel twice the width of the trench and be constructively reinforced, but it will take a longer time for the internal waves of the higher resonant modes to do the same.

6. CONCLUSIONS

6.1 Interaction of Water Waves with a Stratified Rectangular Trench

The major objective of this study has been to investigate, experimentally and theoretically, the dynamics of internal resonance in a rectangular trench due to time-periodic surface waves that propagate in a direction perpendicular to the longitudinal axis of the trench; the trench is partially filled with a heavier fluid and the fluid outside the trench is homogeneous. Also of interest are the effects of resonant oscillations of the internal waves in the trench on the waves on the free surface.

Much of the investigation was done with a particular combination of constant-depth channel and trench used in the experiments. This is because the case of a trench in an infinite region could not be modelled in the laboratory due to wave reflections from the ends of the wave tank. A linear two-layer model and a linear three-layer model were developed to study this problem, these models include a vigorous treatment of the effects of energy dissipation in the boundary layers adjacent to the density interface and at the solid surfaces; the flows in the boundary layers are assumed to be laminar. The theoretical predictions that were obtained using these models were compared to the experimental measurements. The problem of wave propagation over a rectangular trench with a two-layer fluid in the trench and a homogeneous fluid in an infinite region outside the trench was studied theoretically. The following major conclusions can be drawn from this investigation:

1. Wave motions at the dye interface of fresh water and salt water can be measured in real time using a scanning laser beam and detector system. The dye interface coincides with the top of the diffuse salinity interface in the quiescent fluid. Wave-induced mixing of the fresh water and the dyed salt water limits the wave motions that can be measured with this instrument to those with a sharp dye interface.

2. For the lowest mode of oscillation of the internal waves in the trench, the wavelength of the surface waves in the constant-depth channel was large compared to the wavelength of the internal waves and the trench dimensions. When the constant-depth channel and the trench were filled with fresh water, the effects of the change in water depth in the trench region on the surface waves were very small. The effects of flow separation at the upstream edge of the trench on the free surface motions were not apparent in these experiments.

3. For a stratified fluid in the trench, when the frequency of the surface waves in the constant-depth channel corresponded to the natural frequency of the internal waves in the trench, the internal waves attained large amplitudes relative to the amplitudes of the surface waves.

4. The predicted wave heights of the internal waves in the trench using the linear theory agreed quite well with the experimental measurements, even when nonlinear effects were significant. The linear theory did not do so well in predicting the amplitudes of the wave crest and the wave trough, due to nonlinear effects in the experimentally recorded wave profiles. The effects of viscosity and density stratification on the frequencies of resonant oscillation of the internal waves in the trench were predicted well by the linear theory.

5. The experimental results indicated that when the ratio of the internal wave height to the depth of the lower fluid is small compared to the product of the

depth of the lower fluid and the wave number of the internal wave, that is, when $H_I/K_2h_2^2 \ll 1$, second order effects in the standing internal wave profiles were small. (The variables H_I, K_2, and h_2 are, respectively, the internal wave height, the internal wave number, and the depth of the lower fluid.)

6. When the value of the dimensionless parameter, $H_I/K_2h_2^2$, was small the experimentally recorded profiles of the density interface compared well with the finite amplitude standing internal wave solutions of Thorpe (1968).

7. The response characteristics of the stratified fluid in the trench for wave periods near trench resonance tend to be an effective linear filter for higher frequency components in the surface waves.

8. When the dimensionless parameter, $H_I/K_2h_2^2$, was increased by decreasing the depth of the lower fluid h_2, nonlinear effects in the internal motions in the trench became more apparent. The observed waveforms were non-symmetrical about the still density interface, and the internal wave looked like a single "hump" travelling back and forth between the vertical walls of the trench.

9. The frequency of resonance of the internal waves in the trench decreased as the thickness of the diffuse salinity interface increased. This frequency shift was predicted well by the three-layer viscous theory, and also by the three-layer inviscid theory when viscous effects were small. The effects of the density transition region on the trench response were more pronounced when the depth of the lower fluid was decreased.

10. When the thickness of the diffuse salinity interface was small compared to the wavelength of the internal waves and the fluid depths, the difference between the frequencies of resonance of the internal waves in the trench as predicted by the two-layer theory and the three-layer theory was very small.

11. Viscous effects on the internal motions in the trench were more important when

the depth of the lower fluid was small compared to the wavelength of the internal waves. The ratio of the amplitude of the internal waves in the trench relative to the amplitude of the surface waves decreased substantially compared to that for a deeper lower fluid. The experimentally recorded wave heights and the resonant frequencies of the internal waves agreed quite well with the predictions of the linear viscous theory. The linear inviscid theory could not predict the frequency shift in the response curve due to viscous effects.

12. It was shown experimentally that the damping of the internal waves in the trench could be related to constant values of the modulus of decay, even when nonlinear effects were significant. The two-layer viscous theory predicted the wave height of the internal motions better than the three-layer viscous theory; the two-layer viscous theory overestimated energy dissipation in the trench, whereas the three-layer viscous theory underestimated damping significantly.

13. The effects of internal oscillations on the waves on the free surface were negligible for these experiments.

14. The two-layer model was applied to the problem of a time-periodic progressive wave that propagates over a stratified rectangular trench in an infinite region. As mentioned earlier this problem could not be investigated in the laboratory so the following conclusions are solely based on the theoretical model:

    a) Resonant oscillations of internal waves in the trench occur when $K_2\ell = n\pi$, $(n = 1, 2, \ldots)$, where K_2 is the wave number of the internal wave and ℓ is the trench width.

    b) The trench response is very sensitive to viscous effects near the frequencies of resonant oscillation of the internal waves; a small degree of damping reduces the response predicted using the two-layer inviscid theory substantially. The lowest mode of oscillation has the largest amplification factor and

frequency bandwidth. The asymmetric modes ($n = 1, 3, 5, \ldots$) have larger amplification factors and frequency bandwidths compared to the symmetric modes ($n = 2, 4, 6, \ldots$).

c) A significant portion of the incident wave energy can be dissipated in a stratified trench when the internal waves in the trench are "at resonance." When the internal waves are "off resonance," the energy of the incident wave is nearly completely conserved in the process of wave-trench interaction.

d) Large reflections of incident waves occur when the frequencies of the surface waves correspond to the frequencies of resonant oscillation of the internal waves in the trench, that is, when $K_2\ell = n\pi$, ($n = 1, 2, \ldots$). For these conditions the wavelengths of the surface waves are large compared to the width and depth of the trench.

e) The reflection coefficient of surface waves also has maximum values when $K_1\ell = (n - \frac{1}{2})\pi$, ($n = 1, 2, \ldots$), where K_1 is the wave number of the surface waves in the trench region. For these conditions the wavelengths of the surface waves and the width and depth of the trench are of the same order of magnitude.

f) A case study using prototype dimensions of a navigation channel and typical density ratios indicates that the wave periods corresponding to internal resonance can also be found in resonant conditions for surface waves in harbors. When the internal waves are "at resonance," local velocities near the trench boundaries could be significantly larger than those corresponding to a non-stratified fluid in the trench, thus internal resonance could lead to more serious bottom erosion.

6.2 Recommendations for Future Studies

Some knowledge of the dynamics of the interaction of water waves with a stratified fluid in a rectangular trench are gained in this study. However, this work does not present the results in a comprehensive model that would incorporate nonlinear effects, arbitrary density stratifications, and variable trench geometries. Instead, some aspects of these physical effects were investigated theoretically and experimentally, while many uncertainties still remain that need further investigation:

1. The theoretical results of this study were obtained by matching solutions of the trench region and the region of the constant-depth channel along vertical boundaries at the edges of the trench. The effects of flow separation, which are most acute at these locations, are neglected in the analysis. Flow separation effects were not apparent in the experiments, possibly because the location of the trench was near an antinode of the standing surface waves, due to the end wall at the downstream edge of the trench. Hence, the amplitude of the horizontal velocity near the "mouth" of the trench in the experiments might be substantially less than that for a trench in an infinite region. As a way to investigate the effects of flow separation, a node of the standing surface waves can be established above the trench by placing the end wall further downstream. This problem can be formulated theoretically and the results compared directly to measurements of surface and internal motions as well as fluid velocities in the trench region.

2. The above arrangement of the constant-depth channel and trench also allows the effects of internal oscillations on transmission and reflection of surface waves to be investigated in the laboratory. For instance, if large reflections of surface waves occur for a resonant mode of oscillation of the internal waves in the trench, the corresponding free surface motions in the constant-depth channel

downstream of the trench would be different from those when the trench is "off resonance."

3. It has been assumed throughout this study that the time-periodic surface waves propagate in a direction perpendicular to the longitudinal axis of the trench. The more general problem of propagation of obliquely incident waves over a trench where the depths before and after the trench are constant but not necessarily equal can be treated in a similar manner.

4. This study has not considered the effects of variable trench geometry, and trapezoidal channels are commonly found in harbors. The shearing motions on the slopes of a trapezoidal channel might be significantly larger than that on the vertical walls of a rectangular trench, thus leading to more serious erosion during conditions of internal resonance. For the linear problem, the variable trench geometry can be handled in a straightforward manner by standard finite element methods. We have formulated the finite element problem for the linear case though the results are not presented here. In reality, the run-up and run-down of internal waves on the slopes of a trapezoidal channel may change the dynamics of internal oscillations in the trench in important ways. Recently, Zelt (1986) developed a finite element model based on a set of long wave equations in the Lagrangian description, which can compute the run-up of non-breaking surface waves on sloping boundaries with an arbitrary curved shoreline. A similar formulation for a two-fluid system may be useful for studying the effects of run-up and run-down of internal waves on trench resonance.

5. For a rectangular trench, the nonlinear problem can be formulated by developing the solutions in the trench region and in the constant-depth channel using nonlinear long wave equations. The final solution is obtained by imposing continuity of total mass flow and surface elevation at the vertical boundaries at the

upstream and downstream edges of the trench. Generalized long wave equations of the Boussinesq class for a two-layer fluid of constant depths have been developed by Zhu (1986) and applied to study the problem of internal solitons generated by moving bottom obstacles.

REFERENCES

Bartholomeusz, E. F. 1958 The reflexion of long waves at a step. *Proc. Cambridge Phil. Soc.* **54**, 106-118.

Benjamin, T. B. 1966 Internal waves of finite amplitude and permanent forms. *J. Fluid Mech.* **25**, 241-270.

Benjamin, T. B. 1967 Internal waves of permanent form in fluids of great depth. *J. Fluid Mech.* **29**, 559-592.

Biesel, F. 1949 Calcul de l'amortissement d'une houle dans un liquide visqueux de profondeur finie. *La Houille Blanche* **4**, 630-634.

Burnside, W. 1889 On the small wave-motions of a heterogeneous fluid under gravity. *Proc. London Math. Soc.* **20**, 392-397.

Carnahan, B., Luther, H. A. & Wilkes, J. O. 1969 *Applied Numerical Methods.* John Wiley & Sons.

Case, K. M. & Parkinson W. C. 1957 Damping of surface waves in an incompressible liquid. *J. Fluid Mech.* **2**, 172-184.

Chernous'ko, F. L. 1966 On free oscillations of a viscous fluid in a vessel. *J. Appl. Math. Mech.* **30**, 990-1003.

Dean, R. G. & Ursell, F. 1959 Interaction of a fixed, semi-immersed circular cylinder with a train of surface waves. *Report No. 37, Ralph M. Parsons Laboratory for Water Resources and Hydrodynamics, Massachusetts Institute of Technology.*

Dean, R. G. & Dalrymple, R. A. 1984 *Water Waves Mechanics for Engineers and Scientists.* Prentice-Hall.

Dore, B. D. 1968 Oscillations in a non-homogeneous viscous fluid. *Tellus* **20**, 514-523.

Dore, B. D. 1969a A contribution to the theory of viscous damping of stratified wave flows. *Acta Mechanica* **8**, 25-33.

Dore, B. D. 1969b The decay of oscillations of a non-homogeneous fluid within a container. *Proc. Cambridge Phil. Soc.* **65**, 301-307.

Gill, A. E. 1982 *Atmosphere-ocean dynamics*. Academic Press.

Goring, D. G. 1978 Tsunamis: The propagation of long waves onto a shelf. *Report No. KH-R-38, W. M. Keck Laboratory of Hydraulics and Water Resources, California Institute of Technology.*

Hammack, J. L. 1972 Tsunamis: A model of their generation and propagation. *Report No. KH-R-28, W. M. Keck Laboratory of Hydraulics and Water Resources, California Institute of Technology.*

Hammack, J. L. 1980 Baroclinic Tsunami Generation. *J. Physical Oceanography* **10**, 1455-1467.

Hannoun, I. A. & List, E. J. 1988 Turbulent mixing at a shear-free density interface. *J. Fluid Mech.* **189**, 211-234.

Harrison, W. J. 1908 The influence of viscosity on the oscillations of superposed fluids. *Proc. London Math. Soc.* **6**, Ser. 2, 396-405.

Head, M. J. 1983 The use of miniature four-electrode conductivity probes for high resolution measurement of turbulent density or temperature variations in salt-stratified water flows. PhD thesis, University of California, San Diego.

Helal, M. A. & Molines, J. M. 1981 Non-linear internal waves in shallow water. A theoretical and experimental study. *Tellus* **33**, 488-504.

Hunt, J. N. 1952 Viscous damping of waves over an inclined bed in a channel of finite width. *La Houille Blanche* **6**, 836-842.

Hunt, J. N. 1961 Interfacial waves of finite amplitude. *La Houille Blanche* **16**, 515-525.

Imberger, J. 1986 *Personal communication.*

Johns, B. 1968 A boundary layer method for the determination of the viscous damping of small amplitude gravity waves. *Quart. J. Mech. Appl. Math.* **21**, 93-103.

Jonnson, I. G. 1966 Wave boundary layers and friction factors. *Proc. 10th Intl Conf. Coastal Engng., Tokyo, Japan, ASCE,*. 127-148.

Jonsson, I. G. 1978 A new approach to oscillatory rough turbulent boundary layers.

Series Paper 17, Institute of Hydrodynamics and Hydraulic Engineering, Technical University of Denmark.

Kelly, R. E. 1969 Wave diffraction in a two-fluid system. *J. Fluid Mech.* **36**, 65-73.

Keulegan, G. H. 1959 Energy dissipation in standing waves in rectangular basins. *J. Fluid Mech.* **6**, 33-50.

Kirby, J. T. & Dalrymple, R. A. 1983 Propagation of obliquely incident water waves over a trench. *J. Fluid Mech.* **133**, 47-63.

Kreisel, G. 1949 Surface waves. *Quart. Appl. Math.* **7**, 21-44.

Lamb, H. 1945 *Hydrodynamics*. Dover. 1932 editon.

Lassiter, J. B. 1972 The propagation of water waves over sediment pockets. PhD thesis, Massachusetts Institute of Technology.

Lee, J. J., Ayer, R. M. & Chiang, W. L. 1980 Interactions of waves with submarine trenches. *Proc. 17th Intl Conf. Coastal Engng., Sydney, Australia, ASCE,*. 812-822.

Lee, J. J. & Ayer, R. M. 1981 Wave propagation over a rectangular trench. *J. Fluid Mech.* **110**, 335-347.

Lepelletier, T. G. 1980 Tsunamis: Habors oscillations induced by nonlinear transient long waves. *Report No. KH-R-41, W. M. Keck Laboratory of Hydraulics and Water Resources, California Institute of Technology.*

Lighthill, J. 1978 *Waves in Fluids*. Cambridge University Press.

Love, A. E. H. 1891 Wave-motion in a heterogeneous heavy fluid. *Proc. London Math. Soc.* **22**, 307-316.

Marine Board (National Research Council) 1983 Criteria for the depths of dredged navigational channels. *Wastington, D. C.: National Academy Press.*

Mei, C. C. & Black, J. L. 1969 Scattering of surface waves by rectangular obstacles in waters of finite depth. *J. Fluid Mech.* **38**, 499-511.

Mei, C. C. & Liu, L. F. 1973 The damping of surface gravity waves in a bounded liquid. *J. Fluid Mech.* **59**, 239-256.

Mei, C. C. 1983 *The Applied Dynamics of Ocean Surface Waves*. Wiley-Interscience.

Miles, J. W. 1967 Surface-wave scattering matrix for a shelf. *J. Fluid Mech.* **28**, 755-767.

Miles, J. W. 1982 On surface-wave diffraction by a trench. *J. Fluid Mech.* **115**,

315-325.

Neumann, G. & Pierson, W. J. 1966 *Principles of Physical Oceanography*. Prentice-Hall.

Newman, J. N. 1965a Propagation of water waves past long two-dimensional obstacles. *J. Fluid Mech.* **23**, 23-29.

Newman, J. N. 1965b Propagation of water waves over an infinite step. *J. Fluid Mech.* **23**, 399-415.

Penny, W. G. & Price, A. T. 1952 Some gravity wave problems in the motion of perfect liquids. Part II. Finite periodic stationary gravity waves in a perfect liquid. *Phil. Trans. Roy. Soc. London* **244**, 254-284.

Raichlen, F. 1965 Wave-induced oscillations of small moored vessels. *Report No. KH-R-10, W. M. Keck Laboratory of Hydraulics and Water Resources, California Institute of Technology.*

Rattray, M. 1960 On the coastal generation of internal tides. *Tellus* **12**, 54-62.

Sanford, L. P. 1984 The interaction of high frequency internal waves and the bottom boundary layer on the continental shelf. PhD thesis, Joint Program in Oceanography and Oceanographic Engineering, Woods Hole Oceanographic Institution/Massachusetts Institute of Technology.

Skjelbreia, J. E. 1982 *Personal communication*.

Stokes, G. G. 1851 On the effect of the internal friction of fluids on the motion of pendulums. *Trans. Cambridge Phil. Soc.* **9**, part 2, 8-106.

Synolakis, C. E. 1986 The runup of long waves. PhD thesis, California Institute of Technology.

Tadjbakhsh, I. & Keller, J. 1960 Standing surface waves of finite amplitude. *J. Fluid Mech.* **8**, 442-451.

Thorpe, S. A. 1968 On standing internal gravity waves of finite amplitude. *J. Fluid Mech.* **32**, 489-528.

Ting, C. K. F. & Raichlen, F. 1986 Wave interaction with a rectangular trench. *J. Waterway, Port, Coastal and Ocean Engng., ASCE* **112**, No. 3, 454-460.

Turner, J. S. 1973 *Buoyancy Effects in Fluids*. Cambridge University Press.

Ursell, F. 1952 Edge waves on a sloping beach. *Proc. Roy. Soc. London* **A214**, 79-97.

Ursell, F., Dean, R. G. & Yu, Y. S. 1960 Forced small-amplitude water waves: A

comparison of theory and experiment. *J. Fluid Mech.* **7**, 33-52.

Whitham, G. B. 1974 *Linear and Nonlinear Waves*. Wiley-Interscience.

Wunsch, C. 1968 On the propagation of internal waves up a slope. *Deep Sea Res.* **15**, 251-258.

Wunsch, C. 1969 Progressive internal waves on slopes. *J. Fluid Mech.* **35**, 131-144.

Yanowitch, M. 1962 Gravity waves in a heterogeneous incompressible fluid. *Comm. Pure App. Math.* **15**, 45-61.

Yih, C. S. 1960 Gravity waves in stratified fluid. *J. Fluid Mech.* **8**, 481-508.

Yih, C. S. 1977 *Fluid Mechanics*. West River Press.

Yih, C. S. 1980 *Stratified Flows*. Academic Press.

Zelt, J. A. 1986 Tsunamis: The response of harbors with sloping boundaries to long wave excitation. *Report No. KH-R-47, W. M. Keck Laboratory of Hydraulics and Water Resources, California Institute of Technology*.

Zhu, J. 1986 Internal solitons generated by moving disturbances. Ph.D. thesis, California Institute of Technology.

APPENDIX

Transient Excitation of Long Waves in a Rectangular Channel

The problem is illustrated in figure A.1. A homogeneous fluid of depth h is contained in a rectangular channel of length L and width $2b$. Let (x, z) be a Cartesian coordinate system with the x axis on the undisturbed free surface and z measured positive upwards; the wave motion is assumed to be two-dimensional in the (x, z) plane. Surface waves are generated by a vertical boundary that moves in simple-harmonic motion at $x = 0$; a vertical wall is located at $x = L$. The long wave equations, which include nonlinear and dispersive effects, and viscous dissipation in a thin laminar boundary layer adjacent to the bottom had been derived by Lepelletier (1980). The corresponding linearized equations are:

$$\frac{\partial \eta}{\partial t} + h\frac{\partial u}{\partial x} = 0, \tag{A.1}$$

$$\frac{\partial u}{\partial t} + g\frac{\partial \eta}{\partial x} - \frac{h^2}{3}\frac{\partial^3 u}{\partial x^2 \partial t} + \frac{1}{h}\left(1 + \frac{h}{b}\right)\left(\frac{\nu\sigma}{2}\right)^{1/2}(1-i)u = 0 \tag{A.2}$$

wherein η is the surface displacement, u is the depth average horizontal velocity, g is the acceleration of gravity, ν is the kinematic viscosity, σ is the circular frequency given by 2π/wave period, and $i = \sqrt{-1}$. Dispersive and viscous effects, respectively, are given by the third and the fourth terms in (A.2). In order to account for dissipation due to friction at the side walls, the coefficient of the dissipation term

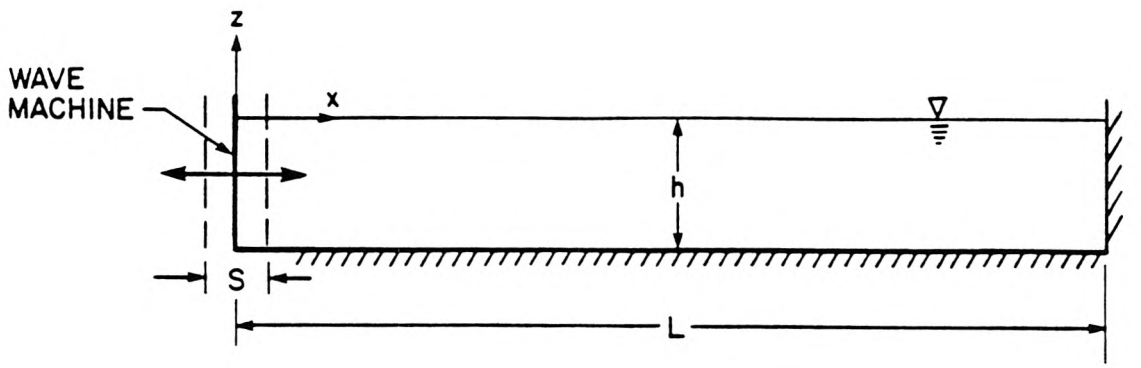

Figure A.1. Schematic drawing of the rectangular channel.

in (A.2) has been multiplied by $(1 + h/b)$. Equation (A.2) is slightly different from that obtained by Lepelletier (1980), which does not have the imaginary part in the dissipation term; this will be discussed. The initial conditions are:

$$\eta(x, 0) = 0, \qquad 0 < x < L, \tag{A.3}$$

$$u(x, 0) = 0, \qquad 0 < x < L. \tag{A.4}$$

The boundary conditions are:

$$u(0, t) = \frac{i}{2} S\sigma e^{-i\sigma t}, \qquad t > 0, \tag{A.5}$$

$$u(L, t) = 0, \qquad t > 0. \tag{A.6}$$

For simplicity, the variables are nondimensionalized as follows:

$$\eta^* = H\eta,$$

$$x^* = Lx,$$

$$t^* = \frac{L}{\sqrt{gh}}t,$$

$$u^* = \frac{H}{h}\sqrt{gh}\,u$$

where starred symbols represent the original dimensional variables. The characteristic wave height H can be determined from the following consideration: when the wave plate is displaced in the x direction a distance of $S/2$, the free surface rises by $H = Sh/2L$. In dimensionless form, equations (A.1)–(A.6) are given by:

$$\frac{\partial \eta}{\partial t} + \frac{\partial u}{\partial x} = 0, \tag{A.7}$$

$$\frac{\partial u}{\partial t} + \frac{\partial \eta}{\partial x} - \frac{\beta}{3}\frac{\partial^3 u}{\partial^2 x \partial t} + \gamma(1-i)u = 0, \tag{A.8}$$

$$\eta(x,0) = 0, \qquad 0 < x < 1, \tag{A.9}$$

$$u(x,0) = 0, \qquad 0 < x < 1, \tag{A.10}$$

$$u(0,t) = i\alpha e^{-i\alpha t}, \qquad t > 0, \tag{A.11}$$

$$u(1,t) = 0, \qquad t > 0 \tag{A.12}$$

where

$$\alpha = \frac{\sigma L}{\sqrt{gh}}, \tag{A.13}$$

$$\beta = \left(\frac{h}{L}\right)^2, \tag{A.14}$$

$$\gamma = \left(\frac{\nu\sigma}{2}\right)^{1/2}\left(1 + \frac{h}{b}\right)\frac{L}{h\sqrt{gh}}. \tag{A.15}$$

Eliminating η from (A.7) and (A.8), we obtain:

$$\frac{\partial^2 u}{\partial t^2} - \frac{\partial^2 u}{\partial x^2} - \frac{\beta}{3}\frac{\partial^4 u}{\partial x^2 \partial t^2} + (1-i)\gamma\frac{\partial u}{\partial t} = 0. \tag{A.16}$$

The steady-state solution of (A.16) can be written as:

$$u = u(x)e^{-i\alpha t}. \tag{A.17}$$

Substituting (A.17) into (A.16) yields:

$$\left(1 - \frac{1}{3}\beta\alpha^2\right)\frac{d^2u}{dx^2} + \alpha^2\left(1 + (1+i)\frac{\gamma}{\alpha}\right)u = 0. \tag{A.18}$$

From (A.18), and after using the boundary conditions (A.11) and (A.12), the steady-state solution is found to be:

$$u(x,t) = -\frac{i\alpha}{\sin k}\sin k(x-1)e^{-i\alpha t} \tag{A.19}$$

where

$$k = \frac{\alpha}{\left(1 - \frac{1}{3}\beta\alpha^2\right)^{1/2}}\left[1 + (1+i)\frac{\gamma}{2\alpha}\right] + O\left(\frac{\gamma^2}{\alpha^2}\right). \tag{A.20}$$

The wave number k given by (A.20) includes a term of $O(\gamma/\alpha)$; the real part is the viscous correction to the wavelength, and the imaginary part is the attenuation rate. It is well known in the theory of Stokes for an oscillatory boundary layer near a smooth wall that the shear stress and the tangential velocity are out of phase by $\pi/4$. Lepelletier (1980) neglected this phase shift and used an equivalent expression for the laminar shear stress that yields the same energy loss in a wave period. The consequence of this approximation is that the attenuation rate is of $O(\gamma/\alpha)$, whereas the viscous correction to the wavelength is only of $O(\gamma^2/\alpha^2)$.

From (A.7) and (A.19), the steady-state free surface displacement is found to be:

$$\eta(x,t) = -\frac{k}{\sin k}\cos k(x-1)e^{-i\alpha t}. \tag{A.21}$$

The transient problem is given by (A.16), with the following boundary conditions:

$$u(0,t) = 0, \qquad t > 0, \tag{A.22}$$

$$u(1,t) = 0, \qquad t > 0. \tag{A.23}$$

In addition, the transient solution must vanish as $t \to \infty$, that is:

$$u(x,\infty) = 0, \qquad 0 < x < 1. \tag{A.24}$$

The transient solution can be written in the form:

$$u(x,t) = u(x)e^{st}, \qquad \Re[s] < 0 \tag{A.25}$$

where $\Re$ denotes the real part of a complex number. Substitution of (A.25) into (A.16) yields:

$$\left(1 + \frac{1}{3}\beta s^2\right)\frac{d^2u}{dx^2} + s^2\left(-1 - (1-i)\frac{\gamma}{s}\right)u = 0. \tag{A.26}$$

From (A.26), and after using (A.22) and (A.23), we obtain:

$$u(x,t) = 2iC_n \sin a_n(x-1)e^{(ia_n + s_n t)} \tag{A.27}$$

where

$$a_n = n\pi, \qquad (n = 1,2,\ldots), \tag{A.28}$$

$$s_n = -\frac{\gamma}{2\left(1 + \frac{1}{3}\beta a_n^2\right)} - i\left[\frac{a_n}{\left(1 + \frac{1}{3}\beta a_n^2\right)^{1/2}} - \frac{\gamma}{2\left(1 + \frac{1}{3}\beta a_n^2\right)}\right], \qquad (n = 1,2,\ldots) \tag{A.29}$$

and C_n, $(n = 1,2,\ldots)$ are constants to be determined. From (A.7) and (A.27), we obtain:

$$\eta(x,t) = -\frac{2ia_nC_n}{s_n}\cos a_n(x-1)e^{(ia_n + s_n t)}. \tag{A.30}$$

The general solution must include the steady-state solution given by (A.21) and the transient solution given by (A.30), that is:

$$\eta(x,t) = -\frac{k}{\sin k}\cos k(x-1)e^{-i\alpha t} - \sum_{n=1}^{\infty}\frac{2ia_nC_n}{s_n}\cos a_n(x-1)e^{(ia_n + s_n t)}. \tag{A.31}$$

The unknown constants C_n are obtained by imposing the initial condition (A.9). The final solution is given by:

$$\eta(x,t) = -\frac{k}{\sin k}\cos k(x-1)e^{-i\alpha t} + \sum_{n=1}^{\infty}(-1)^n\frac{2k^2}{k^2 - a_n^2}\cos a_n(x-1)e^{s_n t}. \tag{A.32}$$

The dimensional form of (A.32) is given by (5.1.1).